Mathematical modeling of artificial ground freezing systems for mining industries

by

Ahmad Zueter

Submitted to the Department of Mining and Materials Engineering
in partial fulfillment of the requirements for the degree of

Doctor of Philosophy

at

McGill University

September 2022

Abstract

As Canada is aiming at net zero emissions by 2050, it is imperative for the mining industry to find and deploy engineering solutions which not only augment fossil-fuel consumption but also reduce the carbon footprint of mining operations. In this context, while artificial ground freezing (AGF) is a key geotechnical method to support mining infrastructure and contain industrial contaminants, AGF is an energy intensive technology releasing significant amounts of greenhouse gases. Further, many techniques applied in AGF systems to minimize the refrigeration load are not well-understood at the fundamental level due to the multi-scale and multi-physics nature of AGF operations. In order to explore engineering solutions that minimize energy expenditures and carbon footprint of AGF, it is vital to understand the thermophysical processes at the fundamental and applied levels, and then propose novel AGF systems of superior engineering and environmental performance. Accordingly, this thesis investigates two different types of AGF systems: 1) selective artificial ground freezing (S-AGF), which is employed in the Cigar Lake Mine (Saskatchewan, Canada) and 2) thermosyphon-based AGF employed in the Giant Mine (Northwest Territories, Canada).

S-AGF systems are currently employed in the Cigar Lake Mine to prevent infiltration of underground water towards the mining operations near the orebody at a depth of 400-460 meters by freezing the entire zone. This is achieved by circulating a refrigerated coolant through freeze-pipes installed from the surface. Since ground freezing is not needed above the orebody (above 400 meters depth), the freeze-pipes are insulated with an air cavity in this region to reduce the cooling load. In this thesis, we develop a fundamental and applied understanding of S-AGF systems. First, a fully-conjugate model is developed based on conservation principles of mass, momentum, and energy. This model helped in scaling the air insulation chamber to maximize its insulation capacity and thus reduce the overall cooling load of the system. Afterwards, reduced-order models based on space marching algorithms are created to mimic S-AGF systems in field scale. The reduced-order model is validated against experimental measurements in lab-scale and then verified with the fully-conjugate model in field-scale. The the reduced-order model decreases the computational time of fully-conjugate ones by 99%. This is essential in S-AGF systems due to their large zones (hundreds of meters) and long operational periods (several months to years), thus showing potential in industrial modeling. Lastly, the reduced-order model is implemented to investigate applied aspects of S-AGF systems, such as freeze-pipes eccentricity where, as compared with ideal concentric freeze-pipes, the cooling load is found to increase by 20% and the ground freezing process is delayed by 17%.

On the other hand, thermosyphon-based AGF systems are employed in the Giant Mine

to contain arsenic waste in underground chambers. Particularly, 100-meters deep thermosyphons are installed around the chambers to freeze the surrounding ground and therefore prevent arsenic from leaking. In this thesis, a thermal resistance network model is firstly derived and coupled with a ground freezing model based on the enthalpy-porosity method. The model is well-validated against field data obtained from the Giant Mine. While thermosyphons can operate passively in cold seasons by exploiting the cold energy of naturally available wind, they require energy-intensive mechanical refrigeration units to operate in warm seasons. Accordingly, a novel year-round sustainable AGF system is proposed in this thesis based on a ground-coupled cold-energy-storage system. Lastly, a fully-conjugate model is derived based on the conservation principles of mass, momentum, and energy for thermosyphon based AGF systems to investigate the boiling phenomena in deep thermosyphons considering the bubble nucleation theory.

Résumé

Alors que le Canada vise l'objectif de zèro émission nette d'ici 2050, il est impératif que l'industrie minière trouve et déploie des solutions d'ingénierie qui non seulement augmentent la consommation de combustibles fossiles, mais réduisent également l'empreinte carbone des opérations minières. Dans ce contexte, alors que la congélation artificielle du sol (AGF) est une méthode géotechnique clé pour soutenir les infrastructures minières et contenir les contaminants industriels, l'AGF est une technologie énergivore qui libère des quantités importantes de gaz à effet de serre. De plus, de nombreuses solutions énergétiques d'AGF ne sont pas bien comprises au niveau fondamental en raison de la nature multi-échelle et multi-physique des opérations AGF. Afin d'explorer des solutions d'ingénierie qui minimisent les dépenses énergétiques et l'empreinte carbone d'AGF, il est essentiel de comprendre les processus thermophysiques aux niveaux fondamental et appliqué, puis de proposer de nouveaux systèmes AGF aux performances techniques et environnementales supérieures. En conséquence, cette thèse étudie deux types différents de systèmes AGF : 1) la congélation artificielle sélective du sol (S-AGF), qui est utilisée à la mine de Cigar Lake (Saskatchewan, Canada) et 2) l'AGF à base de thermosiphon utilisée dans la mine Giant (Territoires du Nord-Ouest, Canada).

Les systèmes S-AGF sont actuellement utilisés dans la mine de Cigar Lake pour empêcher l'infiltration d'eau souterraine vers les opérations minières à proximité du corps minéralisé à une profondeur de 400 à 460 mètres en gelant toute la zone. Ceci est réalisé en faisant circuler un liquide de refroidissement réfrigéré à travers des tuyaux de congélation installés à partir de la surface. étant donné que la congélation du sol n'est pas nécessaire au-dessus du corps minéralisé (au-dessus de 400 mètres de profondeur), les tuyaux de congélation sont isolés avec une cavité d'air dans cette région pour réduire la charge de refroidissement. Dans cette thèse, nous développons une compréhension fondamentale et appliquée des systèmes S-AGF. Tout d'abord, un modèle entièrement conjugué est développé sur la base des principes de conservation de la masse, de la quantité de mouvement et de l'énergie. Ce modèle a aidé à mettre à l'échelle la chambre d'isolation d'air pour maximiser sa couche d'isolation et ainsi réduire la charge de refroidissement globale du système. Ensuite, des modèles d'ordre réduit basés sur des algorithmes de marche dans l'espace sont créés pour imiter les systèmes S-AGF à l'échelle du champ. Le modèle d'ordre réduit est validé par rapport à des mesures expérimentales à l'échelle du laboratoire, puis vérifié avec le modèle entièrement conjugué à l'échelle du terrain. Le modèle d'ordre réduit a réduit le temps de calcul des modèles entièrement conjugués de 99%. Ceci est essentiel dans les systèmes S-AGF en raison de leurs grandes zones (des centaines de mètres) et de leurs longues périodes de fonctionnement

(plusieurs mois à plusieurs années), montrant ainsi un potentiel en modélisation industrielle. Enfin, le modèle d'ordre réduit est mis en œuvre pour étudier les aspects appliqués des systèmes S-AGF, tels que l'excentricité des tuyaux de congélation où, par rapport aux tuyaux de congélation concentriques idéaux, la charge de refroidissement augmente de 20 à 200% et le processus de gel du sol est retardé de 17

D'autre part, des systèmes AGF à base de thermosiphon sont utilisés à la mine Giant pour contenir les déchets d'arsenic dans des chambres souterraines. Notamment, des thermosiphons de 100 mètres de profondeur sont installés autour des chambres pour geler le sol environnant et ainsi empêcher les fuites d'arsenic. Dans cette thèse, un modèle de réseau de résistance thermique est d'abord dérivé et couplé à un modèle de gel du sol basé sur la méthode enthalpie-porosité. Le modèle est bien validé par rapport aux données de terrain obtenues de la mine Giant. Alors que les thermosiphons peuvent fonctionner passivement pendant les saisons froides en exploitant l'énergie froide du vent naturellement disponible, ils nécessitent des unités de réfrigération mécaniques énergivores pour fonctionner pendant les saisons chaudes. En conséquence, un nouveau système AGF durable toute l'année est proposé dans cette thèse basé sur un système de stockage d'énergie froide couplé au sol. Enfin, un modèle entièrement conjugué est dérivé sur la base des principes de conservation de la masse, de la quantité de mouvement et de l'énergie pour les systèmes AGF à base de thermosiphon afin d'étudier les phénomènes d'ébullition dans les thermosiphons profonds compte tenu de la théorie de la nucléation des bulles.

To my parents, Hanan and Fawzi

To my sister, Reem

I love you

Acknowledgments

This dissertation has been a product of collaboration and support of lots of exceptional, talented, and caring people whom I have had the ultimate pleasure to know and work with. First, I would like to express my deep gratitude to my thesis advisor, Prof. Agus P. Sasmito. Your trust, guidance, empathy, and availability pushed me to excel and exceed my limits. I am genuinely lucky to have been supervised by you. Further, I would like to sincerely thank my PhD mentor Dr. Mahmoud Alzoubi; your support at the personal and professional levels in my 1st year will never be forgotten. I would like to also thank my colleagues at the Mine Multi-physics lab: Dr. Saad Akhtar, Minghan Xu, Saad Tareen, Mohmamad Roshan, Putra Gani, Ika Rahayu, and Matthew Fong. Our collaboration, ice-cream runs, group dinners and picnics, created unique memories that I will cherish forever.

This dissertation was made possible through the generous support from the McGill Engineering Doctoral Award (MEDA) and the Fonds de recherche du Québec - Nature et technologies (FRQNT) - Bourses de doctorat (B2X). The funding from these agencies allowed me to pursue my research manifesto with freedom and thus their contribution is greatly acknowledged. I would like to also thank the annual research excellence awards of the mining department at McGill University.

I would like to give a special recognition to my best friend and roommate Abdalla Ghazal; the PhD journey was made much easier because of your selfless support. I would like to also thank my friends in Canada, Ahmad Dalaq, Mostafa El Yousef, Khalil Hindawi, and Mohammad Shokr, in addition to other dear friends outside Canada, Mohammad El Maoud, Mohammad Dirar, Anas Obaid, Mostafa Ajjawi, and Amjad Murad.

Lastly, I could not be where I am today if it weren't for the unwavering love, faith, and endearment of my family. To my brothers Mohammad and Rami, my sister, Reem, and my parents, Hanan and Fawzi; I owe you guys everything. Thank you.

Contribution of Authors

In accordance with the guidelines on manuscript based (article-based) thesis preparation provided by the office of Graduate and Postdoctoral Studies (GPS) at McGill University, my contributions and that of my co-authors are provided as follows.

I, Ahmad Zueter, am the first author of all the chapters presented in this dissertation. Specifically, my primary contributions to the research presented in this dissertation are listed below. I took the lead in

- conceptualizing the problem;
- developing the mathematical methodology;
- writing the code for data analysis, visualization, statistical analysis, and numerical simulations (MATLAB and FLUENT);
- validating and verifying the simulation results;
- conducting formal analysis and data curation; and
- writing the original drafts, coordinating the reviews from other team members, responding to reviewers during the peer-review process and editing the manuscript.

This work benefited from the invaluable support of my co-authors, Mahmoud Alzoubi (postdoctoral researcher), Minghan Xu (Ph.D. student), Aurelien Nie-Rouquette (graduated masters student), Mohammad-Saad Tareen (Ph.D. student), Prof. Ali Madiseh, Prof. Ferri Hassani, Eng. Greg Newman (CEO of Newmans Geotechnique Inc.), and Prof. Agus Sasmito (Thesis supervisor).

For chapter 3, Aurelien Nie-Rouquette established the experimental setup and obtained the experimental data whereas Dr. Mahmoud Alzoubi provided useful insights in formulating the mathematical model and helped in reviewing the manuscripts. For chapter 4, Minghan Xu derived the analytical models and helped in reviewing the manuscripts whereas Dr. Mahmoud Alzoubi provided useful insights in formulating the numerical model and helped in reviewing the manuscripts. For chapter 5, Prof. Ali Madiseh and Prof. Ferri Hassani helped in administrating the project. For chapter 6, Mohammad-Saad Tareen helped in reviewing the manuscript. For chapter 7, Eng. Greg Newman supplied field data, provided field perspective, and helped in reviewing the manuscript.

Prof. Agus Sasmito supported me in formulating the research problem for my thesis, supervised the research, acquired the funding, administered the project and assisted with the review & editing of all the chapters in this dissertation.

Journal Articles

Seven journal articles are the outcome of this thesis, in addition to other conference articles and presentations, as follows:

1. **Zueter A.F.**, Tareen M., Newman G., Sasmito A.P., 2022, "Dynamic CFD modeling coupled with heterogeneous boiling for deep two phase closed thermosyphons in artificial ground freezing", *submitted to the International Journal of Heat and Mass Transfer*.

2. **Zueter A.F.**, Sasmito A.P., 2022, "Cold energy storage as a solution for year-round renewable artificial ground freezing: Case study of the Giant Mine Remediation Project", *submitted to the Journal of Renewable Energy*.

3. **Zueter A.F.**, Akhtar S., and Sasmito A.P., 2022, "Monte-Carlo Analysis of Operational Parameters in Selective Artificial Ground Freezing Applications", *accepted at Journal of Sustainable Mining*.

4. **Zueter A.F.**, Madiseh A.G., Hassani F.P., Sasmito A.P., 2021, "Effect of freeze pipe eccentricity in selective artificial ground freezing applications", *ASME Journal of Thermal Sciences and Engineering Applications*, pp. 1-33.

5. **Zueter A.F.**, Newman G., Sasmito A.P., 2021, "Numerical study on the cooling characteristics of hybrid thermosyphons: Case study of the Giant Mine, Canada", *Cold Regions Science and Technology*, 189, p. 103313.

6. **Zueter A.F.**, Xu M., Alzoubi M.A., Sasmito A.P., 2021, "Development of conjugate reduced-order models for selective artificial ground freezing: Thermal and computational analysis", *Applied Thermal Engineering*, 190, p. 116782.

7. **Zueter A.**, Nie-Rouquette A., Alzoubi M.A., Sasmito A.P., 2020, "Thermal and Hydraulic Analysis of Selective Artificial Ground Freezing Using Air Insulation: Experiment and modeling", *Computers and Geotechnics*, 120, p. 103416.

Contents

List of Figures

List of Tables

Chapter 1

Introduction

1.1 Background & Motivation

In 2021, 5% of Canada's total GDP was attributed to the mining industry accounting for one in every 26 jobs [1]. The significance of the mining industry on the Canadian economic and social sectors is undeniable; accordingly, new technologies have always been proposed to tackle the evolving challenges of the mining operations. These challenges can occur at different stages, ranging from minerals discovery to waste management upon mine closure. As researchers, we thoroughly study these challenges with objective of generating fundamental and applied knowledge to adapt and optimize mining systems. In my thesis, two Canadian mines are selected due to their substantial challenges at technical, economic, environmental, and social levels: 1) the Cigar Lake Mine in northern Saskatchewan and 2) the Giant Mine near Yellowknife, Northwest Territories. Our motivation to study these two mines is provided in the next subsections:

1.1.1 The Cigar Lake Mine

The Cigar Lake Mine (Saskatchewan, Canada) contains the second richest high-grade uranium deposits in the world [2]. While the deposits were discovered in 1981, construction

Figure 1-1: Flooding of the Cigar Lake Mine in 2010

was delayed for two decades due to geological and social challenges. As such, the orebody is located at 400 meters below the ground surface [3] and is surrounded by weak sandstone. Additionally, adopting strict environmental standards is compulsory to protect not only the local ecosystem but also the Indigenous communities who rely on hunting and fishing in the vicinity [4]. In 2005, the mine construction was launched with production planned in two years. Nevertheless, underground water flooded the mine several times causing catastrophic damages as shown in Fig. 1-1 and several years of delay. The water was also rich with toxic radioactive substances such as radon exposing the workers to great risks. In 2010, the flooding issues were eventually resolved by a geotechnical support method called the artificial ground freezing (AGF).

Existing AGF systems require drilling around 300 boreholes from the surface for the insertion of freeze-pipes, as shown in Fig. 1-2. Powerful ammonia refrigeration plants connected to the national grid provide chilled coolants to selectively freeze zones of interest encapsulating the orebody at a depth of 400-460 meters. In the passive zone where ground freezing is not needed (above the orebody), the pipes are insulated using an air cavity to reduce the cooling load, introducing the concept of selective artificial ground freezing (S-AGF), as shown in Fig. 1-3.

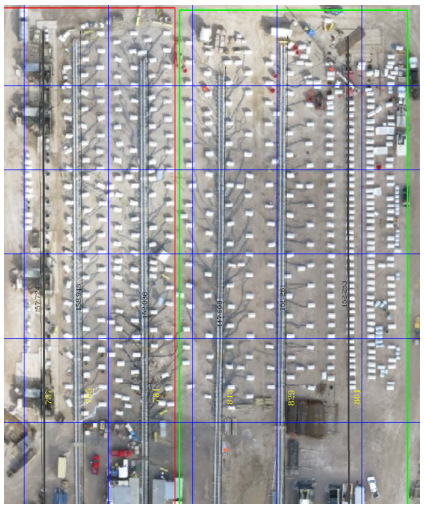

Figure 1-2: Around 300 freeze-pipes (white structures) installed from the surface at the Cigar Lake Mine to artificially freeze the construction site near the ore-body at a depth of 400-460 meters below the ground surface and thus prevent underground water infiltration

S-AGF is the most favorable state-of-the-art geotechnical support method due to its reliability and minimal contamination of the ground [5]. Nevertheless, there are two main problems with existing S-AGF systems: 1) high refrigeration load and 2) immense greenhouse emissions. In the case of the Cigar Lake Mine, energy-intensive refrigeration plants run at a capacity of 2,200 tons to provide chilled coolants at a temperature of around -30 [°C] through 297 freeze-pipes [3]. The annual energy consumption is thus estimated at 67.8 GWh, whereas the corresponding greenhouse emissions are projected at 44 kilotons of CO_2, 3390 kg of CH_4, and 1356 kg of N_2O [6]. The economic expenses of refrigeration are estimated at 273 million dollars [3]. A new expansion plan will be launched soon including 250 more freeze-pipes, aggravating the economic and environmental burden. Accordingly, more fundamental and applied understanding is needed in S-AGF to also meet the objectives of the Canadian Minerals and Metals Plan (CMMP) for sustainable mineral extraction while substantially reducing the operational and environmental costs of S-AGF systems.

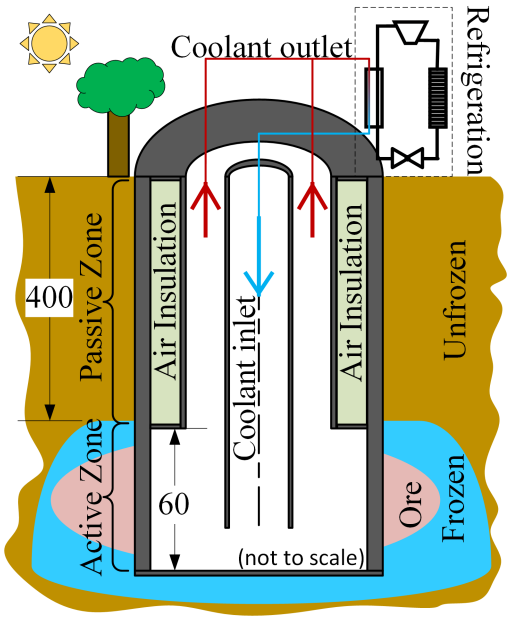

Figure 1-3: Selective Artificial Ground Freezing System in the Cigar Lake Mine (all units in meters)

1.1.2 The Giant Mine

The Giant Mine was a major economic force of the Northwest Territories (NT), producing 7 million ozt of gold over the second half of the twentieth century [7]. Despite these economic benefits, gold mining created a massive environmental burden amounting for 237,000 tons of a lethal byproduct called arsenic, which has been stored in 10 underground chambers and 5 stopes distributed over four different areas as shown in Fig. 1-4. The chambers were securely surrounded by impenetrable permafrost, preventing arsenic from leaking outside the mine [8]. Nevertheless, global warming and mining intensified permafrost thawing, thus compromising the arsenic containment. Arsenic leakage poses several environmental and social catastrophes. The mine waste is situated along the shoreline of Yellowknife Bay on Great Slave Lake, one of the largest freshwater bodies in Canada [9]. Arsenic concentration in Yellowknife Bay is five times higher than that of drinkable water [10], influencing the fish habitat. Chief Edward Sangris of Dettah, the Dene First Nation community closest to the mine, affirmed that fish became scarce and contaminated near the waste [11],[12]. The

First Nation people of Dettah are severely affected by this catastrophe as they cannot safely practice hunting and fishing in the vicinity – not to mention the demise and health issues in the 1950s due to arsenic consumption [11],[12].

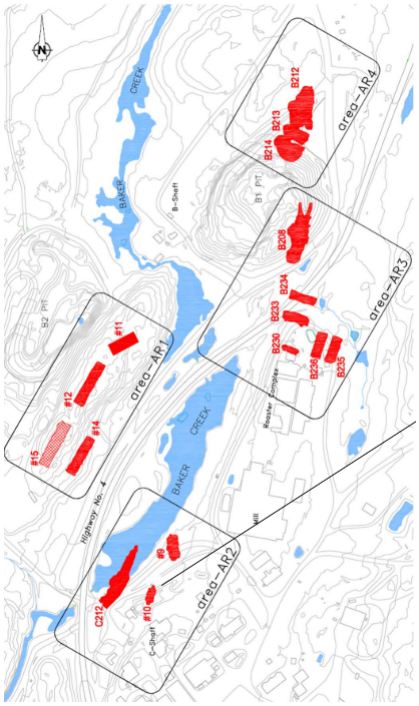

Figure 1-4: Underground chambers and stopes storing arsenic at the Giant Mine [13]

To mitigate the impact of arsenic leakage resulting from permafrost thawing, the Canadian Government initiated the Giant Mine Remediation Project (GMRP) in collaboration with the Yellowknives Dene First Nation. Among various containment methods, a reliable one called the frozen block was selected, where the environmental waste is encapsulated in a frozen shell. To this end, several artificial ground freezing (AGF) technologies have been installed and field-tested around chamber 10, which is one of the smallest arsenic chambers, as shown in Fig. 1-5. Careful consideration at the technical, economic, and environmental levels of the chosen AGF method is required since the system will need to run *indefinitely*. AGF methods that employ mechanical refrigeration units approaches can result in huge economic and environmental costs amounting for 1% of the provincial energy expenditures and greenhouse emissions [6,14]. A novel AGF system is needed to securely contain environ-

mental waste of the GMRP while substantially reducing the environmental and economic costs.

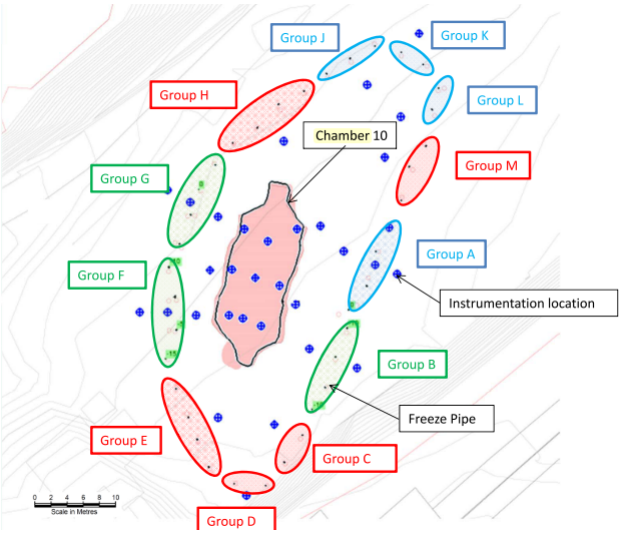

Figure 1-5: Field tests of different artificial ground freezing technologies around chamber 10 (each group indicate a different artificial ground freezing system) [13]

1.1.3 Introduction to Artificial Ground Freezing

Artificial ground freezing (AGF) is a geotechnical engineering method implemented in a variety of applications, including geotechnical support, environmental waste management, underground water control, and permafrost stabilization. As compared to other geotechnical methods such as chemical or cement grouting, AGF is preferred due to its adaptability to a wide range of project scales; AGF can be applied to support small civil units or long roads extending for hundreds of kilometers. AGF is also suitable for various ground conditions, from fine sand to sedimentary rocks. In addition, AGF results in minimal ground contamination as they do not incorporate any foreign materials into the ground. This is particularly significant to preserve the natural habitat in vicinity of AGF applications, especially those located near lakes and water resources.

In principle, AGF systems aim at creating a strong, solid, and impenetrable ground by artificially decreasing the ground temperature to subzero levels and thus freezing the

ground water content. Heat sinks at subzero temperatures are therefore needed to extract thermal energy from the ground. The heat sinks are driven by either electrical-power-based refrigeration plants or naturally available cold resources. Accordingly, AGF methods can be classified into three main types: 1) active methods, 2) passive methods, and 3) hybrid methods.

Active AGF methods are driven by refrigeration plants that require external energy resources. Based on the type of these resources, active AGF methods can be further sub-classified into open-loop and closed-loop methods. In open-loop methods, pre-refrigerated liquified gas (e.g., nitrogen) is pumped through freeze-pipes into the ground; the vaporized fluid then evaporates and exhausts to the environment. In the contrary, closed-loop methods use refrigeration plants installed in vicinity of the AGF site to cool down a brine, which is pumped into the ground and returned to the refrigeration plant. Detailed literature on active AGF systems can be found in our previous review paper [15]. Regardless of the active AGF type, all active AGF systems share the same issue: tremendous energy expenditures. Consequently, energy-saving methods were proposed to decrease the cooling load of AGF plants. Among such methods, the concept of selective artificial ground freezing (S-AGF) is applied for deep AGF applications. Freeze-pipes of S-AGF applications are designed to selectively freeze particular zones of interest while insulating the remaining part of the ground using air insulation, as shown in Fig. 1-3.

Unlike active ones, passive AGF methods exploit available cold wind near the AGF site. A heat transfer device, called thermosyphon, is employed to extract heat from the ground to the cold wind, as shown in Figure 1-6. Thermosyphons are pressure vessels that contain a refrigerant of a subzero boiling temperature. The lower portion of the thermosyphon is embedded inside the ground where ground freezing is needed, while the upper portion is equipped with fins to maximize heat transferred to the air. The passive AGF cycle is as follows: the refrigerant extracts heat from the ground, evaporates, flows upward, releases the heat to the cold air, and then falls back to the ground level.

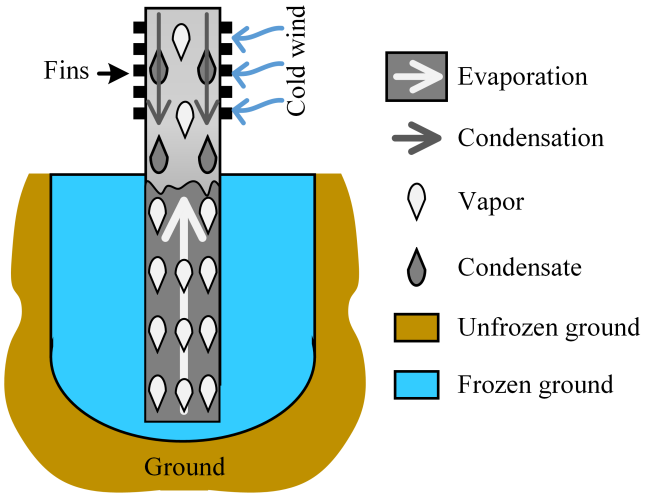

Figure 1-6: Not-to-scale schematic of thermosyphons operation in passive artificial ground freezing systems (P-AGF).

1.2 Objectives

Evidently, passive AGF systems rely on the availability of cold wind, and thus they are commonly used in cold northern regions. In large AGF applications, passive cooling of cold wind during winter season is not sufficient. Hybrid AGF systems are therefore employed incorporating refrigeration plants to the thermosyphons. The objective of this thesis is to propose methods through mathematical techniques that can minimize the refrigeration costs and greenhouse gas emissions associated with two types AGF systems typically used in mining applications: 1) selective artificial ground freezing (S-AGF) and 2) hybrid artificial ground freezing (H-AGF) using thermosyphons. Fundamental and applied subobjectives are accordingly presented as follows:

- To develop fundamental understanding of natural convection in air enclosures of S-AGF systems.
- To develop fundamental understanding of the boiling and condensation phenomena in deep thermosyphons.
- To develop couple mathematical models of heat transfer devices alongside with the

ground freezing process.

At the applied level:

- To develop computationally efficient reduced-order models for field-scale S-AGF applications.
- To uncover best practices that can be implemented for S-AGF and H-AGF systems.
- To propose novel AGF systems that rely mostly on renewable energy resources.

1.3 Thesis organization

This thesis is divided into two halves: 1) selective artificial ground freezing (S-AGF) and 2) thermosyphon-based artificial ground freezing. First, chapter 2 presents up-to-date literature review in these two systems. After that, chapters 3, 4, and 5 are dedicated for obtaining fundamental and applied understanding of S-AGF whereas chapters 6, 7, and 8 are devoted for obtaining fundamental and applied understanding of thermosyphon-based AGF systems in addition to proposing a novel system of superior environmental and thermal performance. Final conclusions are made in chapter 9.

In chapter 3, a fully-conjugate mathematical model based on the conservation principles of mass, momentum and energy for the freeze pipe is coupled with a ground freezing model based on the enthalpy-porosity method. The mathematical model is validated against experimental measurements of the ground and coolant. Moreover, the natural convection inside the air insulation chamber is further validated at a wide-range of Rayleigh numbers against other experimental studies from the literature. The results emphasize the important role of the air insulation layer to minimize the energy expenditures of S-AGF systems. Also, the thickness of the air insulation layer is scaled to maximize its insulation capacity.

In chapter 4, a computationally efficient reduced-order numerical model based on a space-marching algorithm is derived to simulate S-AGF systems in field-scale conditions. Deriving

such a model is essential due to the large nature of S-AGF systems resulting in high computational needs. The results of the reduced-order model are validated against experimental data in lab-scale and then further verified in field-scale with the fully-conjugate model derived in chapter 2. The computational time of the reduced-order model is 99% less than that of the fully-conjugate one, while retaining the solution accuracy. The impact of some operational parameters, such as the coolant inlet temperature and flow rate, are also examined in this chapter.

Chapter 5 addresses the effect of the freeze-pipe eccentricity in S-AGF applications. Particularly, the reduced-order model derived in chapter 3 is adjusted to capture the impact of the freeze-pipes eccentricity. The results show that freeze-pipe eccentricity can significantly affect the completion time of the ground freezing process as well as the cooling load of the AGF system.

In chapter 6, more sustainable AGF methods are considered using thermosyphons. A novel computational-fluid-dynamic (CFD) model is derived to deeply examine the boiling phenomena in deep thermosyphons such as that operating at the Giant Mine (100 meters deep) considering the bubble nucleation theory. The model is well-validated against experimental measurements and is extended to mimic field scenarios. The effect of three main parameters is examined: 1) initial filling volume of the working fluid inside the thermosyphons, 2) initial charge pressure inside the thermosyphon, and 3) wind temperature.

In chapter 7, the case of the Giant Mine Remediation Project is considered in this thesis due to its high environmental significance. In this chapter, a thermal network model is derived to simulate hybrid thermosyphons and is coupled with a ground freezing model based on the enthalpy-porosity method. The model is validated against field data from the Giant Mine Remediation Project. After model validation, the impact of several operational parameters is examined. Overall, it is found that activating refrigeration plants during warm seasons can significantly speed up the ground freezing process, but will result in large energy expenditures and accordingly significant greenhouse gas emissions.

In chapter 8, we propose a novel ground-coupled cold energy storage (CES) system to enhance the efficiency of thermosyphon-based AGF systems solely using sustainable resources without running mechanical refrigeration units. The idea is to store winter cold energy in the ground using assistant thermosyphons located in the vicinity of the Giant Mine field. Then, in warmer seasons, a heat transfer fluid (HTF) is circulated to extract the stored cold energy and release it to the primary thermosyphon operating in the Giant Mine field. Our novel concept is demonstrated mathematically using our well-validated model derived in chapter 4 and chapter 6.

Lastly, in chapter 9, concluding remarks are made, highlighting our contribution to knowledge and discussing potential future work.

Chapter 2

Literature review of selective artificial ground freezing and thermosyphon-based artificial ground freezing

Preface

In this chapter, we present up-to-date literature of selective artificial ground freezing and thermosyphon-based artificial ground freezing. The literature review cover the applied and fundamental aspects of these systems. Main gaps and conclusions are highlighted.

"**A. F. Zueter** and A. P. Sasmito, initial draft the we aim to further extend and submit as a review article"

Abstract

This thesis addresses two types of artificial ground freezing systems: 1) selective artificial ground freezing (S-AGF) as used in the Cigar Lake Mine and 2) thermosyphon-based artificial ground freezing as employed in the Giant Mine. The literature review is accordingly divided into two main sections for each one of them. In the first section, we present previous literature on energy saving studies for AGF systems followed by particular studies on S-AGF. After that, fundamental review on natural convection in vertical air enclosures is provided. In the second section, a review over different types of thermosyphon-based AGF systems is given, followed by analysis of various experimental and numerical investigations. Finally, computational-fluid-dynamics (CFD) studies of thermosyphons are examined. The literature review reveals that there is a need for more fundamental and applied understanding of S-AGF systems, especially the passive zone in field-scale scenarios. As for thermosyphons-based AGF systems, more mathematical models and innovative ideas are needed to enhance our fundamental understanding of thermosyphons operation and better exploit winter cold energy.

Contents

2.1 Selective Artificial Ground Freezing

Selective artificial ground freezing (S-AGF) is a concept in deep AGF applications that aims at reducing the cooling load of the refrigeration plants by insulating the freeze-pipe in the passive zone where ground freezing is not needed. S-AGF systems are especially useful for underground mining applications where the active mining zone is located much below the ground surface. For instance, the Cigar Lake Uranium Mine in Canada [1], [2], [3] and the

Banji Coal Mine in China [4] use an S-AGF system to prevent underground water inflow. The active zone of the Cigar Lake Mine extends between 400-460 meters below ground surface, whereas that of the Banji Mine extends between 315-442 meters. Furthermore, the S-AGF concept can also be implemented in civil applications located in the immediate vicinity of underground structures to limit frozen body growth in these regions and thereby avoid potential structural damages associated with frost heave deformation [5].

In some AGF applications, underground water seepage can be significant and should be considered [6]. If the groundwater seepage velocity is higher than 2 meters/day, energy-intensive refrigeration systems based on liquid nitrogen are highly recommended, as installed for the construction of Sophiaspoor tunnel (Netherlands) [7], the Universita subway station (Naples, Italy) [8], and the Nanjing Metro Line (China) [9]. When the groundwater seepage velocity is in the range of 1-2 meters/day, AGF methods through brine circulation in freeze-pipes can be implemented [10], [11].

2.1.1 Mathematical studies on energy saving AGF systems

Several studies were conducted in attempts to minimize the energy requirement of AGF systems. Huang et al. [12] and Marwan et al. [13] developed optimization techniques to determine freeze pipes layout that yields in the least energy consumption. Huang et al. [12] derived a thermo-hydraulic model of the ground freezing process coupled with Nelder-Mead simplex method to optimize the freeze-pipe arrangements. Marwan et al. [13], on the other hand, optimized the freezing time and energy using the ant colony optimization method coupled with a thermo-hydraulic model of the ground. Alzoubi et al. [14], [15], [16], [17] revealed massive energy saving potential by proposing the concept of freezing on demand for long term AGF applications. A fully-conjugate model [18] coupling the freeze-pipes and the ground process was developed based on the enthalpy-porosity method [19], [20] and validated against experimental measurement. As demonstrated mathematically and experimentally, the freezing on demand concept avoids over-cooling the ground by operating

AGF refrigeration plants when necessary only, thereby substantially reducing the energy expenditures and greenhouse emissions.

While many novel ideas and optimization techniques and were proposed for AGF applications, the literature on S-AGF is very limited. Vitel et al. [21] and Tounsi et al. [22] derived numerical models to predict the ground temperature and displacement in the active zone of S-AGF systems for the case of the Cigar Lake Uranium Mine. Wang et al. [4] derived a thermal mathematical model for S-AGF systems of the Banji Coal Mine assuming Dirichlet boundary condition at the pipe wall. Evidently, the thermal and hydraulic aspects of S-AGF freeze-pipes is still not well understood. Particularly, the capacity of the freeze-pipes to freeze the active zone and air insulation layers to isolate the coolant from the passive zone is not yet examined. Understanding these phenomena is essential to predict the freezing time and energy expenditures of S-AGF systems.

2.1.2 Fundamentals of natural convection in an air enclosure

Consequently, the objective of chapters 3-5 of this thesis is to develop fundamental and applied understanding of S-AGF systems to minimize their energy consumption. This motivates us to acquire fundamental understanding of heat transfer inside air enclosures to better understand the role of the air cavity insulation in S-AGF systems. Natural convection inside enclosures is characterized by the Rayleigh number [23], Ra, defined as

$$Ra \sim \frac{\text{time scale of diffusion heat transfer}}{\text{time scale of convection heat transfer}} \tag{2.1}$$

Accordingly, systems of low Rayleigh number indicate a heat transfer mechanism where conduction dominates over convection and vice versa. Particularly, for different types of natural convection systems, a critical Rayleigh number, Ra_{cr} exists below which thermal transport is solely dominated by diffusion and above which is the onset of convective thermal transport [24], [25]. In the case of two walls of a temperature difference of ΔT enclosing a

fluid of particular kinematic viscosity, ν, and thermal diffusivity, α, the Rayleigh number is expressed as [26]

$$Ra = \frac{g\beta L^3}{\nu\alpha}\Delta T \tag{2.2}$$

where L is the characteristic length, β is the thermal expansion coefficient, and g is the gravitational acceleration. Below Ra_{cr}, the conductive Nusselt number, Nu_{cond}, can be used to evaluate the heat transfer coefficient, h, along the walls of the enclosure. The conductive Nusselt number for natural convection in enclosures is obtained analytically through well-established derivations of heat conduction as [23]

$$Nu_{cond} = hL/k = 1 \tag{2.3}$$

where h is the heat transfer coefficient, L is the characteristic length, and k is the thermal conductivity of air. Beyond, Ra_{cr}, the Nusselt number exceeds unity due to significant natural convection currents that circulates through the enclosure transferring thermal energy from the hot plate to the cold one. Several Nusselt correlations are available in the literature for the case of rectangular enclosure given low aspect ratios [26], [27] and high aspect ratios [26], [28]. While employing correlations of high aspect ration rectangular enclosures may hold using the narrow slot approximation [29], [30] in forced convective flow, natural convection is usually very sensitive to the geometry of the enclosure.

In S-AGF applications, the air cavity is annular in geometry. The most commonly employed Nusselt correlations for vertical annular enclosures of gases are given in Table 2.1. Given the geometry of the Cigar Lake freeze-pipes, the minimum and maximum Rayleigh numbers can range between 3.7×10^3 and 2.3×10^4, as shown in Fig. 2-1. By comparing the convective Nusselt number as predicted by correlations in Table 2.1 with that of the conductive Nusselt number within this range, the conductive Nusselt number is higher than the convective Nusselt number predicted by Kumar and Kalam [31] as well as that predicted by Sherrif [33], indicating that heat is mainly transferred by thermal diffusion rather than

Reference	Correlation	H/L	Ra
Kumar and Kalam [31]	$Nu = 0.09Ra^{0.278}\frac{D_o}{D_i}^{0.34+0.329\frac{D_i}{D_o}}\frac{L}{H}^{0.122}\frac{D_i}{L}ln\frac{D_o}{D_i}$	$1 < H/L < 10$	$Ra < 10^6$
Keyhani et al. [32]	$Nu = 0.123Ra^{0.279}$	$H/L = 20$	$10^3 < Ra < 10^7$
Sherrif N. [33]	$Nu = 0.25Ra^{0.3}(H/L)^{-}0.25$	$38 < H/L < 228$	$10^5 < Ra < 10^8$

Table 2.1: Nusselt correlations of annular air enclosures where H is the height of the cavity and L is the characteristic length equivalent to the difference between the outer diameter of the air cavity, D_o, and the inner diameter of the cavity, D_i

convection. Nevertheless, The Nusselt number predicted Keyhani is higher within our range of Rayleigh number. This could be attributed to the fixed aspect ratio of Keyhani's experiment as it is the only correlation that does not consider the effect of the aspect ratio. Overall, the aspect ratio of all correlations are much smaller than that of the field exceeding 1.4×10^5. Thus, novel analytical techniques are needed to determine the heat transfer regime in the annular air cavities of S-AGF systems.

Ideally, the annular air cavity is supposed to be concentric around a vertical axis to achieve maximum insulation. Nevertheless, installing concentric air cavities over 400 meters depth is practically difficult. The 400-meters-deep air chamber is composed of forty 10-meters-long pipes connected together. The pipes zigzag around the casing forming an *eccentric* air cavity. This significantly affects the insulation capacity of the air cavity as observed in horizontal air insulation of solar receivers [34], [35]. The corresponding conductive Nusselt number of an *eccentric* air cavity is expressed as [23]

$$Nu_{cond} = \frac{ln(D_o/D_i)}{cosh^{-1}[(D_o^2 + D_i^2 - 4E^2)/(2D_oD_i)]}, \tag{2.4}$$

where E is the difference between the centers of the two pipes. The minimum value of E is zero in the case of concentric pipes whereas the maximum value is $E = (D_o - D_i)/2$ which occurs when the walls of the inner pipe collide with that of the outer pipe. A non-dimensional

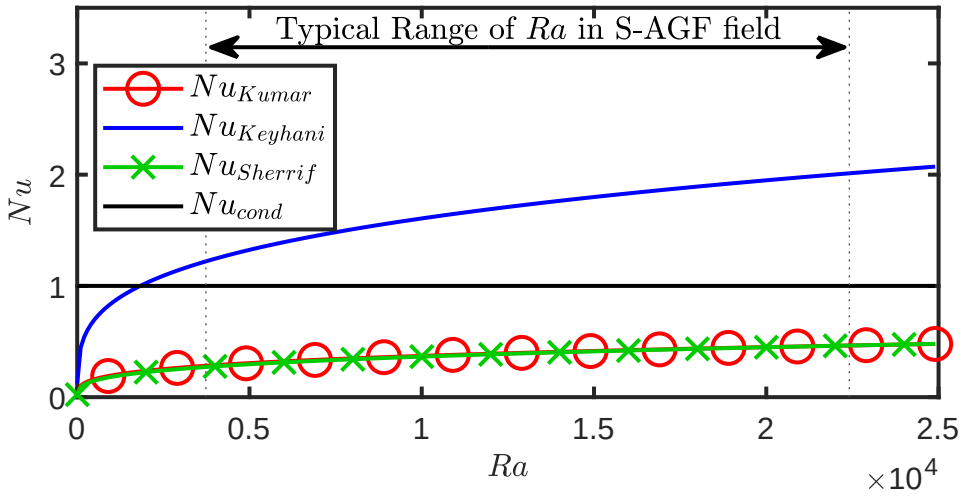

Figure 2-1: Comparison between conductive [23] and convective [31], [32], [33] Nusselt number of natural convection in air enclosures given typical range of Ra in S-AGF field applications, calculated based on the geometry of Cigar Lake freeze-pipes and considering a minimum and maximum ΔT of 5° and 30°, respectively.

repersentation of the effect of pipe eccentricity in the case of the Cigar Lake Mine on the conductive Nusselt number is shown in Fig. 2-2. Evidently, the conductive Nusselt number can increase by ten times due the eccentric behavior of the air cavity, indicating added heat dissipation in the passive zone.

Heat transfers from a hot medium to a colder one in three mechanisms: 1) conduction, 2) convection, and 3) *radiation*. Our discussion thus far considers the first two methods only. Nevertheless, radiative heat transfer in annular air enclosures is equally important for two main reasons: 1) high optical transmissivity of air (almost identical to that of vacuum) [36] and 2) high optical emissivity of steel pipes forming the annular enclosure [37]. Thus, fundamental understanding and mathematical modeling of radiation in S-AGF is needed to accurately determine heat dissipation in the passive zone.

In CFD studies, the discrete ordinate method (DOM) [36] is considered one of the most accurate techniques to evaluate radiation heat transfer due to its ability to couple a radiative transport equation (RTE) with a thermal energy transport equation. The governing RTE of

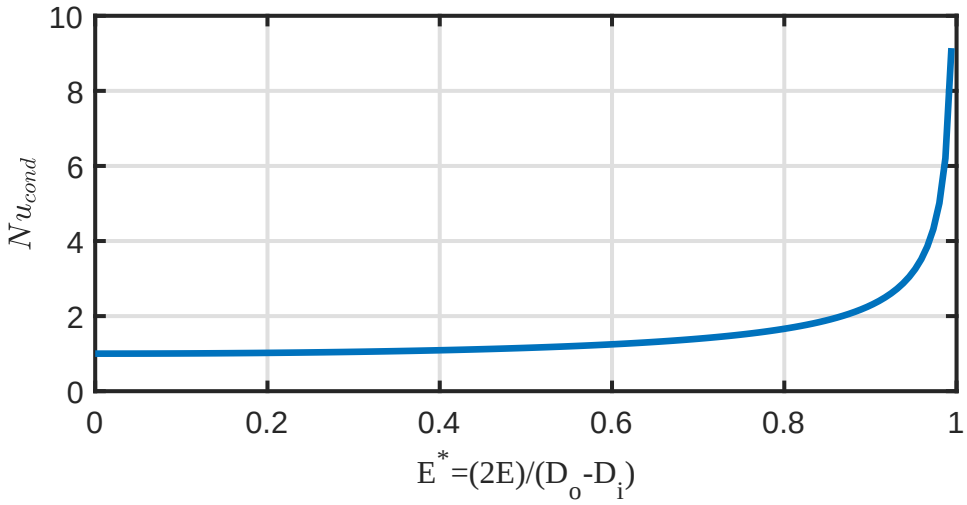

Figure 2-2: The effect of annular air cavity eccentricity on the conductive Nusselt number

a non-scattering and non-emissive medium such as air can be simplified to [38]

$$\nabla \cdot (I\vec{s}) = 0 \tag{2.5}$$

where I is the radiation intensity, and $\vec{s}$ is a direction vector. The incident radiative heat flux at a wall is calculated by integrating the incoming radiation to a certain computational cell as:

$$q_{rad,in} = q_i = \int_{\vec{s}\cdot\vec{n}>0} I_{in}(\vec{s}\cdot\vec{n})d\Omega \tag{2.6}$$

As the incoming radiative rays impact the walls, they can be either reflected or absorbed ($q_i = q_r + q_{ab}$). The *absorbed* radiation which is *converted to thermal energy* relies on the wall emissivity, ϵ, as:

$$q_{rad\to th} = q_{ab} = \epsilon_w q_i. \tag{2.7}$$

On the other hand, the amount of thermal energy that is emitted and *converted to radiant* energy is given as:

$$q_{th\to rad} = q_e = \epsilon_w \sigma T^4 \tag{2.8}$$

The net change in thermal energy of the walls due to radiation is evaluated as the difference between the absorbed radiation and emitted one as:

$$q_{th,net} = q_{ab} - q_e \tag{2.9}$$

On the other hand, the overall radiative flux leaving the surface equals to the sum of the reflected flux q_{rf} and the radiant energy emitted by the wall q_e:

$$q_{rad,out} = q_{rf} + q_e = (1 - \epsilon_w) q_{rad,in} + \epsilon_w \sigma T^4 \tag{2.10}$$

While the DOM method can accurately evaluate radiative heat transport for a wide range of geometries, they increase the computational cost of the problem. Further, DOM methods cannot be easily integrated with non-CFD studies. Accordingly, other simplified methods based on optical view factors are often considered to quickly estimate the radiative heat transfer from one end of a geometry to another. For the case of annular air cavities, radiative heat transfer, Q_{rad}, between the outer and inner cylinders is given as [26]

$$Q_{rad} = \frac{2\pi \ r_{in} \ r_{out} \ \epsilon_w \ \sigma}{r_{out} + (1 - \epsilon_w) r_{in}} (T_{out}^4 - T_{in}^4), \tag{2.11}$$

where r, eps, and σ denote radius, wall emissivity, and Stefan-Boltzman constant, respectively, whereas subscripts in and out indicate the inner and outer cylinders of the annulus.

While the view factor method can be more computationally efficient than the DOM to evaluate radiative heat transfer as compared to the DO method, the view factor method is restrictive at low aspect ratio of the annulus due to the increasing effect of the upper and lower plates enclosing the annulus. Thus, if the aspect ratio is in the order of unity, the view factor method may not be accurate unless the method is adjusted to also consider the impact of the upper and lower plates rather than using the simplified form in Eq. 2.11.

2.2 Thermosyphon-Based Artificial Ground Freezing

Two-phase-closed-thermosyphons (TPCT) are used in several AGF applications in northern regions due to their ability to exploit available cold energy of the wind to freeze the ground. The first TPCT was invented by the end of the nineteenth century by Perkin and Buck [39], [40]. Around seventy years later, an Alaska based engineer Erwin Long obtained the United States patent for using two-phase-closed-thermosyphons to support permafrost foundation in 1965 [41]. The first in-situ installations of TPCT in permafrost regions dates back to 1960 with the objective of stabilizing the foundations of two communication sites at Aurora (Manitoba, Canada) and Glenallen (Alaska, US) [42]. Since then, thermosyphons have been widely employed across northern regions for foundation stabilization, hazardous waste management, and many other applications. Several developments were thus made to adapt to the various project-specific challenges associated with industrial and civil activities on permafrost regions.

This literature review presents the various types of thermosyphons presently used in northern industries in addition to those proposed in the academic literature. The thermosyphons are classified based on their geometry and cold energy source. Following that, field applications of TPCT available in the academic literature will be reviewed. Afterwards, mathematical and experimental studies on thermosyphon-based AGF are reviewed, trailed by fundamental discussion on thermosyphons operation.

2.2.1 Classification of Thermosyphons Based on Geometry & Orientation

1. **Vertical TPCT**

   Vertical TPCT is the most traditional type of thermosyphons. The entire TPCT, including the condenser and evaporator sections, are perpendicular to the ground surface. A thermopile, also known as "Long thermopile" in recognition for Erwin Long [43], is

a special kind of vertical TPCT that supports a structural load. Vertical TPCTs are considered the easiest to fabricate and install though this significantly depends on the size of the thermosyphon. The evaporator section can be as shallow as five meters as in pipeline [44], [45], [46] and roadway support applications [47], [48], [49], but can also exceed 100 meters in other applications as in the Giant Mine Remediation Project [50], [51], [52]. The condenser section is finned and sized according to the anticipated heat absorbed at the evaporator section.

Improvements have been proposed to increase the heat extraction capacity of vertical TPCTs. Vasiliev et al. [53] experimentally proposed the use of wicked TPCTs (also known as heat pipes) which include a mesh along the vessel wall to accelerate the natural convection cycle by exploiting the capillary forces of the wick. Enhancement of heat extraction rate by 20% is achieved experimentally. Zhang et al. [54] also proposed filling the TPCT with a magnetic nanofluid due to their favorable thermal conductivity. Experimental results demonstrated high thermal energy extracted by a nanofluid TPCT and more even temperature along the evaporator wall. Nevertheless, field installation of wicked or nanofluid TPCT in AGF applications is rare or none-existent. This might be attributed to much lower thermal resistance of natural convection inside traditional TPCT as compared to the thermal resistance of heat conduction in the ground and heat convection to the wind. Accordingly, improving the natural convection cycle does not yield in substantial improvement to the heat extraction capacity of TPCT.

Nevertheless, a low temperature gradient across the evaporator is a desired criteria resulting in lower heave forces. A team of Russian industrial engineers achieved a similar objective in 1993 by manufacturing the thermosyphon with an aluminum alloy rather than steel. Aluminum alloys also exhibit desired non-corrosive qualities. In attempts to further exploit winter cold wind, further improvements were made on the condenser section by augmenting the radiator fins by additional secondary fins.

This results in a higher surface area of the condenser leading to a lower wind thermal resistance.

2. **Inclined TPCT**

   In geometrically wide applications like some roads and civil structures, vertical TPCT cannot freeze the underlying ground at the center. In such cases, inclined TPCTs are sometimes used as they are installed at an angle with respect to the ground surface. Thus, the evaporator section can extend and cover the structure width. The 4,000 km long Qinghai-Tibet Highway (China) includes inclined TPCTs at several locations such as Chumaerhe [55] and Amdo [56] where the TPCTs are installed at angle of 70 degrees with respect to the ground surface. Typically, the inclination angle of inclined TPCTs can go as low as 50 degrees [57].

3. **L-shaped TPCT**

   The majority of existing TPCTs take the form of an L-shape. These TPCTs have a vertical condenser section yet an inclined evaporator. The first known installation of L-shaped thermosyphons was in 1975 at the Ross River School (Yukon Territory, Canada) [58]. Since then, this technology has attracted a worldwide interest. Several experimental [59], [60], [61] and numerical studies [55], [62] were thus conducted to better understand the effect of inclination angle on supporting various types of foundations. The inclination angle of the evaporator section is typically lower than that of inclined TPCTs, thus allowing the evaporator section to extend deeper below targeted structures. A flat thermosyphon is a special kind of L-shaped thermosyphons where the evaporator section is inclined at an angle of 0 degrees (parallel to the ground surface). Such flat thermosyphons were firstly installed in Galena's Warm Storage building in Alaska [63].

   Kukkapalli et al. [64], [65] also designed inclined evaporators of T-shape and Y-shape, in addition tree-like T-shape and Y-shape evaporators. Numerical analysis revealed that

the thermal performance of these designs is preferrable over the traditional type of L-shaped thermosyphons. Nonetheless, the results were not supported by experimental measurement or field data. To the best of the authors knowledge, T-shape and Y-shape evaporators have not been installed yet in the industry.

4. **Loop TPCT**

   In this unique design, the working fluid flows over a loop of connected piping segments, where the evaporator is embedded in the ground and the condenser is positioned above ground surface. Loop TPCTs can have as many bends as desired along the evaporator, thus providing more design flexibility. This is especially important in the design of TPCTs associated with stabilizing the foundations of mining dams and dikes due to their very large extent and irregular geometry [66], [67]. However, as can be expected the installation cost of loop TPCT is, in general, higher than other types discussed in previous subsections. Loop TPCTs were initially tested at Winnipeg, Canada, in 1994 [63]. Loop thermosyphons are now being implemented to stabilize the foundatin of the Hot Spring road [68], [69].

5. **Hairpin TPCT**

   Hairpin TPCT, also referred to as buried TPCTs, can take the form of any geometry discussed till this point, with the exception being that the condenser section is embedded slightly below the ground surface. This type of TPCTs was created to preserve the aesthetic scenery along certain highways [61], [70] such as the Chena Hot Spring Road and Thompson Drive in Alaska. Further, hairpin TPCTs increases the level of safety of roadways since the condensers are buried rather than installed at the shoulder of the roads. The installation cost of hairpin TPCTs is usually lower because the buried condensers are not finned. Nonetheless, this in turn reduces the heat extraction capacity of TPCTs.

2.2.2 Classification of thermosyphons based on the driving source of cold energy

In addition to their geometry, thermosyphons can be classified by the driving source of cold energy as follows:

1. **Passive TPCT**

   Passive TPCT are seasonal devices that rely only on the availability of cold wind to extract heat from the ground. In some applications, a lone passive TPCT is sufficient to cool the ground. However, several studies revealed that, in large scale applications, passive TPCT need to be supported by other techniques to keep the ground frozen, such as insulation boards [71], [72], [73] or crushed rock ventilation [74], [75], [76]. This is evidently observed along the Qinghai-Tibet highway and railway in China.

2. **Hybrid TPCT**

   Unlike passive TPCT, hybrid TPCTs feature the ability to operate during cold and warm seasons since they are coupled with alternative sources of cold energy, mostly using refrigeration plants. Hybrid TPCTs are often installed to accelerate forming a solid frozen ground due to the availability of refrigeration plants that can pump coolant continuously at very low temperature (around -30 [°C]) towards a secondary condenser. Once the desired frozen ground is formed, refrigeration plants are shut down, and passive cooling resume the freezing process. Hybrid TPCTs are now installed more frequently in Russia [77] and other cold regions. Perhaps the most notable application of hybrid thermosyphons is located in the Kotzebue, Alaska, where 370 load bearing hybrid thermosyphons are employed to support the Maniilaq Medical Center [63]. Further, hybrid thermosyphons form a water retention dike for the Diavik Mine at Lac De Gras (Northwest Territories, Canada) [78]. The performance of hybrid thermosyphons have been experimentally demonstrated in controlled laboratories [58] and in field conditions [79], [80]. The use of hybrid thermosyphons has also been tested at very large

scale for the case of the Giant Mine Remediation Project [81].

Instead of integrating mechanical cooling units to the thermosyphon, other applications employ traditional freeze-pipes (based on pumping refrigerated coolant to the ground) to speed up the ground freezing process. Once the frozen ground is formed the freeze-pipes are removed from the boreholes to place thermosyphons resuming the ground freezing process using available cold wind. This has been installed at the Kuparuk River Module Crossing in Russia [82]. To run hybrid thermosyphons in remote areas using sustainable resources, Wagner et al. [83] proposed and tested powering mechanical refrigeration units by photovoltaic solar panels. As an alternative for energy-intensive refrigeration plants, Waters [46] conceptually proposed storing cold energy during winter seasons to be used in warmer seasons. Recently, Alzoubi et al. [84], [85] provided more elaborate mathematical and conceptual proposal on the concept of cold energy storage and further developed preliminary numerical models demonstrating the high benefits of the CES concept.

3. **Active TPCT**

   Active thermosyphons are ones that only employ refrigeration systems rather than cold air. Such type of thermosyphons is typically used in relatively warm regions. Perhaps the most well-known application of active thermosyphons is the at Oak Ridge National Project [86], [87] to contain chemical contaminants.

2.2.3 Experimental and mathematical studies on thermosyphon-based AGF

Thermosyphons in artificial ground freezing applications have been studied using two main methodolgies: 1) Experimental setups (in controlled laboratories or field) and 2) numerical techniques. Early experimental studies were conducted to test the impact of various operational parameters, such as the wind temperature [88] and the working fluid inside the

thermosyphon [53]. Other experimental studies were performed to test the applicability of thermosyphons given the atmospheric and ground conditions in particular regions. Haynes et al. [89], [90] and Zarling et al. [39], [91], [92] examined commercial thermosyhons employed in Alaska to test the effect of the wind speed, condenser inclination, evaporator inclination, horizontal evaporator length, and integration of mechanical refrigeration units. Several field tests were also conducted along the Qinghai-Tibet roadways [93], [94], [95], railways [96], [97], and power transmission lines [98], [99], [100].

Numerical analysis conducted in the literature aims at predicting thermosyphons performance in field conditions. Some numerical models employ commercial standards to estimate the heat extraction capacity of thermosyphons [101], [102], [103]. Nevertheless, the vast majority of numerical models are based on thermal resistance network models, where empirical or semi-empirical correlations are used to estimate the heat transfer coefficient of the wind, working fluid condensation, and working fluid evaporation. Accordingly, many mathematical studies have investigated *passive* cooling of thermosyphons in AGF applications. Yang et al. [104], [105] developed a 2D thermal network model to monitor the freezing expansion of soil in winter seasons. Zhi et al. [106], Xu et al. [107], and Abdalla et al. [108], [109] simplified the thermal resistance network by neglecting the thermal resistance of the evaporation and condensation thermosyphon while including that of wind flow only. Wang et al. and Tian et al. [110], [111] assumed a similar superconductor thermosyphon model, but varies the wind heat transfer coefficient according to the wind speed. In 2011, Zhang et al. [112] derived a pioneering thermal network model including the conduction, evaporation, and condensation thermal resistances inside the thermosyphon in addition to the wind thermal resistance. This thermal resistance model was then employed by several researchers [113], [114], [115], [116]. Pei et al. [117], [118] improved this model and considered the inclination angle of the thermosyphon.

2.2.4 CFD studies on thermosyphons

Apart from AGF, thermosyphons have been used as a heat transfer device in several applications such geothermal energy extraction [119], [120], [121] and electronics cooling [122], [123], [124]. Accordingly, CFD studies that examine the boiling and condensation phenomena in thermosyphons have been conducted in the literature for various purposes.

Alizadehdakhel et al. [125] derived a 2D CFD model for thermosyphons based on the conservation principles of mass, momentum, and energy. The VoF method [126] is employed to model to determine the equivalent thermophysical properties, as well as the velocity and temperature fields, across the thermosyphon. The evaporation and condensation rate, S, are modeled using Schepper et al. [127] correlation given as

$$S_{v\to\ell} = \begin{cases} 0.1\rho_v\alpha_v(T_{sat}-T)/T_{sat} & ,T > T_{sat}; \\ 0.1\rho_\ell\alpha_\ell(T_{sat}-T)/T_{sat} & ,T < T_{sat}, \end{cases} \tag{2.12}$$

where ρ is the density and α is the volume fraction whereas subscripts v, ℓ, and sat refer to vapor phase, liquid phase, and saturation (temperature), respectively. Fadhl et al. [128] used the same methodology examining water as the working fluid inside the thermosyphon and validated the model against experimental data. Fadhl et al. [129] then tested thermosyphon performance with other commercial refrigerants such as R134a and R404a. The bubbles formed in these refrigerants are much smaller than that of water, possibly due to the different critical nucleation site radius. Xu et al. [130] considered the effect surface wettability for mini-thermosyphons in electriconics cooling applications. Kamburova et al. [131] and Abdullahi et al. [132] numerically investigated the impact of the condenser capacity and thermosyphon inclination angle, respectively. Jouhara et al. [133] extended the geometry to 3D in order to observe the geyser boiling phenomena mathematically. Kafeel and Turan [134] derived a more complex Eulerian mathematical model that treats each phase independently and thus require more computational resources.

The discussed studies thus far assume that a nucleation site is formed once the liquid temperature exceeds the saturation temperature. Wang et al.[135] considered the excess temperature needed, dT_i, to form a nucleation site and thus adjusted the evaporation model as

$$S_{\ell \to v} = \begin{cases} \beta \rho_\ell \alpha_\ell (T_{sat} - T)/T_{sat} & , \alpha_\ell \neq 1 \text{ and } T > T_{sat} \text{ (bubble already forming);} \\ 0 & , \alpha_\ell = 0 \text{ and } T < T_{sat} + dT_i \text{ (no bubble);} \\ \beta \rho_\ell \alpha_\ell (T_{sat} - T)/T_{sat} & , \alpha_\ell = 0 \text{ and } T > T_{sat} + dT_i \text{ (bubble nucleation).} \end{cases} \tag{2.13}$$

This improved model was employed to observe the geyser boiling phenomena of water [135] and investigate lab-scale thermosyphons in shallow geothermal applications using ammonia [136]. After that, Wang et al. [137] derived a novel pressure-based evaporation model based on the Hertz-Knudsen [138] kinetic theory of gases. The pressure-based model also considers the variation of the saturation pressure according to the liquid's temperature. Wang et al. [4] demonstrated that the variation of the saturation pressure in deep thermosyphons can be quite significant in geothermal applications due to the huge hydrostatic pressure accumulating at the bottom of the thermsyphon.

Conclusion

In this chapter, up-to-date knowledge is presented on two types of artificial ground freezing considered in this thesis: 1) selective artificial ground freezing (S-AGF) and 2) thermosyphon based artificial ground freezing. The following conclusions are made:

- Mathematical models of S-AGF systems are very limited and mainly focused on the active zone. Accordingly, there is a need for fundamental and applied understanding of the passive zone.

- The passive zone of S-AGF is highly affected by the presence of an annular air enclosure

to minimize heat dissipation from the ground to the coolant. This annular enclosure often has very high aspect ratio much larger than that considered in the literature of natural convection in air enclosure. Accordingly, more mathematical approaches are needed to better understand the heat transfer regime of such high-aspect-ratio air enclosures.

- The impact of several operational parameters are not examined in the literature such as coolant temperature, flow rate, as well as freeze-pipe eccentricity. Thus, conjugate models of fast computational algorithms need to be developed to examine these parameters effectively.

- As for thermosyphon-based AGF systems, the present mathematical models in the literature focus on passive thermosyphons only. More models of hybrid thermosyphons are needed.

- Further, hybrid thermosyphons in their present form require energy intensive refrigeration plants. More innovative approaches to run thermosyphons using sustainable resources are needed.

- Lastly, the boiling phenomena in deep thermosyphons has not been examined yet in the literature. Bubble nucleation models of boiling in deep thermosyphons are needed.

Bibliography

[1] A. Zueter, A. Nie-Rouquette, M. A. Alzoubi, A. P. Sasmito, Thermal and hydraulic analysis of selective artificial ground freezing using air insulation: Experiment and modeling, Computers and Geotechnics 120 (2020) 103416.

[2] A. F. Zueter, M. Xu, M. A. Alzoubi, A. P. Sasmito, Development of conjugate reduced-order models for selective artificial ground freezing: Thermal and computational analysis, Applied Thermal Engineering 190 (2021) 116782.

[3] A. F. Zueter, A. G. Madiseh, F. P. Hassani, A. P. Sasmito, Effect of Freeze Pipe Eccentricity in Selective Artificial Ground Freezing Applications, ASME Journal of Thermal Science and Engineering Applications 14 (2022) 011015.

[4] B. Wang, C. Rong, H. Cheng, Z. Yao, H. Cai, Research and application of the local differential freezing technology in deep alluvium, Advances in Civil Engineering 2020.

[5] J. S. Harris, Ground freezing in practice, Thomas Telford, 1995.

[6] M. A. Alzoubi, A. Madiseh, F. P. Hassani, A. P. Sasmito, Heat transfer analysis in artificial ground freezing under high seepage: Validation and heatlines visualization, International Journal of Thermal Sciences 139 (2019) 232–245.

[7] C. Crippa, V. Manassero, Artificial ground freezing at sophiaspoortunnel (The Netherlands)—Freezing parameters: Data acquisition and processing, in: GeoCongress 2006: Geotechnical Engineering in the Information Technology Age, 2006, pp. 1–6.

[8] S. Papakonstantinou, G. Anagnostou, E. Pimentel, Evaluation of ground freezing data from the Naples subway, Proceedings of the Institution of Civil Engineers-Geotechnical Engineering 166 (3) (2013) 280–298.

[9] J. Hu, Y. Liu, Y. Li, K. Yao, Artificial ground freezing in tunnelling through aquifer soil layers: A case study in Nanjing Metro Line 2, Ksce journal of civil engineering 22 (10) (2018) 4136–4142.

[10] E. Pimentel, A. Sres, G. Anagnostou, Modelling of ground freezing in tunnelling, in: Underground Space–The 4th Dimension of Metropolises, ITA and World Tunnel Congress, Prague, Vol. 1, 2007, pp. 331–336.

[11] E. Pimentel, S. Papakonstantinou, G. Anagnostou, Numerical interpretation of temperature distributions from three ground freezing applications in urban tunnelling, Tunnelling and Underground Space Technology 28 (2012) 57–69.

[12] S. Huang, Y. Guo, Y. Liu, L. Ke, G. Liu, Study on the influence of water flow on temperature around freeze pipes and its distribution optimization during artificial ground freezing, Applied Thermal Engineering 135 (2018) 435–445.

[13] A. Marwan, M.-M. Zhou, M. Z. Abdelrehim, G. Meschke, Optimization of artificial ground freezing in tunneling in the presence of seepage flow, Computers and Geotechnics 75 (2016) 112–125.

[14] M. A. Alzoubi, A. P. Sasmito, A. Madiseh, F. P. Hassani, Intermittent freezing concept for energy saving in artificial ground freezing systems, in: Energy Procedia, Vol. 142, 2017, pp. 3920–3925.

[15] M. A. Alzoubi, A. P. Sasmito, A. Madiseh, F. P. Hassani, Freezing on demand (FoD): An energy saving technique for artificial ground freezing, in: Energy Procedia, Vol. 158, Elsevier, 2019, pp. 4992–4997.

[16] M. A. Alzoubi, A. Zueter, A. Nie-Rouquette, A. P. Sasmito, Freezing on demand: A new concept for mine safety and energy savings in wet underground mines, International Journal of Mining Science and Technology 29 (4) (2019) 621–627.

[17] M. A. Alzoubi, A. Nie-Rouquette, S. A. Ghoreishi-Madiseh, F. P. Hassani, A. P. Sasmito, On the concept of the freezing-on-demand (FoD) in artificial ground freezing for long-term applications, International Journal of Heat and Mass Transfer 143.

[18] M. A. Alzoubi, A. Nie-Rouquette, A. P. Sasmito, Conjugate heat transfer in artificial ground freezing using enthalpy-porosity method: Experiments and model validation, International Journal of Heat and Mass Transfer 126 (2018) 740–752.

[19] M. Kaviany, Principles of Heat Transfer in Porous Media, Springer Science & Business Media, 2012.

[20] V. R. Voller, C. Prakash, A fixed grid numerical modelling methodology for convection-diffusion mushy region phase-change problems, International Journal of Heat and Mass Transfer 30 (8) (1987) 1709–1719.

[21] M. Vitel, A. Rouabhi, M. Tijani, F. Guérin, Thermo-hydraulic modeling of artificial ground freezing: Application to an underground mine in fractured sandstone, Computers and Geotechnics 75 (2016) 80–92.

[22] H. Tounsi, A. Rouabhi, M. Tijani, F. Guerin, Thermo-Hydro-Mechanical Modeling of Artificial Ground Freezing: Application in Mining Engineering, Rock Mechanics and Rock Engineering (2019) 1–19.

[23] W. M. Rohsenow, J. P. Hartnett, Y. I. Cho, Handbook of heat transfer, Vol. 3, McGraw-Hill New York, 1998.

[24] A. Bejan, Convection Heat Transfer, John Wiley & Sons, 2013.

[25] W. L. Heitz, J. Westwater, Critical rayleigh numbers for natural convection of water confined in square cells with L/D from 0.5 to 8, Journal of Heat Transfer 93 (2) (1971) 188–195.

[26] Y. A. Cengel, S. Klein, W. Beckman, Heat transfer: a practical approach, Vol. 141, McGraw-Hill New York, 1998.

[27] I. Catton, Natural convection in enclosures, in: International Heat Transfer Conference Digital Library, Begel House Inc., 1978.

[28] R. K. MacGregor, A. F. Emery, Free Convection Through Vertical Plane Layers—Moderate and High Prandtl Number Fluids, Journal of Heat Transfer 91 (3) (1969) 391–401. doi:10.1115/1.3580194.

[29] O. Erge, E. M. Ozbayoglu, S. Z. Miska, M. Yu, N. Takach, A. Saasen, R. May, CFD analysis and model comparison of annular frictional pressure losses while circulating yield power law fluids, in: SPE Bergen One Day Seminar, OnePetro, 2015.

[30] S. H. Bittleston, O. Hassager, Flow of viscoplastic fluids in a rotating concentric annulus, Journal of non-newtonian fluid mechanics 42 (1-2) (1992) 19–36.

[31] R. Kumar, M. A. Kalam, Laminar thermal convection between vertical coaxial isothermal cylinders, International journal of heat and mass transfer 34 (2) (1991) 513–524.

[32] M. Keyhani, F. A. Kulacki, R. N. Christensen, Free convection in a vertical annulus with constant heat flux on the inner wall, Journal of Heat Transfer 105 (3) (1983) 454–459.

[33] N. Sherrif, Experimental Investigation of Natural Convection in Single and Multiple Vertical Annuli with High Pressure Carbon Dioxide, in: Third International Heat Transfer Conference,, Chicago, 1966, pp. 132–138.

[34] A. C. Ratzel, C. E. Hickox, D. K. Gartling, Techniques for reducing thermal conduction and natural convection heat losses in annular receiver geometries, ASME Journal of Heat Transfer 101 (1) (1979) 108–113.

[35] A. A. Hachicha, I. Rodríguez, C. Ghenai, Thermo-hydraulic analysis and numerical simulation of a parabolic trough solar collector for direct steam generation, Applied Energy 214 (2018) 152–165.

[36] A. Pokaipisit, M. Horprathum, P. Limsuwan, Vacuum and air annealing effects on properties of indium tin oxide films prepared by ion-assisted electron beam evaporation, Japanese Journal of Applied Physics 47 (6R) (2008) 4692.

[37] A. Nie-Rouquette, Experimental and Numerical Investigation of Insulated Bayonet Tubes for Artificial Ground Freezing, McGill University (Canada), 2018.

[38] J. R. Howell, M. P. Menguc, R. Siegel, Thermal radiation heat transfer, CRC press, 2015.

[39] J. P. Zarling, F. D. Haynes, Thermosyphon-based designs and applications for foundations built on permafrost, in: Society of Petroleum Engineers - International Arctic Technology Conference, Anchorage, 1991, pp. 449–458. doi:10.2523/22114-ms.

[40] H. Ma, Heat Pipes, John Wiley & Sons, New Jersey, 2006.

[41] E. Long, Means for Maintaining Permafrost Foundations (1965).

[42] E. Long, The Long Thermopile, in: First International Conference on Permafrost, Lafayette, 1963, pp. 487–491.

[43] A. Wagner, Review of Thermosyphon Applications, Tech. rep., US Army Corps of Engineers, Hanover (2014).

[44] C. H. A. Liguori, J.A. Maple, Third International Conference on Permafrost Iio Mep3Jiotobji , Ehe ' Ik), in: Third International Conference on Permafrost, Edmonton, 1978, pp. 151–157.

[45] C. E. Heuer, Application of Heat Pipes on the Trans-Alaska Pipeline., Tech. Rep. 79-26 (1979).

[46] Waters, Heat pipes to stabilize pilings on elevated Alaska pipeline sections, Pipeline and Gas Journal 201 (10) (1974) 46–59.

[47] L. Guo, Y. You, Q. Yu, Z. Shi, H. Li, X. Wang, Field investigation on the influence of periglacial processes on pile foundations on the Qinghai–Tibet plateau, Permafrost and Periglacial Processes 32 (3) (2021) 335–348. doi:10.1002/ppp.2092.

[48] J. Liu, B. Tai, J. Fang, Ground temperature and deformation analysis for an expressway embankment in warm permafrost regions of the Tibet plateau, Permafrost and Periglacial Processes 30 (3) (2019) 208–221. doi:10.1002/ppp.2007.

[49] W. Ma, Z. Wen, Y. Sheng, Q. Wu, D. Wang, W. Feng, Remedying embankment thaw settlement in a warm permafrost region with thermosyphons and crushed rock revetment, Canadian Geotechnical Journal 49 (9) (2012) 1005–1014. doi:10.1139/T2012-058.

[50] M. Noel, D. Hockley, Thermal analysis of an experimental thermosyphon installed at the Giant Mine in Yellowknife, NT, Canada, in: 57th Canadian Geotechnical Conference and 5th joint CGS-IAH Conference, Quebec, 2004.

[51] J. Vogan, R. Royer, A. Conron, K. Farris, Giant Mine State of Knowledge Review: Arsenic Dust Management Strategies (August).

[52] SRK Consulting (Canada) Inc., Freeze Optimization Study Update for MVEIRB and Parties Aboriginal Affairs and Northern Development Freeze Optimization Study Update for MVEIRB and Parties, Tech. Rep. August (2012).

[53] L. L. Vasiliev, L. P. Grakovich, L. E. Pylilo, Application for Heat Pipes for Freezing Grounds, in: Third International Heat Pipe Conference, Palo Alto, 1978, pp. 109–113.

[54] Y. Zhang, K. Han, B. Xu, Z. Chang, Experimental study on the temperature evenness of heat pipe using magnetic nano-fluids as the working medium in permafrost regions, Advanced Materials Research 614-615 (2013) 327–330. doi:10.4028/www.scientific.net/AMR.614-615.327.

[55] Y. Tian, Z. Yang, Y. Liu, X. Cai, Y. Shen, Long-term thermal stability and settlement of heat pipe-protected highway embankment in warm permafrost regions, Engineering Geology 292 (2021) 106269.

[56] J. Wu, W. Ma, Z. Sun, Z. Wen, In-situ study on cooling effect of the two-phase closed thermosyphon and insulation combinational embankment of the Qinghai-Tibet Railway, Cold Regions Science and Technologydoi:10.1016/j.coldregions.2009.11.002.

[57] W. Pei, M. Zhang, S. Li, Y. Lai, Y. Dong, L. Jin, Laboratory investigation of the efficiency optimization of an inclined two-phase closed thermosyphon in ambient cool energy utilization, Renewable Energy 133 (2019) 1178–1187. doi:10.1016/j.renene.2018.08.078.

[58] D. W. Hayley, Application of Heat Pipes to Design of Shallow Foundations on Permafrost, in: Fourth Canadian Permafrost Conference, Ottawa, 1982, pp. 535–544.

[59] Z. Yan, M. Zhang, Y. Lai, W. Pei, T. Luo, F. Yu, S. Yang, Countermeasures combined with thermosyphons against the thermal instability of high-grade highways in per-

mafrost regions, International Journal of Heat and Mass Transfer 153 (2020) 119047. doi:10.1016/j.ijheatmasstransfer.2019.119047.

[60] Y. Dong, Y. Lai, M. Zhang, S. Li, Laboratory test on the combined cooling effect of L-shaped thermosyphons and thermal insulation on high-grade roadway construction in permafrost regions, SCIENCES IN COLD AND ARID REGIONS 1 (4) (2009) 307–315.

[61] Y. Lai, H. Guo, Y. Dong, Laboratory investigation on the cooling effect of the embankment with L-shaped thermosyphon and crushed-rock revetment in permafrost regions, Cold Regions Science and Technology 58 (3) (2009) 143–150. doi:10.1016/J.COLDREGIONS.2009.05.002.

[62] W. Pei, M. Zhang, X. Wan, Y. Lai, C. Wang, Numerical optimization of the installing position for the L-shaped TPCT in a permafrost embankment based on the spatial heat control, Solar Energy 224 (March) (2021) 1406–1425. doi:10.1016/j.solener.2021.06.044.
URL https://doi.org/10.1016/j.solener.2021.06.044

[63] E. Yarmak, E. L. Long, Recent Developments in Thermosyphon Technology, in: Cold Regions Impacts on Transportation and Infrastructure: Proceedings of the Eleventh International Conference, 2002, pp. 656–662.

[64] V. Kukkapalli, S. Kim, Roadway embankment stabilization on permafrost using thermosyphons with Y-shaped evaporators, IOP Conference Series: Materials Science and Engineering 507 (1). doi:10.1088/1757-899X/507/1/012017.

[65] V. K. Kukkapalli, J. H. Kim, S. Kim, Optimum design of thermosyphon evaporators for roadway embankment stabilization in the arctic regions, Journal of Mechanical Science and Technology 35 (10) (2021) 4757–4764. doi:10.1007/s12206-021-0941-1.

[66] E. Ramos, M. Sen, C. Treviño, A steady-state analysis for variable area one- and two-phase thermosyphon loops (1985). doi:10.1016/0017-9310(85)90145-0.

[67] T. Başaran, S. Küçüka, Flow through a rectangular thermosyphon at specified wall temperatures, International Communications in Heat and Mass Transfer 30 (7) (2003) 1027–1039. doi:10.1016/S0735-1933(03)00161-1.

[68] M. Zhang, Y. Lai, W. Pei, L. Jin, Effect of inclination angle on the heat transfer performance of a two-phase closed thermosyphon under low-temperature conditions, Journal of Cold Regions Engineering 28 (4). doi:10.1061/(ASCE)CR.1943-5495.0000074.

[69] A. Forsström, E. L. Long, J. P. Zarling, S. Knutsson, A. Forsstrom, E. L. Long, J. P. Zarling, S. Knutsson, Thermosyphon cooling of Chena Hot Springs Road, in: Cold Regions Engineering Cold Regions Impacts on Transportation and Infrastructure: Proceedings of the Eleventh International Conference, Anchorage, AK, United states, 2002, pp. 645–655.

[70] J. Xu, D. J. Goering, Experimental validation of passive permafrost cooling systems, Cold Regions Science and Technology 53 (3) (2008) 283–297. doi:10.1016/j.coldregions.2007.09.002.

[71] A. M. Wagner, J. P. Zarling, E. Yarmak, E. L. Long, Unique Thermosyphon Roadway Test Site Spanning 11 years, 63rd Canadian Geotechnical Conference & 6th Canadian Permafrost Conference (January 2015) (2010) 1770–1776.

[72] G. Cheng, Q. Wu, W. Ma, Innovative designs of permafrost roadbed for the Qinghai-Tibet Railway, Science in China, Series E: Technological Sciences 52 (2) (2009) 530–538.
URL http://dx.doi.org/10.1007/s11431-008-0291-6

[73] J. Wu, W. Ma, Z. Sun, Z. Wen, In-situ study on cooling effect of the two-phase closed thermosyphon and insulation combinational embankment of the Qinghai-Tibet Railway (2010). doi:10.1016/j.coldregions.2009.11.002.

[74] E. A. Priscilla, L. Pasi, O. Thomas, Z. Vallos, Embankment stabilization techniques for railroads on permafrost, in: 2016 Joint Rail Conference, JRC 2016, Columbia, SC, United states, 2016, pp. Rail Transportation Division –.
URL http://dx.doi.org/10.1115/JRC2016-5731

[75] Q. H. Mei, J. Chen, J. C. Wang, X. Hou, J. Y. Zhao, S. H. Zhang, H. M. Dang, J. W. Gao, Strengthening effect of crushed rock revetment and thermosyphons in a traditional embankment in permafrost regions under warming climate, Advances in Climate Change Research 12 (1) (2021) 66–75. doi:10.1016/j.accre.2021.01.002.
URL https://doi.org/10.1016/j.accre.2021.01.002

[76] Y. Qin, G. Li, Permafrost warming under the earthen roadbed of the Qinghai-Tibet Railway (2011). doi:10.1007/s12665-011-1014-z.

[77] P. Georgy, Russian approaches to permafrost engineering, in: International Conference on Permafrost Proceedings, Fairbanks, 2008, pp. 1391–1397.

[78] I. Holubec, Flat loop thermosyphon foundations in warm permafrost, Tech. rep., I. Holubec Consulting Inc., Northwest Territories (2008).

[79] A. M. Wagner, Creation of an artificial frozen barrier using hybrid thermosyphons, Cold Regions Science and Technology 96 (2013) 108–116.

[80] A. M. Wagner, E. Yarmak, The performance of artificial frozen barriers, in: ISCORD 2013: Planning for Sustainable Cold Regions, 2013, pp. 116–127.

[81] A. F. Zueter, G. Newman, A. P. Sasmito, Numerical study on the cooling characteristics of hybrid thermosyphons: Case study of the Giant Mine, Canada, Cold Regions

Science and Technology 189 (February) (2021) 103313. doi:10.1016/j.coldregions.2021.103313.
URL https://doi.org/10.1016/j.coldregions.2021.103313

[82] J. W. Rooney, C. H. Riddle, R. L. Scher, Foundation rehabilitation at ADOT/PF Jim River maintenance camp, in: Society of Petroleum Engineers - Arctic Technology Conference 2011e, Anchorage, 1991, pp. 829–840. doi:10.2523/22226-ms.

[83] A. M. Wagner, J. B. Maakestad, E. Yarmak, T. A. Douglas, Artificial ground freezing using solar-powered thermosyphons, Tech. rep. (2021).

[84] M. Alzoubi, S. Ali Ghoreishi-Madiseh, A. P. Sasmito, N. Kunz, A. Guimaraes, Renewable energy-based artificial ground freezing as an adaptation solution for sustainability of permafrost in post-climate change conditions, IOP Conference Series: Earth and Environmental Science 268 (1).

[85] M. A. Alzoubi, S. Poncet, A. P. Sasmito, Hybrid artificial ground freezing as a sustainable solution for containing hazardous-waste in critical environmental projects, Cold Regions Science and Technology 192.

[86] S. W. Lynn, S. Rock, C. Rhodes, Evaluation of a vertical frozen soil barrier at oak ridge national laboratory, Remediation 10 (3) (2000) 15–33.

[87] E. L. Long, E. Yarmak, Engineering and Economic Variables of Long Duration Frozen Barriers, in: Ground Freezing 2000-Frost Action in Soils, CRC Press, 2000, pp. 169–173.

[88] Y. Lee, U. Mital, A two-phase closed thermosyphon, International Journal of Heat and Mass Transfer 15 (9) (1972) 1695–1707. doi:10.1016/0017-9310(72)90098-1.

[89] F. D. Haynes, J. P. Zarling, Thermosyphons and foundation design in cold regions (1988). doi:10.1016/0165-232X(88)90072-9.

[90] F. D. Haynes, J. P. Zarling, G. E. Gooch, Performance of a thermosyphon with a 37-meter-long, horizontal evaporator, Cold Regions Science and Technology 20 (3) (1992) 261–269. doi:10.1016/0165-232X(92)90033-Q.

[91] J. P. Zarling, F. D. Haynes, J. J. Gagnon, Thermal Stabilization of Permafrost with Thermosyphons, in: International Conference on Offshore Mechanics and Arctic Engineering, 1990, pp. 323–328.

[92] D. F. Haynes, J. P. Zarling, W. F. Quinn, G. E. Gooch, Laboratory tests with a hybrid thermosyphon, in: Proceedings of the 10th International Conference on Ocean, Offshore and Arctic Engineering, Vol. 4, American Society of Mechanical Engineers, Stavanger, 1991, pp. 93–99.

[93] Y. Song, L. Jin, J. Zhang, In-situ study on cooling characteristics of two-phase closed thermosyphon embankment of Qinghai-Tibet Highway in permafrost regions, Cold Regions Science and Technology 93 (2013) 12–19. doi:10.1016/j.coldregions.2013.05.002.
URL http://dx.doi.org/10.1016/j.coldregions.2013.05.002

[94] Y. Shen, R. Zuo, J. Liu, Y. Tian, Q. Wang, Characterization and evaluation of permafrost thawing using GPR attributes in the Qinghai-Tibet Plateau, Cold Regions Science and Technology 151 (3) (2018) 302–313. doi:10.1016/j.coldregions.2018.03.028.

[95] F. Yu, J. Qi, M. Zhang, Y. Lai, X. Yao, Y. Liu, G. Wu, Cooling performance of two-phase closed thermosyphons installed at a highway embankment in permafrost regions, Applied Thermal Engineering 98 (2016) 220–227. doi:10.1016/j.applthermaleng.2015.11.102.
URL http://dx.doi.org/10.1016/j.applthermaleng.2015.11.102

[96] S. Zhang, F. Niu, S. Wang, J. Wang, Y. Sun, Necessity of cooling methods for transportation infrastructure construction in permafrost regions of Qinghai–Tibet Plateau, Bulletin of Engineering Geology and the Environment 80 (9) (2021) 6705–6723. doi:10.1007/s10064-021-02349-5.
URL https://doi.org/10.1007/s10064-021-02349-5

[97] N. Fujun, X. Jian, L. Zhanju, W. Qingbai, C. Guodong, Permafrost Characteristics of the Qinghai-Tibet Plateau and Methods of Roadbed Construction of Railway, Acta Geologica Sinica - English Edition 82 (5) (2008) 949–958. doi:10.1111/j.1755-6724.2008.tb00650.x.

[98] Y. Zhou, X. Wang, F. Niu, F. He, C. Guo, D. Liu, D. Jiang, Frost Jacking Characteristics of Transmission Tower Pile Foundations with and without Thermosyphons in Permafrost Regions of Qinghai–Tibet Plateau, Journal of Cold Regions Engineering 35 (2) (2021) 04021004. doi:10.1061/(asce)cr.1943-5495.0000246.

[99] L. Guo, Y. Xie, Q. Yu, Y. You, X. Wang, X. Li, Displacements of tower foundations in permafrost regions along the QinghaiTibet Power Transmission Line, Cold Regions Science and Technology 121 (2016) 187–195.
URL http://dx.doi.org/10.1016/j.coldregions.2015.07.012

[100] Y. You, M. Yang, Q. Yu, X. Wang, X. Li, Y. Yue, Investigation of an icing near a tower foundation along the QinghaiTibet Power Transmission Line, Cold Regions Science and Technology 121 (2016) 250–257.
URL http://dx.doi.org/10.1016/j.coldregions.2015.05.005

[101] Y.-P. Yang, S.-H. Zhou, Q.-C. Wei, Numerical Analysis of Proper Thermosyphon Inclination Angle Used in Permafrost Embankment, China Railway Science 27 (3) (2006) 1–7.

[102] G.-F. Lu, Y.-P. Yang, Q.-C. Wei, L.-X. Zhang, Study of using thermosyphon-insulated board to enhance the stability of permafrost embankment, Journal of the China Railway Society 29 (6) (2007) 118–122.

[103] D. Duan, Y. Yang, Q. Wei, L. Zhang, Study on enhancing the stability of permafrost embankments with thermosyphon-insulated boards, Journal of Beijing Jiaotong University 32 (1) (2008) 24–28.

[104] P. Yang, Numerical Analysis and Application Research of Heat Pipe to Solve Soil Frost Heaving Problem, Journal of East China Jiaotong University 15 (4).

[105] P. Yang, W. Cunzhen, Numerical investigations and engineering applications on freezing expansion of soil restrained two-phase closed thermosyphons, International Journal of Thermal Sciences 41 (4) (2002) 341–347.

[106] W. Zhi, S. Yu, M. Wei, Q. Jilin, J. C. Wu, Z. Wen, Y. Sheng, W. Ma, J. L. Qi, J. C. Wu, Analysis on effect of permafrost protection by two-phase closed thermosyphon and insulation jointly in permafrost regions, Cold Regions Science and Technology 43 (3) (2005) 150–163.

[107] J. Xu, A. Eltaher, P. Jukes, Three-dimensional FE model for pipeline in permafrost with thermosyphon protection, in: Arctic Technology Conference, Vol. 1, Houston, 2011, pp. 535–544.

[108] B. Abdalla, C. Fan, C. Mckinnon, V. Gaffard, Numerical study of thermosyphon protection for frost heave, in: ASME 2015 34th International Conference on Ocean, Vol. 5A, Newfoundland, 2015, pp. 1–6.

[109] B. A. Abdalla, H. Mei, C. McKinnon, V. Gaffard, Numerical evaluation of permafrost thawing in arctic pipelines and mitigation strategies, in: Arctic Technology Conference 2016, Newfoundland, 2016.

[110] J.-L. Wang, S.-M. Liao, Numerical heat transfer analysis and optimization for thermosyphons coupled with natural ground in permafrost regions, China Railway Science 27 (6) (2006) 1–6.

[111] Y.-H. Tian, J.-K. Liu, Y.-P. Shen, 3-D finite element analysis of cooling effect of Qinghai-Tibet Railway embankment with thermosyphons in permafrost regions, Chinese Journal of Geotechnical Engineering 35 (2013) 113–119.

[112] M. Zhang, Y. Lai, J. Zhang, Z. Sun, Numerical study on cooling characteristics of two-phase closed thermosyphon embankment in permafrost regions, Cold Regions Science and Technology 65 (2) (2011) 203–210.

[113] Y. Mu, G. Li, Q. Yu, W. Ma, D. Wang, F. Wang, Numerical study of long-term cooling effects of thermosyphons around tower footings in permafrost regions along the Qinghai-Tibet Power Transmission Line, Cold Regions Science and Technology 121 (2016) 237–249.

[114] M. Zhang, W. Pei, Y. Lai, F. Niu, S. Li, Numerical study of the thermal characteristics of a shallow tunnel section with a two-phase closed thermosyphon group in a permafrost region under climate warming, International Journal of Heat and Mass Transfer 104 (2017) 952–963.

[115] W. Pei, M. Zhang, S. Li, Y. Lai, L. Jin, W. Zhai, F. Yu, J. Lu, Geotemperature control performance of two-phase closed thermosyphons in the shady and sunny slopes of an embankment in a permafrost region, Applied Thermal Engineering 112 (2017) 986–998.

[116] L. Chen, W. Yu, Y. Lu, W. Liu, Numerical simulation on the performance of thermosyphon adopted to mitigate thaw settlement of embankment in sandy permafrost zone, Applied Thermal Engineering 128 (2018) 1624–1633.

[117] W. Pei, M. Zhang, Z. Yan, S. Li, Y. Lai, Numerical evaluation of the cooling performance of a composite L-shaped two-phase closed thermosyphon (LTPCT) technique in permafrost regions, Solar Energy 177 (2019) 22–31.

[118] W. Pei, M. Zhang, Y. Lai, Z. Yan, S. Li, Evaluation of the ground heat control capacity of a novel air-L-shaped TPCT-ground (ALTG) cooling system in cold regions, Energy 179 (2019) 655–668.

[119] A. D. Atrens, H. Gurgenci, V. Rudolph, CO2 thermosiphon for competitive geothermal power generation, Energy & fuels 23 (1) (2009) 553–557.

[120] A. Franco, M. Vaccaro, On the use of heat pipe principle for the exploitation of medium–low temperature geothermal resources, Applied Thermal Engineering 59 (1-2) (2013) 189–199.

[121] B. M. Adams, T. H. Kuehn, J. M. Bielicki, J. B. Randolph, M. O. Saar, On the importance of the thermosiphon effect in CPG (CO2 plume geothermal) power systems, Energy 69 (2014) 409–418.

[122] N. Lamaison, C. L. Ong, J. B. Marcinichen, J. R. Thome, Two-phase mini-thermosyphon electronics cooling: Dynamic modeling, experimental validation and application to 2U servers, Applied Thermal Engineering 110 (2017) 481–494.

[123] C.-C. Chang, S.-C. Kuo, M.-T. Ke, S.-L. Chen, Two-phase closed-loop thermosyphon for electronic cooling, Experimental Heat Transfer 23 (2) (2010) 144–156.

[124] T.-E. Tsai, H.-H. Wu, C.-C. Chang, S.-L. Chen, Two-phase closed thermosyphon vapor-chamber system for electronic cooling, International Communications in Heat and Mass Transfer 37 (5) (2010) 484–489.

[125] A. Alizadehdakhel, M. Rahimi, A. A. Alsairafi, CFD modeling of flow and heat transfer in a thermosyphon, International Communications in Heat and Mass Transfer 37 (3) (2010) 312–318. doi:10.1016/j.icheatmasstransfer.2009.09.002.

[126] C. W. Hirt, B. D. Nichols, Volume of fluid (VOF) method for the dynamics of free boundaries, Journal of computational physics 39 (1) (1981) 201–225.

[127] S. C. K. De Schepper, G. J. Heynderickx, G. B. Marin, Modeling the evaporation of a hydrocarbon feedstock in the convection section of a steam cracker, Computers & Chemical Engineering 33 (1) (2009) 122–132.

[128] B. Fadhl, L. C. Wrobel, H. Jouhara, Numerical modelling of the temperature distribution in a two-phase closed thermosyphon, Applied Thermal Engineering 60 (1-2) (2013) 122–131. doi:10.1016/j.applthermaleng.2013.06.044.
URL http://dx.doi.org/10.1016/j.applthermaleng.2013.06.044

[129] B. Fadhl, L. C. Wrobel, H. Jouhara, CFD modelling of a two-phase closed thermosyphon charged with R134a and R404a, Applied Thermal Engineering 78 (2015) 482–490. doi:10.1016/j.applthermaleng.2014.12.062.
URL http://dx.doi.org/10.1016/j.applthermaleng.2014.12.062

[130] Z. Xu, Y. Zhang, B. Li, C. C. Wang, Y. Li, The influences of the inclination angle and evaporator wettability on the heat performance of a thermosyphon by simulation and experiment, International Journal of Heat and Mass Transfer 116 (2018) 675–684. doi:10.1016/j.ijheatmasstransfer.2017.09.028.
URL https://doi.org/10.1016/j.ijheatmasstransfer.2017.09.028

[131] V. Kamburova, A. Ahmedov, I. K. Iliev, I. Beloev, I. R. Pavlović, Numerical modelling of the operation of a two-phase thermosyphon, Thermal Science 22 (2018) S1311–S1321. doi:10.2298/TSCI18S5311K.

[132] B. Abdullahi, A. El-Sayed, R. K. Al-Dadah, S. Mahmoud, A. F. Mahrous, N. M. az Muhammad, S. B. Abbakar, Experimental and numerical investigation of thermosyphon heat pipe performance at various inclination angles, Journal of Advanced Research in Fluid Mechanics and Thermal Sciences 44 (1) (2018) 85–98.

[133] H. Jouhara, B. Fadhl, L. C. Wrobel, Three-dimensional CFD simulation of geyser boiling in a two-phase closed thermosyphon, International Journal of Hydrogen Energy 41 (37) (2016) 16463–16476. doi:10.1016/j.ijhydene.2016.02.038.
URL http://dx.doi.org/10.1016/j.ijhydene.2016.02.038

[134] K. Kafeel, A. Turan, Axi-symmetric simulation of a two phase vertical thermosyphon using Eulerian two-fluid methodology (2013).
URL https://www.scopus.com/inward/record.uri?eid=2-s2.0-84901195743{&}doi=10.1007{%}2Fs00231-013-1155-6{&}partnerID=40{&}md5=f1fe1c11a0999e6273872a152076b445

[135] X. Wang, Y. Wang, H. Chen, Y. Zhu, A combined CFD/visualization investigation of heat transfer behaviors during geyser boiling in two-phase closed thermosyphon, International Journal of Heat and Mass Transfer 121 (2018) 703–714.

[136] X. Wang, H. Yao, J. Li, Y. Wang, Y. Zhu, Experimental and numerical investigation on heat transfer characteristics of ammonia thermosyhpons at shallow geothermal temperature, International Journal of Heat and Mass Transfer 136 (2019) 1147–1159. doi:10.1016/j.ijheatmasstransfer.2019.03.080.
URL https://doi.org/10.1016/j.ijheatmasstransfer.2019.03.080

[137] X. Wang, Y. Zhu, Y. Wang, Development of pressure-based phase change model for CFD modelling of heat pipes, International Journal of Heat and Mass Transfer 145 (2019) 118763. doi:10.1016/j.ijheatmasstransfer.2019.118763.
URL https://doi.org/10.1016/j.ijheatmasstransfer.2019.118763

[138] M. Knudsen, The cosine law in the kinetic theory of gases, National Aeronautics and Space Administration, 1967.

Chapter 3

Thermal and hydraulic analysis of selective artificial ground freezing using air insulation: experiment and modeling

Preface

Fundamental understanding of selective artificial ground freezing (S-AGF) constitutes the first step in the optimization process. The content of this chapter presents the development of a fully-conjugate model that couples the ground freezing process with the coolant flow and natural convection of air. The model is validated against experimental measurements conducted at our laboratory by a previous masters student. Scale analysis is also implemented to better understand the various forms of heat transfer across the air cavity.

" **A. Zueter**, A. Nie-Rouquette, M. A. Alzoubi, and A. P. Sasmito. Thermal and hydraulic analysis of selective artificial ground freezing using air insulation: experiment and

modeling. *Computers and Geotechnics*, 120:103416, 2020. doi.org/10.1016/j.compgeo.2019.103416 "

Abstract

In some artificial ground freezing (AGF) applications of civil or mining projects, only particular parts of the ground need to be frozen. Selective artificial ground freezing (S-AGF) is an AGF technique where a specific portion of the freeze pipe is insulated, usually by an air gap, to prevent any undesirable ground freezing. In this study, a laboratory scale experimental setup that mimics actual S-AGF systems has been established. The experimental rig is built in a fully controlled environment and equipped with advanced instrumentation. Additionally, a mathematical model coupling the flow of the coolant, air, and porous ground is developed by solving the conservation equations of mass, momentum, and energy. The mathematical model is then validated against the experimental measurements of the ground and outlet coolant temperatures. Moreover, the natural convection inside the air gap is further validated at higher Rayleigh numbers with an experimental study from the literature. The results indicate that the energy consumption of AGF plants can be significantly reduced by applying the S-AGF concept, as compared to convectional AGF systems. Also, it is found that the optimum air gap thickness, L_{opt}, relates to the cavity height, H, and Rayleigh number, Ra_H, as $L_{opt} \sim 2HRa_H^{-1/4}$.

Contents

3.1 Introduction

Artificial ground freezing (AGF) is a highly reliable geotechnical support method that is environmentally friendly and compatible with different ground conditions [1]. Selective artificial ground freezing (S-AGF) is an AGF technique that aims to selectively freeze particular zones of interest, called the active zones. In areas where ground freezing is not required (passive zone), the freeze pipe is insulated, often by an air layer, to reduce heat transfer between the ground and the coolant, as shown in Fig. 3-1(a). The notion of S-AGF has already been applied in yellow the Cigar Lake uranium mine located in northern Saskatchewan, Canada [2]. In this mine, the active zone is located between depths of $400[m]$ and $460[m]$ below the ground surface [2]. Since ground freezing is not needed in the upper $400[m]$, the freeze pipe is insulated by an annular air gap between the casing and the coolant. This air gap reduces the intensive cooling load of the S-AGF system due to the low thermal conductivity of air. S-AGF can also be attractive in AGF applications located in the immediate vicinity of underground civil structures to limit frozen body growth in these regions and thereby avoid potential structural damages associated with frost heave deformation [3].

Numerous analytical [4], [5], [6], [7] and numerical [8], [9], [10], [11], [12], [13], [14] models have been developed to better understand AGF systems. Despite the reliability of AGF technology, one of its major drawbacks is the huge energy consumption required to continuously supply subzero coolant. Consequently, different energy-saving methods were proposed to decrease the cooling load of AGF plants. Huang et al. and Marwan et al. [15], [16] developed optimization techniques based on Nelder–Mead and ant colony optimization methods, respectively, to find the optimum position of freeze pipes that yields in the least energy consumption. Alzoubi et al. [17], [18], [19], [20] revealed massive energy saving

potential by proposing the concept of freezing on demand for long term AGF applications. This concept, which was modeled mathematically and validated experimentally, minimizes energy consumption due to over-cooling while maintaining a desired thickness of the frozen body.

Multiple experimental setups mimicking in-situ AGF systems were established to validate the mathematical models and monitor the performance of AGF systems [21], [22], [23], [24], [25], [26], [27]. Stander [21] tested AGF in two different scenarios: using a single freeze pipe or a group of pipes arranged in a circular pattern to resemble actual AGF systems. The frozen body growth around the freeze pipes was monitored and presented as contour plots. Victor [22] extended Stander's work by building a similar prototype but adding the influence of seepage flow. More recently, Alzoubi et al. [25] conceived and developed a fully controlled experiment containing two freeze pipes and equipped with more than 80 thermocouples. This experiment was utilized to validate a mathematical model based on the enthalpy porosity method. Sudisman et al. [26], [27] also conducted freezing tests on a small laboratory scale and used infrared thermograph observations to address and visualize the effects of water flow on the thermal distribution.

As noted in the literature review, the vast majority of mathematical models and experimental studies analyze and optimize conventional artificial ground freezing (C-AGF) systems, similar to the one shown in Fig. 3-1(b). The studies that examined S-AGF systems, on the other hand, are very limited. Vitel et al. [2] developed a thermal and hydraulic model to predict temperature distribution within the ground, analyze the impact of geological conditions on the freezing process, and optimize the freeze pipe positions for the case of the Cigar Lake underground mine. Tounsi et al. [28] built a thermo-hydro-mechanical model to investigate the mechanical impact of freezing on mining areas and to predict ground temperature and displacement based on data-set collected in the Cigar Lake underground mine.

To date, the concept of S-AGF has not yet been tested experimentally in a controlled environment. In addition, conjugate heat transfer models, that include the coolant, annular

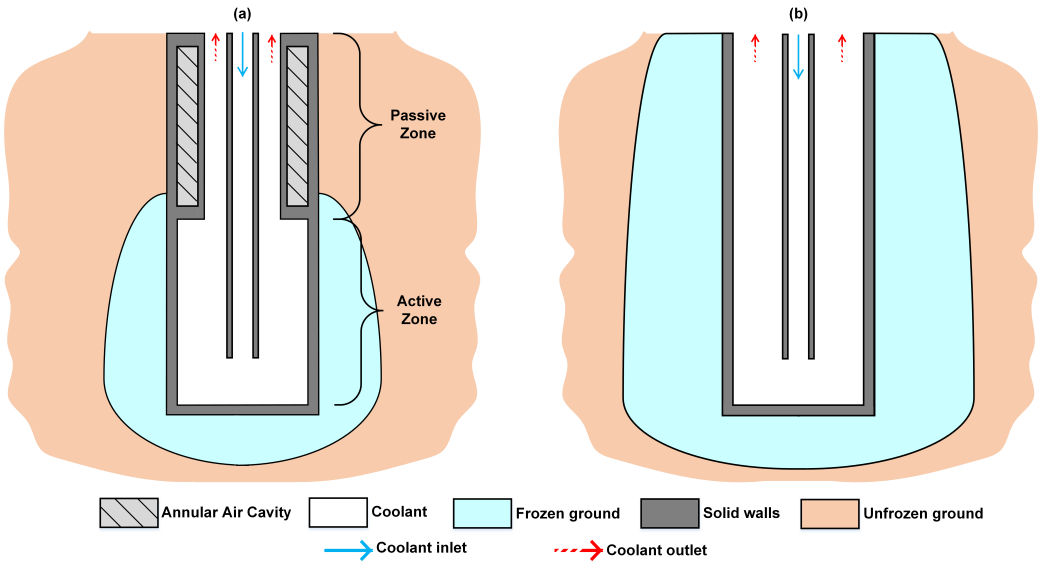

Figure 3-1: Schematic diagrams of: a) selective artificial ground freezing (S-AGF), and b) conventional artificial ground freezing (C-AGF).

air gap, and saturated porous ground structure, have not yet been developed. Hence, the primary objective of this study is to gain a better understanding of the thermal and hydraulic aspects of the entire S-AGF system experimentally and mathematically. This paper particularly addresses S-AGF as an energy saving technique, with the aim to study the influence of various parameters on the cooling load and optimize the insulation of the freeze pipe in the passive zone.

To this end, comprehensive documentation of the experimental rig and flow regulation is provided. Then, a mathematical model based on the conservation equations of mass, momentum, and energy is derived and validated against the experimental measurements. The potential of energy saving of S-AGF is then compared to that of C-AGF. Furthermore, the influence of temperature difference between the coolant inlet temperature and the ground, as well as the flow rate of the coolant, on the energy consumption is analyzed. Finally, the various heat transfer mechanisms inside the air insulation are deeply examined. Based on this heat transfer analysis within the air gap, the geometrical design of the air insulation layer is optimized, employing scale analysis, to minimize heat extraction from the ground in the passive zone and consequently decrease the total cooling load of the S-AGF plants.

3.2 Experimental setup

3.2.1 Physical model

The experimental rig consists of two main parts: 1) a supply chiller that can supply a coolant with a temperature as low as -30 [°C], and 2) an aluminum tank that is filled with saturated sand where a freeze pipe is installed vertically, as shown in Fig. 3-2(a). A positive displacement pump, controlled by a variable frequency drive (VFD), provides the flow that is further regulated by control valves, a pressure gauge, and a flow meter. The coolant passes through a primary loop in order to keep a steady and cold coolant temperature. The rig is equipped with three band-type heaters along the tank walls to pre-condition the ground temperature (prior to initializing the freezing process). The chiller, VFD, and band heaters are all controlled by a labview program.

The aluminum tank has a height of 1638 [mm] and an outer diameter of 549 [mm] standing on the top of 9.5 [mm] aluminum base, as can be seen from Fig. 3-2(b). Insulation layers were installed at the top, sides, and bottom of the tank to isolate the tank from the surrounding. At the top, the tank is sealed by 63.5 [mm] styrofoam. The sides of the tank are first covered by a closed-cell moisture resistant layer, followed by 25.4 [mm] foam and two layers of 82.6 [mm] thick fiberglass insulation. The bottom of the tank is insulated by two 12.7 [mm] styrofoam plates.

The freeze pipe consists of three concentric stainless steel 316 (SS316) tubes, as noted in Fig. 3-2(b). The annular air gap is formed by fixing two 6.35 [mm] collars between the middle and outer tubes separated by an axial distance of 749 [mm]. The freeze pipe is supported by a metal plate attached to the bottom of the freeze pipe. A 12.7 [mm] teflon ring is installed between the support and the pipe to prevent undesired metal to metal conduction.

Sixteen T-type thermocouples are distributed around the freeze pipe, as shown in Fig. 3-2(c), to measure ground temperatures at two different levels displayed in Fig. 3-2(b). The thermocouples are supported by teflon plates attached to the freeze pipe. The inlet and outlet

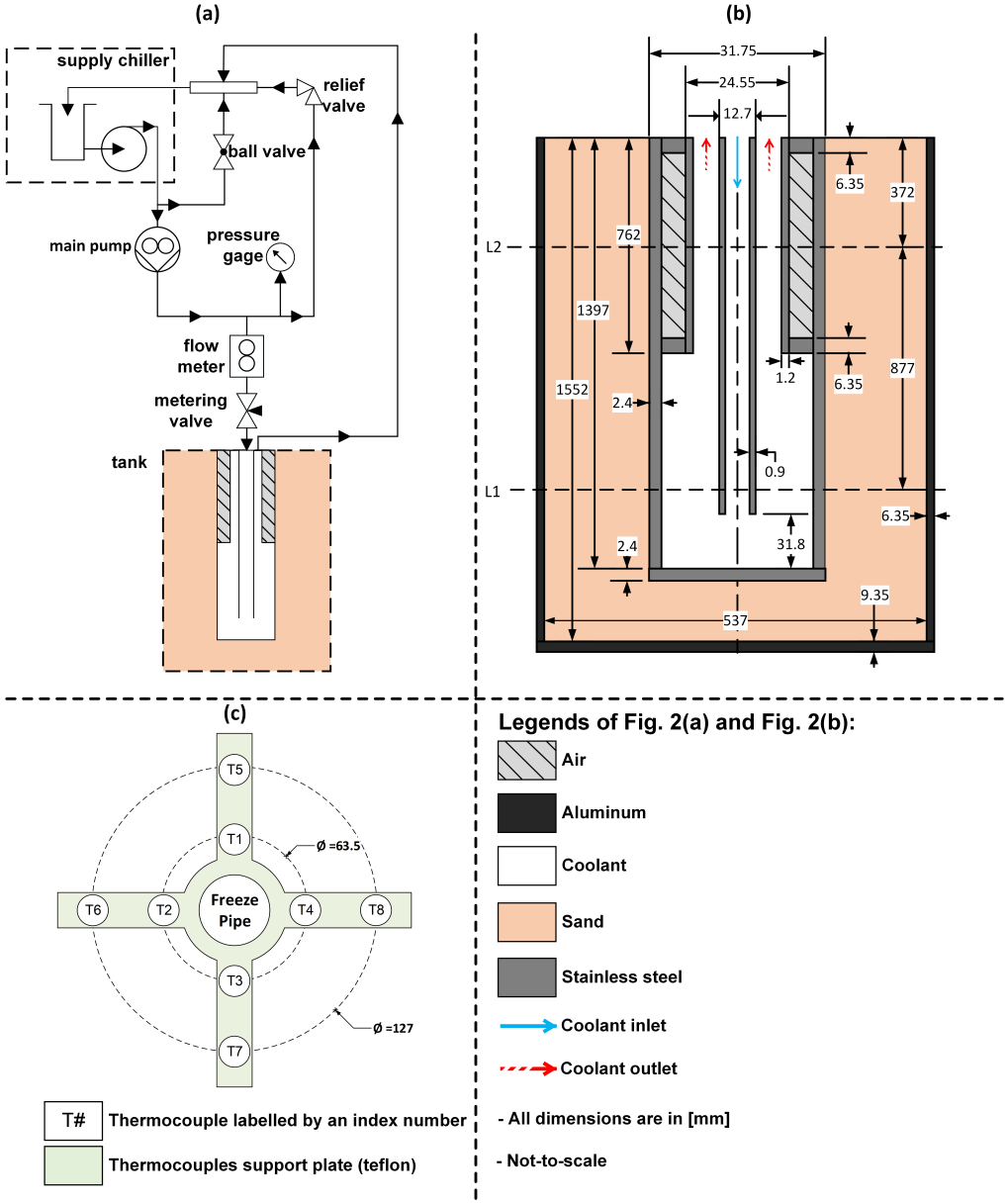

Figure 3-2: Experimental setup of the present study: a) flow diagram, b) schematic diagram of the tank and freeze pipe where L1 and L2 refer to the levels where thermocouples are installed, and c) thermocouples distribution around the freeze pipe. Each thermocouple is labeled by an index number according to its distance and orientation from the center of the freeze pipe.

temperatures of the coolant are also monitored by K-type thermocouples. All instrumentation readings, including thermocouples, pressure gauges, and flow meters, are connected to a data acquisition (DAQ) system and are recorded by a LabVIEW code.

3.2.2 Materials

In addition to the air and stainless steel tubes, two main materials take part inside the tank: the coolant and the sand. The coolant comprises 55% ethylene glycol and 45% water. The sand, on the other hand, consists of 90.5% quartz and 9.5% albite. The sand components were determined by x-ray diffraction (XRD). In order to find the porosity of the sand, a 1-L vessel packed with dry sand was first weighed. Then, water was added gradually to the vessel until the sand became fully saturated, and the new weight of the vessel was again measured. The weight of the water was found by calculating the difference between the weights of fully saturated sand and dry sand. The porosity was then evaluated by dividing the volume of the water by the overall volume of the vessel. The permeability is also measured experimentally and agrees with Carman-Kosney equation (see Eq. (3.31)) [29].

The thermophysical properties measured in this study are the density, thermal conductivity, specific heat, and viscosity, when applicable. To find the density of a material, a titration column was filled to a pre-determined level and placed on a 10[mg] accurate digital scale. The density is then calculated by dividing the reading of the digital scale (mass) over the occupied volume of the titration column. The thermal conductivity and viscosity were measured by a thermal properties analyzer and a viscometer, respectively. The specific heat was measured by using a calorimeter comprising a thermocouple and a heating element. The sand and coolant properties are provided in Table 3.1 and Fig. 3-3, respectively.

3.2.3 Data reproducibility test

To ensure the repeatability of the experimental results, two experiments were conducted under the same operational conditions. The thermocouples measurements in the inlet, outlet,

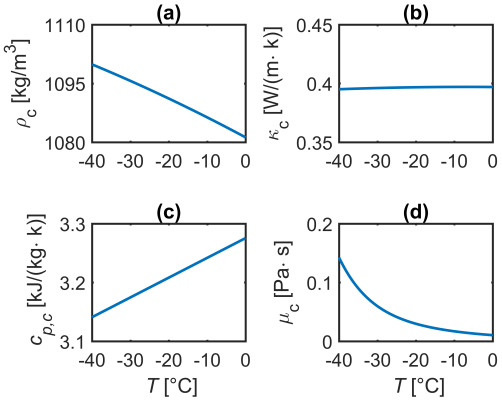

Figure 3-3: Temperature dependent thermophysical properties of the coolant (55% ethylene glycol and 45% water): a) density, b) thermal conductivity, c) specific heat, d) dynamic viscosity.

Quantities	Value
Thermal conductivity [W/(m.K)]	3.73
Density [kg/m^3]	2,634
Specific heat capacity [J/(kg.K)]	946
Porosity [m^3/m^3]	0.37
Permeability [m^2]	4.94×10^{-12}

Table 3.1: Properties of the sand particles used in this study.

and the ground, as well as the flow meter readings, show very good agreement as shown in Fig. 3-4. The flow meter reading of exp. #1 is slightly smaller than that of exp. #2 due to the flow resistance of the piping network. Consequently, the outlet temperature of exp. #1 is slightly higher. However, the ground temperature is not significantly affected by this small discrepancy in the flow rate.

3.3 Numerical model development

As can be seen from Fig. 3-5, S-AGF systems consist of four different zones: 1) subzero coolant flowing through the freeze pipe, 2) air flowing inside an annular enclosure, 3) porous ground structure surrounding the freeze pipe, and 4) stainless steel tubes. All zones are assumed to be filled with their corresponding material at any time. Because the model is

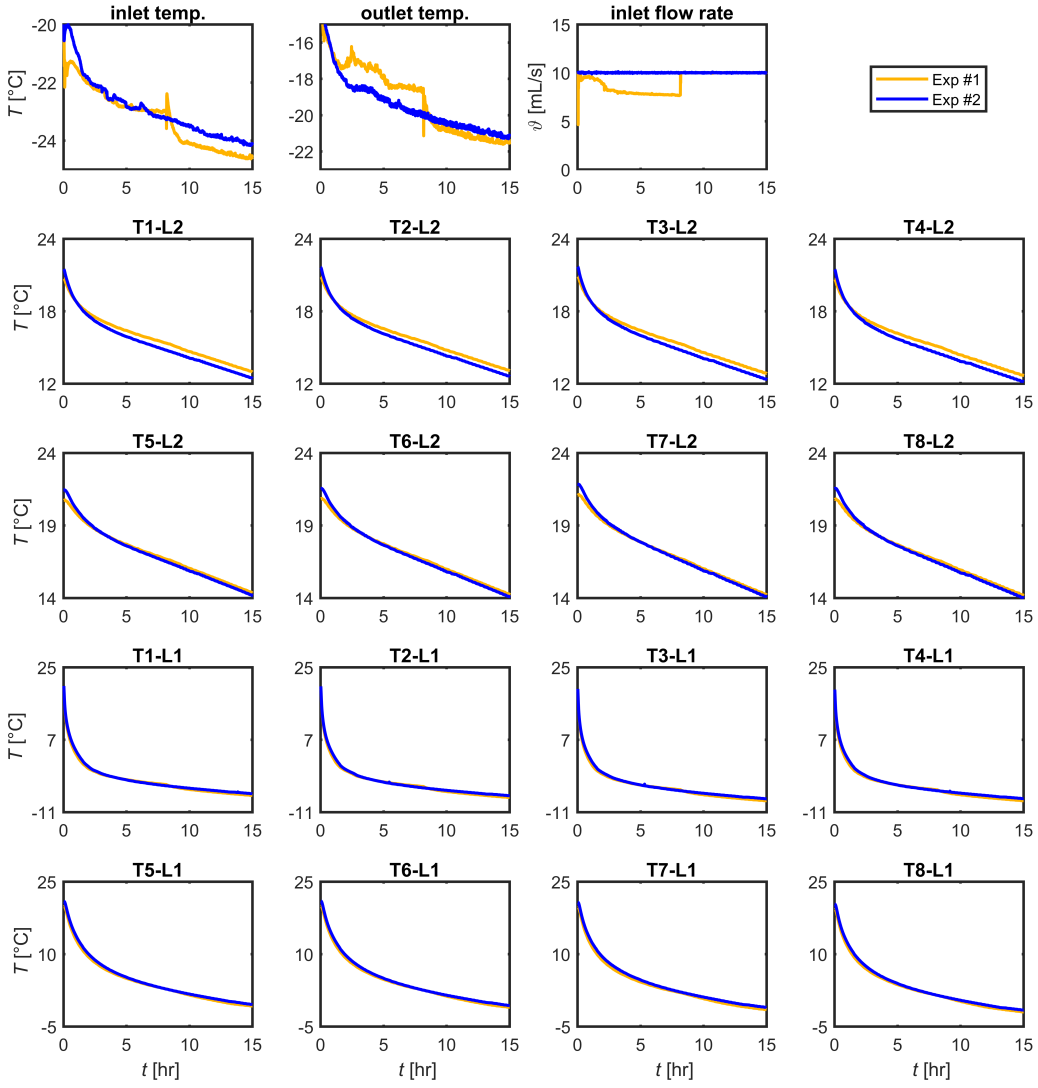

Figure 3-4: Reproducibility of experimental measurements. The title of each subplot refers to the position of the thermocouples as shown in Fig. 3-2(b) and Fig. 3-2(c).

symmetrical around the freeze pipe central axis, and the change of physical quantities, such as temperature and velocity, in the angular direction is negligible as compared to that of axial and radial directions, axisymmetric model is assumed to be valid and considered in this study. In the next subsections, the governing equations as well as the initial and boundary conditions of each zone will be illustrated in detail.

3.3.1 Governing equations

Coolant flow

Throughout this study, the Reynold's number of the coolant did not exceed ~ 100; as a consequence, the flow of the coolant inside the freeze pipe is set to be laminar. The governing equations of the coolant can be written as:

- Conservation of mass:

$$\frac{\partial \rho_c}{\partial t} + \nabla \cdot \vec{v}_c = 0 \tag{3.1}$$

- Conservation of momentum:

  Momentum balance can be written as:

$$\frac{\partial}{\partial t}(\rho_c \vec{v}_c) + \nabla \cdot (\rho_c \vec{v}_c \vec{v}_c) = -\nabla P + \nabla \cdot \mu_c (\nabla \vec{v}_c + \nabla \vec{v}_c^T) + \rho_c \vec{g} \tag{3.2}$$

  The first and second terms in the left-hand side of Eq. (3.2) represent the transient and convective momentum terms. The normal and deviatoric stresses, in addition to the gravitational body force, are considered in the right-hand side.

- Conservation of energy:

$$\frac{\partial}{\partial t}(\rho_c h) + \nabla \cdot (\rho_c \vec{v}_c h) = \nabla \cdot (\kappa_c \nabla T) \tag{3.3}$$

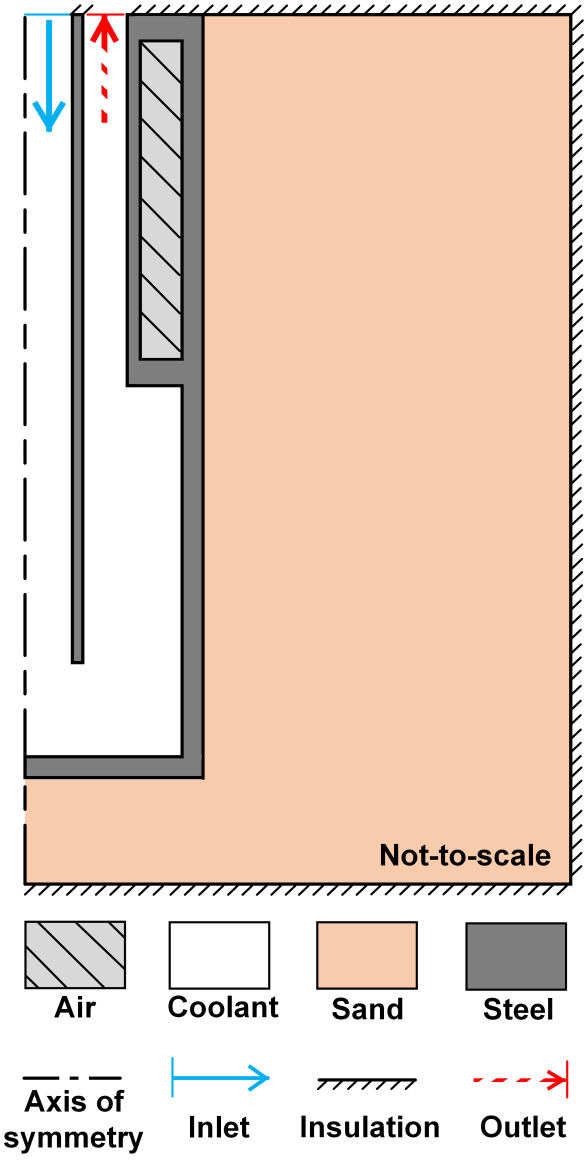

Figure 3-5: Computational domain and boundaries of the S-AGF system.

where the enthalpy, h, represents the sensible heat.

Air enclosure

Three major points need to be highlighted before modeling air flow:

1. The air flow regime can be turbulent, especially at high Rayleigh numbers Ra_L:

$$Ra_L = \frac{g\beta_a L^3}{\nu_a \alpha_a} \Delta T_a \tag{3.4}$$

   where the characteristic length, L, is the air gap thickness, and ΔT_a is the temperature difference between the hot and cold surfaces. The transition between laminar and turbulent regime begins at around $Ra_L \sim 10^5$ [30]. In the current study, the Rayleigh number ranges between as low as 10^1 to as high as 10^6. Therefore, both laminar and turbulent models were employed accordingly. In the following discussion, it shall be noted that the total velocity of air, v_a, of *turbulent* flows equals the sum of the mean and fluctuating velocities as $\vec{v}_a = \overline{v}_a + v'_a$.

2. Because air is a highly transmissive fluid, radiative heat exchange between the enclosing walls of the air cavity can be significant, and it is therefore considered.

3. Air is a compressible fluid modeled as an ideal gas ($\rho_a = \frac{P}{R_a T}$).

The governing conservation equations of the air flow can be written as:

- Conservation of mass:

$$\frac{\partial \rho_a}{\partial t} + \nabla \cdot \vec{v}_a = 0 \tag{3.5}$$

- Conservation of momentum:

$$\frac{\partial}{\partial t}(\rho_a \vec{v}_a) + \nabla \cdot (\rho_a \vec{v}_a \vec{v}_a) = -\nabla P + \nabla \cdot \overline{\overline{\tau}} + \rho_a \vec{g} \tag{3.6}$$

where the shear stress $\bar{\bar{\tau}}$ depends on the equivalent viscosity of air $\mu_{e,a}$ as:

$$\bar{\bar{\tau}} = \mu_{e,a}\left[(\nabla \vec{v}_a + \nabla \vec{v}_a^T) - \frac{2}{3}(\nabla \cdot \vec{v}_a)\bar{\bar{\iota}}\right] \tag{3.7}$$

In laminar air flows, the equivalent viscosity is identical to the molecular viscosity of air ($\mu_{e,a} = \mu_a$). However, in turbulent flows, the effective viscosity is increased due to the effect of turbulence as:

$$\mu_{e,a} = \mu_a + \mu_t \tag{3.8}$$

- Conservation of energy

  Two different kinds of energy spread inside the air gap: 1) thermal energy and 2) radiant energy. The amount of radiant energy passing through any medium is either absorbed, reflected, or transmitted. that is:

$$\zeta + \xi + \varrho = 1 \tag{3.9}$$

where ζ, ξ, ϱ are the absorptivity, reflectivity, and transmissivity of the medium, respectively. In this study, the following assumptions have been made in regards to the optical properties of air and those of steel walls:

1. Due to the small absorption coefficient of air and the short distance between the air walls in addition to the negligible air reflectivity, air is assumed to be fully transmissive. Thus, within the air domain, Eq. (3.9) simplifies to $\varrho_a = 1$.
2. Radiation scattering and refracting by air is neglected.
3. Steel walls are assumed to be opaque ($\varrho_w = 0$). Following this assumption, Eq. (3.9) for steel walls becomes $\zeta_w + \xi_w = 1$. Because the emissivity, ϵ, of a material equals its absorptivity (Kirchoff's law [31]), wall reflectivity can be written in terms of the emissivity utilizing Eq. 3.9 as $\xi_w = 1 - \epsilon_w$.

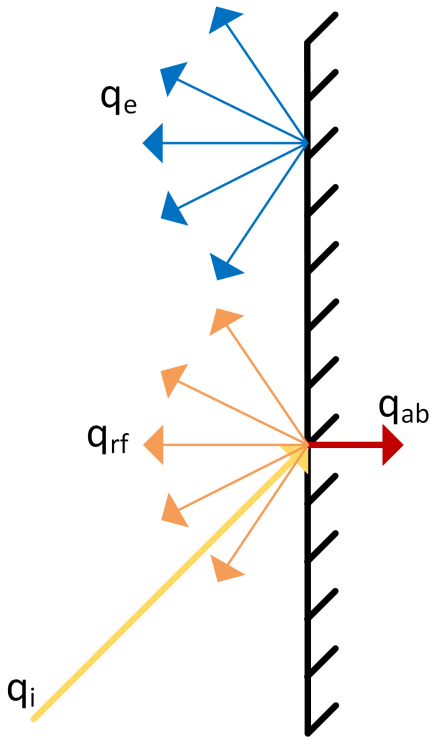

Figure 3-6: Thermal and radiant energy coupling at air enclosure walls: 1) q_i: total incident radiative flux, 2) q_{rf}: reflected flux, 3) q_{ab}: absorbed flux, 4) q_e: emitted flux.

4. Emitted and reflected rays by the walls are diffused evenly in all directions, as shown in Fig. 3-6.

Since air absorptivity is negligible, there is no coupling between the thermal and radiant energy inside the air domain. In other words, the two kinds of energies are coupled at the enclosing walls only. In the following points, the thermal and radiant energy balance, as well as the thermal/radiant energy coupling at the walls, will be explained.

– Thermal energy balance:

$$\frac{\partial}{\partial t}(\rho_a h) + \nabla \cdot (\rho_a \vec{v}_a h) = \nabla \cdot \left[\kappa_{e,a} \nabla(T)\right] \tag{3.10}$$

the equivalent thermal conductivity of air $\kappa_{e,a}$ in laminar buoyant flow is identical to the molecular air thermal conductivity κ_a. In the presence of turbulent flows,

the equivalent thermal conductivity becomes:

$$\kappa_{e,a} = \kappa_a + \kappa_t \tag{3.11}$$

where the turbulent thermal conductivity is $\kappa_t = \frac{c_{p,a}\mu_t}{Pr_t}$.

– Radiant energy balance:

The radiant transport equation (RTE) of a non-scattering and non-emissive medium (air) can be simplified to [32]:

$$\nabla \cdot (I\vec{s}) = 0 \tag{3.12}$$

where I is the radiation intensity, and $\vec{s}$ is a direction vector.

– Thermal/radiant energy coupling at the walls:

The incident radiative heat flux at the wall is evaluated as:

$$q_{rad,in} = q_i = \int_{\vec{s}\cdot\vec{n}>0} I_{in}(\vec{s}\cdot\vec{n})d\Omega \tag{3.13}$$

The incident radiation can be either reflected or absorbed ($q_i = q_r + q_{ab}$), as illustrated in Fig. 3-6. The amount of radiant energy that is absorbed and converted to thermal energy relies on the wall emissivity as:

$$q_{rad\to th} = q_{ab} = \zeta_w q_i = \epsilon_w q_i \tag{3.14}$$

The amount of thermal energy that is emitted and converted to radiant energy is a function of wall temperature and emissivity:

$$q_{th\to rad} = q_e = \epsilon_w \sigma T^4 \tag{3.15}$$

The net change in thermal energy of the steel walls due to radiation is evaluated

as the difference between the absorbed and emitted heat fluxes as:

$$q_{th,net} = q_{ab} - q_e \tag{3.16}$$

On the other hand, the overall radiative flux leaving the surface equals to the sum of the reflected flux q_{rf} and the radiant energy emitted by the wall q_e:

$$q_{rad,out} = q_{rf} + q_e = (1 - \epsilon_w) q_{rad,in} + \epsilon_w \sigma T^4 \tag{3.17}$$

Finally, the net radiative intensity is distributed evenly in all directions:

$$I_{out} = q_{rad,out}/\pi \tag{3.18}$$

- Turbulence balance

In the current study, the realizable $k - \varepsilon$ model, an improvement over the standard $k - \varepsilon$ model, is used in turbulent air flows. The realizable $k - \varepsilon$ model has been validated against numerous turbulent applications including boundary layer flows [33]. This model requires two additional equations representing the balance of turbulent kinetic energy and turbulent dissipation rate expressed as:

$$\frac{\partial}{\partial t}(\rho_a k) + \nabla \cdot (\rho_a k \vec{v}_a) = \nabla \cdot \left[(\mu_a + \frac{\mu_t}{\sigma_k}) \nabla k \right] + G_k + G_{b,k} - \rho_a \varepsilon \tag{3.19}$$

$$\frac{\partial}{\partial t}(\rho_a \varepsilon) + \nabla \cdot (\rho_a \varepsilon \vec{v}_a) = \nabla \cdot \left[(\mu_a + \frac{\mu_t}{\sigma_\varepsilon}) \nabla \varepsilon \right] - \rho_a C_2 \frac{\varepsilon^2}{k + \sqrt{\varepsilon \nu_a}} + C_{1\varepsilon} \frac{\varepsilon}{k} C_{3\varepsilon} G_{b,\varepsilon} \tag{3.20}$$

where G_k takes into account the generation of turbulent kinetic energy because of the mean velocity. $G_{b,k}$ and $G_{b,\varepsilon}$ represent the generation of turbulent kinetic energy and dissipation rate due to buoyancy and are evaluated as:

$$G_{b,k} = \beta \frac{\mu_t}{Pr_t} \vec{g} \cdot \nabla T \tag{3.21}$$

$$G_{b,\varepsilon} = -\frac{\mu_t}{\rho Pr_t}\vec{g} \cdot \nabla\rho \tag{3.22}$$

More information about the different constants used in this model can found in [33].

Porous ground

The porous ground consists of sand particles and voids filled by frozen or unfrozen water. Local volume averaging (LVA) technique is used which dictates that the whole system can be described in terms of a small length scale, l, that is much smaller than the system length, Λ, yet larger than particle length, l_p, as:

$$l_p < l << \Lambda \tag{3.23}$$

In the LVA method, it is convenient to consider the Darcian velocity, v_d, in writing the governing equations:

$$\vec{v}_d = \psi\vec{v}_l \tag{3.24}$$

where ψ is the porosity of the ground and v_l is the pore velocity of the water.

Before addressing the conservation equations, different volume fractions will be clarified. In the porous ground, a volume element is occupied by sand particles and pores, which are filled by frozen and/or unfrozen water ($V_v = V_u + V_f$). The porosity, ψ, and liquid fraction, γ, can be defined as:

$$\psi = \frac{V_v}{V} \tag{3.25}$$

$$\gamma = \frac{V_u}{V_v} \tag{3.26}$$

Alzoubi et al. provided a visual explanation of the presented volume fractions as used in this study [25].

- Conservation of mass

$$\frac{\partial \rho_g}{\partial t} + \nabla \cdot (\rho_g \vec{v}_d) = 0 \tag{3.27}$$

where ρ_g is the volume averaged density of the porous ground.

- Conservation of momentum

$$\frac{1}{\psi}\frac{\partial}{\partial t}(\rho_u \vec{v}_d) + \frac{1}{\psi^2}\left[\nabla \cdot (\rho_u \vec{v}_d \vec{v}_d)\right] = -\nabla P + \frac{1}{\psi}\nabla \cdot \left[\mu_u(\nabla \vec{v}_d + \nabla \vec{v}_d^T)\right] + S_D + S_E + S_m + \rho_u \vec{g} \tag{3.28}$$

The Darcy and Ergun source terms (S_D and S_E) represent the viscous and inertial losses and are expressed as a function of the permeability, K, as:

$$S_D = -\frac{\mu_u}{K}\vec{v}_d \tag{3.29}$$

$$S_E = -\frac{C_E}{K^{\frac{1}{2}}}\rho_u |v_d| \vec{v}_d \tag{3.30}$$

Where C_E is the Ergun coefficient. In the present model, the effect of the inertial term can be neglected due to the small seepage velocity. The permeability was measured experimentally and agrees with Carman-Koseny equation as [29]:

$$K = \frac{l_p^2 \psi^3}{180(1-\psi)^2} \tag{3.31}$$

The mushy source term, S_m, is introduced to control the Darcian velocity in the mushy zone and is formulated as:

$$S_m = -\vec{v}_d C_m \frac{(1-\gamma)^2}{\gamma^3} \tag{3.32}$$

In the immediate vicinity of pure ice ($\gamma = 0$), a very small number is added to the denominator in Eq. 3.32 to prevent division by zero.

- Conservation of energy

The local thermal equilibrium (LTE) has been employed to simplify the energy equation of the porous medium. The idea behind the LTE assumption is that the temperature within each elementary volume is uniform throughout the voids and solid particles of the porous structure. To ensure the validity of the LTE assumption, the time scale must satisfy the following conditions [29]:

$$\frac{\psi(\rho c_p)_v l^2}{t}\left(\frac{1}{\kappa_v}+\frac{1}{\kappa_p}\right) << 1 \tag{3.33}$$

and

$$\frac{(1-\psi)(\rho c_p)_p l^2}{t}\left(\frac{1}{\kappa_v}+\frac{1}{\kappa_p}\right) << 1 \tag{3.34}$$

The length scale has to also meet the following condition [29]

$$\frac{\psi\kappa_v}{A\Lambda^2}\left(\frac{1}{\kappa_v}+\frac{1}{\kappa_p}\right) << 1 \tag{3.35}$$

and

$$\frac{(1-\psi)\kappa_p l}{A\Lambda^2}\left(\frac{1}{\kappa_v}+\frac{1}{\kappa_p}\right) << 1 \tag{3.36}$$

Based on the LTE assumption, the conservation of energy of the porous medium can be formulated as:

$$\frac{\partial}{\partial t}[\psi(\gamma\rho_u h_u + (1-\gamma)\rho_f h_f) + (1-\psi)\rho_p h_p] + \nabla\cdot(\rho_u h_u \vec{v}) = \nabla\cdot(\kappa_e \nabla T) - S_H \tag{3.37}$$

where the enthalpy terms, h, consider the sensible heat only as $h = \int c_p dT$. The latent heat of fusion is introduced to the energy equation using the source term S_H as:

$$S_H = \psi\rho_u \Delta H \frac{\partial\gamma}{\partial t} + \nabla\cdot[\rho_u \vec{v}\gamma\Delta H] \tag{3.38}$$

The effective thermal conductivity, κ_e, is evaluated using the parallel-arrangement approach as [29]:

$$\kappa_e = \psi\kappa_v + (1-\psi)\kappa_p \tag{3.39}$$

Stainless steel walls

The energy flow within the solid steel domain is governed by the conduction equation as:

$$\frac{\partial}{\partial t}(\rho_s h) = \nabla \cdot (\kappa_s \nabla T) \tag{3.40}$$

3.3.2 Initial conditions

Throughout this study, the following initial conditions were set for the entire system at $t = 0$:

$$T_{initial} = 21[^{\circ}\mathrm{C}] \tag{3.41}$$

$$\vec{v}_{initial} = 0 \tag{3.42}$$

3.3.3 Boundary conditions

The temperature and velocity boundary conditions along the axis of symmetry shown in Fig. 3-5 are modeled as:

$$\partial\vec{v}_{axis}/\partial r = 0 \tag{3.43}$$

$$\partial T_{axis}/\partial r = 0 \tag{3.44}$$

Furthermore, a no-slip boundary condition is considered along the surface of solid walls (i.e, freeze pipe and tank walls) as:

$$\vec{v}_w = 0 \tag{3.45}$$

The remaining boundary conditions of each zone are given as follows:

Coolant

The coolant enters and exits from the inlet and outlet boundaries, respectively, while thermally interacting with the steel walls.

- Inlet

  Dirichlet boundary conditions for coolant inlet velocity and temperature:

$$\vec{v} = \vec{v}_{in} \tag{3.46}$$

$$T = T_{in} \tag{3.47}$$

- Outlet

  Dirichlet boundary condition for the coolant outlet pressure, and Neumann boundary condition for temperature:

$$P = P_{out} = 0 \tag{3.48}$$

$$\vec{n} \cdot \nabla T = 0 \tag{3.49}$$

- Coolant/steel wall interaction

  Thermally coupled boundary condition:

$$\kappa_c \frac{\partial T_{c,w}}{\partial n} = \kappa_s \frac{\partial T_{s,w}}{\partial n}; \qquad T_{c,w} = T_{s,w} \tag{3.50}$$

Air

The air gap is completely enclosed by steel walls. The thermal interaction with the steel walls includes the radiative heat transfer (as explained in section 3.3.1) as:

$$\kappa_a \frac{\partial T_{a,w}}{\partial n} + q_{th,net} = \kappa_s \frac{\partial T_{s,w}}{\partial n}; \qquad T_{a,w} = T_{s,w} \tag{3.51}$$

Ground

The porous ground loses heat to the freeze pipe and is insulated along the tank wall. The corresponding boundary conditions are:

- Thermal interaction with the freeze pipe:

$$\kappa_g \frac{\partial T_{g,w}}{\partial n} = \kappa_s \frac{\partial T_{s,w}}{\partial n}; \qquad T_{g,w} = T_{s,w} \tag{3.52}$$

- Tank wall insulation:

$$q_{tank} = 0 \tag{3.53}$$

3.4 Numerical Simulations

The computational domain and mesh were created using ANSYS Workbench 18.1. The spatial and transient terms were formulated by second order schemes. The velocity and pressure fields are implicitly solved together using the coupled algorithm. Model computation of the governing equations, as well as the boundary and initial conditions, were conducted by ANSYS Fluent 18.1.

More than 5×10^4 cells were created inside the narrow air enclosure to accurately capture the temperature and velocity gradients induced by the buoyant forces. Overall mesh independence study was conducted by varying the mesh size of the whole system between 8.42×10^5 and 1.26×10^6 elements. The difference in the ground temperature within this range was less than 0.05 [° C] ensuring that the model is mesh independent.

3.5 Model validation

The mathematical model is validated against the measurements of two different experimental setups as follows:

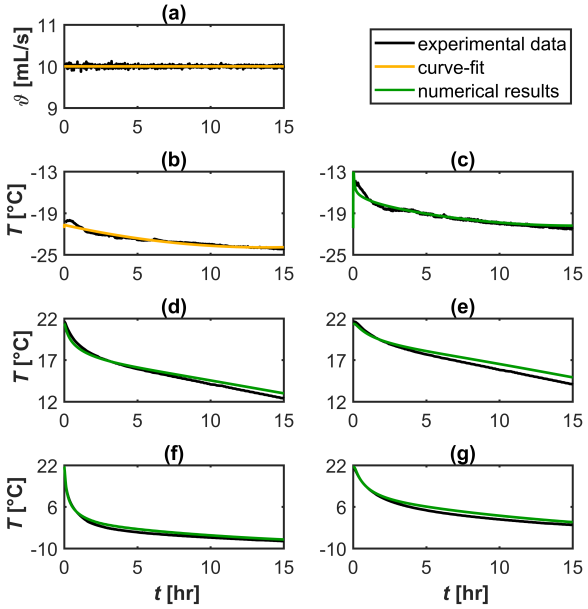

Figure 3-7: Curve-fit and validation of the mathematical model against experimental measurements at low Rayleigh number: (a) inlet flow rate, (b) coolant inlet temperature, (c) coolant outlet temperature, (d) average temperature readings of $T1 \rightarrow T4$ at level 2, (e) average temperature readings of $T5 \rightarrow T8$ at level 2, (f) average temperature readings of $T1 \rightarrow T4$ at level 1, (f) average temperature readings of $T5 \rightarrow T8$ at level 1. Schematic diagrams displaying the locations of the thermocouples according to their levels and index numbers can be found in Fig. 3-2(b) and Fig. 3-2(c).

3.5.1 Validation at low Rayleigh number

First, the numerical model validity is tested against the experimental measurements at low Ra_L. The small air gap thickness results in a low Rayleigh number ($Ra_L \sim 100$) indicating a laminar flow regime within the air cavity. The coolant flow rate is fixed at 10 [mL/s], as shown in Fig. 3-7. The inlet temperature in the mathematical model was curve-fitted to resemble the transient experimental inlet temperature. The ground temperature is calculated at two different levels, shown in Fig. 3-2(b), to validate the mathematical model in the passive and active zones.

Very good agreement is noted between the numerical results and experimental measurements. The temperature drop in the passive zone is significantly smaller than that of the active zone due to the air gap insulation. Because the temperature difference between the

coolant and ground is higher at the start of the experiment than that at the end, the temperature drop in the ground is faster at the beginning. This is attributed to the proportional relationship between heat flux and temperature difference. Additionally, the outlet temperature increases with time because heat transfer between the coolant and pipe decreases.

3.5.2 Validation at high Rayeigh number

At higher air gap thickness and/or temperature difference between air bounds, the Rayleigh number drastically increases by orders of magnitude and the flow behavior within the air gap changes entirely. To ensure the validity of the present mathematical model at higher Rayleigh numbers, the current numerical model was again validated against another experimental study, conducted by Keyhani et al. [34], in which Ra_L goes to as high as 2 $\times 10^5$. The experimental rig consists of a heater located at the center of a cylinder that is capped-off at both ends by aluminum plates, as shown in Fig. 3-8. The electrical heating rod supplies a uniform heat flux while the outer cylinder wall is maintained at a fixed temperature of 25 $[^\circ C]$.

The governing equations of air are the same as those provided in section 3.3.1. The boundary and initial conditions were nonetheless changed to meet the specifications of the operational conditions of this experiment. The adjusted boundary and initial conditions are given as:

- Initial conditions

$$T = T_{initial}, \qquad \vec{v} = \vec{v}_{inital} = 0 \tag{3.54}$$

- no slip boundary conditions at all walls:

$$\vec{v}_w = 0 \tag{3.55}$$

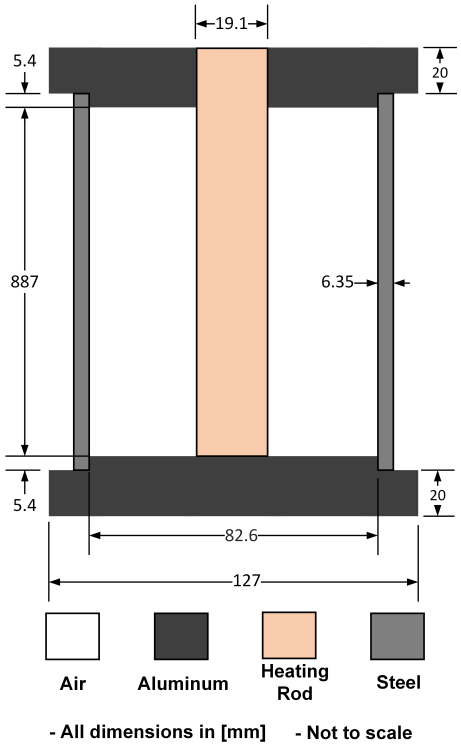

Figure 3-8: Non-to-scale schematic diagram of the experimental setup built by Keyhani et al. [34] (all dimensions are in millimeters).

- steady and uniform heat flux along the heating rod surface:

$$q_{rod} = q_{constant} \tag{3.56}$$

- Fixed temperature of 25 $[°C]$ along the outer cylinder:

$$T_{outer\ cylinder} = T_{constant} \tag{3.57}$$

- Insulation along the outer aluminum caps walls:

$$q_w = 0 \tag{3.58}$$

- Thermal interaction between the air gap and surrounding solid walls is given by

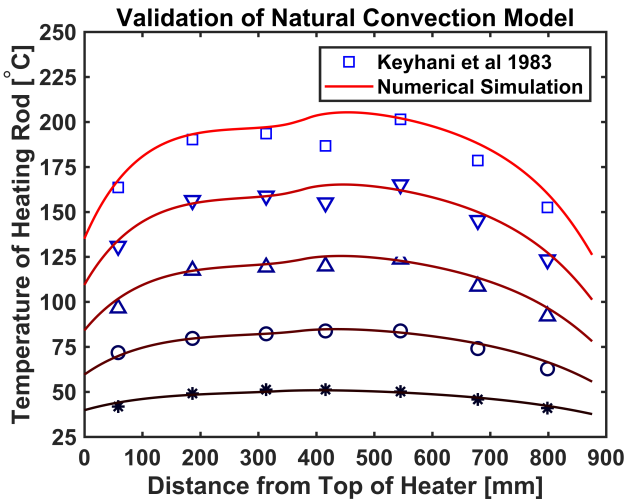

Figure 3-9: Validation of temperature profile on the heater rod surface against the experimental measurements of Keyhani et al. study [34]: $*$ 10.2W, $\circ$ 28.3W, Δ 53.99W, ∇ 83.65W, $\square$ 119.34W.

Eq. (3.51).

The overall heater power ranges between 10 [W] and 120 [W], as shown in Fig. 3-9. The simulation time of each case lasted for 2 hours to ensure that the system reached a steady state. As shown in Fig. 3-9, a very good agreement is noted between the numerical and experimental data. At low heating power, the temperature profile, along the rod surface, is approximately uniform because the small temperature difference between the rod and the outer wall is unable to induce effective buoyant flow. As the heating power increases, the ends of rod become notably cooler than the middle due to the development of significant buoyant jets striking the ends of the rod. At very high heat flux, the flow becomes more turbulent which leads to the formation of inner vortices and causes temperature fluctuations around the center of the rod, as can be depicted from Fig. 3-9.

3.6 Results and discussion of results

One of the main goals of S-AGF is to reduce the energy consumption of ground freezing systems. In this section, a comparison between the required cooling load of S-AGF and that

of C-AGF is conducted. Then the influence of temperature difference between the ground and the coolant as well as the coolant flow rate is examined. Finally, the air cavity aspect ratio, $\Gamma = L/H$, is optimized to minimize heat gain in the passive zone. The results in this section has been, in general, normalized so that they can be easily utilized in other studies and practical applications.

3.6.1 Selective artificial ground freezing (S-AGF) VS conventional artificial ground freezing (C-AGF)

In order to quantify energy savings that can be credited to the application of S-AGF, the cooling load needed by S-AGF is compared to that of C-AGF given the same coolant inlet temperature, coolant flow rate, and initial ground temperature. The geometry of conventional freeze pipe outer and inner tubes is also identical to that of S-AGF. However, unlike S-AGF geometry, there is no air cavity in the C-AGF model; the thickness of the annular gap of the coolant is uniform throughout the C-AGF freeze pipe (see Fig. 3-1(b)).

As the coolant flows through the freeze pipe, the coolant temperature increases due to heat extraction from the ground. The cooling load required by the coolant can be determined as:

$$\dot{Q}_c = \dot{m}_c c_{p,c}(T_{outlet} - T_{inlet}) \tag{3.59}$$

The rate of heat gain in the passive and active zones can be derived from Eq. (3.52) as:

$$q = \kappa_s \frac{\partial T_{s,w}}{\partial n_s} \tag{3.60}$$

where the subscript w can refer to the freeze pipe walls of the active or passive zone. The overall heat gain of the freeze pipe can be found by averaging the cooling load over the surface area of the freeze pipe. The overall heat extraction of S-AGF may also be evaluated by calculating the weighted mean of the active and passive heat gains.

The comparison, shown in Fig. 3-10, reveals that the overall cooling load required by

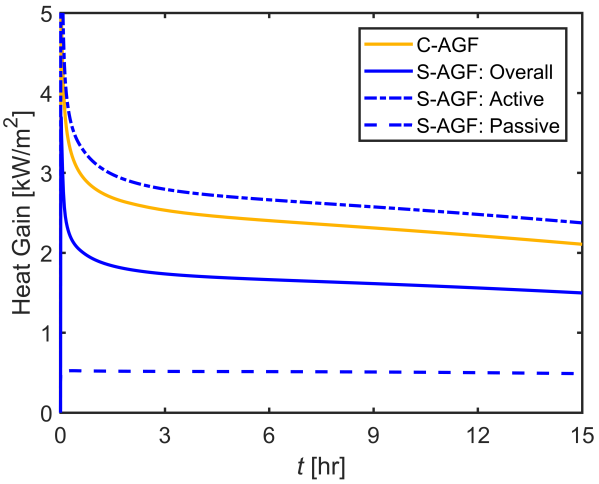

Figure 3-10: Comparison between the heat gained by S-AGF and C-AGF freeze pipes.

S-AGF system is about 1.5 times less than that of C-AGF. In particular, for the first 15 hours of operation, the total energy consumption of S-AGF is 3.0 [kWh] as compared to 4.3 [kWh] in C-AGF. Energy saving of S-AGF is attributed to the air cavity insulation which significantly decreases heat gain in the passive zone. Interestingly, heat gain in the active zone of S-AGF is slightly higher than that of C-AGF. In S-AGF freeze pipe, the coolant strikes the bottom plate of the air gap and forms vortices. As a result, heat extraction in this area (just below the air cavity) rises causing higher heat gain in the active zone of S-AGF as compared to that of C-AGF.

3.6.2 Influence of inlet flow and ground conditions

Heat gained by a coolant in a freeze pipe is proportional to the temperature difference between the ground and the coolant, $T_c - T_g$, as well as the heat transfer coefficient, $\hbar$, as:

$$q = \hbar(T_g - T_c) \tag{3.61}$$

$\hbar$ can be characterized by Reynold's number, Re_{inlet}, at the inlet while $T_g - T_c$ can be scaled as the temperature difference between the ground initial temperature and the coolant inlet

temperature (ΔT), respectively.

In agreement with Eq. (3.61), the numerical results show that the heat gain in the active and passive zones is linearly proportional to ΔT, as can be depicted in Fig. 3-11(a). While there is also a proportional relationship between Re_{inlet} and heat gain, the relationship is non-linear as can be seen from Fig. 3-11(b). Alzoubi and Sasmito [35] provided more details on the nature of the non-linear relationship between Re_{inlet} and $\hbar$ of freeze pipes in the active zone. Heat extraction in the passive zone at different Re_{inlet} is highly related to the temperature increase of the coolant in the active zone. At low Re_{inlet}, the coolant flow rate is small, resulting in long thermal interaction between the coolant and the ground. As a consequence, the coolant temperature increases, and the temperature difference between the ground and the coolant ($T_g - T_c$) decreases leading to low heat gain. By conducting similar analysis at high Re_{inlet}, it can be deduced that heat gain in the passive zone is larger at higher Re_{inlet} than that of low Re_{inlet}.

3.6.3 Analysis and optimization of air insulation

Energy saving in S-AGF systems is mainly attributed to the passive zone insulation. It is therefore of great importance to study the passive zone behavior and optimize heat insulation. In this zone, the coolant and the ground are separated by a vertical annular air enclosure. The air cavity is surrounded by a cold inner wall and a warm outer wall as well as non-adiabatic top and bottom plates.

Nusselt's number correlations of annular air enclosure are often related to the aspect ratio, $\Gamma = L/H$, because the heat transfer regime can change according to Γ [36]. At very low Γ, heat transfer within the air cavity is governed by conduction. As Γ increases and approaches unity, convective heat transfer becomes more significant. The influence of the air cavity aspect ratio on the overall heat gain of the passive zone will be deeply analyzed in this subsection.

The total rate of heat gain in the passive zone can be calculated by employing Eq. (3.51)

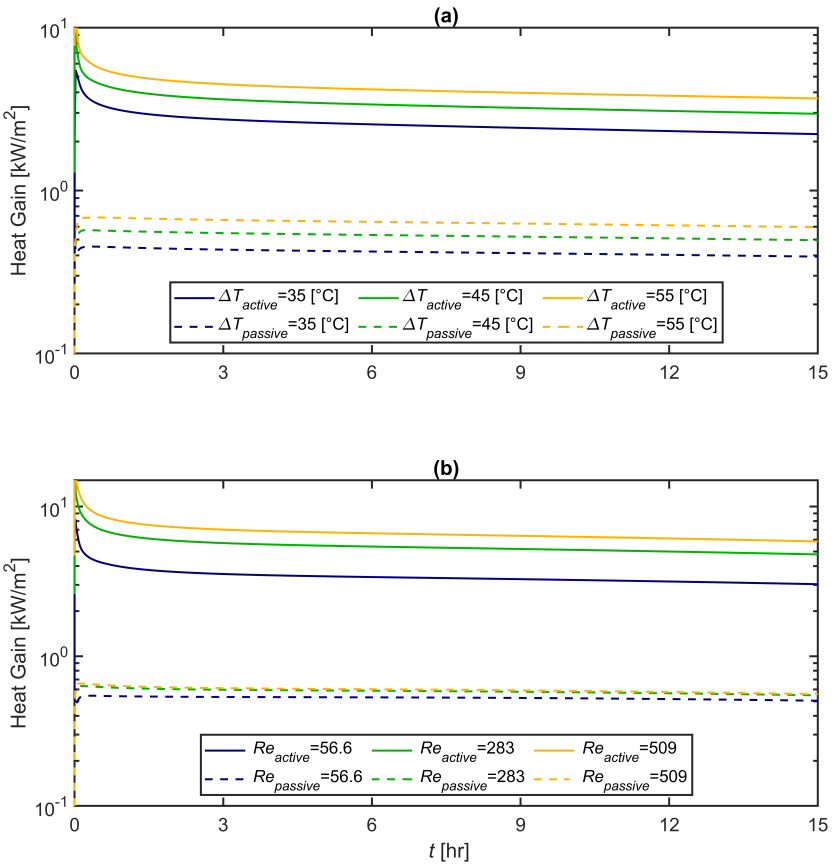

Figure 3-11: Heat gain in the active and passive zones at: a) different temperature difference between the ground initial temperature and coolant inlet temperature ΔT, and b) different inlet Reynold's numbers, Re.

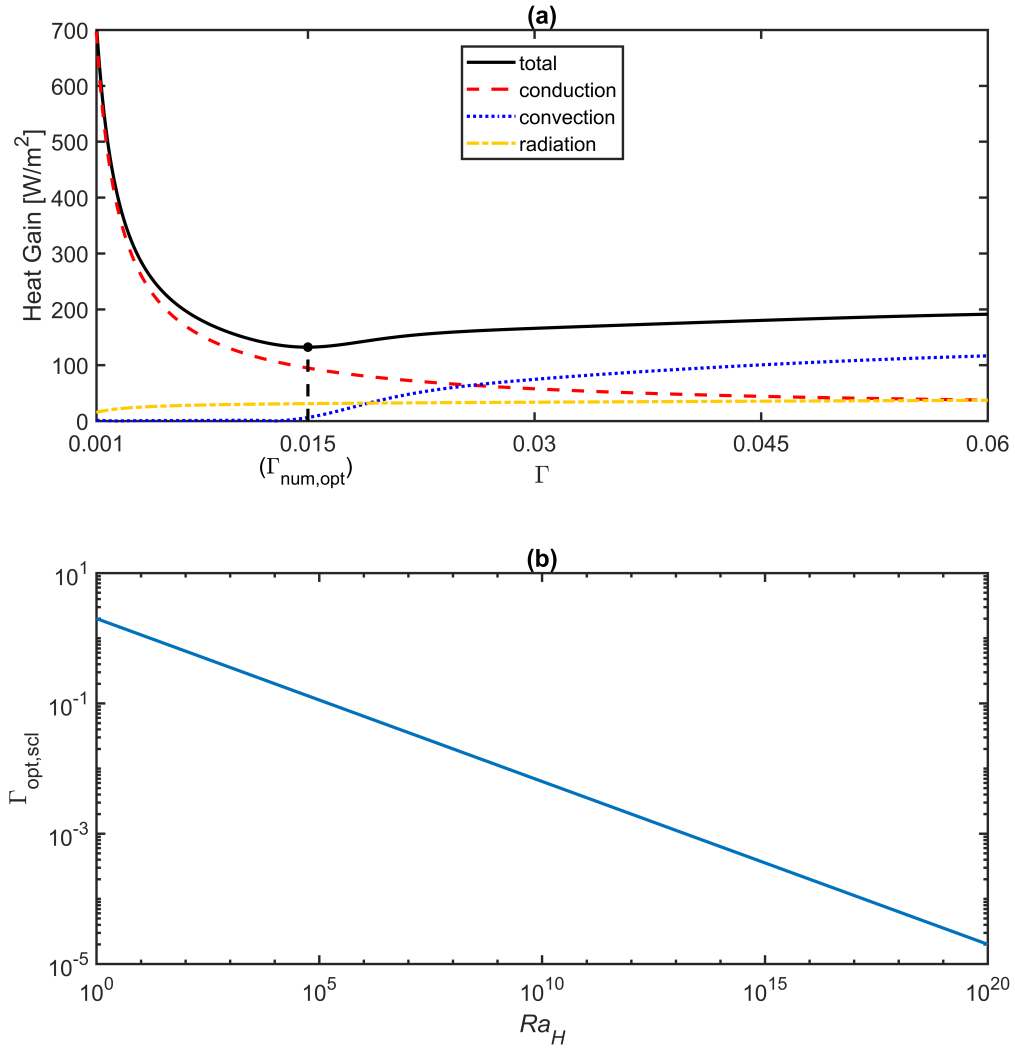

Figure 3-12: Optimization of air cavity: a) contribution of each heat transfer mechanism as a function of air cavity aspect ratio, $\Gamma = L/H$, in the passive zone ($t = 15[hr]$ - the results are normalized against the surface area of the inner wall of the air cavity), and b) The optimum aspect ratio as per Eq. (3.68) as a function of Rayleigh number.

as: $\dot{Q}_{ao,total} = k_s(\partial T_{s,ao}/\partial n) * A_{ao}$. By evaluating the total heat gain at different aspect ratios, the numerical results reveal the existence of an optimum aspect ratio, $\Gamma_{opt,num}$, at $\Gamma = 0.015$, as can be seen from Fig. 3-12. To physically understand the total heat gain plot, let's examine the various heat transfer mechanisms within the air gap as a function of the aspect ratio. The air cavity extracts heat from the ground by three different mechanisms: 1) conduction 2) convection (buoyancy) and 3) radiation. By applying heat transfer balance on the outer wall of the air cavity, the total rate of heat gain in the passive zone can be expressed as:

$$\dot{Q}_{ao,total} = k_s \frac{\partial T_{s,ao}}{\partial n} A_{ao} = \underbrace{2\pi H \frac{\Delta T_a}{ln(r_{ao}/r_{ai})}}_{conduction} + \underbrace{q_{th,net} A_{ao}}_{radiation} + \dot{Q}_{convection} \tag{3.62}$$

where ΔT_a refers to the difference between the average temperature of the outer wall and that of the inner wall. The radiation expression written in Eq. (3.62) is obtained from Eq. (3.16). The radiative heat transfer is almost constant, as shown in Fig. 3-12, because the difference in ΔT_a at different aspect ratios is not large enough to induce significant change in radiative heat gain. The emissivity of new stainless steel pipes, such as the ones used in this study, is considered to be 0.3 [37]. It can be noted that radiation can make up to 25% of the total heat transfer. In practice, as steel pipes get weathered, their emissivity increases substantially [38], and the radiative heat transfer becomes more significant.

Unlike radiative heat, the conductive and convective heat transfer mechanisms are obviously influenced by the aspect ratio, $\Gamma = L/H$, as can be noted in Fig. 3-12. When the aspect ratio is small, conduction is the dominant heat transfer mechanism. As the aspect ratio increases, the distance between air gap walls gets larger, and the contribution of the conductive heat transfer shrinks. The convective heat transfer, on the other hand, remains negligible at low aspect ratios. Beyond a certain limit around $\Gamma = 0.014$, the convective heat transfer arouses and gradually becomes more significant than conductive heat transfer.

The various heat transfer mechanisms can be further analyzed by studying the radial

temperature distribution across the air gap (along level 2 line as shown in Fig. 3-2(b)). When $\Gamma = 0.013$, the temperature distribution is linear, as can be seen from Fig. 3-13(a), indicating that conduction is dominant over convection. At larger Γ, the buoyant jets become stronger and start forming thermal boundary layers. The larger the aspect ratio (up to $\Gamma = 1$), the more distinct the thermal boundary layers, and the higher the convective heat transfer coefficient as given by various Nusselt's number correlations of annular air enclosures [36], [39].

Following Fig. 3-12, decreasing the aspect ratio below $\Gamma_{opt,num}$ increases the total heat gain by conduction. On the other hand, increasing the aspect ratio above $\Gamma_{opt,num}$ raises the significance of convective heat and increases the total heat gain. From the previous discussion, it can be deduced that the best insulation in the passive zone can be achieved if the flow inside the cavity is designed to be on the verge of the boundary layer regime when convective heat transfer starts becoming significant. For this regime to begin, the air gap thickness should be large enough to fit in the thermal boundary layers on both sides of the cavity. In other words, boundary layer regime is initialized when:

$$L > 2\delta \tag{3.63}$$

Quantifying the thermal boundary layer thickness, δ, can be best achieved by performing a scale analysis of the annular air enclosure (as inspired by [40]). Since the air flow satisfies the Boussinesq approximation conditions ($\beta_a(T - T_{reference}) << 1$)[41], the Boussinesq approximation is employed to simplify the analysis. The radial and axial momentum equations can be reduced to a single equation, by eliminating the pressure, as:

$$\begin{aligned}\frac{\partial}{\partial z}\Big[v_r\frac{\partial v_r}{\partial r} + v_z\frac{\partial v_r}{\partial z}\Big] - \frac{\partial}{\partial r}\Big[v_r\frac{\partial v_z}{\partial r} + v_z\frac{\partial v_z}{\partial z}\Big] \\ = \nu_a\Bigg\{\frac{\partial}{\partial z}\Big[\frac{1}{r}\Big(\frac{\partial v_r}{\partial r} + \frac{\partial^2 v_r}{\partial r^2}\Big) + \frac{\partial^2 v_r}{\partial z^2}\Big] - \frac{\partial}{\partial r}\Big[\frac{1}{r}\frac{\partial v_z}{\partial r} + \frac{\partial^2 v_z}{\partial r^2} + \frac{\partial^2 v_z}{\partial z^2}\Big]\Bigg\} + g\beta_a\frac{\partial T}{\partial r}\end{aligned} \tag{3.64}$$

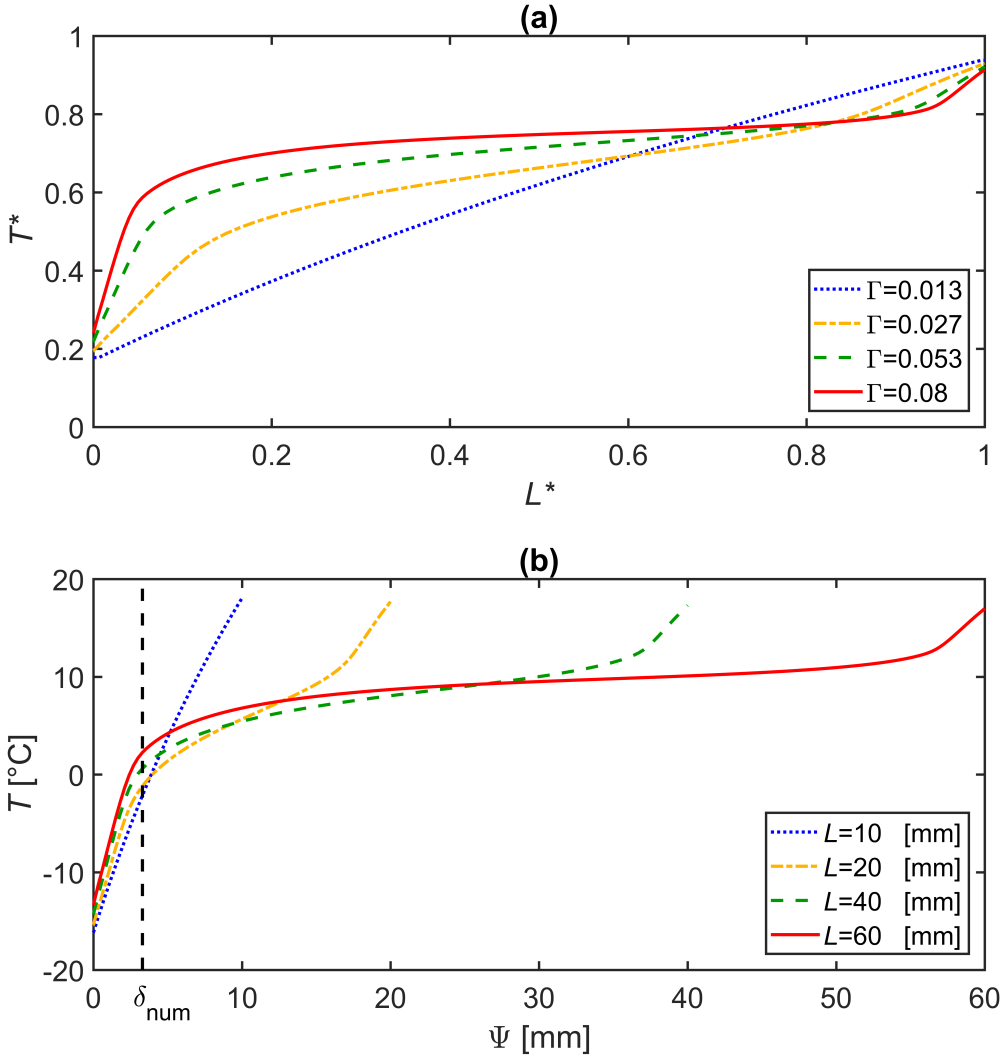

Figure 3-13: Temperature distribution of air across the middle of air gap height at different air aspect ratios (along L2 line as shown in Fig. 3-2(b)): a) non-dimensional form: the x-axis and y-axis are non-dimensionalized as $L^* = \frac{r-r_{ai}}{L}$ and $T^* = \frac{T-T_{c,inlet}}{\Delta T}$, respectively, and b) dimensional form where $\Psi = r - r_{ai}$. The thermal boundary layer thickness is $\delta_{num} \approx 3.3[mm]$.

the energy equation is governed by:

$$v_r \frac{\partial T}{\partial r} + v_z \frac{\partial T}{\partial z} = \alpha_a \Big[\frac{1}{r} \frac{\partial T}{\partial r} + \frac{\partial^2 T}{\partial r^2} + \frac{\partial^2 T}{\partial z^2} \Big] \tag{3.65}$$

In the following scale analysis, changes in r, w, T are scaled by $\delta, H, \Delta T_a$. The following considerations have been taken into account to determine the dominant terms of the governing equations:

- $v_r << v_z$.
- $\delta << H$.
- $\delta << r_{ai}$ and $\delta << r_{ao}$.
- The transient terms were neglected because their magnitude is smaller by at least 2 orders of magnitudes than the dominant convective and diffusive terms especially after few hours of operation.

The thermal boundary layer thickness can be scaled by Eq. (3.64) and Eq. (3.65) as:

$$\delta_{scl}^2 \sim \nu_a \frac{v_z}{g \beta_a \Delta T_a} \sim \alpha_a \frac{H}{v_z} \tag{3.66}$$

The two scales written in Eq. (3.66) can be solved together, by eliminating v_z, to find a unique expression for the thermal boundary layer thickness in an annular enclosure as:

$$\delta_{scl} \sim H Ra_H^{-1/4} \tag{3.67}$$

Eq. (3.67) shows that the thermal boundary layer thickness of a vertical annular air enclosures heated from the sides relies strongly on the cavity height H and the temperature difference between the hot and cold walls ($Ra_H \sim \Delta T_a$). By utilizing Eq. (3.63) and Eq. (3.67) together, the optimum heat insulation of the air gap can be obtained when the aspect ratio of the air

cavity is scaled as:

$$\Gamma_{opt,scl} \sim 2Ra_H^{-1/4} \tag{3.68}$$

The accuracy of the scale analysis derivation of the thermal boundary layer thickness, δ_{scl}, and optimum air cavity aspect ratio, $\Gamma_{opt,scl}$, will now be tested against the numerical results. As per Eq. (3.67), $\delta_{scl} \sim 4$ [mm] which approximately agrees to $\delta_{num} \approx 3.3$[mm] of the numerical model displayed in Fig. 3-13(b). Fig. 3-13(b) also shows that the thermal boundary layer thickness in the boundary layer regime is independent from the air gap thickness, L, and thereby further validates the derivation of δ_{scl}. In regards to the optimum aspect ratio, according to Eq. (3.68), $\Gamma_{opt,scl} \sim 0.01$ which is scalable to the optimum aspect ratio as per the numerical results shown in Fig. 3-12 ($\Gamma_{opt,num} = 0.015$). Small deviations in the comparison between the scale analysis and numerical results can be attributed to: 1) influence of radiation, 2) heat transfer between the air cavity and top and bottom plates, and 3) the assumptions used in the scale analysis.

From practical perspective, if numerical simulations are too computationally expensive to be conducted, the temperature difference between the hot and cold walls of the air cavity (ΔT_a) may not be known. Nevertheless, it is found that replacing ΔT_a by the temperature difference between the ground initial temperature and coolant inlet temperature (ΔT) still gives reasonable approximation very close to the results obtained in the previous paragraph. This will often be the case when the temperature increase of the coolant in the active zone and temperature decrease in the ground is insignificant. If the influence of the active zone on the coolant temperature is large, Nusselt's number correlations can be used to approximate heat gain and temperature increase of the coolant in the active zone. In addition, by looking again at Fig. 3-12, the increase of convective heat gain slightly beyond $\Gamma_{opt,num}$ is less severe than increasing conductive heat gain by lowering the aspect ratio below $\Gamma_{opt,num}$. Since $\Gamma_{opt,scl}$ provides an approximation rather than an exact value for the optimum aspect ratio, it can be preferable, from practical point of view, to design the air cavity aspect ratio slightly larger than $\Gamma_{opt,scl}$.

We end this discussion by comparing the cooling performance of a freeze pipe designed as per this study to a typical S-AGF freeze pipe assuming similar coolant properties to the one used in this study and considering $\Delta T_a = 35$ [°C]. The passive zone length of both tubes is 400 [m] while the outer diameter is 115 [mm]. In typical S-AGF freeze pipes, air gap thickness is often set to 19 [mm]. Nonetheless, the recommended air gap thickness according to equation (3.68) (or Fig. 3-12(b)) is $L_{opt,scl} \sim 3.5$ [cm]. Because air gap thickness of typical freeze pipes is less than $L_{opt,scl}$, conduction is dominant over convection in these pipes as can be implied by Fig. 3-12(a). Heat transfer by conduction is also dominant over convection at $L_{opt,scl}$. The conductive heat gain per unit length is evaluated by the conduction definition shown in Eq. (3.62) as 8.5 [W/m] and 5.5 [W/m] in a typical S-AGF freeze pipe and a recommended freeze pipe, respectively. Radiative heat gain, on the other hand, is calculated to be 12.7 [W/m] in both cases (assuming same $\Delta T_a = 35$ [°C] and $\epsilon = 0.3$). Radiative heat transfer is relatively larger than conductive heat transfer in this case due to the high air gap thickness. Since convective heat transfer is negligible, the overall heat gain of a typical S-AGF freeze pipes sums up to 21.2 [W/m], as compared to 18.2 [W/m] of an optimum freeze pipe. As can be noted, heat gain in the passive zone of an optimum freeze pipe is about 20% less than that of typical freeze pipes used in practice. The heat gain can be further reduced by minimizing heat gain from radiation by, for example, coating the cavity wall with non-emissive materials.

3.7 Conclusion

In this study, an experimental setup that resembles selective artificial ground freezing (S-AGF) systems is built at McGill mining and multiphysics laboratory. The experimental measurements are reproducible and reliable. Detailed documentation regarding building the experimental setup and measurements of the materials thermophysical properties has been provided. Furthermore, a fully conjugate heat transfer model is developed and validated

against the experimental measurements. The natural convection mathematical model of air is further verified at higher Rayleigh numbers against other experimental studies.

The results indicate that applying the S-AGF concept can substantially reduce the cooling load as compared to conventional artificial ground freezing (C-AGF) systems. Furthermore, the cooling load is found to be proportional to the temperature difference between the ground and coolant inlet temperature, as well as the Reynold's number of the flow. Finally, by using scale analysis, it is found that the optimum air gap aspect ratio, $\Gamma = L/H$, is scaled to the Rayleigh number as $\Gamma_{opt} \sim 2Ra_H^{-1/4}$.

Acknowledgment

The authors would like to thank the Ultra Deep Mining Network (UDMN) (241695 Tri-Council (NCE – UDMN) 2-003), Cameco Corporation, Newmans Geotechnique Inc., and Orano Canada Inc. (previously Areva Resource Canada Inc.). The first author wishes to thank McGill Engineering Doctoral Award (MEDA) and Werner Graupe International Fellowship.

Bibliography

[1] G. Newman, L. Newman, D. Chapman, T. Harbicht, Artificial Ground Freezing: An Environmental Best Practice at Cameco's Uranium Mining Operations in Northern Saskatchewan, Canada, in: 11th International Mine Water Association Congress–Mine Water–Managing the Challenges, 2011.

[2] M. Vitel, A. Rouabhi, M. Tijani, F. Guérin, Thermo-hydraulic modeling of artificial ground freezing: Application to an underground mine in fractured sandstone, Computers and Geotechnics 75 (2016) 80–92.

[3] J. S. Harris, Ground freezing in practice, Thomas Telford, 1995.

[4] P. Eskilson, Thermal analysis of heat extraction boreholes.

[5] H. Y. Zeng, N. R. Diao, Z. H. Fang, A finite line-source model for boreholes in geothermal heat exchangers, Heat Transfer—Asian Research 31 (7) (2002) 558–567.

[6] Y. Zhou, Y.-j. Wang, J.-z. Wang, Analytical solution for nonlinear infinite line source problem with temperature-dependent thermal properties, Heat and Mass Transfer 51 (1) (2015) 143–152.

[7] N. R. Diao, H. Y. Zeng, Z. H. Fang, Improvement in modeling of heat transfer in vertical ground heat exchangers, HVAC&R Research 10 (4) (2004) 459–470.

[8] Y. W. Bekele, H. Kyokawa, A. M. Kvarving, T. Kvamsdal, S. Nordal, Isogeometric analysis of THM coupled processes in ground freezing, Computers and Geotechnics 88 (2017) 129–145.

[9] P. Yang, J.-m. Ke, J. G. Wang, Y. K. Chow, F.-b. Zhu, Numerical simulation of frost heave with coupled water freezing, temperature and stress fields in tunnel excavation, Computers and Geotechnics 33 (6-7) (2006) 330–340.

[10] J. Zhou, Y. Tang, Artificial ground freezing of fully saturated mucky clay: Thawing problem by centrifuge modeling, Cold Regions Science and Technology 117 (2015) 1–11.

[11] M. Vitel, A. Rouabhi, M. Tijani, F. Guérin, Modeling heat transfer between a freeze pipe and the surrounding ground during artificial ground freezing activities, Computers and Geotechnics 63 (2015) 99–111.

[12] M. Vitel, A. Rouabhi, M. Tijani, F. Guérin, Modeling heat and mass transfer during ground freezing subjected to high seepage velocities, Computers and Geotechnics 73 (2016) 1–15.

[13] M. A. Alzoubi, A. P. Sasmito, Development and validation of enthalpy-porosity method for artificial ground freezing under seepage conditions, in: ASME 2018 5th Joint US-European Fluids Engineering Division Summer Meeting, American Society of Mechanical Engineers Digital Collection, 2018.

[14] M. A. Alzoubi, A. Madiseh, F. P. Hassani, A. P. Sasmito, Heat transfer analysis in artificial ground freezing under high seepage: Validation and heatlines visualization, International Journal of Thermal Sciences 139 (2019) 232–245.

[15] S. Huang, Y. Guo, Y. Liu, L. Ke, G. Liu, Study on the influence of water flow on temperature around freeze pipes and its distribution optimization during artificial ground freezing, Applied Thermal Engineering 135 (2018) 435–445.

[16] A. Marwan, M.-M. Zhou, M. Z. Abdelrehim, G. Meschke, Optimization of artificial ground freezing in tunneling in the presence of seepage flow, Computers and Geotechnics 75 (2016) 112–125.

[17] M. A. Alzoubi, A. Zueter, A. Nie-Rouquette, A. P. Sasmito, Freezing on demand: A new concept for mine safety and energy savings in wet underground mines, International Journal of Mining Science and Technology 29 (4) (2019) 621–627.

[18] M. A. Alzoubi, A. P. Sasmito, A. Madiseh, F. P. Hassani, Freezing on Demand (FoD): An Energy Saving Technique for Artificial Ground Freezing, in: Energy Procedia, Vol. 158, Elsevier, 2019, pp. 4992–4997.

[19] M. A. Alzoubi, A. P. Sasmito, A. Madiseh, F. P. Hassani, Intermittent Freezing Concept for Energy Saving in Artificial Ground Freezing Systems, in: Energy Procedia, Vol. 142, 2017, pp. 3920–3925.

[20] M. A. Alzoubi, A. Nie-Rouquette, S. A. Ghoreishi-Madiseh, F. P. Hassani, A. P. Sasmito, On the concept of the freezing-on-demand (FoD) in artificial ground freezing for long-term applications, International Journal of Heat and Mass Transfer 143.

[21] W. Ständer, Mathematische Ansätze zur Berechnung der Frostausbreitung in Ruhendem Grundwasser im Vergleich zu Modelluntersuchungen für Verschiedene Gefrierrohranordnungen im Schactund Grundbau, no. 28, Technische Hochschule Fridericiana, Institut für Bodenmechanik und Felsmechanik, 1967.

[22] H. Victor, Die Frostausbreitung beim künstlichen Gefrieren von Böden unter dem Einfluss strömenden Grundwassers, Vol. 42, Univ., Inst. f. Bodenmechanik u. Felsmechanik, 1969.

[23] E. Pimentel, A. Sres, G. Anagnostou, Modelling of ground freezing in tunnelling, in: Underground Space–The 4th Dimension of Metropolises, ITA and World Tunnel Congress, Prague, Vol. 1, 2007, pp. 331–336.

[24] E. Pimentel, A. Sres, G. Anagnostou, Large-scale laboratory tests on artificial ground freezing under seepage-flow conditions, Geotechnique 62 (3) (2012) 227.

[25] M. A. Alzoubi, A. Nie-Rouquette, A. P. Sasmito, Conjugate heat transfer in artificial ground freezing using enthalpy-porosity method: Experiments and model validation, International Journal of Heat and Mass Transfer 126 (2018) 740–752.

[26] R. A. Sudisman, M. Osada, T. Yamabe, Heat Transfer Visualization of the Application of a Cooling Pipe in Sand with Flowing Pore Water, Journal of Cold Regions Engineering 31 (1) (2016) 4016007.

[27] R. A. Sudisman, M. Osada, T. Yamabe, Experimental Investigation on Effects of Water Flow to Freezing Sand around Vertically Buried Freezing Pipe, Journal of Cold Regions Engineering 33 (3) (2019) 4019004.

[28] H. Tounsi, A. Rouabhi, M. Tijani, F. Guérin, Thermo-Hydro-Mechanical Modeling of Artificial Ground Freezing: Application in Mining Engineering, Rock Mechanics and Rock Engineering (2019) 1–19.

[29] M. Kaviany, Principles of heat transfer in porous media, Springer Science & Business Media, 2012.

[30] N. Moran, M. Katz, Numerical investigation of a thermosiphon flow in a cylindrical enclosure with non-uniform boundary conditions, International Journal of Thermal Sciences 139 (2019) 292–302.

[31] M. F. Modest, Radiative heat transfer, Academic press, 2013.

[32] J. R. Howell, M. P. Menguc, R. Siegel, Thermal radiation heat transfer, CRC press, 2015.

[33] A. Fluent, 18.1, Theory Guide, Ansys (2017).

[34] M. Keyhani, F. A. Kulacki, R. N. Christensen, Free convection in a vertical annulus with constant heat flux on the inner wall, Journal of Heat Transfer 105 (3) (1983) 454–459.

[35] M. A. Alzoubi, A. P. Sasmito, Thermal performance optimization of a bayonet tube heat exchanger, Applied Thermal Engineering 111 (2017) 232–247.

[36] W. M. Rohsenow, J. P. Hartnett, Y. I. Cho, Handbook of heat transfer, Vol. 3, McGraw-Hill New York, 1998.

[37] Y. S. Touloukian, D. P. DeWitt, Thermophysical properties of matter-the tprc data series. volume 7. thermal radiative properties-metallic elements and alloys, Tech. rep. (1970).

[38] A. J. Baldwin, J. E. R. Lovell-Smith, The emissivity of stainless steel in dairy plant thermal design, Journal of food engineering 17 (4) (1992) 281–289.

[39] O. G. Martynenko, P. P. Khramtsov, Free-convective heat transfer: with many photographs of flows and heat exchange, Springer Science & Business Media, 2005.

[40] A. Bejan, Convection heat transfer, John wiley & sons, 2013.

[41] A. Demuren, H. Grotjans, Buoyancy-driven flows—Beyond the boussinesq approximation, Numerical Heat Transfer, Part B: Fundamentals 56 (1) (2009) 1–22.

Chapter 4

Development of conjugate reduced-order models for selective artificial ground freezing: Thermal and computational analysis

Preface

Selective artificial ground freezing (S-AGF) systems often occupy large domains (hundreds of meteres) and run for long periods (several months to years). While the fully conjugate model derived in the previous chapter resulted in significant fundamental understanding, employing such fully-conjugate model is impractical in field scenarios due to their intensive computational cost. In this chapter, we derive a semi-conjugate model based on a space-marching algorithm to substantially minimize the computational cost of modeling S-AGF in field scenarios.

" **A. F. Zueter**, M. Xu, M. A. Alzoubi, and A. P. Sasmito. Development of con-

jugate reduced-order models for selective artificial ground freezing: Thermal and computational analysis. *Applied Thermal Engineering*, 190:116782, 2021. doi.org/10.1016/j.applthermaleng.2021.116782 ”

Abstract

Selective artificial ground freezing (S-AGF) applications usually extend to very deep levels (more than 400 meters); numerical modeling of such large AGF applications encounters two main issues: i) Predicting the variable heat extraction capacity along the freeze-pipe depth and ii) the extremely long computational time. In this paper, we develop novel semi-conjugate reduced-order models that accurately predict heat extraction along the freeze-pipe while substantially reducing the computational time. In regards to the thermal modeling novelty, the freeze-pipe boundary condition of S-AGF is mathematically derived considering the development of the coolant flow temperature and boundary layer. As for the computational novelty, fast semi-conjugate reduced-order algorithms are developed for S-AGF, with the optional incorporation of analytical solutions and spatial correction. The models are validated against experimental data and verified with established fully-conjugate models. The thermal results demonstrate that the phase transition front profile of the frozen ground is primarily shaped by the thermal development of the flow. On the other hand, the computational results reveal that the computational time of the reduced-order algorithms is decreased by more than 99%, as compared with the established models. In short, our proposed reduced-order models are proven to be reliable and computationally efficient, which shows potential for practical field application.

Contents

4.1 Introduction

Since the development of artificial ground frezing (AGF) technologies in the 19th century [1], AGF systems have been used in numerous applications such as underground mines [2], [3], hazardous waste management [4], [5], and tunneling [6], [7]. Selective artificial ground freezing (S-AGF) is a concept in AGF that aims to reduce the cooling load of the refrigeration plants by insulating the freeze-pipe in the passive zone where ground freezing is not needed, as shown in Fig. 4-1. S-AGF systems are especially useful for deep underground mining applications where the active zone, which needs to be frozen, is located much below the ground surface. For instance, the Cigar Lake Uranium Mine in Canada and the Banji Coal Mine in China use an S-AGF system to freeze an active zone situated at a depth of more than 400 meters below the ground surface [8], [9]. Successful and cost-effective operation of S-AGF applications require appropriate understanding and mathematical modeling of the ground freezing problem, which mainly includes heat transfer between the ground and the coolant flowing across the freeze-pipe. Nonetheless, one of these difficulties is often encountered in computing mathematical models of such large AGF applications: 1) Inaccurate prediction of the heat extraction capacity along the freeze-pipe depth or 2) extremely long computational time.

Some researchers avoided the latter of these difficulties by deriving analytical solutions of the ground freezing problem. Hu et al. developed analytical solutions to calculate the ground temperature field considering a single freeze-pipe [10], two freeze-pipes [11], multiple pipes in a straight row [12], and multi-row freeze-pipes [13]. Fixed freeze-pipe wall temperature

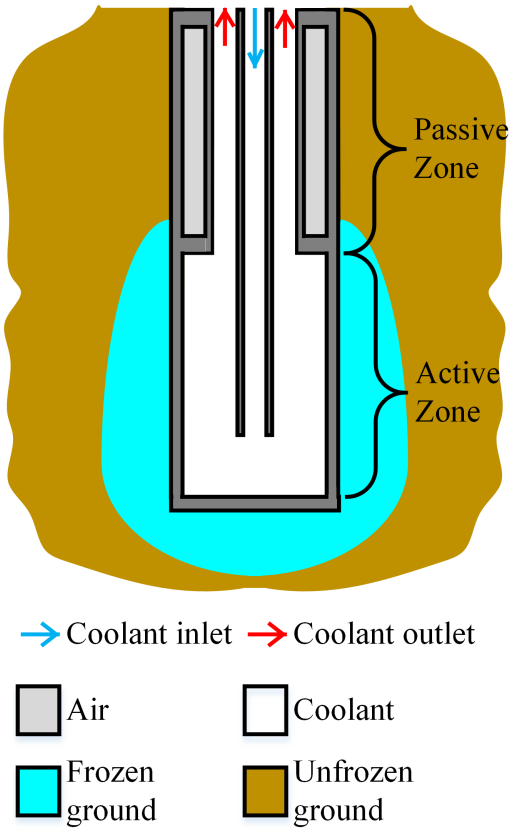

Figure 4-1: The operating principle of selective artificial ground freezing (S-AGF). The ground is divided into two zones: 1) Active zone where ground freezing is desired and 2) passive zone where ground freezing is not needed (not-to-scale).

was assumed in these studies. Cai et al. [14] predicted ground temperature profile using stochastic medium theory while setting fixed temperature boundary condition at the freeze-pipe wall. Xu et al. [15], [16] also considered fixed pipe-wall temperature but proposed a singularly perturbation solution calculating a two-phase Stefan problem accurately for low Stefan numbers. While the analytical models are indeed computationally efficient, they are based on several assumptions and limitations that can significantly undermine their accuracy and practicality in field-conditions.

Consequently, the vast majority of AGF studies were conducted numerically. Cai et al. [17] compared different ground freezing techniques for tunneling applications. The numerical model set the freeze-pipe temperature to be equal to the brine inlet temperature. Vitel et al. [18] developed a model for groundwater seepage in which pipe wall temperature was also assumed to be fixed. Vasilyeva et al. [19] solved a two-phase Stefan problem for a heterogeneous porous ground; The freeze-pipe was modeled as a line-source. Yang et al. [20] considered that freeze-pipe wall temperature would be higher than brine inlet temperature due to heat gain from the ground. Consequently, it was presumed that the freeze-pipe wall temperature would be 2 [°C] higher than coolant inlet temperature throughout the freeze-pipe length. Despite the higher accuracy of the numerical models as compared with analytical ones, most of the numerical studies available in the literature adapt non-conjugate models, meaning that coolant temperature is not mathematically correlated to the heat gain from the ground. The freeze-pipe is therefore assumed to maintain a fixed and uniform temperature or heat flux. However, accurate calculation of the coolant heat gain is vital as it is directly linked to the energy consumption of AGF plants (which can potentially cost tens to hundreds of millions of dollars [21]).

Fully-conjugate models have therefore been recently developed to mathematically model coolant flow alongside heat transfer in the ground. Thus, freeze-pipe heat extraction from the ground is correlated to the coolant temperature and velocity profiles. These fully-conjugate models provide valuable fundamental insights and accurately predict the energy consump-

tion. Alzoubi et al. [22] derived and validated a fully-conjugate AGF model based on the enthalpy-porosity method [23]. It was found that coolant Reynolds number has higher effect on the heat transfer performance than coolant inlet temperature although detailed analysis on development of the coolant flow and boundary layer was not provided. Alzoubi et al. [24], [25] then utilized this model to unveil the huge energy savings potential of the freezing on demand concept for long AGF applications. Following the enthalpy-porosity method, Zueter et al. [8] also developed and validated a fully-conjugate model for selective artificial ground freezing (S-AGF) systems and determined an optimum air gap thickness that results in highest energy saving. Despite the high accuracy of the fully-conjugate models, they demand extremely large mesh count and small time step to capture the coolant flow complications. As a result, employing fully-conjugate models under field conditions is impractical without tremendous computational resources. For this reason, present fully-conjugate models of AGF are constrained to lab-scale or field-scale of relatively small computational domain or short operational time. Furthermore, none of these studies investigated the effect of the development of the coolant temperature and thermal boundary layer on the phase-front profile.

Apart from AGF, many studies were conducted to investigate and minimize the computational time of numerical models in a wide ray of applications [26]. Ghosh et al. [27], Zucatti et al [28], Ding et al. [29], and Yu et al. [30] adapted reduced-order algorithms in solving the energy equation to significantly enhance the computational performance. Han et al. [31], Braun et al. [32] and Muratori et al. [33] provided more detailed computational analysis of reduced-order models. Han et al. [31] created a reduced-order numerical model to study heat transfer between oil pipelines and the surrounding ground. The computational time of the reduced-order model was around 200 times less than that of a traditional finite volume method, while preserving the solution accuracy. In modeling convective heat transfer of rotating detonation combustors, Braun et al. [32] revealed that a reduced order model is 7000 times faster than a 3D model while retaining good accuracy. On the other hand,

Muratori et al. [33] developed a semi-conjugate reduced-order 1+1D model to predict the thermal behavior of a fuel cell. The results were accurately validated against experimental data; furthermore, the computational time of the 1+1D model was found to be 97% less than a 2D model. In attempts to reduce the computational time of AGF applications particularly, Vasilyeva et al. [19] recently developed a *non-conjugate* (i.e., the coolant temperature is not correlated to the heat gain from the ground) reduced-order model based on the construction of the coarse grid approximation using the generalized multiscale finite element method. While the computational benefits were not highlighted, the results demonstrate the accuracy of the reduced model in monitoring the temperature distribution of the ground.

From the literature presented thus far, three main unresolved issues of AGF models can be noted. First, the boundary settings of the freeze-pipe is often assumed to have a uniform temperature or heat-flux. This is not physical since the coolant temperature increases as it extracts heat from the ground; in addition, the coolant capacity to extract heat changes as the thermal boundary layer of the coolant develops. Although few mathematical studies have considered fully-conjugate modeling in small lab-scale simulations employing traditional numerical solvers, these models are computationally expensive and impractical to use in field-scale; furthermore, these studies did not investigate the impact of the thermal development of the coolant temperature and boundary layer on the phase-front profile. Second, computationally efficient reduced-order AGF models that thermally couple the coolant flow with the ground have not yet been developed although conjugate modeling is essential in calculating energy consumption of AGF plants, as well as accurately predicting the phase front expansion and profile. Third, the few *non-conjugate* reduced-order models of AGF do not target S-AGF systems despite their need for computationally efficient models due to their extremely large nature (typically more than 400 meters deep).

In order to tackle these issues, this study presents novel methods in *thermal* and *computational* modeling of S-AGF systems to enhance the accuracy of heat extraction calculation by the freeze-pipe and improve the computational efficiency of the derived models. In re-

gards to the thermal aspect, a novel framework for setting appropriate freeze-pipe boundary conditions according to the coolant flow rate, inlet temperature, and thermophysical properties is derived considering the development of the thermal boundary layer of the flow. As for the computational aspect, the study proposes novel conjugate reduced-order algorithms for AGF that couple the coolant flow to the ground temperature. Further, this is the first study the builds a reduced-order model for S-AGF applications. Particularly, four different semi-conjugate 1+1D algorithms are proposed to optimize the computational time in different length-scales. Analytical solutions are also derived and merged with numerical ones in hybrid algorithms in attempts to further reduce the computational time in certain scenarios. Additionally, some of the proposed algorithms involve spatial correction of the ground temperature to improve the accuracy of the solution when necessary.

The layout of this paper is as follows. The mathematical model of the current study is introduced, including detailed derivation of the freeze-pipe boundary model. After that, four different semi-conjugate 1+1D algorithms are illustrated, followed by derivation and description of computational methodology of analytical and numerical solutions. In the results and discussion section, the reliability of these models are firstly validated against experimental data in lab-scale and secondly verified with an established fully-conjugate 2D model from our previous work [8] in lab-scale and field-scale. After verifying the reliability of the models, their computational efficiency are highlighted and optimized in lab-scale and field-scale. Finally, thermal analysis will be conducted to ensure the accuracy of the freeze-pipe boundary settings of the proposed models as compared with fully-conjugate ones and then study the operational parameters of AGF systems.

4.2 Mathematical model formulation

In this section, the mathematical model of this study is explained. First, the governing equations of the computational domain are presented. After that, the initial and boundary

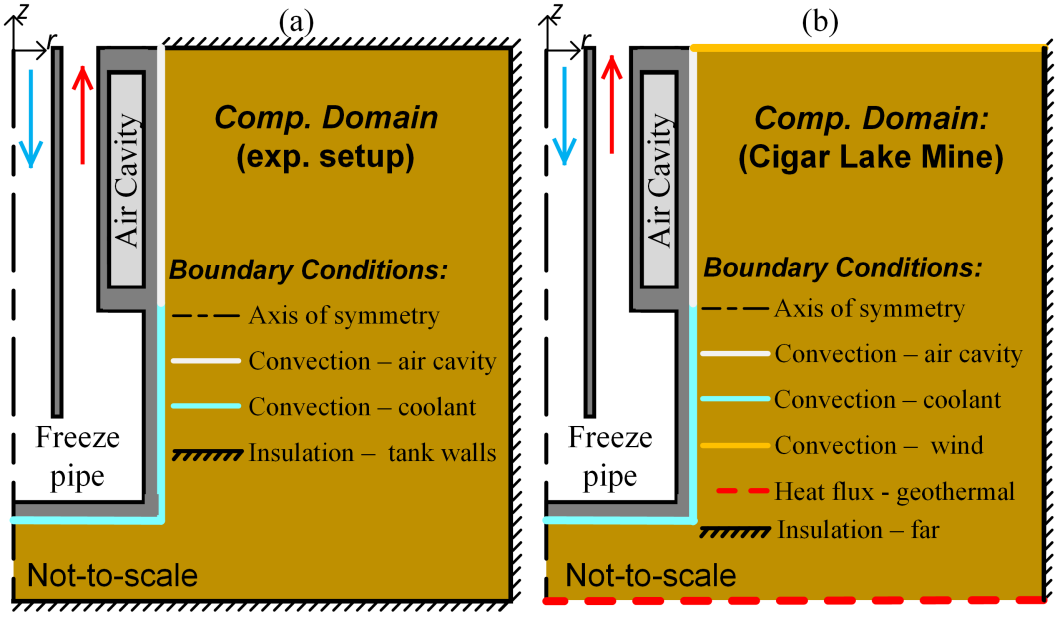

Figure 4-2: Computational domain and boundary conditions of the mathematical model in a) lab-scale and b) field-scale.

conditions are given for various simulation scenarios. The novel development of freeze-pipe boundary setting is derived in Sec. 4.2.2.

4.2.1 Governing equations

The computational domain of this study is the ground, as shown in Fig. 4-2. The ground is a porous medium which consists of sand particles and frozen/unfrozen water. For AGF systems similar to this study, the local thermal equilibrium (LTE) assumption [34] between the sand particles and the water is valid as shown by Zueter et al. [8]. Considering LTE, heat conduction in the ground can be calculated by balancing the transient and diffusive terms of the energy equation as

$$\frac{\partial H_g}{\partial t} = \nabla \cdot (k_g \nabla T_g), \tag{4.1}$$

where the ground volumetric enthalpy, H_g, is related to the ground temperature, T_g, as [35]

$$H_g = (1-\gamma)\int_{T_{ref}}^{T_g}(\rho c_p)_s\ dT_g + \gamma\int_{T_{ref}}^{T_g}(\rho c_p)_\ell\ dT_g + \gamma(\rho L)_\ell, \tag{4.2}$$

where T_{ref} is an arbitrary reference temperature and γ is the liquid fraction calculated based on the temperature as

$$\gamma = \begin{cases} 0 & ,\ T_g < T_{sol}; \\ \frac{T_g - T_{sol}}{T_{liq} - T_{sol}} & ,\ T_{sol} \leq T_g \leq T_{liq}; \\ 1 & ,\ T_g > T_{liq}, \end{cases} \tag{4.3}$$

where T_{sol} is the solidus temperature and T_{liq} is the liquidus temperature. The phase-dependent thermophysical properties of Eq. (4.2) represent the equivalent thermophysical properties of frozen/unfrozen water and sand. These properties are calculated by volume averaging as the LTE assumption is valid. Thus, the equivalent volumetric heat capacities and volumetric latent heat are calculated as

$$(\rho c_p)_s = (1-\phi)\ (\rho c_p)_p + \phi(\rho c_p)_f \tag{4.4}$$

$$(\rho c_p)_\ell = (1-\phi)\ (\rho c_p)_p + \phi(\rho c_p)_u \tag{4.5}$$

$$(\rho L)_\ell = (1-\phi)\ (\rho L)_p + \phi(\rho L)_u = \phi(\rho L)_u, \tag{4.6}$$

where ϕ is the porosity and subscripts p, f, u, s, and ℓ denote sand, frozen water, unfrozen water, equivalent frozen ground, and equivalent unfrozen ground, respectively. The term $(1-\phi)\ (\rho L)_p = 0$ because sand does not undergo phase-change in AGF applications. Multiple correlations are available in the literature to predict the equivalent thermal conductivity of a porous medium. As per the experimental measurements of Zueter et al. [8], the equivalent thermal conductivity of the ground correlates to the parallel arrangement approach as [34]

$$k_g = (1-\phi)\ k_p + \phi\ \left[\gamma\ k_u + (1-\gamma)\ k_f\right]. \tag{4.7}$$

4.2.2 Initial and boundary conditions

The mathematical model of this study is firstly validated in lab-scale and then extended to field-scale dimensions and conditions. Thus, both lab-scale and field-scale initial and boundary conditions are discussed in this section.

Initial condition

A uniform ground initial temperature is considered throughout this study as

$$T_g(t = 0) = T_o. \tag{4.8}$$

In lab-scale, the ground was reconditioned to a uniform initial temperature of 21.5 [°C] before starting the experiment. However, in field-scale, the ground temperature is approximated to be uniform at 7 [°C] as per field measurements of the Cigar Lake Uranium Mine [36].

The temperature difference between the initial condition and the coolant temperature is proportional to the heat extraction by the freeze-pipe. The impact of this temperature difference lasts for a shorter period in the active zone as compared to the passive zone since the ground temperature drops very quickly in the active zone near the pipe wall. In the passive zone, higher temperature difference between the coolant and the ground increases the Rayleigh number of the air flow inside the air cavity and can change the buoyant flow regime, leading to a larger heat transfer rate from the ground to the coolant. Detailed analysis on the effect of the initial condition on the heat extraction in the passive zone can be found in [8].

Freeze-pipe boundary condition

Our study contributes to the thermal and computational modeling of AGF systems. In this subsection, we present a novel framework for properly setting the freeze-pipe boundary condition in AGF applications.

The main source of heat extraction in AGF applications is the heat convection from the coolant. Mathematical modeling of heat convection along the outer freeze-pipe wall, which is directly in contact with the ground, can be expressed as

$$q_{o,w}(z_c) = -k_g \frac{\partial T_g(z_c)}{\partial n}\bigg|_{o,w} = h(z_c)\Big[\, T_g(z_c)|_{o,w} - T_c(z_c)\Big], \tag{4.9}$$

where $q_{o,w}$ is the heat flux at the outer wall of the freeze-pipe, k_g is the thermal conductivity of the ground, n is a normal vector to the boundary, and z_c is the axial distance measured from the bottom of freeze-pipe. Eq. 4.9 shows that the convective heat flux along the outer pipe wall is dependent on the axial distance (i.e., $q_{o,w} = q_{o,w}(z_c)$) due to the variations of the convective heat transfer coefficient, $h(z_c)$, coolant temperature, $T_c(z_c)$, and ground temperature in contact with outer wall of the pipe, $T_g(z_c)|_{o,w}$. The intensity of the convective heat flux is therefore influenced by the heat transfer coefficient, h, and the coolant temperature, T_c. These two parameters shall be set carefully to evaluate the convective heat flux accurately. Next, we will evaluate $h(z_c)$ in the active zone. The methodology used for finding $h(z_c)$ in the active zone can be implemented to a wide range of conventional AGF systems. After that, we will calculate $h(z_c)$ in the passive zone to extend our model to S-AGF systems. By the end of this subsection, the evaluation of the coolant temperature along the height of freeze-pipe, $T_c(z_c)$, will be explained.

In the active zone located at the lower portion of the freeze-pipe, the governing thermal resistance is the flow of the coolant in the annulus. In order to accurately evaluate the heat transfer coefficient at the pipe wall, the hydrodynamics of the flow needs to be examined. As the coolant enters the freeze-pipe and strikes the bottom plate, it then starts flowing upward extracting heat from the ground, as shown in Fig. 4-2. Throughout this study, the flow regime is laminar in the annular section since the Reynolds number of the flow there is always less than 2000, which is the minimum critical Reynolds number for a flow in a concentric annulus [37], [38]. Also, since the Reynolds number is relatively small, the hydrodynamic entrance

length is too short (in the order of millimeters in lab-scale and centimeters in fields scale) [38], [39] and can be safely neglected. Nevertheless, the thermal entrance length is very long due to the large Prandtl number of AGF coolants. Shah and London [39] determined and tabulated the local Nusselt number of a thermally developing annular flow at different diameter ratios as a function of a dimensionless axial distance, z_c^*, given as

$$z_c^* = \frac{z_c/D_h}{Pe} = \frac{z_c/D_h}{Re\ Pr}, \tag{4.10}$$

where Pe, Re, and Pr are the thermal Peclet number, Reynolds number, and Prandtl number whereas z_c is the dimensional axial distance of the flow and D_h is the hydraulic diameter. These tabulated data are employed to find the Nusselt number for lab-scale and field-scale annular flow of the coolant in the active zone, as shown in Fig. 4-3. This figure also demonstrates that the thermal development of the flow is highly significant throughout the the entire height of the active zone. After obtaining the local Nusselt number as per Fig. 4-3, the local convective heat transfer coefficient in the active zone to be emloyed in Eq.(4.9) is calculated as

$$h(z_c) = \frac{Nu(z_c)\ k_c}{D_h}. \tag{4.11}$$

In the passive zone which is located at the higher portion of the freeze-pipe, the thermal resistance of the air chamber is larger by around two orders of magnitude than the thermal resistances of the coolant annular flow and the thermal resistance of the pipe wall conduction. Hence, the coolant temperature of the annular flow, $T_c(z_c)$ is approximated to be equal to the inner wall temperature of the air cavity, $T_{in}(z_c)$. Furthermore, the boundary temperature along the outer wall of the freeze-pipe, $T_g(z_c)|_{o,w}$, is approximated to be equal to the outer wall temperature of the air cavity, $T_{out}(z_c)$. In such tall annular air cavities, buoyant heat transfer can be significant only when the thickness of the air cavity exceeds $2y_aRa$ [8],

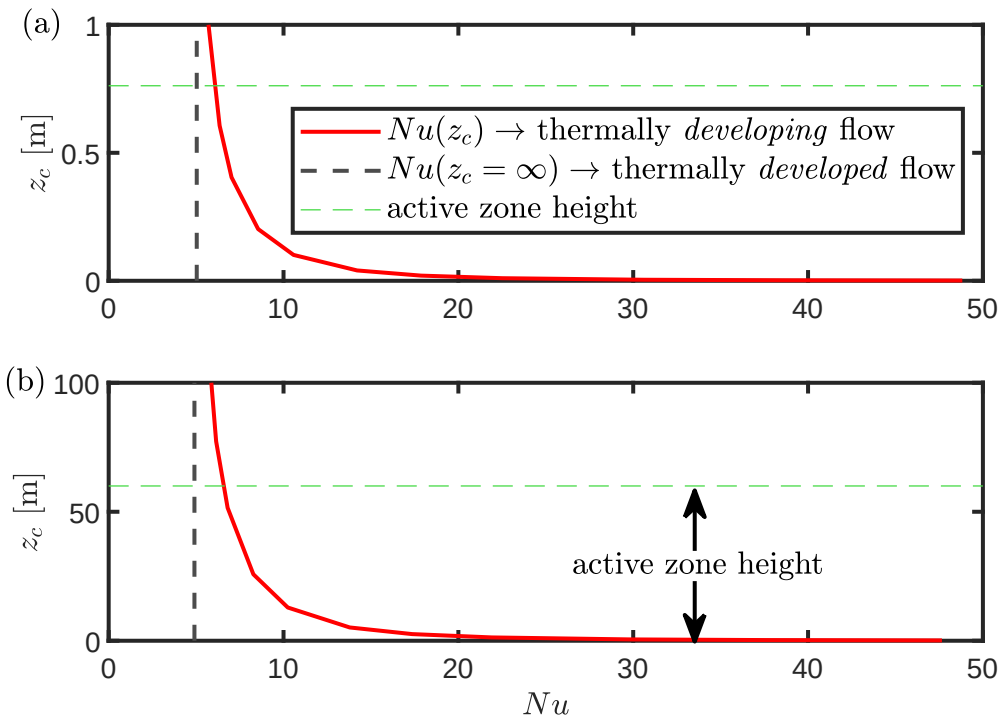

Figure 4-3: Local Nusselt number of a thermally developing annular flow as a function of the distance covered by the flow, z_c, where $z_c = 0$ at the entrance of the annular region (bottom of the freeze-pipe in this study), in a) lab-scale and b) field-scale. This figure is based on Eq. (4.10) and the tabulated data of the analytical solutions of Shah and London [39].

[40], where y_a is the height of the air cavity and Ra is the Rayleigh number calculated as

$$Ra = \frac{gVy_a^3}{\nu_a \alpha_a} \Delta T_a. \tag{4.12}$$

Throughout this study, the thickness of the air cavity is considerably less than $2y_a Ra$; consequently, buoyant heat transfer is neglected. Thus, heat transfer between the cavity walls is governed by conduction and radiation, which can be calculated per unit height as [41]

$$Q_{o,w} = \underbrace{\frac{2\pi\ k_a}{ln(r_{out}/r_{in})}(T_{out} - T_{in})}_{conduction} + \underbrace{\frac{2\pi\ r_{in}\ r_{out}\ \varepsilon\ \sigma}{r_{out} + (1-\varepsilon)r_{in}}(T_{out}^4 - T_{in}^4)}_{radiation}, \tag{4.13}$$

where subscripts *out* and *in* refer to the outer wall and inner wall of the air cavity, respectively. Heat flux along the boundary wall (outer wall of the freeze-pipe that is attached to ground) in the passive zone can then be expressed as [41]

$$\begin{aligned} q_{o,w}(z_c) &= \underbrace{\frac{k_a\big[T_{out}(z_c) - T_{in}(z_c)\big]}{(r_{out}+\delta)\ ln(r_{out}/r_{in})}}_{conduction} + \underbrace{\frac{r_{in}\ r_{out}\ \varepsilon\ \sigma\big[T_{out}^4(z_c) - T_{in}^4(z_c)\big]}{(r_{out}+\delta)(r_{out}+(1-\varepsilon)r_{in})}}_{radiation} \\ &= U(z_c)\big[T_{out}(z_c) - T_{in}(z_c)\big], \end{aligned} \tag{4.14}$$

where δ is the pipe wall thickness and $U(z_c)$ represents the overall heat transfer coefficient, which can now be derived from Eq. (4.14) as

$$U(z_c) = \underbrace{\frac{k_a}{(r_{out}+\delta)\ ln(r_{out}/r_{in})}}_{conduction} + \underbrace{\frac{r_{in}\ r_{out}\ \varepsilon\ \sigma\big[T_{out}^2(z_c) + T_{in}^2(z_c)\big]\big[T_{out}(z_c) + T_{in}(z_c)\big]}{(r_{out}+\delta)(r_{out}+(1-\varepsilon)r_{in})}}_{radiation}. \tag{4.15}$$

This overall heat transfer coefficient, $U(z_c)$, is plugged in as the convective heat transfer coefficient, $h(z_c)$, in Eq. (4.9).

In addition to the heat transfer coefficient, the second main parameter that impacts convection heat flux along the freeze-pipe wall is the coolant temperature, T_c. The coolant temperature increases as it extracts heat from the ground. This can be modeled by applying

the first law of thermodynamics per unit area of the freeze-pipe as

$$\Delta T_c(z_c) = \frac{q_{o,w}(z_c)}{\dot{m}_c c_{p,c}} \tag{4.16}$$

where $q_{o,w}$ is obtained from Eq. (4.9). Overall, the coolant temperature is connected to the ground by solving Eq. (4.16) alongside with the governing equations and boundary conditions even though the coolant is outside the computational domain, creating a semi-conjugate model.

Other boundary conditions

In this subsection, other boundary conditions apart the freeze-pipe boundary will be presented for lab-scale and field-scale models. In lab-scale, the computational domain is surrounded by an axi-symmetric boundary and insulated walls as shown in Fig. 4-2(a). At the axi-symmetric boundary, the temperature gradient in the radial direction is zero [41] as

$$\left.\frac{\partial T_g}{\partial r}\right|_{axis} = 0. \tag{4.17}$$

Similarly, the temperature field does not change with respect to a perpendicular direction to an insulated wall boundary [41] as

$$\left.\frac{\partial T_g}{\partial n}\right|_{insulation} = 0, \tag{4.18}$$

where n represents a perpendicular direction to a wall.

In field-scale, the top and bottom boundaries are nevertheless changed to simulate field conditions, as shown in Fig. 4-2(b). The upper boundary is subject to atmospheric heat convection as [41]

$$-k_g \left.\frac{\partial T_g}{\partial n}\right|_{top\ boundary} = h(T_g|_{top\ boundary} - T_{atm}), \tag{4.19}$$

where the atmospheric temperature, T_{atm}, is curve-fitted following the readings of the Cigar

Lake station [42] starting from the year 2018 as

$$T_{atm}\ [\mathrm{K}] = 267 - 21.3\cos(2\times10^{-7}t\ [\mathrm{s}]) - 1.7\sin(2\times10^{-7}t\ [\mathrm{s}]). \tag{4.20}$$

At the bottom of the computational domain, geothermal heat flux is set along the lower boundary as [41]

$$-k_g\frac{\partial T_g}{\partial n}\bigg|_{bottom\ boundary} = q_{geo}, \tag{4.21}$$

where $q_{geo} = 0.06$ [W m^{-2}]. Concerning the far insulation boundary in field-scale, a boundary independence study was conducted to ensure that the insulation boundary is too distant to affect the temperature profile near the freeze-pipe. A distance of 30 meters was noted to be sufficient to obtain a boundary-independent solution.

4.3 Solution algorithm

This subsection is dedicated to present our novel reduced-order algorithms in great detail, including all steps and equations.

4.3.1 Introduction to 1+1D modeling

In this study, a 2D axi-symmetric problem is dimensionally reduced to a 1+1D axi-symmetric problem, *where a 2D domain is discretized into a number of 1D grid-lines which are solved in series following a certain order*. In convective heat transfer problems, a 2D domain is typically reduced to a series of 1D grid-lines *perpendicular* to the convective heat source.

In regards to AGF, since the coolant in the 2D axi-symmetric problem flows in the axial direction, a 1+1D axi-symmetric mesh should include 1D radial grid-lines perpendicular to the pipe to calculate radial heat conduction from the ground to the freeze-pipe. These 1D radial grid-lines are solved in series, one after the other. Since these grid-lines extend in the radial direction, they only compute radial conduction and neglect axial ones. Consequently,

if axial conduction is significant, additional 1D axial grid lines need to be solved in order to enhance the solution accuracy, which nevertheless increases computational time.

The 1D grid-lines can be solved numerically or analytically. numerical solutions are preferred in solving two-phase grid lines due to the complexity of finding accurate analytical solutions for two-phase Stefan problem. Nevertheless, single-phase grid-lines can be solved analytically *if* they prove to be more computationally efficient than numerical solutions of single-phase grid-lines.

In the light of the previous discussion, the impact of incorporating axial conduction and analytical solutions to the novel 1+1D algorithms derived specifically for AGF applications will be investigated. In the following subsections, four different 1+1D semi-conjugate algorithms are developed and proposed to optimize the computational speed of AGF simulations while preserving the solution accuracy. These four models are distinguished by two main criteria: 1) Addition of axial correction and 2) inclusion of analytical solutions. The algorithms of these models are simplified by a single flow chart in Fig. 4-4, and are described in more detail in the following subsections.

4.3.2 Hybrid 1+1D algorithm without axial correction (M-1)

This model considers only radial conduction between the freeze-pipe wall and the side wall as can be seen from Fig. 4-4. Solution of 1D axial grid-lines is neglected in this algorithm to speed up the simulation. Nevertheless, this may compromise its accuracy if axial heat conduction is significant. Analytical solutions are considered in the single-phase 1D radial lines of the passive zone to possibly enhance the computational speed. The algorithm of this model is explained in the following steps:

1. Initially, the temperature and enthalpy fields of the computational domain are set according to the initial condition.

2. Energy diffusion between the freeze-pipe wall and the side boundary is calculated along

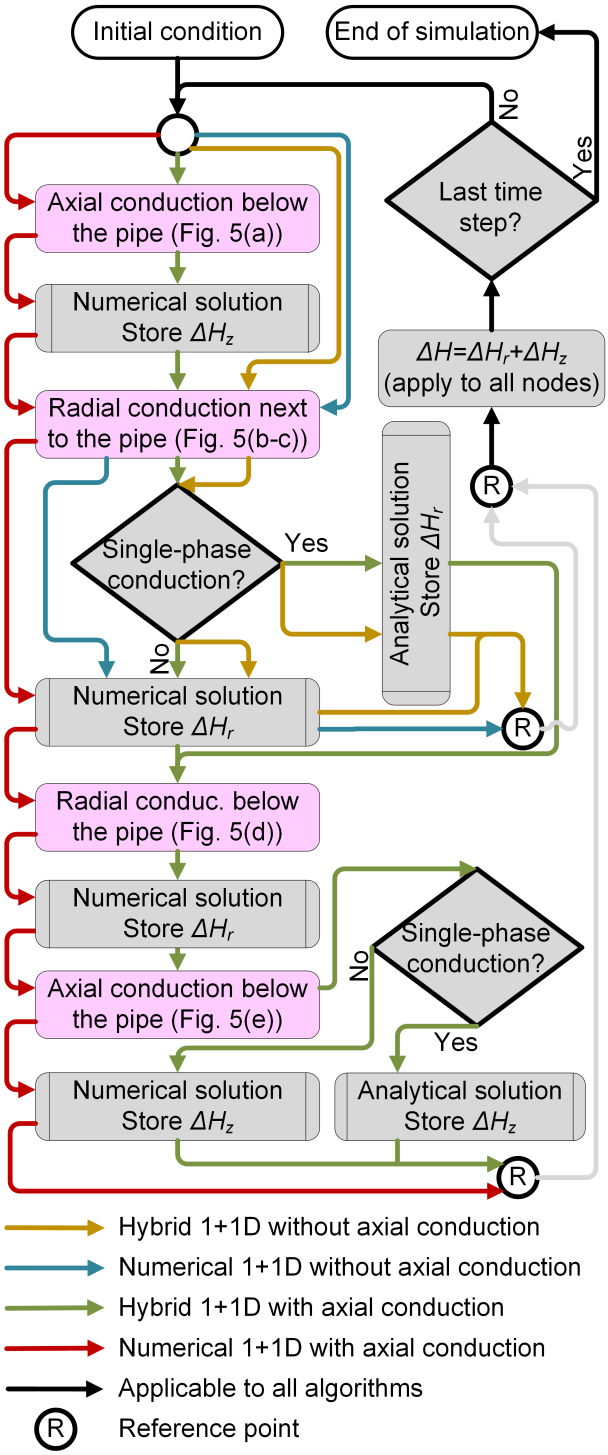

Figure 4-4: Flowchart describing the algorithm of each of the proposed models.

the lowest radial grid-line next to the bottom of the freeze-pipe as shown in Fig. 4-5(b) (The axial grid-lines shown in Fig. 4-5(a) are neglected in this algorithm). The governing equation of this 1D grid-line is Eq. (4.1), bounded by freeze-pipe wall and an insulated wall modeled by Eq. (4.9) and Eq. (4.18), respectively. In this lowest grid-line only, Eq. (4.16) is not coupled to the governing equation and boundary conditions; instead, the coolant temperature, $T_c(z_c)$, in Eq. (4.9) is set to be equal to the coolant inlet temperature.

3. The upper 1D grid-lines are then solved in series from the bottom to the top, as shown in Fig. 4-5(c). Similar to the previous step, the governing equation and boundary conditions of the 1D grid-lines are given by Eqs. (4.1,4.9,4.18). Nevertheless, Eq. (4.16) is also coupled with Eqs. (4.1,4.9,4.18) to calculate the coolant temperature $T_c(z_c)$ at every grid-line. In this hybrid algorithm, single-phase grid-lines and two-phase grid-lines are solved analytically and numerically, respectively.

4. Once all grid-lines are covered, the temperature and enthalpy fields of the present time step are set as an initial condition to solve for the temperature and enthalpy fields of the next time step.

5. Steps (2-4) are repeated until the end of the simulation.

4.3.3 Numerical 1+1D algorithm without axial correction (M-2)

This algorithm is almost identical to the former one as they both do not include axial conduction to achieve faster computation, but they may not yield accurate results if axial conduction is significant. The only difference between the two algorithms is that M-2 employs numerical solutions throughout the simulation, as shown in Fig. 4-4 (analytical solutions are not used at all). This modification is motivated by our observation that calculating analytical solutions require numerical integration repeated over a large number of eigenvalues, leading to a slow computation. The algorithm of M-2 is given as follows:

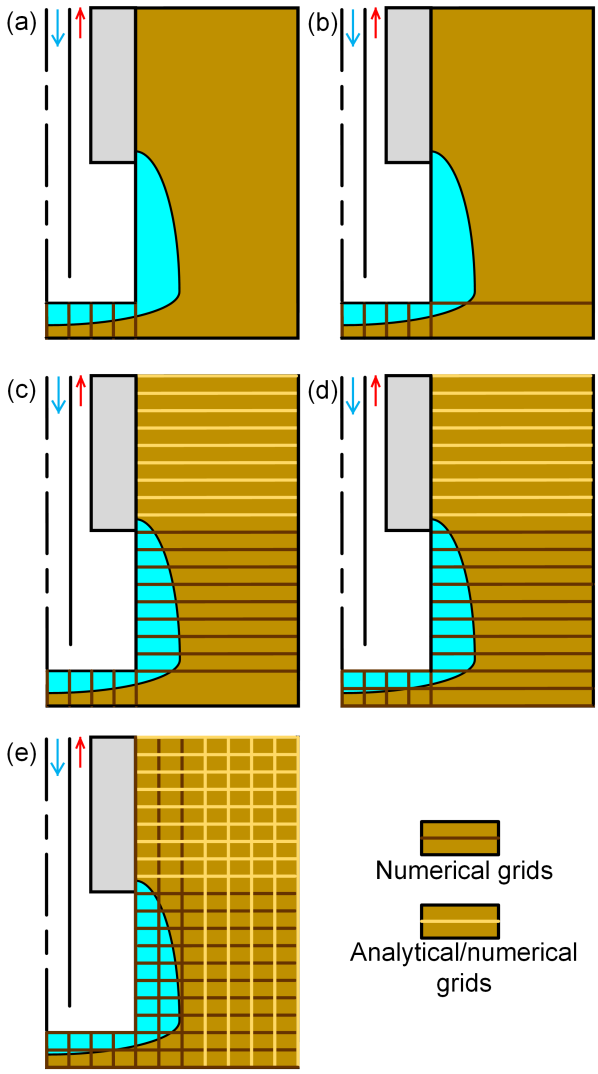

Figure 4-5: Not-to-scale schematics that clarify the 1+1D algorithms: a) Starting with a 1D solution of all 1D grid-lines between the bottom of the freeze-pipe and the lower boundary (applicable to M-3 and M-4 only). b) Follwing that, a 1D solution of the lowest radial grid-line next to the bottom of the freeze-pipe is obtained (applicable to all proposed algorithms). c) Then, 1D solution of all 1D grid-lines between the side pipe wall and the side boundary is obtained in series from the bottom to the top (applicable to all proposed models). d) After that, 1D solution of all 1D grid-lines between the axi-symmetric boundary and the opposite boundary is calculated (applicable to M-3 and M-4 only). e) Finally, 1D solution of all 1D grid-lines between the bottom and upper boundaries is found (applicable to M-3 and M-4 only). The process is repeated at every time step. Light grid-lines are solved analytically in hybrid models and numerically in numerical models. The legends of Fig. 4-1 for the coolant, air, and ground are consistent with this figure.

1. Initially, the temperature and enthalpy fields of the computational domain are set according to the initial condition.

2. Heat conduction along the 1D grid-lines between the freeze-pipe wall and the side boundary are solved in series starting from the lowest grid-line till the top of the computational domain using Eqs. (4.1,4.9,4.18,4.16), exactly as explained in steps (2-3) of the previous section and shown in Fig. 4-5(b-c). The only exception is that the M-2 model solves single-phase grid-lines *numerically*, while M-1 solves single-phase grid-lines *analytically*.

3. Once all grid-lines are covered, the temperature and enthalpy fields of the present time step are set as an initial condition to solve for the temperature and enthalpy fields of the next time step.

4. Steps (2-3) are repeated until the end of the simulation.

4.3.4 Hybrid 1+1D algorithm with axial correction (M-3)

Unlike the previous algorithms, this algorithm involves axial conduction. Including axial conduction enhances the solution accuracy if axial temperature diffusion is significant. Nevertheless, more 1D grid-lines need to be solved due to the addition of axial grid-lines, resulting in lower computational efficiency. Particularly, three more computational sets need to be solved as shown in Fig. 4-4. Additionally, this model includes analytical solutions to calculate single-phase grid-lines to perhaps enhance the computational efficiency. The following steps illustrate the M-3 algorithm:

1. Initially, the temperature and enthalpy fields of the computational domain are set according to the initial condition.

2. A numerical solution is obtained for the change in the enthalpy field due to axial conduction, $\Delta H_z(t + \Delta t)$, below the bottom of the freeze-pipe, as shown in Fig. 4-5(a).

The governing equation of these 1D grid-lines is Eq. (4.1), which is bounded by the freeze-pipe convective boundary from the top, given by Eq. (4.9). The convective heat transfer coefficient in this step only is assumed to be 1000 [W/(m^{2}K)] [43]. The bottom boundary in lab-scale simulations is different from that of field scale, as shown in Fig. 4-2. An insulated wall modeled by Eq. (4.18) is considered in lab-scale whereas geothermal heat flux given by Eq. (4.21) is set in field-scale. Also, the coolant temperature is approximated to be equal to the coolant inlet temperature. Overall, the impact of this step on the coolant and ground temperature is found to be negligible due to the extremely small area of the bottom plate of the freeze-pipe as compared to that of the freeze-pipe side wall.

3. Similar to steps (2-3) of section 4.3.2, the change in the enthalpy field due to radial conduction, $\Delta H_r(t + \Delta t)$, is calculated between the freeze-pipe wall and the insulated boundary employing Eqs. (4.1,4.9,4.18,4.16), as shown in Fig. 4-5(b-c). The coolant temperature used in the solution of the lowest radial grid-line shown in Fig. 4-5(b) equals to the coolant temperature obtained from the previous step.

4. Numerical solutions are obtained to calculate the change in the enthalpy field due to radial conduction $\Delta H_r(t + \Delta t)$ along all the radial grid-lines located below the bottom of the freeze-pipe, as shown in Fig. 4-5(d). In this step, the governing equation (Eq. (4.1)) is bounded by axi-symmetric boundary and insulated boundary modeled by Eqs. (4.17,4.18). The grid-lines are solved seperately and in-series. Nevertheless, the order of the grid-lines solution is insignificant in this step since the coolant flow does not take part in the calculation of these grid-lines.

5. $\Delta H_z(t+\Delta t)$ is calculated along the axial grid-lines located between the top and bottom of the computational domain, as shown in Fig. 4-5(e), using Eq. 4.1 bounded by top and bottom boundary conditions. In lab-scale, the top and bottom boundaries are insulated; consequently, Eq. (4.18) is used for both boundary settings. In field-scale,

atmospheric convection (Eq. (4.19)) and geothermal flux (Eq. (4.21)) are set on the top and bottom boundaries, respectively. In this step, analytical solutions are used in calculating the temperature distribution of single-phase grid-lines. As in the previous step, the grid-lines can be solved in any order in this step.

6. By the end of the previous step, each computational cell stores a value for $\Delta H_r(t+\Delta t)$ and $\Delta H_z(t+\Delta t)$. The total change in the enthalpy field can then be calculated by adding the axial enthalpy change to the radial enthalpy change as follows:

$$\Delta H(t+\Delta t) = \Delta H_r(t+\Delta t) + \Delta H_z(t+\Delta t). \tag{4.22}$$

7. The calculated enthalpy field of the present time step is used as an initial condition to calculate the enthalpy field of the next time step.

8. Steps (2-7) are repeated until the end of the simulation.

4.3.5 Numerical 1+1D algorithm with axial correction (M-4)

This algorithm is almost identical to that of the previous model, except that M-4 employs only numerical solutions (without analytical ones) throughout the computational domain to compare between the computational speed of analytical solutions and numerical ones. Since this algorithm takes into account axial conduction, it produces more accurate results than M-1 and M-2. Nonetheless, M-4 requires solving additional grid-lines as compared to M-1 and M-2 which will increase the computational time. This model was developed since we noticed that the analytical solutions of the M-3 models require large number of eigenvalues which decreases its computational efficiency. The algorithm is summarized in Fig. 4-4 and is given as follows:

1. Initially, the temperature and enthalpy fields of the computational domain are set according to the initial condition.

2. $\Delta H_z(t+\Delta t)$ between the bottom of the freeze-pipe and the bottom boundary is calculated exactly as explained in step (2) of the previous model.

3. Similar to steps (2-3) of section 4.3.2, the change in the enthalpy field due to radial conduction, $\Delta H_r(t+\Delta t)$, is calculated between the freeze-pipe wall and the side wall employing Eqs. (4.1,4.9,4.18,4.16), as shown in Fig. 4-5(b-c). The coolant temperature used in the solution of the lowest radial grid-line shown in Fig. 4-5(b) equals to the coolant temperature obtained from the previous step. Unlike M-3 and M-1, this model employs numerical solutions only throughout the simulation for single-phase and two-phase grid-lines.

4. $\Delta H_r(t+\Delta t)$ is calculated using Eqs. (4.1,4.17,4.18) for all radial grid-lines below the freeze-pipe exactly as clarified in step (4) of M-3.

5. $\Delta H_z(t+\Delta t)$ is solved for all axial grid-lines as in step (5) of M-3. Eqs. (4.1,4.18) and Eqs. (4.1,4.21,4.19) are applied in lab-scale and field-scale, respectively. Nonetheless, only numerical solutions are employed for single-phase and two-phase grid-lines.

6. By the end of the previous step, each computational cell stores a value for $\Delta H_r(t+\Delta t)$ and $\Delta H_z(t+\Delta t)$. The total change in the enthalpy field can then be calculated by adding the axial enthalpy change to the radial enthalpy change as follows:

$$\Delta H(t+\Delta t) = \Delta H_r(t+\Delta t) + \Delta H_z(t+\Delta t). \tag{4.23}$$

7. The calculated enthalpy field of the present time step is used as an initial condition to calculate the enthalpy field of the next time step.

8. Steps (2-7) are repeated until the end of the simulation.

4.4 Solutions calculation

This study comprises numerical and analytical solutions. Numerical solutions are mainly employed in solving the enthalpy fields in grid-lines involving phase change using the linearized enthalpy method developed by Swaminathan and Voller [35]. Analytical solutions, nonetheless, are used in hybrid models to calculate single-phase conduction.

4.4.1 Numerical solutions methodology

The integral form of the enthalpy written in Eq. (4.2) can be approximated by a continuous piece-wise function as [44]

$$H = \begin{cases} (\rho c_p)_s (T - T_{sol}) & , \ T < T_{sol}; \\ \gamma \ \overline{\rho c_p} \ (T - T_{sol}) + (\rho L)_\ell & , \ T_{sol} \leq T \leq T_{liq}; \\ (\rho c_p)_\ell (T - T_{liq}) + \overline{\rho c_p}(T_{liq} - T_{sol}) + (\rho L)_\ell & , \ T > T_{liq}. \end{cases} \tag{4.24}$$

In Eq. (4.24), T_{sol} is set as the arbitrary reference temperature, T_{ref}, written in Eq. (4.2). $\overline{\rho c_p}$ represents the averaged solid and liquid volumetric heat capacity calculated as $\overline{\rho c_p} = (\rho_s c_{p,s} + \rho_\ell c_{p,\ell})/2$. The terms including $\overline{\rho c_p}$ are added to approximate the sensible enthalpy change within the mushy zone temperature limits. This approximation is valid for phase change applications in which the change in latent heat is much larger than that of sensible heat between the liquidus and solidus temperatures.

After simplifying the integral form of the enthalpy equation, the transient and diffusive terms of the conduction equation (Eq. (4.1)) can be written in a point-form as

$$d_i(H_i^k - H_i^{old}) = c_{i-1}T_{i-1}^k + c_i T_i^k + c_{i+1}T_{i+1}^k, \tag{4.25}$$

where subscript i and superscript k represent the i-th node and k-th iteration level, respectively. The superscript *old* refers to the enthalpy of the previous time step. The sym-

bols c and d of Eq. (4.25) denote the coefficients of the discretized equation. In this study, second and first order schemes were set for the diffusive and transient terms, respectively.

To solve Eq. (4.25), the linearized enthalpy method of Swaminathan and Voller [35] is adapted. This method expresses the enthalpy term, H_i^k, using a truncated Taylor's series as

$$H_i^k = H_i^{k-1} + \left(\frac{\partial H}{\partial T}\right)_i^{k-1} (T_i^k - T_i^{k-1}), \tag{4.26}$$

where $\partial H/\partial T$ is the slope of Eq. (4.24). A new linear system of equations can then by obtained by substituting the enthalpy term of Eq. (4.26) into Eq. (4.25) as

$$d_i \left[H_i^{k-1} + \left(\frac{\partial H}{\partial T}\right)_i^{k-1} (T_i^k - T_i^{k-1}) - H_i^{old} \right] = c_{i-1} T_{i-1}^k + c_i T_i^k + c_{i+1} T_{i+1}^k, \tag{4.27}$$

where the terms H_i^{k-1} and T_i^{k-1} are known from the previous iteration level. Based on equations above, the iterative scheme to find a numerical solution of a two-phase 1D grid-line is illustrated in Fig. 4-6 and is given as follows:

1. For the first iteration, $T^{k=0}$ and $H^{k=0}$ are assumed to be equivalent to the temperature and enthalpy fields of the previous time step (in the case of the first time step, $T^{k=0}$ and $H^{k=0}$ are obtained from the initial condition).

2. Start a new iteration level (increment the iteration level by 1).

3. The derivative $(\partial H/\partial T)^{k-1}$ is calculated based on Eq. (4.24) using a central second-order accurate finite difference technique across all nodes of the computational domain.

4. The corresponding coefficients of Eq. (4.27) are evaluated for every computational node.

5. The linear set of equations resulting from Eq. (4.27) are then solved implicitly for the temperature using the lower-upper (LU) decomposition method.

6. The enthalpy field is updated according to Eq. (4.24).

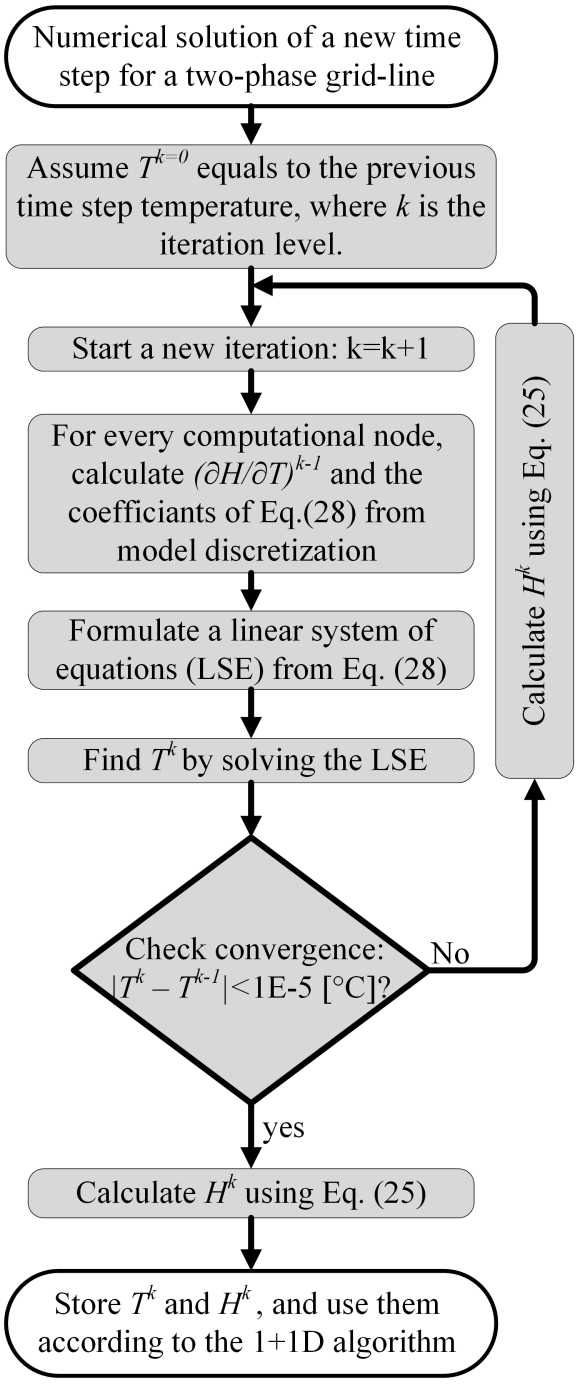

Figure 4-6: Numerical solution algorithm of a two-phase transient conduction problem following the linearized enthalpy method.

7. Steps (2-6) are repeated until convergence is achieved. In this study, the convergence criterion is met when the maximum difference between the temperature fields of two successive iterations is less than 1×10^{-5} [°C] (implying that the enthalpy field is consistent with the temperature field)

Once convergence is reached, the solution is stored and utilized according to the 1+1D algorithm.

4.4.2 Analytical solutions derivation

Analytical solutions are utilized to solve single-phase conduction problems in hybrid algorithms in attempts to increase the computational efficiency. In particular, three finite-extent transient heat conduction problems are formulated as follows: i) A cylindrical heat equation subjected to a convective boundary and a no-flux condition to find the temperature distribution along radial grid-lines shown in Fig. 4-5(c); ii) A rectangular heat equation subjected to no-flux conditions at both ends to solve for the temperature along axial grid-lines shown in Fig. 4-5(e) in lab-scale conditions; and iii) A rectangular heat equation subjected to a convective boundary and a heat flux condition to solve for the temperature along axial grid-lines shown in Fig. 4-5(e) in field-scale conditions. All the transient problems are with respect to a non-uniform initial condition so as to update numerical solutions at each time step. Elaborate analytical treatments for each problem and corresponding exact solutions are provided in Appendix A.

Whilst the governing equations in all problems are homogeneous partial differential equations (PDEs), the homogeneity of boundary condition varies, which results in distinguishing analytical techniques. Among all, the second problem has both homogenenous boundary conditions, and thus the method of separation of variables can be directly applied. The first problem, nonetheless, has one homogeneous and one non-homogeneous boundaries; a linear shift of temperature is required for removing the non-homogeneity prior to separation of variables. Since both boundary conditions in the third problems are non-homogeneous,

the method of superposition is also needed to break down into two sub-problems: a transient homogeneous PDE and a steady-state non-homogeneous ordinary differential equation (ODE).

4.4.3 Computation of numerical and analytical solutions

The computational domain and mesh of the proposed models were created by our own MATLAB codes. Additionally, MATLAB codes were developed to conduct the calculations of the mathematical model according to our prescribed reduced-order algorithms. Throughout this work, we did not use any built-in PDE solvers which MATLAB has. The governing equations and boundary conditions were discretized and solved by our own algorithms and codes. We only used the lower-upper (LU) MATLAB function to calculate the solution of a pre-defined set of linear equations, as explained in step (5) under Sec. 4.4.1. In other words, a matrix describing the set of linear equations were created by our own codes and then fed to the MATLAB LU decomposition function.

Mesh and time step independence study were carried out for lab-scale and field-scale simulations. In lab-scale, a mesh count of 5,000 nodes and time step of 6 minutes were used. In field scale, a mesh count of around 30,000 nodes was sufficient to obtain a mesh-indepent solution as can be seen from Fig. 4-7(a), but we used 50,000 nodes to enhance the resolution of the ground temperature. Similarly, although a time step up to around 4 days provided accurate results, a time step of one day was selected to obtain higher resolution.

Regarding analytical models, the most important parameter that needs to be investigated is the number of eigenvalues. This number is especially signifcant in field scale due to the large length scale of the problem. This can be further understood by solving a 1D conduction problem along the axial direction in field-scale using a numerical solution, 200 eigenvalues analytical solution, and 500 eigenvalues analytical solution. The comparison indicates that the 200 eigenvalues solution oscillates significantly near the ground surface, as shown in Fig. 4-7(b). This oscillation propagates further in future time steps causing the solution

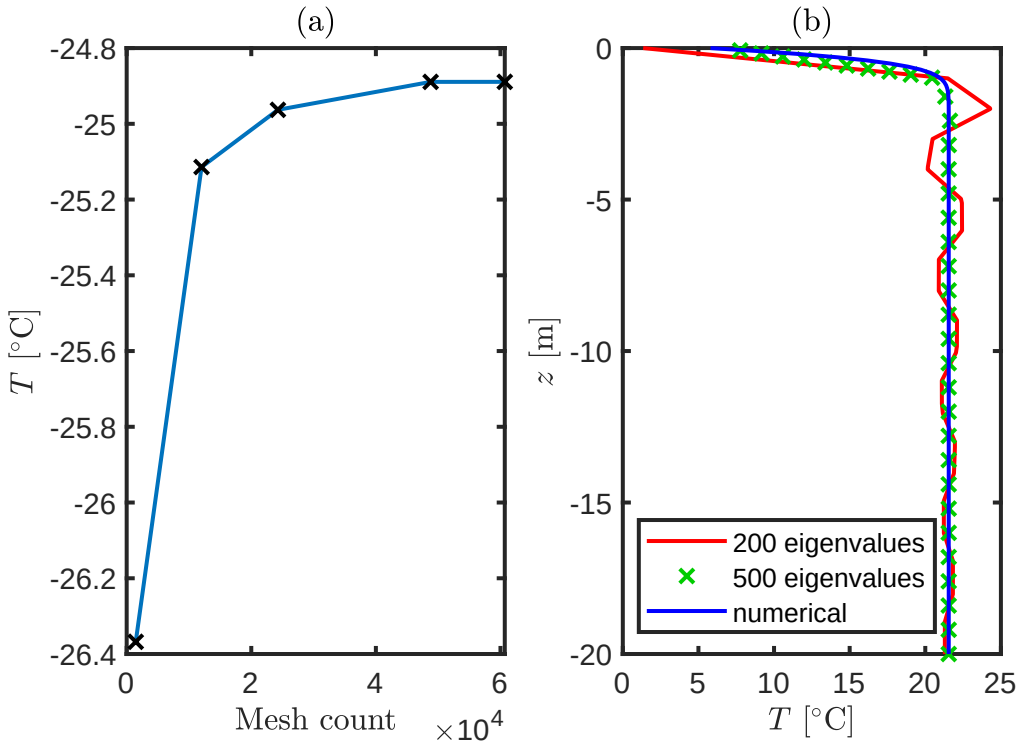

Figure 4-7: Sensitivity analysis of our models: a) Mesh independence study based on the coolant outlet temperature and b) effect of the number of eigenvalues of axial analytical solutions in field-scale.

to diverge. In fact, a continuously stable solution was only obtained as the number of eigenvalues exceeded 1000. The large number of the eigenvalues can significantly undermine the computational efficiency of analytical solutions.

4.5 Results and discussion of results

In this section, the reliability and the computational efficiency of the proposed mathematical models are investigated in lab-scale and field-scale. For simplicity, the different models are provided unique shortcuts as per Table 4.1.

Model	Shortcut
Semi-conjugate hybrid 1+1D without axial correction	M-1
Semi-conjugate numerical 1+1D without axial correction	M-2
Semi-conjugate hybrid 1+1D with axial correction	M-3
Semi-conjugate numerical 1+1D with axial correction	M-4
Semi-conjugate numerical 2D	M-5
Fully-conjugate numerical 2D [8]	M-6
Similar to M-4 but assuming thermally *developed* coolant flow	M-7
Similar to M-4 but assuming fixed temperature boundary in the active zone	M-8

Table 4.1: Shortcuts of the different mathematical models used in the results and discussion section. M-1, M-2, M-3 and M-4 are the proposed models of this study. M-6 is a fully-conjugate model obtained from the literature [8], and M-5 is another 2D model created for the purpose of computational time comparison.

4.5.1 Experimental setup

The experimental and mathematical study of selective artificial ground freezing (S-AGF) conducted in our previous work [8] is selected to validate the proposed models because it is the only experimental setup that resembles S-AGF systems. The experimental setup consists of a freeze-pipe and a saturated porous ground enclosed in an insulated tank. The freeze-pipe is composed of three concentric tubes. A coolant enters the freeze-pipe after being refrigerated to a desired temperature in a chiller. Then, the coolant extracts heat from the

ground and exits through the annulus between the inner tube and the air chamber.

The experimental setup also includes advanced instrumentation to properly run the experiment and report the measurements. In fact, there are more than 80 thermocouples in the porous ground to ensure uniform initial temperature prior to starting the experiment. Furthermore, thermocouples are placed in the vicinity of the freeze-pipe to monitor the temperature of the active and passive zones at four different locations shown in Fig. 4-8. The thermophysical properties of the constituent materials of the experiment are measured and listed in Table 4.2, including the porosity of the ground which is found to be 37%. More comprehensive details on the experiment can be found in [8].

Material	ρ [kg/m^3]	c_p [J/(kg·k)]	k [W/(m·k)]
Experiment Coolant (55% ethylene glycol & 45% water)	1092	3211	0.397
Field Coolant (30% Calcium Chloride & 70% water)	1310	4187	0.493
Sand particles (90.5% quartz & 9.5% albite)	2634	946	3.73
Frozen water	926	2033	2.19
Unfrozen water	1012	4139	0.572

Table 4.2: Thermophysical properties of the materials used in this study as per experimental measurements of [8]. The properties of calcium chloride solution is obtained from [45]. Ground porosity is 37%.

4.5.2 Validation and verification in lab-scale

First, the results of the proposed mathematical models are validated against experimental measurements and verified with a well-established fully-conjugate model in lab-scale [8]. Following the experimental study, the coolant flow rate is set at 10 [mL/s], and the coolant inlet temperature is curve-fitted as

$$T[\mathrm{K}] = 1.32 \times \big(t[\mathrm{s}]\big)^2 \times 10^{-9} - 1.31 \times t[\mathrm{s}] \times 10^{-4} + 252.5. \tag{4.28}$$

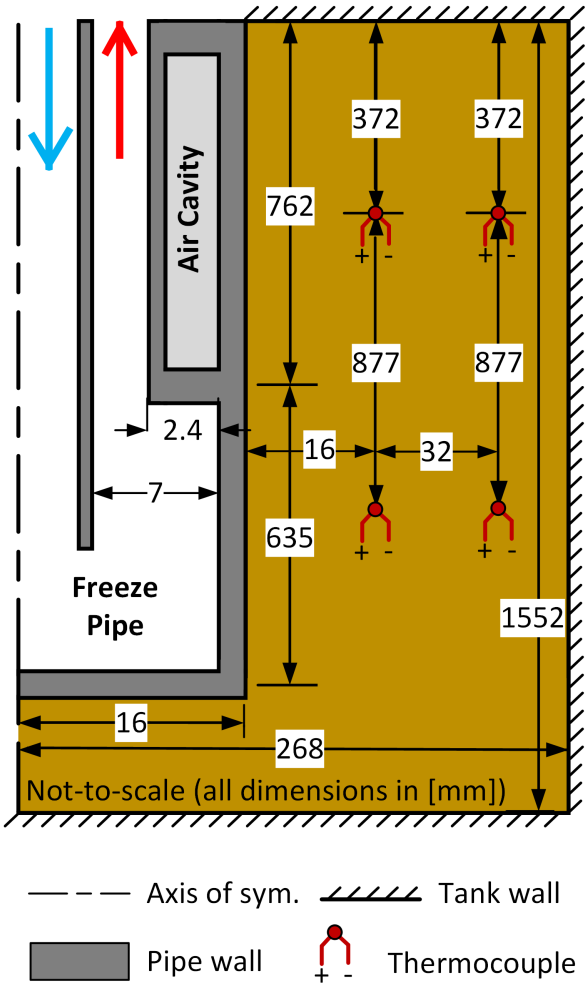

Figure 4-8: Schematic of the experimental setup conceived by Zueter et al. [8] (from our previous work).

The results of the proposed models show a very good agreement with the experimental measurements of the ground temperature, as can be seen from Fig. 4-9(b-e). This confirms the reliability of the proposed models in monitoring the transient ground temperature.

Furthermore, as shown in Fig. 4-9(a), the coolant outlet temperature is predicted accurately by the proposed models as compared with M-6, which is an established fully conjugate model from our previous work [8]. The coolant outlet temperature is a major parameter in the design of AGF plants as it is directly correlated to the cooling load calculated as:

$$\dot{E} = \dot{m}_c c_{p,c}(T_{c,outlet} - T_{c,inlet}). \tag{4.29}$$

In addition to the energy consumption, the frozen body growth is another essential design criteria in AGF systems. Thus, we have compared the phase front position of the proposed models with M-6 as shown in Fig. 4-10. M-3 and M-4 models, which involve axial correction, verify well with the isotherms of the fully-conjugate model. The slight over-prediction of M-3 and M-4 is attributed to the heat gained by the coolant as it flows downward from the inlet to the bottom plate of the freeze-pipe. Nonetheless, M-1 and M-2 models tend to overestimate the phase front expansion due to the exclusion of axial heat gain in these models as they do not include axial correction. The curvatures of the M-1 and M-2 isotherms reflect the change in the local Nusselt number of the active zone due to the thermal development of the flow, as shown in Fig. 4-3.

4.5.3 Computational time analysis in lab-scale

In this subsection, the computational time of the proposed models in lab-scale will be discussed and compared. The semi-conjugate numerical 2D model, M-5, uses the linearized enthalpy method in two dimensions. This model is solely created to establish a fair comparison between its computational time with that of the proposed models. In other words, the proposed models and M-5 employ the same coding practice, compiling software, mesh count,

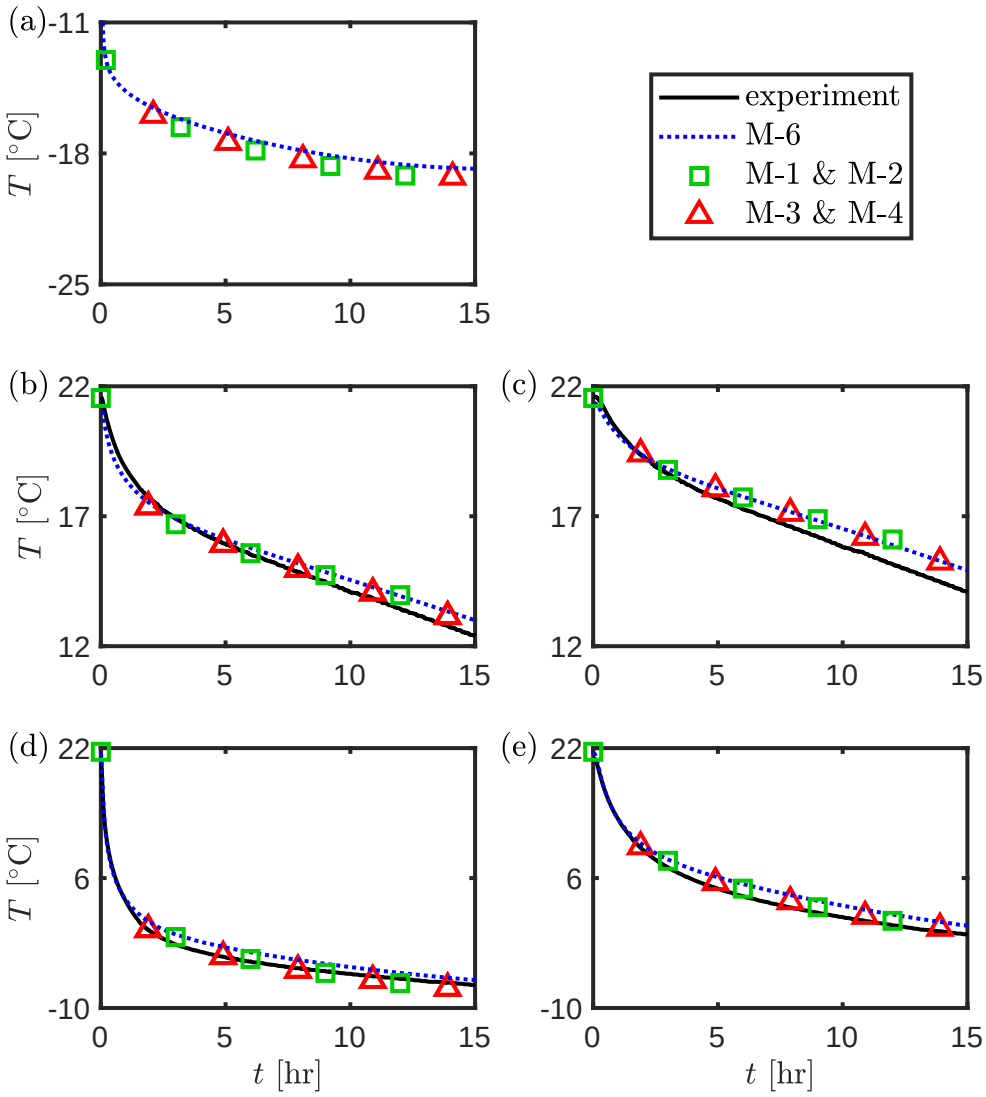

Figure 4-9: Validation of the proposed models against experimental measurements and verification with an established fully-conjugate model, M-6, from our previous work [8]: (a) Coolant outlet temperature, (b) ground temperature at 16[mm] from freeze-pipe wall in the passive zone, (c) ground temperature at 48[mm] from freeze-pipe wall in the passive zone, (d) ground temperature at 16[mm] from freeze-pipe wall in the active zone, and (e) ground temperature at 48[mm] from freeze-pipe wall in the active zone. The exact location of the thermocouples can be found in Fig. 4-8.

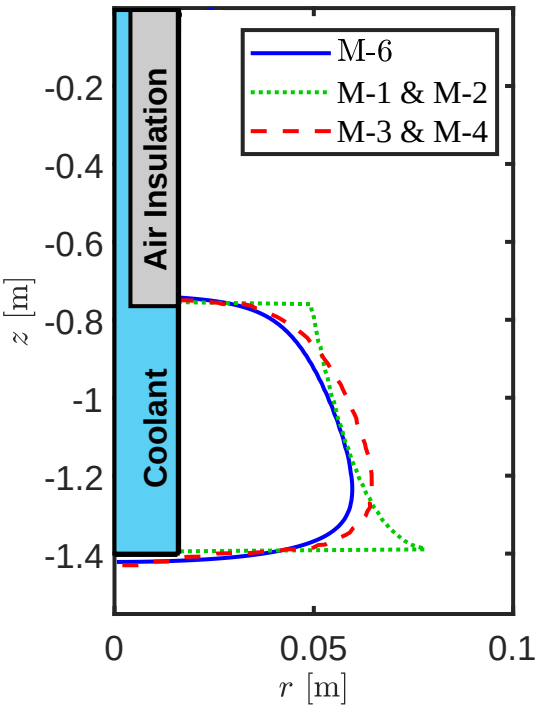

Figure 4-10: Lab-scale verification of the phase front profile derived by our proposed models and an established fully-conjugate model from our previous work [8]. Air insulation thickness is not-to-scale.

number of time steps, convergence criteria, number of processors, etc. The only difference between the proposed models and M-5 is the solution algorithm, which is the main idea of this study.

Evidently, the proposed 1+1D models are much faster than the 2D models, as can be noted from Table 4.3. In particular, as compared with M-5 and M-6, the reduction in the computational time of the proposed models exceed 99%. This confirms the superiority of the 1+1D models over 2D models in regards to the computational time, while still retaining the reliability and accuracy of well-established fully-conjugate models as demonstrated in the previous subsection.

Model	Mesh count	Comp. time [hh:mm:ss]
M-1	13,000	00:04:16
M-2	13,000	00:03:12
M-3	13,192	00:05:15
M-4	13,192	00:04:25
M-5	13,192	14:25:00
M-6	130,000	12:45:00

Table 4.3: Comparison between different models based on the computational time in lab-scale. Apart from the differences highlighted in the table, all simulations were conducted under exactly the same computational conditions (number of processors, number of time steps etc). However, it shall be noted that M-6 is modeled using a highly sophisticated commercial CFD software (Fluent 18.1) while the rest are developed by customized Matlab codes. Fully-conjugate models demand huge number of nodes to capture the air and coolant flow accurately.

Now, the computational time among the proposed models will be investigated. First, the computational time of the numerical 1+1D models (M-2 and M-4) is noted to be shorter than that of the hybrid models in lab-scale. This is often the case when the mesh count is small because the time needed to calculate the inverse of a matrix using the LU decomposition method is too small and often less than the time needed to compute the eigenvalues of the analytical solutions. Secondly, the computational time of M-1 and M-2 is only 20% less than that of M-3 and M-4. This indicates that radial solutions takes most of the computational time due to the denser mesh in the radial direction and larger number of freezing layers, which

require iterative numerical solution (see section 4.4.1).

4.5.4 Verification in field-scale

In this section, the reliability of the models is investigated in field-scale, such as that of Cigar Lake underground mine. Table 4.4 provides the freeze-pipe geometry used in this study. Also, the coolant inlet temperature and flow rate are changed to -30 [°C] and 2.5 [m^3/hr]. The thermophysical properties of the ground is assumed to be similar to that of the experimental setup. Nevertheless, calcium chloride is considered as the coolant since it is commonly used in AGF systems [46], [47]. The properties of calcium chloride solution [45] are listed in Table 4.2. In addition to the coolant, the initial and boundary conditions of the mathematical models in field-scale are also adjusted according to section 4.2.2.

property	value
Active zone height	60 [m]
Passive zone height	400 [m]
Central tube inner diameter	26.92 [mm]
Central tube outer diameter	31.75 [mm]
Middle tube inner diameter	62 [mm]
Middle tube outer diameter	73.03 [mm]
Casing inner diameter	101.6 [mm]
Casing outer diameter	114.3 [mm]

Table 4.4: Geometry of a typical field-scale freeze-pipe as used in this study.

As can be seen from Fig. 4-11, the coolant outlet temperature and ground transient temperature of the proposed models verify well with the fully-conjugate model. In field-scale, the influence of axial correction becomes almost negligible because the axial length scale is two orders of magnitude larger than the radial length scale. Consequently, the results of M-1 and M-2, which do not include axial correction, are almost identical to those of M-3 and M-4, which add axial correction.

Heat extraction from the active and passive zones are also predicted accurately by the proposed models, as noted from Fig. 4-12(a) and Fig. 4-12(b). In the passive zone, the

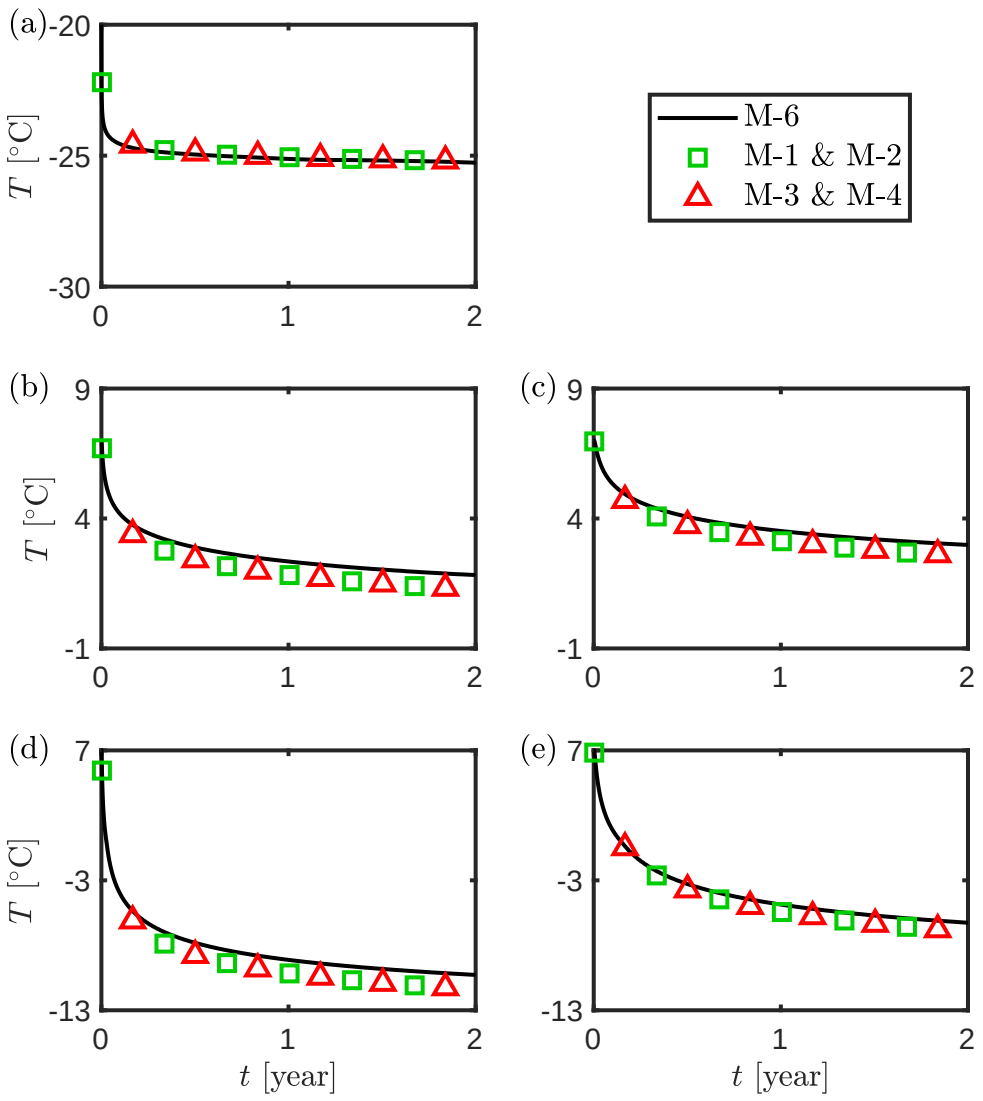

Figure 4-11: Field-scale verification of the proposed models with a fully-conjugate model, M-6, from our previous work [8]: a) outlet temperature, b) temperature recorded at the middle of the passive zone 0.5 [m] away from the central axis, c) temperature recorded at the middle of the passive zone 1 [m] away from the central axis, d) temperature recorded at the middle of the active zone 0.5 [m] away from the central axis, and e) temperature recorded at the middle of the active zone 1 [m] away from the central axis.

radiation and conduction heat gain within the air cavity of the proposed models are somewhat larger than M-6, as can be seen from Fig. 4-12(c) and Fig. 4-12(d), respectively. This could possibly due to the 2D modeling of radiation and conduction in M-6 as compared with 1D modeling of the proposed models. In field-scale, radiative heat gain can be more significant than conductive heat gain due to the high emissivity of the freeze-pipes ($\varepsilon = 0.9$) and the large thickness of air cavities, which effectively reduces conductive heat gain.

As typical S-AGF systems normally operate for 6 months to 2 years (though some of them run indefinitely), the phase front expansion is monitored for two years in the present study, as shown in Fig. 4-13(a-f). First, unlike the results shown in lab-scale, the phase front expansion monitored by the M-1 and M-2 models (which do not include axial correction) is very similar to that of M-3 and M-4 model except near ground surface. M-1 and M-2 cannot capture the phase-front expansion near the ground surface since they do not model axial conduction that takes into account wind heat convection on the surface. Nevertheless, wind convection has negligible effect on the frozen ground profile in the active zone because this zone is often located much below the ground surface (typically more than 400 [m] deep) in S-AGF applications. Accordingly, either M-1 or M-2 could be confidently utilized to monitor the phase front expansion near the freeze-pipe. The small deviations in the phase front expansion in the passive zone is caused by the higher heat flux along the passive zone wall, as shown in Fig. 4-12(b). Nonetheless, this deviation is of little practical importance since phase front expansion is not a criteria of interest in the passive zone.

4.5.5 Computational time analysis in field-scale

Similar to section 4.5.3, the computational performance of the proposed models is examined in field-scale. As can be seen from Table 4.5, a fully-conjugate model requires huge computational resources and develops the solution after more than 2 days. Particularly, a simulation that uses 40 processors, more than 2 million nodes, and small time step of 6 hours was required to yield a converging and accurate solution. This confirms that fully-

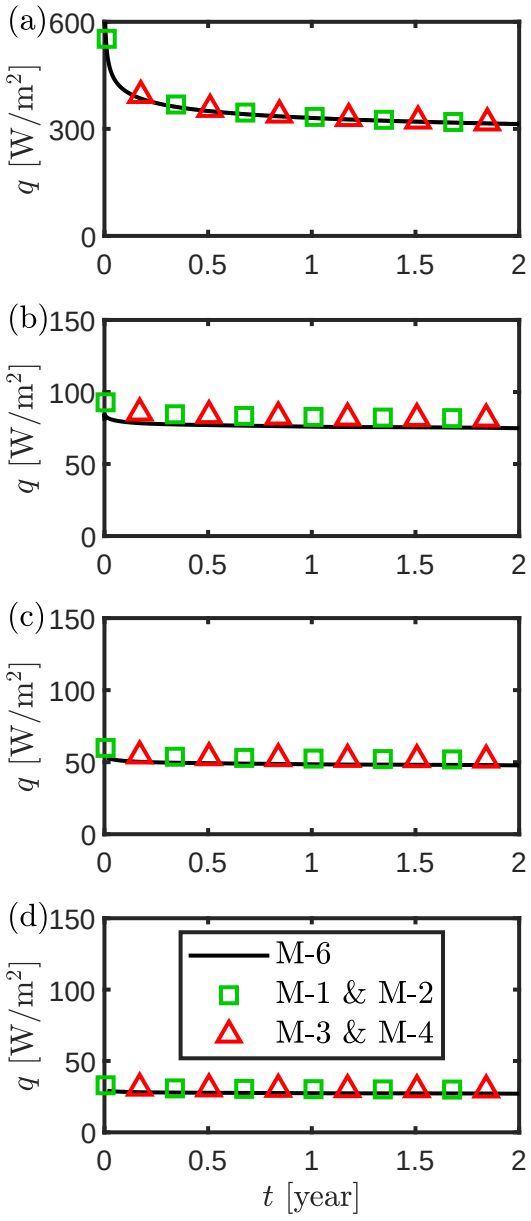

Figure 4-12: Verification of heat extraction as calculated by the proposed models with a fully-conjugate model from our previous work [8] in a) the active zone, and b) the passive zone, in addition to verification of the c) radiation heat flux in the passive zone and d) conduction heat flux in the passive zone.

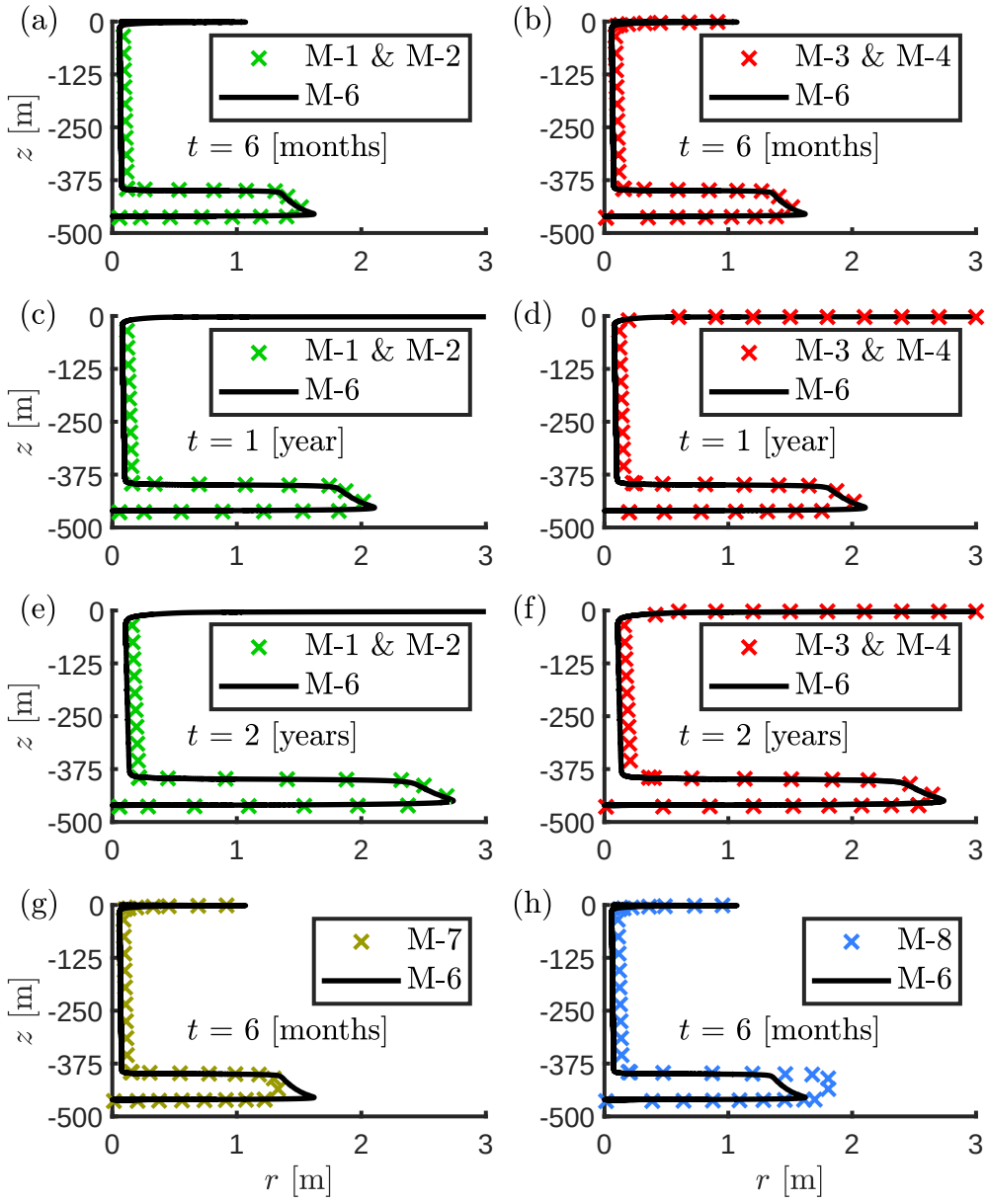

Figure 4-13: Monitoring the phase front expansion predicted by our proposed models (M-1 to M-4) and other models (M-7 and M-8) in comparison with the predicted phase front by M-6, which is an established fully conjugate model from our previous work [8]. The definition of each model is provided in Table 4.1.

conjugate models in field-scale are not practical for industrial use, unlike the semi-conjugate 1+1D models which produce similar results yet with much lesser computational resources and time. Overall, our reduced-order models decreased the computational time by more than 96%, and this percentage would certainly exceed 99% if a single processor is used in M-6 (which is not feasible to simulate since it would last for weeks).

Model	No. processors	Mesh count	Comp. time [hh:mm:ss]
M-1	1	43,900	01:42:26
M-2	1	43,900	01:45:27
M-3	1	47,581	16:30:00
M-4	1	47,581	02:39:01
M-6	40	2,600,000	50:00:00

Table 4.5: Comparison between different models based on the computational time in field-scale. Apart from M-6, all simulations were conducted under exactly the same computational conditions (number of time steps etc.) except for the differences highlighted in the table.

However, the computational performance of semi-conjugate 1+1D models vary according to the algorithm. Obviously, M-1 and M-2 are more computationally efficient than M-3 and M-4 as they do not include axial correction, as can be noted from Table 4.5. Interestingly, unlike lab-scale results, M-1 model is somewhat faster than M-2 model. This is attributed to a denser mesh in the radial direction in field-scale than that in lab-scale. As a result, the computational time needed to evaluate the inverse of a matrix in field-scale is larger than the computational time needed to calculate the analytical solution. Thus, as axial correction has proven to be insignificant in the design of AGF systems as shown in the previous section, hybrid 1+1D model without axial correction seems to be the most suitable option in field-scale. Nevertheless, if axial correction is necessary, axial analytical solutions shall be avoided in the axial direction because an accurate solution requires extremely large number of eigenvalues (more than 1000) which drastically slows down the simulation.

4.5.6 Thermal analysis in field-scale

The high accuracy of the proposed models in monitoring the phase front expansion presented in the previous subsections is attributed to the accurate modeling of the local convective boundary condition for a thermally developing flow. To further highlight the significance of the thermal development of the flow on the Nusselt number, the phase front expansion of M-4 is compared with two different models, namely M-7 and M-8. M-7 assumes a thermally *developed* flow; in other words, the Nusselt number along the active zone boundary is uniform such that $Nu_{active} = Nu(z_c = \infty)$ (see Fig. 4-3). Regarding M-8, a fixed temperature boundary condition is set along the active zone wall according to the inlet temperature of the coolant. This model is created to test the fixed wall temperature assumption that is widely adapted in the literature of AGF. As can be noted from Fig. 4-3 and Fig. 4-13(g), assuming a thermally *developed* flow reduces the Nusselt number and consequently under-predict the phase front expansion. The negative slope of M-7 is caused by the increase in the coolant temperature as it flows upward and extracts more heat from the ground. Fig. 4-13(h) also reveals that a fixed temperature boundary over-predicts the phase front expansion by around 20%. Additionally, the phase front profile is vertical almost throughout the active zone, which is not consistent with that of M-6. To sum up, Fig. 4-13 emphasizes the importance of modeling the coolant as a thermally developing flow in order to accurately predict the phase front profile.

After verifying the accuracy of our models and demonstrating their high computational efficiency, more than 30 AGF scenarios were simulated to study the effects of the coolant flow rate and inlet temperature. Particularly, 20 simulations are conducted varying the coolant flow rate from 1.5 [m^3/hr] to 3.5 [m^3/hr] at a fixed coolant inlet temperature of -30 [°C], and 15 more simulations in which coolant inlet temperature is changed from -40 [°C] to -10 [°C] at a fixed flow rate of 2.5 [m^3/hr]. All other parameters are set according to Section 4.5.4.

The results show that the phase front expansion is somewhat larger at higher flow rate as can be seen from Fig. 4-14(a), indicating higher heat extraction rate. This is attributed

to the longer thermal entrance length, and accordingly higher Nu as implied by Eq. (4.10) and Fig. 4-3, at a larger Re. Due to this proportional relationship between the higher heat extraction rate and the Re, the cooling load required is also proportional to the coolant flow rate, as can be seen from Fig. 4-14(c). The cooling load and phase front expansion are faster at the initial stages of the ground freezing because of the large temperature difference between the ground and the coolant at the start of the AGF process, resulting in a higher heat flux as per Eq. (4.9). However, the phase front expansion gradually slows down because more energy is consumed in over-cooling the frozen ground rather than extending the phase front.

While increasing the coolant flow rate increases the phase front expansion, a much more effective approach is decreasing the coolant inlet temperature, $T_{in,c}$, as can be noted from Fig. 4-14(b). Decreasing $T_{in,c}$ increases the heat extraction rate (see Eq. (4.9)) and consequently lengthens the phase front. However, reducing $T_{in,c}$ to extremely low values may not be recommended as the increase in the phase front expansion becomes smaller at lower $T_{in,c}$, even though the cooling load remains increasing proportionally, as can be depicted from Fig. 4-14(d). This implies that when $T_{in,c}$ is too low, more energy is lost in over-cooling the frozen ground rather than expanding it.

4.6 Conclusion

In this study, novel semi-conjugate reduced-order models have been developed for selective artificial ground freezing applications (S-AGF). The freeze-pipe boundary setting is mathematically derived based on the development of the coolant temperature and thermal boundary layer. This novel derivation also considers the air insulation along the passive zone of the freeze-pipe, where ground freezing is not desired. In addition, novel reduced-order 1+1D algorithms are developed to reduce the computational time of the large S-AGF applications. Particularly, four different variations of the 1+1D algorithms have been considered to

optimize the computational performance at various S-AGF scenarios. The four variations differ due to the optional inclusion of analytical solutions and spatial correction in the vertical direction parallel to the freeze-pipe as follows: i) Hybrid (numerical and analytical) modeling without spatial correction (M-1), ii) numerical modeling without spatial correction (M-2), iii) hybrid modeling with spatial correction (M-3), and iv) numerical modeling with spatial correction (M-4). All the variations are validated against experimental data and further verified with established fully-conjugate model (M-6) from our previous work.

The thermal analysis demonstrates that accurate modeling of the thermal development of the coolant flow is essential in determining the phase front profile in the ground. The coolant flow rate is found to be more significant in shaping the phase front profile than the coolant inlet temperature though the latter is more crucial to the overall phase front expansion. Concerning the computational analysis, the computational time of the proposed models is reduced by more than 99%, as compared with established numerical models that employ conventional CFD solvers (M-6). The computational results also show that merging analytical solutions to the 1+1D models (M-1 and M-3) decrease the computational efficiency in lab-scale. Thus, narrowing down the comparison to the numerical models (M-2 and M-4), M-4 predicts the phase-front profile more accurately than M-2 in *lab-scale* since vertical heat conduction is significant in small lab-scale simulations. Nonetheless, in *field-scale*, all proposed models predict the phase-front profile accurately since axial heat conduction is negligible at large length-scale. Among all, M-1 is preferred because it achieved the highest computational efficiency in field-scale. Overall, the optimum models for lab-scale and field-scale are found to be M-4 and M-1, respectively.

In conclusion, the proposed models have proven to be reliable and computationally efficient, which shows potential for industrial use. Our future work will employ the 1+1D model to carry out further parametric studies in field-scale to optimize S-AGF systems at different ground conditions. The 1+1D model will also be extended to a computationally efficient 1+2D model to study AGF in 3D. More specifically, the effects of freeze-pipe eccentricity

and freeze-pipes layout will be examined.

Acknowledgments

We would like to thank Cameco Corporation, Ultra Deep Mining Network (UDMN), Orano Canada Inc., and Newmans Geotechnique Inc., for their support of our work. The first two authors would like to thank the McGill Engineering Doctoral Award (MEDA).

Appendix A

Cylindrical, convective-insulated boundary conditions

The first analytical solution has been implemented in solving single-phase conduction equation in cylindrical coordinates in lab-scale (see Fig. 4-5(c)). Heat conduction equation in cylindrical coordinates is

$$\frac{\partial^2 T}{\partial r^2} + \frac{1}{r}\frac{\partial T}{\partial r} = \frac{1}{\alpha}\frac{\partial T}{\partial t}, \quad \text{on} \quad a < r < b, \quad t > 0, \tag{A.1}$$

where α is the thermal diffusivity of the unfrozen ground. The corresponding initial and boundary conditions are

$$T(r, t = t_o) = f(r) \tag{A.2}$$

$$-k\frac{\partial T}{\partial r}\bigg|_{r=a} = h\Big[T(r = a) - T_\infty\Big] \tag{A.3}$$

$$\frac{\partial T}{\partial r}\bigg|_{r=b} = 0, \tag{A.4}$$

where t_o is the time of the initial condition and T_∞ corresponds to the coolant temperature. This heat equation is a homogeneous partial differential equation, subject to one homogeneous and another non-homogeneous boundary conditions. Therefore, the method

of separation of variables can be applied after removing the nonhomogeneous boundary condition.

Firstly, a linear shift of the temperature is used to remove the convective nonhomogeneous boundary condition

$$\theta(r,t) = T(r,t) - T_\infty \tag{A.5}$$

Then, the problem becomes

$$\frac{\partial^2\theta}{\partial r^2} + \frac{1}{r}\frac{\partial\theta}{\partial r} = \frac{1}{\alpha}\frac{\partial\theta}{\partial t}, \tag{A.6}$$

subject to

$$\theta(r, t = t_o) = f(r) - T_\infty = F(r) \tag{A.7}$$

$$-k\left.\frac{\partial\theta}{\partial r}\right|_{r=a} = h\theta(r = a, t) \tag{A.8}$$

$$\left.\frac{\partial\theta}{\partial r}\right|_{r=b} = 0, \tag{A.9}$$

where $f(r)$ is the initial temperature profile. Applying the separation of variables, we assume the solution has the form

$$\theta(r,t) = \xi(r)\Gamma(t). \tag{A.10}$$

Substituting this separable form into the PDE gives

$$\frac{1}{\xi}\left(\frac{\mathrm{d}^2\xi}{\mathrm{d}r^2} + \frac{\mathrm{d}\xi}{\mathrm{d}r}\right) = \frac{1}{\alpha\Gamma}\frac{\mathrm{d}\Gamma}{\mathrm{d}t} = -\lambda^2, \tag{A.11}$$

Then, we obtain the exact solution after implementing the boundary and initial conditions

$$T(r,t) = T_\infty + \sum_{n=1}^{\infty} c_n R_n(\lambda_n, r) \exp(-\alpha \lambda_n^2 t), \tag{A.12}$$

where $R_n(\lambda_n, r)$ can be defined after implementing the transformed boundary conditions

$$R_n(\lambda_n, r) = J_0(\lambda_n r)\left[\lambda_n Y_1(\lambda_n a) - \frac{h}{k} Y_0(\lambda_n a)\right] - Y_0(\lambda_n r)\left[\lambda_n J_1(\lambda_n a) - \frac{h}{k} J_0(\lambda_n a)\right]. \tag{A.13}$$

The eigenvalues, λ_n, are found from the following transcendental equation

$$-J_1(\lambda_n b)\left[\lambda_n Y_1(\lambda_n a) - \frac{h}{k} Y_0(\lambda_n a)\right] + Y_1(\lambda_n b)\left[\lambda_n J_1(\lambda_n a) - \frac{h}{k} J_0(\lambda_n a)\right] = 0. \tag{A.14}$$

The coefficients, c_n, can be obtained by using the Fourier-Bessel series

$$c_n = \left\{ \int_{r=a}^{b} r\left[f(r) - T_\infty\right] R_n(\lambda_n, r)\mathrm{dr} \right\} \Big/ \left\{ \int_{r=a}^{b} r R_n^2(\lambda_n, r)\mathrm{dr} \right\}. \tag{A.15}$$

Cartesian, insulated-insulated boundary conditions

The second analytical model solves the heat conduction equation in lab-scale bounded by insulated walls in axial coordinates, as shown in Fig. 4-5(e). The governing equation is written in axial coordinates

$$\frac{\partial^2 T}{\partial \zeta^2} = \frac{1}{\alpha} \frac{\partial T}{\partial t}, \quad \text{on} \quad 0 < \zeta < \ell, \quad t > 0, \tag{A.16}$$

where $\zeta = 0$ at the lower boundary and $\zeta = \ell$ at the upper boundary, which is equivalent to the height of the tank in lab-scale. The corresponding initial and boundary conditions are

$$T(\zeta, t = t_o) = f(\zeta) \tag{A.17}$$

$$\left.\frac{\partial T}{\partial \zeta}\right|_{\zeta=0} = 0 \tag{A.18}$$

$$\left.\frac{\partial T}{\partial \zeta}\right|_{\zeta=\ell} = 0, \tag{A.19}$$

where $f(z)$ is the initial temperature profile. This heat equation is a PDE, subject to homogeneous boundary conditions. Therefore, the method of separation of variables can be applied directly. Applying the separation of variables, we assume the solution has the form

$$T(\zeta, t) = Z(\zeta)\Gamma(t). \tag{A.20}$$

Substituting this separable form into the PDE gives

$$\frac{1}{Z}\frac{\mathrm{d}^2 Z}{\mathrm{d}\zeta^2} = \frac{1}{\alpha\Gamma}\frac{\mathrm{d}\Gamma}{\mathrm{d}t} = -\lambda^2, \tag{A.21}$$

Then, we obtain the exact solution after implementing the boundary and initial conditions

$$T(\zeta, t) = c_0 + \sum_{n=1}^{\infty} c_n \cos\left(\frac{n\pi}{\ell}\zeta\right) \exp(-\alpha\lambda_n^2 t), \tag{A.22}$$

where the eigenfunction, λ_n, is defined as

$$\lambda_n = \frac{n\pi}{\ell} \tag{A.23}$$

The coefficients, c_0 and c_n, can be found by using Fourier cosine series

$$c_0 = \frac{1}{\ell}\int_{\zeta=0}^{\ell} f(\zeta)\mathrm{d}\zeta, \tag{A.24}$$

$$c_n = \frac{2}{\ell}\int_{\zeta=0}^{\ell} f(\zeta)\cos\left(\frac{n\pi}{\ell}\zeta\right)\mathrm{d}\zeta. \tag{A.25}$$

Cartesian, Convective-Flux BCs

The last analytical model to be presented in this study solves the heat conduction equation in the axial direction in field-scale, as shown in Fig. 4-5(e). The conduction equation in Cartesian coordinates is

$$\frac{\partial^2 T}{\partial \zeta^2} = \frac{1}{\alpha}\frac{\partial T}{\partial t} \quad \text{on} \quad 0 < \zeta < \ell, \quad t > 0. \tag{A.26}$$

The total length, ℓ, is the distance between the ground surface and the lower heat flux boundary. The corresponding initial and boundary conditions are

$$T(\zeta, t = t_o) = f(\zeta) \tag{A.27}$$

$$-k\frac{\partial T}{\partial \zeta}\bigg|_{\zeta=0} = q \tag{A.28}$$

$$-k\frac{\partial T}{\partial \zeta}\bigg|_{\zeta=\ell} = h\Big[T(\zeta = \ell) - T_\infty\Big], \tag{A.29}$$

where $f(\zeta)$ is the initial temperature profile, and $q = q_{geo} = 0.06$ [W/m^2] is the constant heat flux at $\zeta = 0$. T_∞ in this analytical solution correspond to the atmospheric temperature.

At first glance, the governing equation is a homogeneous partial differential equation (PDE), yet both of the boundary conditions are nonhomogeneous. Consequently, the method of superposition is required before applying separation of variables. The purpose of superposition is to break down this transient problem into a transient homogeneous PDE and a steady-state nonhomogeneous ODE. These two problems can then be treated and solved separately by using separation of variables, if needed.

Firstly, a linear shift of the temperature is used to remove the convective nonhomogeneous boundary condition

$$\theta(\zeta, t) = T(\zeta, t) - T_\infty. \tag{A.30}$$

Then, the problem becomes

$$\frac{\partial^2 \theta}{\partial \zeta^2} = \frac{1}{\alpha} \frac{\partial \theta}{\partial t}, \tag{A.31}$$

subject to

$$\theta(\zeta, t = t_o) = f(\zeta) - T_\infty = F(\zeta) \tag{A.32}$$

$$-k \frac{\partial \theta}{\partial \zeta}\bigg|_{\zeta=0} = q \tag{A.33}$$

$$-k \frac{\partial \theta}{\partial \zeta}\bigg|_{\zeta=\ell} = h\theta(\zeta = \ell). \tag{A.34}$$

Secondly, we apply the method of superposition by letting

$$\theta(\zeta, t) = \theta_H(\zeta, t) + \theta_{SS}(\zeta) \tag{A.35}$$

where $\theta_H(\zeta, t)$ and $\theta_{SS}(\zeta)$ are the temperatures in a transient homogeneous problem and a steady-state nonhomogeneous problem, respectively. The transient homogeneous problem is

$$\frac{\partial^2 \theta_H}{\partial \zeta^2} = \frac{1}{\alpha} \frac{\partial \theta_H}{\partial t}, \quad \text{on} \quad 0 < \zeta < \ell, \quad t > 0 \tag{A.36}$$

subject to

$$\theta_H(\zeta, t = t_o) = F(\zeta) - \theta_{SS}(\zeta) = g(\zeta) \tag{A.37}$$

$$\left.\frac{\partial \theta_H}{\partial \zeta}\right|_{\zeta=0} = 0 \tag{A.38}$$

$$\left.-k\frac{\partial \theta_H}{\partial \zeta}\right|_{\zeta=\ell} = h\theta_H(\zeta = \ell), \tag{A.39}$$

and the steady-state problem is

$$\frac{\partial^2 \theta_{SS}}{\partial \zeta^2} = 0, \quad \text{on} \quad 0 < \zeta < \ell, \tag{A.40}$$

subject to

$$\left.-k\frac{d\theta_{SS}}{d\zeta}\right|_{\zeta=0} = q \tag{A.41}$$

$$\left.-k\frac{d\theta_{SS}}{d\zeta}\right|_{\zeta=\ell} = h\theta_{SS}(\zeta = \ell). \tag{A.42}$$

Prior to solving the transient problem, the solution of the steady-state problem can be readily obtained

$$\theta_{SS}(\zeta) = \frac{q}{k}(\ell - \zeta) + \frac{q}{h}. \tag{A.43}$$

The transient problem is then solved by the separation of variables and we obtain

$$\theta_H(\zeta, t) = \sum_{n=1}^{\infty} C_n \cos(\lambda_n \zeta) \exp(-\alpha \lambda_n^2 t), \tag{A.44}$$

where

$$C_n = \frac{\int_{\zeta=0}^{\ell} g(\zeta) \cos(\lambda_n \zeta) \mathrm{d}\zeta}{\int_{\zeta=0}^{L} \cos^2(\lambda_n \zeta) \mathrm{d}\zeta}, \tag{A.45}$$

and the eigenvalue, λ_n, is found by the following transcendental equation

$$\lambda_n \tan(\lambda_n \ell) = \frac{h}{k}, \quad \text{for} \quad n = 1, 2, 3, ... \tag{A.46}$$

It is therefore concluded that the final solution to this problem is

$$T(\zeta, t) = \sum_{n=1}^{\infty} C_n \cos(\lambda_n \zeta) \exp(-\alpha \lambda_n^2 t) + \frac{q}{k}(\ell - \zeta) + \frac{q}{h} + T_\infty, \tag{A.47}$$

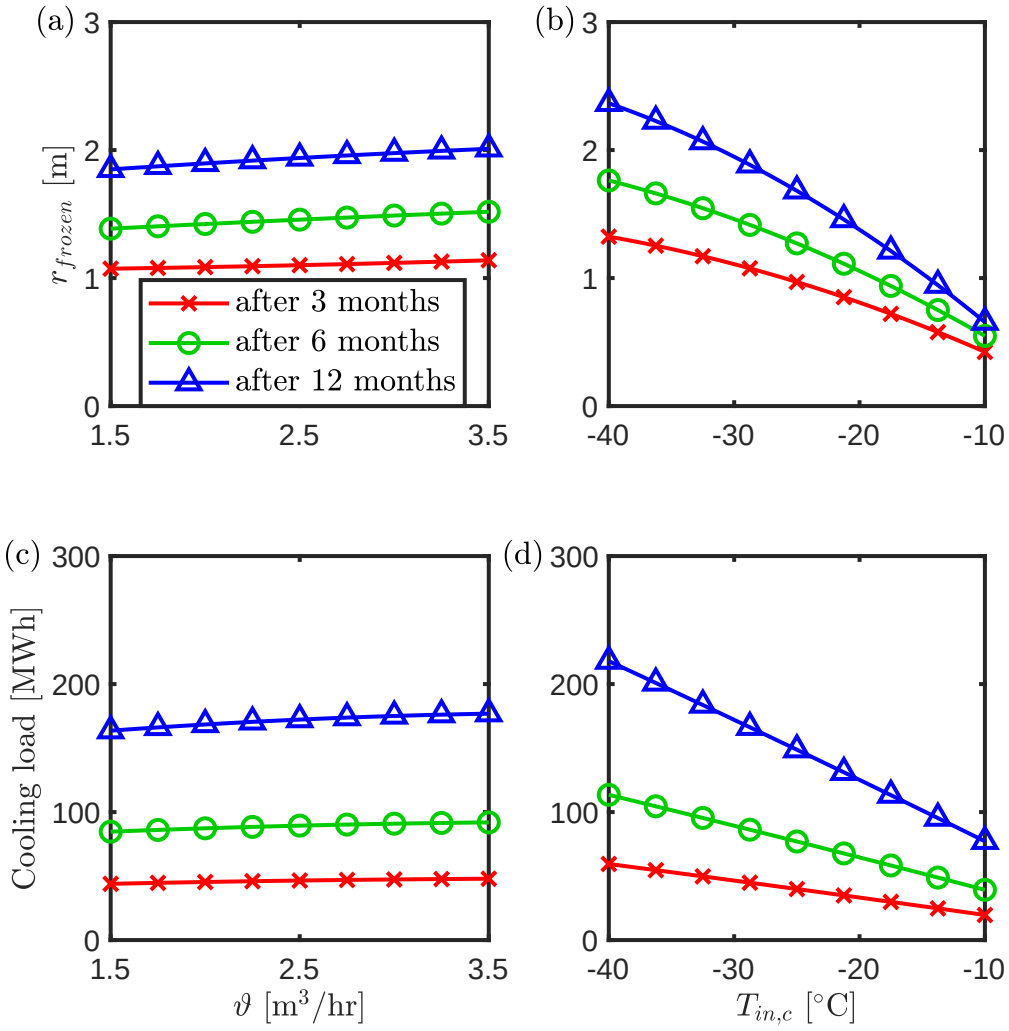

Figure 4-14: The influence of the coolant flow rate (ϑ) and inlet temperature ($T_{in,c}$) on the phase front expansion (r_{frozen}) and cooling load of a single freeze-pipe: a) Phase-front expansion versus coolant flow rate, b) phase-front expansion versus coolant inlet temperature, c) cooling load versus coolant flow rate, and d) cooling load versus coolant inlet temperature.

Bibliography

[1] J. S. Harris, Ground freezing in practice, Thomas Telford, 1995.

[2] H. Tounsi, A. Rouabhi, E. Jahangir, F. Guerin, Mechanical behavior of frozen metapelite: Laboratory investigation and constitutive modeling, Cold Regions Science and Technology (2020) 103058.

[3] M. A. Alzoubi, M. Xu, F. P. Hassani, S. Poncet, A. P. Sasmito, Artificial ground freezing: A review of thermal and hydraulic aspects, Tunnelling and Underground Space Technology 104 (2020) 103534.

[4] H. E. Jamieson, The legacy of arsenic contamination from mining and processing refractory gold ore at Giant Mine, Yellowknife, Northwest Territories, Canada, Reviews in Mineralogy and Geochemistry 79 (1) (2014) 533–551.

[5] M. Alzoubi, S. A. Ghoreishi-Madiseh, A. P. Sasmito, N. Kunz, A. Guimaraes, Renewable energy-based artificial ground freezing as an adaptation solution for sustainability of permafrost in post-climate change conditions, in: IOP Conference Series: Earth and Environmental Science, Vol. 268, IOP Publishing, 2019, p. 12128.

[6] M. Ziegler, Artificial freezing method in geotechnical and tunneling applications, in: Transportation Soil Engineering in Cold Regions, Volume 1, Springer, 2020, pp. 541–549.

[7] A. Mauro, G. Normino, F. Cavuoto, P. Marotta, N. Massarotti, Modeling artificial ground freezing for construction of two tunnels of a metro station in Napoli (Italy), Energies 13 (5) (2020) 1272.

[8] A. Zueter, A. Nie-Rouquette, M. A. Alzoubi, A. P. Sasmito, Thermal and hydraulic analysis of selective artificial ground freezing using air insulation: Experiment and modeling, Computers and Geotechnics 120 (2020) 103416.

[9] B. Wang, C. Rong, H. Cheng, Z. Yao, H. Cai, Research and application of the local differential freezing technology in deep alluvium, Advances in Civil Engineering 2020.

[10] X. Hu, J. Chen, Y. Wang, W. Li, Analytical solution to steady-state temperature field of single-circle-pipe freezing, Rock and Soil Mechanics 34 (3) (2013) 874–880.

[11] X. Hu, L. Zhang, Analytical solution to steady-state temperature field of two freezing pipes with different temperatures, Journal of Shanghai Jiaotong University (Science) 18 (6) (2013) 706–711.

[12] X. Hu, J. Yu, H. Ren, Y. Wang, J. Wang, Analytical solution to steady-state temperature field for straight-row-piped freezing based on superposition of thermal potential, Applied Thermal Engineering 111 (2017) 223–231.

[13] X.-d. Hu, L. Han, Y.-g. Han, Analytical solution to temperature distribution of frozen soil wall by multi-row-piped freezing with the boundary separation method, Applied Thermal Engineering 149 (2019) 702–711.

[14] H. Cai, Z. Liu, S. Li, T. Zheng, Improved analytical prediction of ground frost heave during tunnel construction using artificial ground freezing technique, Tunnelling and Underground Space Technology 92 (2019) 103050.

[15] M. Xu, S. Akhtar, A. F. Zueter, V. Auger, M. A. Alzoubi, A. P. Sasmito, Development of analytical solution for a two-phase stefan problem in artificial ground freezing using singular perturbation theory, Journal of Heat Transfer 142 (12) (2020) 122401.

[16] M. Xu, S. Akhtar, M. A. Alzoubi, A. P. Sasmito, Singular perturbation solution for a two-phase Stefan problem in outward solidification, in: ASME International Mechanical Engineering Congress and Exposition, Vol. 59452, American Society of Mechanical Engineers, 2019, V008T09A050.

[17] H. Cai, S. Li, Y. Liang, Z. Yao, H. Cheng, Model test and numerical simulation of frost heave during twin-tunnel construction using artificial ground-freezing technique, Computers and Geotechnics 115 (2019) 103155.

[18] M. Vitel, A. Rouabhi, M. Tijani, F. Guerin, Modeling heat and mass transfer during ground freezing subjected to high seepage velocities, Computers and Geotechnics 73 (2016) 1–15.

[19] M. Vasilyeva, S. Stepanov, D. Spiridonov, V. Vasil'ev, V. Vasil'ev, Multiscale finite element method for heat transfer problem during artificial ground freezing, Journal of Computational and Applied Mathematics 371 (2020) 112605.

[20] X. Yang, Z. Ji, P. Zhang, J. Qi, Model test and numerical simulation on the development of artificially freezing wall in sandy layers considering water seepage, Transportation Geotechnics 21 (2019) 100293.

[21] G. Newman, L. Newman, D. Chapman, T. Harbicht, Artificial ground freezing: An environmental best practice at Cameco's uranium mining operations in Northern Saskatchewan, Canada, in: 11th International Mine Water Association Congress–Mine Water–Managing the Challenges, 2011, pp. 113–118.

[22] M. A. Alzoubi, A. Nie-Rouquette, A. P. Sasmito, Conjugate heat transfer in artificial ground freezing using enthalpy-porosity method: Experiments and model validation, International Journal of Heat and Mass Transfer 126 (2018) 740–752.

[23] V. R. Voller, C. Prakash, A fixed grid numerical modelling methodology for convection-diffusion mushy region phase-change problems, International Journal of Heat and Mass Transfer 30 (8) (1987) 1709–1719.

[24] M. A. Alzoubi, A. Zueter, A. Nie-Rouquette, A. P. Sasmito, Freezing on demand: A new concept for mine safety and energy savings in wet underground mines, International Journal of Mining Science and Technology 29 (4) (2019) 621–627.

[25] M. A. Alzoubi, A. Nie-Rouquette, S. A. Ghoreishi-Madiseh, F. P. Hassani, A. P. Sasmito, On the concept of the freezing-on-demand (fod) in artificial ground freezing for long-term applications, International Journal of Heat and Mass Transfer 143 (2019) 118557.

[26] Y. Joshi, Reduced order thermal models of multiscale microsystems, Journal of Heat Transfer 134 (3) (2012) 1–11.

[27] R. Ghosh, Y. Joshi, Rapid temperature predictions in data centers using multi-parameter proper orthogonal decomposition, Numerical Heat Transfer, Part A: Applications 66 (1) (2014) 41–63.

[28] V. Zucatti, H. F. S. Lui, D. B. Pitz, W. R. Wolf, Assessment of reduced-order modeling strategies for convective heat transfer, Numerical Heat Transfer, Part A: Applications 77 (7) (2020) 702–729.

[29] C. Ding, X. Cui, R. R. Deokar, G. Li, Y. Cai, K. K. Tamma, An isogeometric independent coefficients (IGA-IC) reduced order method for accurate and efficient transient nonlinear heat conduction analysis, Numerical Heat Transfer, Part A: Applications 73 (10) (2018) 667–684.

[30] B. Yu, G. Yu, Z. Cao, D. Han, Q. Shao, Fast calculation of the soil temperature field around a buried oil pipeline using a body-fitted coordinates-based POD-Galerkin reduced-order model, Numerical Heat Transfer, Part A: Applications 63 (10) (2013) 776–794.

[31] D. Han, B. Yu, Y. Wang, Y. Zhao, G. Yu, Fast thermal simulation of a heated crude oil pipeline with a BFC-Based POD reduced-order model, Applied Thermal Engineering 88 (2014) 217–229.

[32] J. Braun, J. Sousa, G. Paniagua, Numerical assessment of the convective heat transfer in rotating detonation combustors using a reduced-order model, Applied Sciences 8 (6) (2018) 893.

[33] M. Muratori, M. Canova, Y. Guezennec, A spatially-reduced dynamic model for the thermal characterisation of Li-ion battery cells, International Journal of Vehicle Designehicle Design 58 (2-4) (2012) 134–158.

[34] M. Kaviany, Principles of Heat Transfer in Porous Media, Springer Science & Business Media, 2012.

[35] C. R. Swaminathan, V. R. Voller, A general enthalpy method for modeling solidification processes, Metallurgical Transactions B 23 (5) (1992) 651–664.

[36] M. Vitel, A. Rouabhi, M. Tijani, F. Guerin, Thermo-hydraulic modeling of artificial ground freezing: Application to an underground mine in fractured sandstone, Computers and Geotechnics 75 (2016) 80–92.

[37] R. W. Hanks, The laminar-turbulent transition for flow in pipes, concentric annuli, and parallel plates, American Institute of Chemical Engineers Journal 9 (1) (1963) 45–48.

[38] M. A. Ebadian, Z. F. Dong, Forced Convection, Internal Flow in Ducts, in: Handbook of Heat Transfer, Vol. 3, 1998, pp. 5.1–5.137.

[39] R. Shah, A. London, Concentric Annular Ducts, in: Laminar Flow Forced Convection in Ducts, Academic Press, New York, 1978, Ch. XII, pp. 284–321.

[40] A. Bejan, Convection Heat Transfer, John Wiley & Sons, 2013.

[41] Y. A. Cengel, Heat and Mass Transfer: Fundamentals and Applications, 3rd Edition, McGraw-Hill, Boston, 2007.

[42] Government of Canada, Historical Data (2019).
URL https://climate.weather.gc.ca/

[43] M. A. Alzoubi, A. P. Sasmito, Thermal performance optimization of a bayonet tube heat exchanger, Applied Thermal Engineering 111 (2017) 232–247.

[44] M. Faden, A. König-Haagen, D. Brüggemann, An optimum enthalpy approach for melting and solidification with volume change, Energies 12 (5).

[45] P. Nikolaev, M. Shuplik, Low-temperature ground freezing methods for underground construction in urban areas, in: MATEC Web of Conferences, Vol. 265, EDP Sciences, 2019, p. 4020.

[46] G. M. Ali, M. Al-Hussein, A. Bouferguene, Use of finite element analysis for the estimate of freezing & maintenance phase of indirect & direct artificial ground freezing of proposed frozen silt mat, an alternative of timber mat, in: ISARC. Proceedings of the International Symposium on Automation and Robotics in Construction, Vol. 36, IAARC Publications, 2019, pp. 846–853.

[47] Dynalene Inc., Calcium Chloride Series Brines, Tech. rep., Whitehall (2018).
URL https://www.dynalene.com/

Chapter 5

Effect of freeze pipe eccentricity in selective artificial ground freezing applications

Preface

After developing a fast semi-conjugate model in the previous chapter, we employed this model to investigate the effect of freeze-pipe eccentricity which often occurs in selective artificial ground freezing applications due to installation difficulties.

" **A. F. Zueter**, A. G. Madiseh, F. P. Hassani, and A. P. Sasmito. Effect of Freeze Pipe Eccentricity in Selective Artificial Ground Freezing Applications. *ASME Journal of Thermal Sciences and Engineering Applications*, 14(1):011015, 2022. doi.org/10.1115/1.4052595 "

Abstract

Building concentric tubes is one of biggest practical challenges in the construction of freeze-

pipes of selective artificial ground freezing (S-AGF) applications for underground mines. In this study, the influence of tubes eccentricity on phase-front expansion (i.e., expansion of the frozen body) and energy consumption of S-AGF systems is analyzed. A 1+1D semi-conjugate model that solves two-phase transient energy conservation equation is derived based on the enthalpy method. The 1+1D model is firstly validated against experimental data and then verified with a fully-conjugate model from our previous work. After that, the 1+1D model is extended to a field scale of typical underground mines to examine the effect of freeze-pipe eccentricity. The results show that concentric freeze-pipes form the desired frozen ground volume 17% faster than eccentric freeze-pipes. Also, the geometrical profile of the phase-transition-front of the frozen ground is found to be significantly influenced by the freeze-pipe eccentricity. Furthermore, in the passive zone, where S-AGF coolants are isolated from the ground to reduce energy consumption, freeze pipe eccentricity can increase the coolant heat gain by 20%. This percentage can increase up to 200% if radiation heat transfer is minimized.

Contents

5.1 Introduction

Artificial ground freezing (AGF) has been recognized amongst most reliable geotechnical support techniques due to its compatibility with different ground conditions, safe operation,

and environmental advantages over other geothecnical support methods. Nevertheless, AGF is susceptible to some natural and practical challenges [1], [2], [3] that can undermine its operational efficiency such as underground water seepage [4] and high refrigeration load [5], [6]. Selective artificial ground freezing applications (S-AGF) of underground mines (e.g., the Cigar Lake Uranium Mine in Saskatchewan, Canada, and the Banji Coal in Anhui, China) undergo additional difficulties because of their complicated design and profound depth - more than 400 meters deep. The freeze-pipe drill hole of S-AGF systems include a casing pipe, a middle tube, and an inner tube, as shown in Fig. 5-1. Since S-AGF applications target freezing an active zone positioned at a deep level, the upper passive zone is insulated by an air cavity, enclosed by the middle tube and the casing, to minimize the refrigeration load. The inner and middle tubes are typically made up of around 10 meters of piping segments that are connected together. Ideally, the inner and middle tubes are desired to be concentric as shown in Fig. 5-1(a). Nonetheless, in some S-AGF applications, the inner and middle tubes zigzag along the casing depth due to installation difficulties, as shown in Fig. 5-1(b). Practically, the tubes collide with the casing and bend touching the casing tube over a length of around 10 [cm] at the end of each piping segment. The eccentricity of these two tubes negatively impact S-AGF systems because eccentric pipes reduce the heat extraction capacity of the freeze-pipe in the active zone and decrease the insulation efficiency of the air cavity in the passive zone.

The thermal and hydraulic aspects of pipe eccentricity has been addressed in several studies for various applications [7], [8], [9] due to their significant impact. On the hydraulic level, Neto et al. [10] numerically showed that the axial fluid velocity of forced eccentric flow in the larger part of an eccentric annulus is more than twice as large as that of the narrower part for an eccentricity due to the higher flow resistance in the narrower regions. In their analysis of annular eccentric flow in drilling operations, Chang et al. [11] observed lower surge pressure at higher eccentricities. Haciislamoglu and Langlinais [12] reached to a similar conclusion considering non-Newtonian fluids.

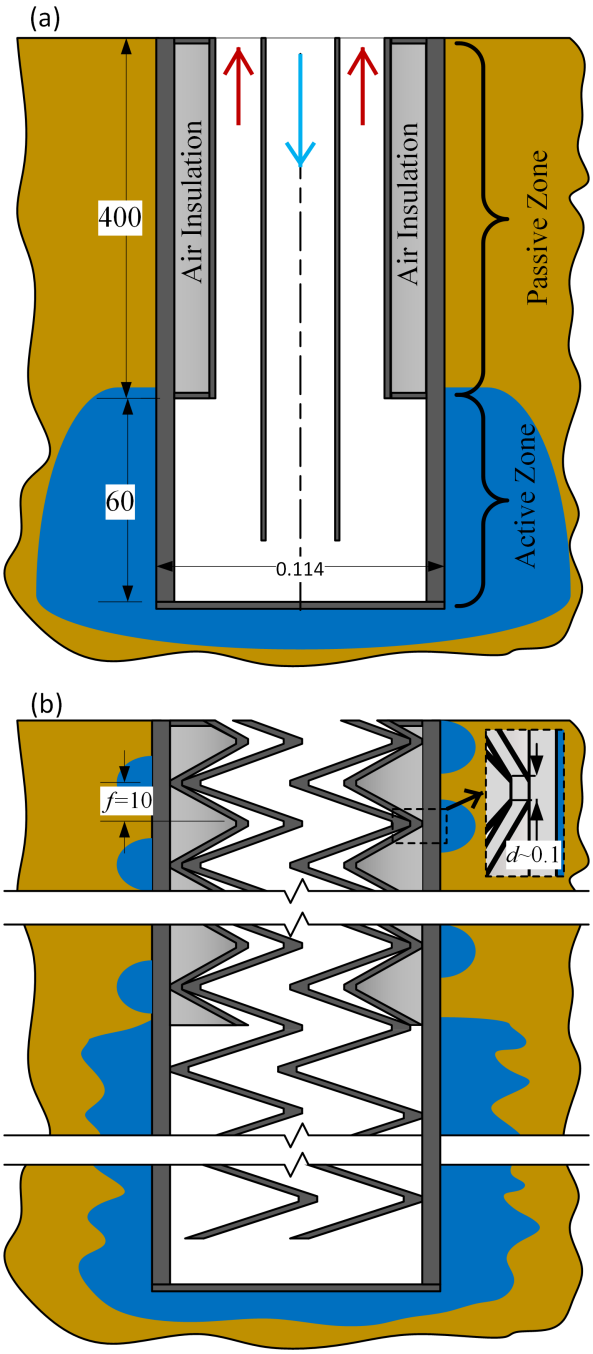

Figure 5-1: Illustration of a) ideal selective artificial ground freezing (S-AGF) pipes and b) eccentric S-AGF pipes. The blue and red arrows represent the coolant inlet and outlet, respectively, whereas the brown and blue colors represent unfrozen ground and frozen ground, resectively. All dimensions in meters (not-to-scale).

On the thermal level, pipe eccentricity was found to be desired and optimized for higher heat transfer rate in some applications. Ali et al. [13] enhanced the heat transfer performance of double-pipe heat exchangers by 223% when shifting the central axis of the inner pipe 40 [mm] away from the central axis of the outer pipe (linear eccentricity of 40 [mm]). Kadivar et al. [14] found that eccentric double-pipe thermal energy storage systems charge the phase change materials (PCM) seven times faster than concentric ones. In general, pipe eccentricity was found to be desirable in applications demanding higher heat transfer rate across the *inner* pipe wall of a double-pipe heat exchangers [15], [16].

On the other hand, pipe eccentricity decreases the convective heat transfer rate across the outer pipe wall. Trombetta [17] analytically determined that the Nusselt number of a completely eccentric annular flow decreases the average Nusselt number at the outer wall by around 70% as compared to concentric flow. Consequently, eccentric pipe design of double-pipe heat exchangers is often avoided when heat transfer is desired at the *outer* pipe wall, such as the double-pipe heat exchangers of AGF and geothermal energy extraction systems [18]. In addition, pipe eccentricity is often not desired when *insulation* is needed at the *inner* pipe wall, as in the design of solar receivers [19], [20].

Despite the evident impact of eccentric flow in many applications, the few studies on S-AGF did not consider the freeze-pipe eccentricity. Vitel et al. [21] and Tounsi et al. [22] et al. derived numerical models to predict ground temperature and displacement in the active zone of S-AGF systems for the case of the Cigar Lake Uranium Mine. Wang et al. [23] derived a thermal mathematical model for S-AGF systems of the Banji Coal Mine assuming Dirichlet boundary condition at the pipe wall. Zueter et al. [24] established the first experimental setup for S-AGF systems considering concentric tubes. A fully conjugate numerical model was also developed in small lab-scale, and an optimum concentric air cavity thickness was scaled. Zueter et al. [25] then derived a reduced-order semi-conjugate model that substantially decreases the computational cost of the large S-AGF systems. The reduced order model accurately predicts the non-uniform heat extraction capacity by the freeze-pipe

taking into account the thermal development of the coolant temperature and boundary layer.

This study aims to develop a deeper understanding on how pipe eccentricities affect the performance of S-AGF systems, namely the frozen ground expansion and energy consumption. Thus, a computationally efficient 1+1D semi-conjugate numerical model that solves a transient two-phase energy conservation equation is developed based on the enthalpy method for the case of eccentric freeze-pipe. After that, phase-transition-front profile and energy consumption of S-AGF systems that include eccentric tubes are compared with those of concentric ones. The main findings will then be highlighted and discussed.

5.2 Experimental Setup

An experimental and numerical study from our previous work [24] will be employed to validate and verify our semi-conjugate 1+1D mathematical model, which will be employed in modeling large S-AGF systems in field scale. This study is chosen as it is the only fully controlled experiment of S-AGF systems available in the literature. The experimental setup is a well-insulated tank that comprises a fully saturated ground and a freeze pipe, as shown in Fig. 5-2. The ground is equipped with several thermocouples to monitor its temperature at different locations. A coolant enters the freeze pipe through the central tube. The coolant then extracts heat from the ground and exits through the annular gap between the air chamber and the central tube. Elaborate details on the experimental setup, flow control, and thermophysical properties can be found in our previous work [24].

5.3 Mathematical Model

The mathematical model of this study is based on solving a transient two-phase energy conservation equation employing the enthalpy method. In this study, the effect of freeze-pipe eccentricity is compared with ideal concetric pipes; accordingly, mathematical description of both models are provided .

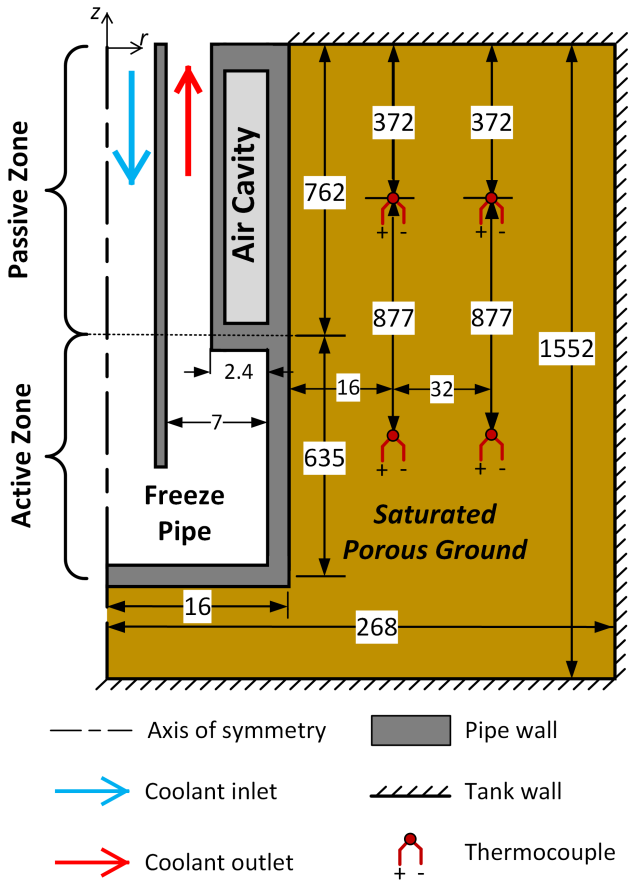

Figure 5-2: Experimental setup developed in our previous work[24]. All units are in [mm] (not-to-scale)

5.3.1 Governing Equations

The computational domain is occupied by saturated porous ground, as shown in Fig. 5-3. The local thermal equilibrium (LTE) assumption between the sand particles and the water content assumption is valid in this study [24], [26]. Accordingly, heat conduction equation in the ground can be modeled using the enthalpy method as

$$\frac{\partial H}{\partial t} = \nabla \cdot (k \nabla T), \tag{5.1}$$

where the ground enthalpy, H, is a function of the porous ground temperature, T, as [27], [28]

$$H = (1-\gamma) \int_{T_{ref}}^{T} (\overline{\rho c_p})_f \; dT_g + \gamma \int_{T_{ref}}^{T} (\overline{\rho c_p})_u \; dT + \phi \gamma \rho_{wt} L_{wt}, \tag{5.2}$$

where subscripts u, f, wt, and ref, refer to unfrozen ground, frozen ground, water and an arbitrary reference temperature, respectively, whereas ϕ is the ground porosity. The liquid fraction, γ, is assumed to change linearly between the solidus temperature T_{sol} and the liquidus temperature T_{liq} as

$$\gamma = \begin{cases} 0 & , \; T < T_{sol}; \\ \dfrac{T - T_{sol}}{T_{liq} - T_{sol}} & , \; T_{sol} \leq T \leq T_{liq}; \\ 1 & , \; T > T_{liq} \end{cases} \tag{5.3}$$

The solidus temperature, T_s, and liquidus temperature, T_ℓ are set at 272.65 [K] and 273.15 [K] as per the experimental measurements of Zueter et al. [24]. The parallel arrangement approach [29] is selected to calculate equivalent thermal conductivity since it accurately predicts the measured thermal conductivity of the experimental study [24]. Thus, the thermal conductivity is based on the porosity, ϕ, and the liquid fraction, γ, as

$$k = \gamma \; k_u + (1-\gamma) \; k_f. \tag{5.4}$$

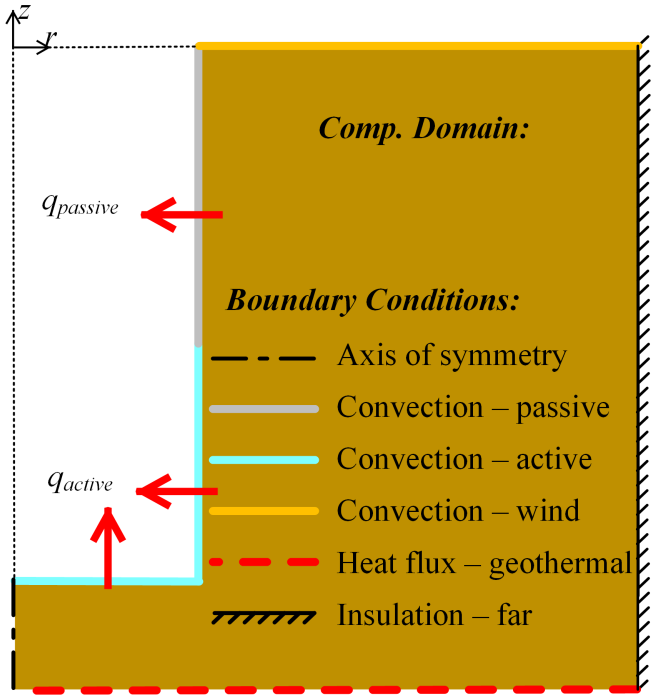

Figure 5-3: Computational domain (saturated porous ground) and boundary conditions of the present study. The red arrows indicate the direction of heat transfer in the active and passive zones.

5.3.2 Initial and Boundary Conditions

Initial Conditions

The initial condition is approximated to be constant as

$$T(t=0) = T_o, \tag{5.5}$$

where $T_o = 7[^{\circ}\mathrm{C}]$ according to field measurements [21].

Boundary Conditions

The computational domain is enclosed by air from the top and geothermal heat flux from the bottom. Accordingly, atmospheric convection at the top boundary is considered as [30]

$$-k\frac{\partial T}{\partial n}\bigg|_{top\ wall} = h_{atm}(T_{top\ wall} - T_{amb}), \tag{5.6}$$

where n is a normal vector to the boundary [30]. The atmospheric heat transfer coefficient, h_{atm}, is estimated at an average value of 3 [W/(m^2·K)] using field measurements of ground surface temperature and air temperature [31]. The ambient temperature, T_{amb}, data [32] is curve-fitted by a sinusoidal function starting from the beginning of the year 2018 as follows

$$T_{atm} = 267 - 21.3\cos(2\times10^{-7}t) - 1.7\sin(2\times10^{-7}t) \tag{5.7}$$

The bottom boundary is subject to a geothermal heat flux of 0.06 [W/m^2] [30]

$$-k\frac{\partial T}{\partial n}\bigg|_{geothermal\ flux} = q, \tag{5.8}$$

Freeze-Pipe Convection Boundary

This subsection is dedicated to discuss and evaluate the convective boundary condition along the outer wall of the casing.

Mathematical modeling of the heat extraction along the freeze pipe wall should include the effect of the freeze pipe eccentricity especially in field-scale. A more accurate modeling of heat extraction of eccentric tubes can be captured in a 3D model since heat flux varies in the angular and axial directions (i.e., $q = f(z,\theta)$). Though a 3D model could be more accurate, simulating 3D models would be computationally expensive especially in field-scale where the computational domain is large (in the order of hundreds of meters) and operational time is long (several years). To avoid that, the angular asymmetry of the heat flux of an eccentric freeze-pipe is averaged over the freeze-pipe angular perimeter as

$$\bar{q}(z) = \frac{1}{2\pi}\int_0^{2\pi} q(z,\theta)d\theta \tag{5.9}$$

Thus, by introducing the averaged heat flux $\bar{q}$, the problem is simplified to an axi-symmetric

2D model.

Heat extraction by the freeze pipe in the passive zone is different from that of the active zone due to the existence of air insulation in the passive region. First, mathematical modeling of the heat extraction in the passive zone is presented. In this zone, the thermal resistance of the air chamber ($O(0.1-1)$) dominates over the convective thermal resistance of the coolant ($O(0.01)$) and conductive thermal resistances of steel tubes ($O(0.001)$). As a consequence, the temperature of the inner wall of the air cavity, T_{in}, is approximated to be equal to the coolant temperature, $T_{c,passive}$. Additionally, the boundary temperature along the outer wall of the casing, $T_{w,passive}$, is approximated to be equal to the outer wall temperature of the air cavity, T_{out}. In other words, the coolant temperature and boundary temperature in the passive zone are approximated as

$$T_{w,passive} \approx T_{out} \tag{5.10}$$

$$T_{c,passive} \approx T_{in} \tag{5.11}$$

Throughout this study, the aspect ratio of the air cavity (height to width ratio of the air chamber) is extremely high. In such cases, the influence of convection is negligible [33]. The heat transfer rate per unit length is then governed by conduction and radiation as

$$\bar{Q}_{passive} = \underbrace{S \cdot k_a \cdot (T_{out} - T_{in})}_{conduction} + \underbrace{\pi D_{in} \varepsilon \sigma (T_{out}^4 - T_{in}^4)}_{radiation}. \tag{5.12}$$

where D_{in} is the inner diameter of the air cavity. For ideal concentric freeze-pipes, the conduction shape factor, S, is given as [30]

$$S = \frac{2\pi}{ln(D_{out}/D_{in})}. \tag{5.13}$$

On the other hand, the conduction shape factor of eccentric air cavities is given as [30]

$$S = 2\pi \cdot \cosh^{-1}\left(\frac{D_{in}^2 + D_{out}^2 - 4\zeta^2}{2 \cdot D_{in} \cdot D_{out}}\right), \tag{5.14}$$

where linear eccentricity, ζ, is the absolute distance between the center of the middle tube and the center of the casing. Heat flux along the outer wall of the casing can be obtained from Eqn. (5.12) as

$$\begin{aligned} \bar{q}_{passive} &= \underbrace{\frac{S \cdot k_a}{\pi(D_{out} + 2\delta)} \cdot (T_{out} - T_{in})}_{conduction} + \underbrace{\frac{D_{in}}{D_{out} + 2\delta}\varepsilon\sigma(T_{out}^4 - T_{in}^4)}_{radiation} \\ &= U_{passive}(T_{out} - T_{in}), \end{aligned} \tag{5.15}$$

where D_{out} is the outer diameter of the air cavity and δ is the thickness of the casing. The combined heat transfer coefficient, $U_{passive}$, can now be derived from Eqn. (5.15) as

$$U_{passive} = \underbrace{\frac{S \cdot k_a}{\pi(D_{out} + 2\delta)}}_{conduction} + \underbrace{\frac{D_{in}}{D_{out} + 2\delta}\varepsilon\sigma(T_{out}^2 + T_{in}^2)(T_{out} + T_{in})}_{radiation}. \tag{5.16}$$

Employing Eqns. (5.10,5.11,5.15,5.16), heat extraction per unit area of the boundary wall (outer wall of the casing) in the passive zone can be expressed as

$$\bar{q}_{passive} = U_{passive}(T_{w,passive} - T_{c,passive}) = -k\left.\frac{\partial T}{\partial n}\right|_{w,passive} \tag{5.17}$$

Moving to the active zone located at lower part of the ground, heat extraction is driven by the convection of the annular flow of the coolant. The Nusselt number for a laminar flow in concentric and eccentric annular ducts is determined analytically in the literature for a wide range of diameter ratios [34], [35]. In this study, these correlations are employed to determine the Nusselt number for concentric and eccentric pipes. In regards to concentric ones, the influence of the thermal entrance length of the flow is found to be significant; consequently, Nusselt data [34] for thermally developing flows inside concentric annular ducts are also

employed. Elaborate details on concentric tubes modeling can be found in our previous work [25].

Nonetheless, since the freeze pipes in field-scale are highly eccentric, a different Nusselt correlation is used to take into account the reduction of the Nusselt number due to the eccentricity. In particular, a Nusselt correlation is curve-fitted based on analytical solutions of laminar flows inside eccentric annular ducts as per the the analytical study conducted by Michael and Trombetta [17]. Given a diameter ratio of 0.3125, the averaged Nusselt number for a thermal *developed* annular flow relies on the eccentricity, e, as

$$\overline{Nu}_{developed\ flow} = 3.4e^2 - 6.6e + 4.9, \tag{5.18}$$

where e is defined as

$$e = d_i/(R_o - R_i) \tag{5.19}$$

where d_i is the absolute distance between the center of the inner tube and the center of the casing while R_o and R_i are the radii of the casing and inner tube, respectively, as displayed in Fig. 5-1. Following Eqn. (5.20), the heat transfer coefficient in the active zone is inversely proportional to the eccentricity, as can be seen from Fig. 5-4.

Zueter et al. [25] found that the thermal development of the thermal boundary layer is highly significant on the Nusselt number of the annular flow. On average, the Nusselt number was determined to be around 50% higher across the depth of the active zone in field-scale simulations. Since the eccentricity along the active zone is continuously changing, the thermal boundary layer keeps developing. Consequently, the Nusselt number calculated by Eqn. (5.20) is multiplied by 1.5 as a correction factor to consider the impact of the thermal development of the flow as

$$\overline{Nu}_{developing\ flow} = \frac{h_{active} l}{k_c} \approx 1.5\overline{Nu}_{developed\ flow} \tag{5.20}$$

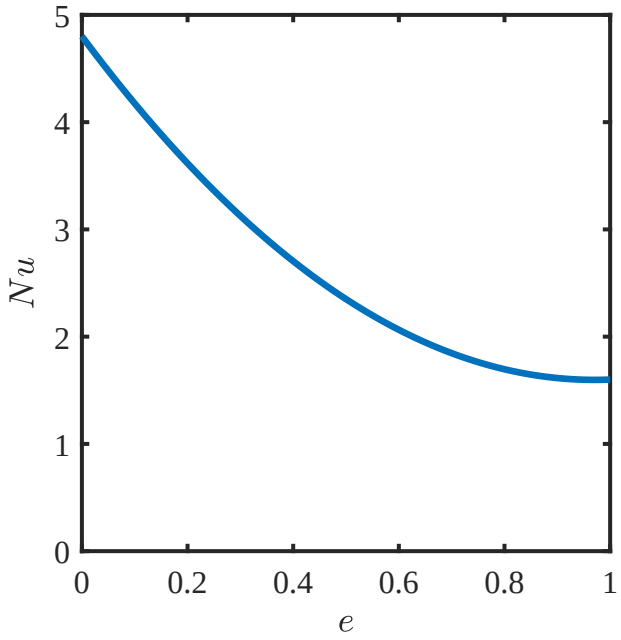

Figure 5-4: Variation of the thermally developed Nusselt number as a function of the freeze-pipe eccentricity in the active zone.

The heat extraction per unit area of the outer wall of the casing in the active zone can now be calculated as [30]

$$\bar{q}_{active} = h_{active}(T_{w,active} - T_{c,active}) = -k\frac{\partial T}{\partial n}\bigg|_{w,active} \tag{5.21}$$

Now that heat extraction by the freeze pipe in the passive and active zones are modeled, the increase in the coolant temperature is formulated. The coolant temperature, T_c, written in Eqn. (5.17,5.21) increases as more heat is extracted from the ground. A semi-conjugate model is derived, based on the first law of thermodynamics, to calculate the coolant heat gain per unit length of the freeze-pipe as

$$\Delta T_c = \frac{\pi D_w \cdot \bar{q}}{\dot{m}_c \cdot c_{p,c}}, \tag{5.22}$$

where the heat flux, q, is obtained from Eqns. (5.17,5.21) and D_w is the diameter of the boundary wall (outer wall of the casing).

5.4 Solution of Mathematical Model

Numerous analytical [36], [37], [38] and numerical [39], [40], [41] solution methodologies were developed in the literature of AGF to solve the governing equations and boundary conditions. In this study, we employ A 1+1D semi-conjugate numerical algorithm equipped with spatial correction in the axial direction developed in our previous work [25] due to its high computational efficiency especially for field-scale S-AGF systems. In this section, the solution algorithm is firstly presented. Then, the numerical solution methodology and choice of numerical parameters are illustrated.

5.4.1 Solution Algorithm

A reduced-order semi-conjugate algorithm developed from our previous work [25] is used in this study to reduce the expensive computational costs of the problem due to the large computational domain and long operational time of S-AGF applications. This algorithm can reduce the computational time of the large S-AGF application study by 99% while accurately predicting the ground phase transition front profile and heat extraction by the freeze-pipe[25].

The 1+1D algorithm is based on reducing a 2D grid into multiple 1D grid lines which are solved separately following a particular order. In some 1+1D models, the influence of axial conduction parallel to the freeze-pipe is negligible and can be ignored to further enhance the computational speed. Nevertheless, axial conduction is considered in this study due to the freeze-pipe eccentricity which results in significant axial temperature diffusion. Thus, axial and radial conduction are calculated separately and then are added together to find the temperature at each computational node. The 1+1D algorithms that include axial conduction are described in great details in our previous work [25].

5.4.2 Numerical Solutions Methodology

The enthalpy is expressed in an intergral form as shown in Eqn. (5.2). This expression is approximated by a piece-wise function [25], [28]. After that, the discretized point-form of the governing equations and boundary conditions are written as

$$b_i(H_i - H_i^{old}) = c_{i-1}T_{i-1} + c_iT_i + c_{i+1}T_{i+1}, \tag{5.23}$$

where the subscripts of the above equation denote node locations and the superscript *old* refer to the previous time-step. The coefficients c and b are derived from discretizing the equations. First and second order accurate schemes were adapted in descritizing the transient and spatial variations, respectively.

The linearized enthalpy algorithm, created by Swaminathan and Voller [27], is chosen to solve Eqn. (5.23). This algorithm linearizes Eqn. (5.23) by writing the enthalpy field in terms of the temperature field using a truncated Taylor's series. Then, the linear system of equations is solved implicitly by calculating the inverse of a matrix using the LU decomposition method. Finally, convergence is reached when the maximum temperature difference between two successive iterations drop to below 1E-5 [K], implying that the enthalpy field is consistent with the temperature field. Elaborate details on the numerical algorithm can be found in [25], [27].

5.4.3 Choice of Numerical Parameters

MATLAB codes are developed to generate the mesh and compute the solution. Mesh independence and time step independence studies are conducted to ensure the accuracy of the solution. A mesh count of more than 11,000 nodes and time step of 6 minutes are chosen in lab scale. Nevertheless, a mesh count of more than 45,000 nodes and a time step of 1 day are used in field-scale.

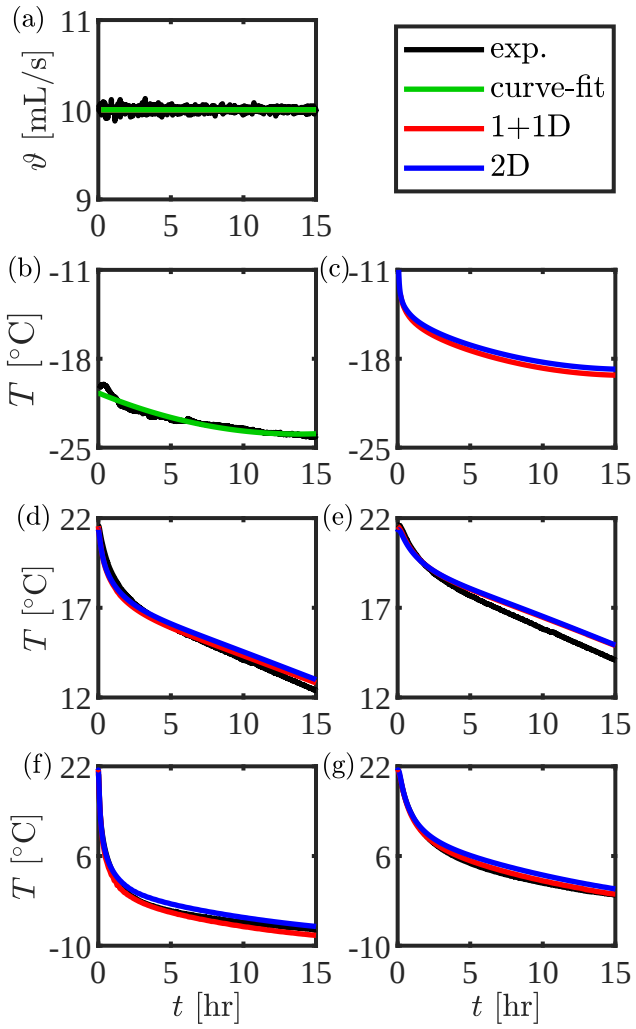

Figure 5-5: Validation and verification of the 1+1D semi-conjugate model against experimental data [24] and with a 2D fully conjugate model from our previous work [24]: a) Coolant inlet flow rate, b) coolant inlet temperature, c) coolant outlet temperature d) ground temperature 31.75[mm] from the central axial in the passive zone e) ground temperature 63.5[mm] from the central axial in the passive zone, f) ground temperature 31.75[mm] from the central axial in the active zone, g) ground temperature 63.5[mm] from the central axial in the active zone. exact location of the thermocouples can be found in [24].

5.5 Results and Discussion

Firstly, the 1+1D semi-conjugate model is validated against experimental measurements [24] and then further verified with a fully conjugate model from the literature in lab-scale [24]. After that, the model is extended to a field scale, and the influence of tubes eccentricity is examined

5.5.1 Validation & Verification

The 1+1D semi-conjugate mathematical model is validated against an experimental study from our previous work[24]. The phase-transition-front profile of our present semi-conjugate model has also been verified with a fully conjugate model [24].

In order to simulate the insulated experimental setup condition, the boundary conditions along the tank walls are adjusted as

$$\left.\frac{\partial T}{\partial n}\right|_{tank\ wall} = 0. \tag{5.24}$$

Additionally, the initial temperature is set at 21.5 [°C] in agreement with the experimental study. The coolant inlet temperature and flow rate are given in Fig. 5-5(a) and Fig. 5-5(b), respectively. All details on the geometry and material properties can be found in [24].

As can be seen from Fig. 5-5, the ground temperature calculations of the 1+1D mathematical model agree well with the experimental data. In fact, the 1+1D model predicts ground temperature and coolant outlet temperature with the same level of accuracy as that of the 2D fully conjugate model.

In addition to the transient ground temperature, the phase-transition-front profile ($T = 0$[°C] isotherm) of the 1+1D semi-conjugate model is verified with that of the fully-conjugate 2D model [24], as shown in Fig. 5-6. Other isotherms are also shown in the same contour plot to further ensure the accuracy of the 1+1D model. The predicted phase-transition-front profile, as well as other isotherms, of the 1+1D model are consistent with that of the fully-

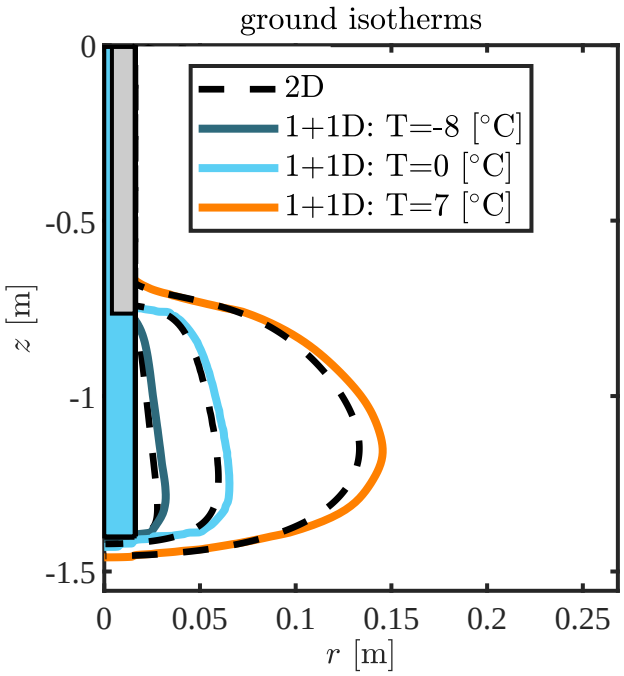

Figure 5-6: Lab-scale verification of the isotherms of the 1+1D semi-conjugate model with a 2D fully-conjugate model from our previous work [24]. The blue and gray boxes refer to the coolant and air insulation, respectively (the thickness of the air is not-to-scale)

conjugate 2D model. As the 1+1D model has proven to be reliable, it is used in this study due to its computational efficiency.

5.5.2 Influence of Eccentricity in Field-Scale

In this section, we investigate the impact of freeze-pipe eccentricity. Field-scale freeze-pipes extend to a depth of 460 meters, as shown in Tab. 5.1. The passive zone occupies more than 85% of the freeze-pipe length, making up the top 400 meters. The active zone extends for 60 meters below the active zone, as shown in Fig. 5-1.

A single type of rocks is observed in the passive zone as can be seen from Tab. 5.2 whereas three different types of rocks occupy the active zone. The thermophysical properties and porosity are set as per Tab. 5.3 and Tab. 5.2, respectively.

In this section, two different field-scale simulations were considered to understand and investigate the effect of freeze-pipe eccentricity. In subsection 5.5.2, the side boundary (col-

ored in black in Fig. 5-3) is set at a distance of 30 meters from the central axis of the pipes in order to ensure a boundary independent simulations which clearly illustrate the effect of freeze-pipe eccentricity on the phase-transition-front profile. In subsection 5.5.2, the side boundary distance is reduced to 3 meters which is typically half the distance between two freeze-pipes in fields scale.

Table 5.1: Geometry of a typical field-scale freeze-pipe as used in this study.

property	value
Active zone height	60 [m]
Passive zone height	400 [m]
Inner tube inner diameter	26.92 [mm]
Inner tube outer diameter	31.75 [mm]
Middle tube inner diameter	62 [mm]
Middle tube outer diameter	73.03 [mm]
Casing inner diameter	101.6 [mm]
Casing outer diameter	114.3 [mm]

Table 5.2: Position, porosity, and volumetric latent heat content of three types of soil making up the computational domain in field scale of S-AGF systems, such as that of the Cigar Lake Uranium Mine. z_{top} and z_{bottom} represent the position of the top and bottom limits of each type of soil ($z = 0$ is the top of the computational domain representing the ground surface as shown in Fig. 5-3).

Material	$z_{top} \rightarrow z_{bottom}$ [m]	ϕ [-]	$\phi\rho_{wt}L_{wt}$ [J/m^3]
Soil-1	$0 \rightarrow -428$	6%	2.03E7
Soil-2	$-428 \rightarrow -440$	15%	5.07E7
Soil-3	$-440 \rightarrow -500$	4%	1.35E7

Boundary-Independent Modeling

The 1+1D semi-conjugate model is modeled in field scale to examine the effect of freeze pipe eccentricity on the phase-transition-front profile in the active zone and coolant heat gain in the passive zone. Particularly, an eccentric freeze pipe that zigzags as shown in Fig. 5-1 is

Table 5.3: Thermophysical properties of the three types of soil in Tab. 5.2.

Material	$\overline{\rho c_p}$ [J/m^3/K]	k [W/m/K]
Frozen soil-1	1.42E6	3.87
Unfrozen soil-1	1.51E6	3.58
Frozen soil-2	1.57E6	2.63
Unfrozen soil-2	1.81E6	2.15
Frozen soil-3	1.33E6	2.49
Unfrozen soil-3	1.39E6	2.36

compared with an ideal concentric freeze pipe. Typical tubes geometry of AGF freeze pipes is considered in this study as listed in Tab. 5.1. In this subsection, the side boundary of the ground is set at a distance of 30 meters away from the pipes to clearly visualize the effect of the freeze-pipe eccentricity on the phase-transition-front profile. As shown in Fig. 5-1, a zigzag interval is completed every 10 meters ($f = 10$ [m]), and the inner pipes collide and stick with the casing pipe over a distance of 10 [cm] ($d = 10$ [cm]) at the end of each zigzag interval.

The phase-transition-front profile of concentric pipes is significantly different from that of eccentric ones, as can be seen from Fig. 5-7. In the case of concentric pipes, the phase transition front is only formed in the active zone due to air insulation in the passive zone. The non-uniformity of the phase-transition-front profile in the active zone is attributed to the different types of rocks occupying this area, especially the latent heat content which is proportional to the porosity. The phase-transition-front therefore extends to a lesser extent in the middle of the active zone due to the higher porosity of the rocks in this region, as indicated in Tab. 5.2.

Unlike the results of concentric pipes, frozen ground is formed throughout the freeze-pipe length in the case of eccentric pipes - in the active and passive zones. This implies that the air insulation capacity in the case of eccentric pipes is less than that of concentric ones, resulting in higher heat dissipation from the ground to the coolant and consequently freezing the ground in the passive zone. Furthermore, the zigzag behavior of phase-transition-front

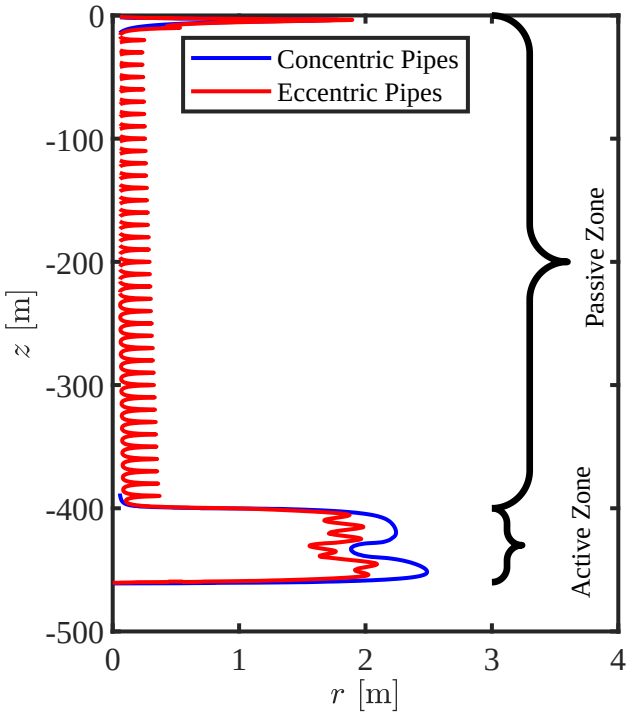

Figure 5-7: Field-scale comparison of the phase-transition-front profile considering eccentric and concentric freeze-pipes after six months of operation. $r = 0$ represent the central axis of the pipes, and $z = 0$ is the ground surface, as shown in Fig. 5-3.

profile of eccentric pipes reflects the zigzag behavior of the pipes in Fig. 5-1(b). The phase-transition-front zigzags every 10 meters in Fig. 5-7, which is in agreement with our defined zigzag interval in the model as per Fig. 5-1(b).

Overall, the phase-transition-front expansion of eccentric tubes is found to be around 16% smaller than that of concentric ones, as shown in Fig. 5-7. Specifically, after six months of operation, the minimum frozen ground extent of eccentric pipes is 1.6 [m] whereas that of concentric pipes is 1.9 [m] (as measured from the central axis of the casing). This is attributed to the inversely proportional relationship between the eccentricity and Nusselt number (see Eqn. (5.20)). Lower Nusselt number of eccentric tubes, as compared with concentric ones, indicate a lower heat transfer coefficient and consequently lower heat flux at the pipe wall, as can be depicted from Fig. 5-8(a).

Secondly, in the passive zone where freeze pipe isolation is desired, the total heat gain

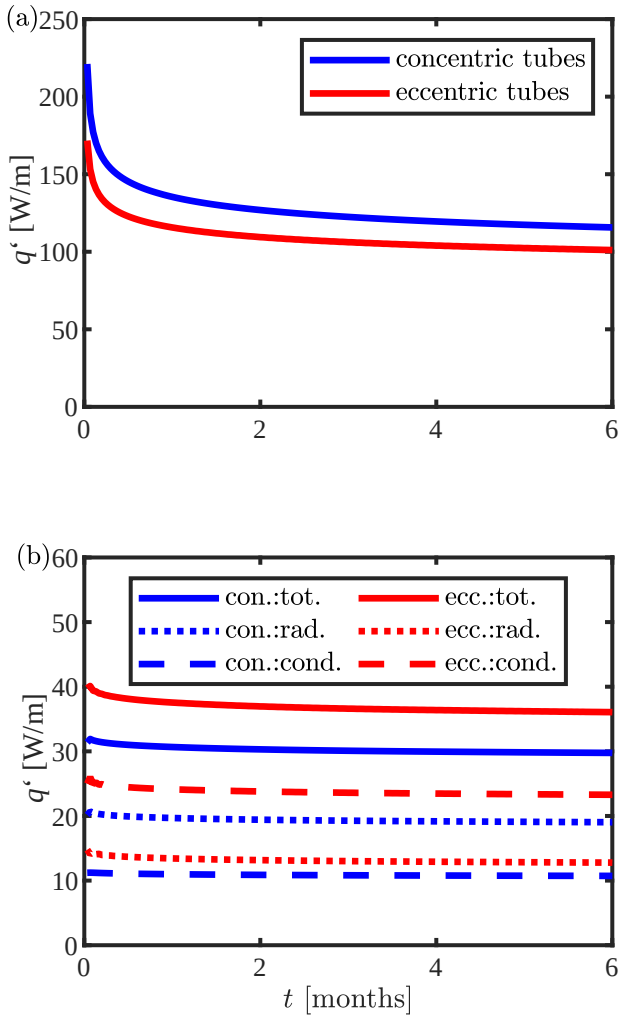

Figure 5-8: Field-scale comparison of heat extraction from concentric and eccentric freeze pipes in a) the active zone and b) the passive zone.

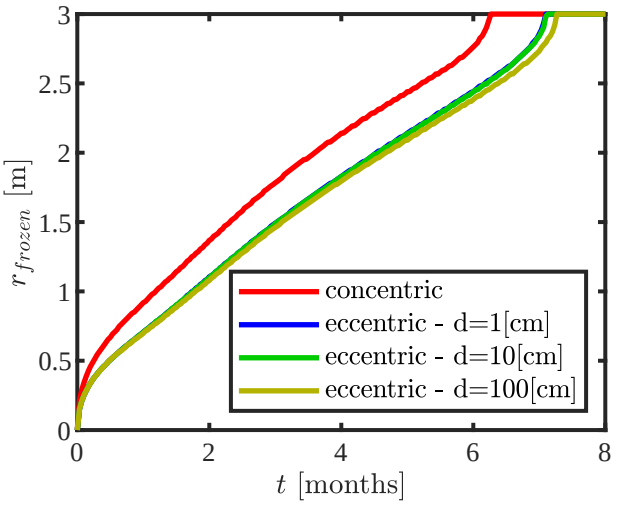

Figure 5-9: Closure time considering a distance of 3 [m]. r_{frozen} is the frozen ground radius in the active zone.

of the coolant of eccentric freeze pipe is around 20% larger than that of concentric one, as can be seen from Fig. 5-8(b). A closer examination on the various heat transfer mechanisms reveals that conductive heat transfer of eccentric pipes is more than twice that of concentric ones. Nonetheless, the better insulation of concentric freeze-pipe results in a higher temperature difference between the walls of the air cavity and consequently higher radiation heat flux. Radiation heat transfer is significant in this study because of the high emissivity of the freeze pipe walls ($\varepsilon = 0.9$). If the emissivity is lower, the effect of radiation heat transfer becomes less significant, and conductive heat transfer dominates. In such a case, total heat gain of eccentric freeze pipe can be two times higher than that of concentric ones. Achieving such low pipe emissivity requires pipe coating with low emissive materials; nevertheless, deeper techno-economic analysis would be needed to investigate the feasibility of coating pipes extending for more than 400 meters.

Closure Time & Energy Consumption Analysis

In field condition, multiple adjacent freeze-pipes work together in order to freeze the ground. Typically, the pipes are separated by a distance of 6 meters from each other; consequently,

each pipe is required to freeze a radial distance of 3 meters. In this subsection, the side boundary (colored in black in Fig. 5-3) is thus set at a distance of 3 meters in order to mimic field conditions and evaluate the closure time - the time at which the desired radial distance (3 meters) is frozen in the active zone.

The ground freezing duration of concentric pipes is found to be one month shorter than that of eccentric pipes, as can be seen from Fig. 5-9. This is attributed to the higher heat extraction capacity of concentric pipes in the active zone, as discussed in Fig. 5-8. Fig. 5-9 also indicates that the colliding distance of the inner pipes with the casing (d in Fig. 5-3) has a negligible effect in the range of 1$\sim$10 centimeters as their closure time is identical. Nevertheless, the closure time is slightly delayed by a few days when $d = 1$[m]. Overall, the results clearly demonstrate the superior performance of ideal concentric pipes as compared with eccentric ones in regards to freezing duration of the active zone.

We will end this discussion by highlighting the overall energy consumption by each freeze-pipe in the active and passive zones. In the active zone, energy extracted by the freeze-pipe is around 3 [MWh] higher than that of eccentric pipes as shown in Fig. 5-10(a). Noting that there are hundreds of freeze-pipes in AGF plants, the total energy extracted in a period of six months can reach more than 1 [GWh], which can cause long delays in creating the frozen ground and thereby completing the construction of the mine. Such delays are undesirable in AGF applications of the mining industry as they can cause substantial economic losses.

In the passive zone where coolant insulation is desired, freeze-pipe eccentricity is found to increase heat dissipation by 18-50%, as shown in Fig. 5-10(b). Particularly, when d is in the range of $1 \sim 10$ [cm], heat dissipation of eccentric pipes is higher by 18% than that of concentric pipes. This percentage increases up to 50% if $d = 100$ [cm]. Overall, Heat gained by the coolant in the passive zone dominates over that of the active zone since the passive zone (400 meters long) is more than 8 times longer than the active zone (60 meters long). Ultimately, building concentric freeze-pipes can significantly minimize heat gained by the coolant in the passive zone, especially if radiation heat transfer is minimized as discussed at

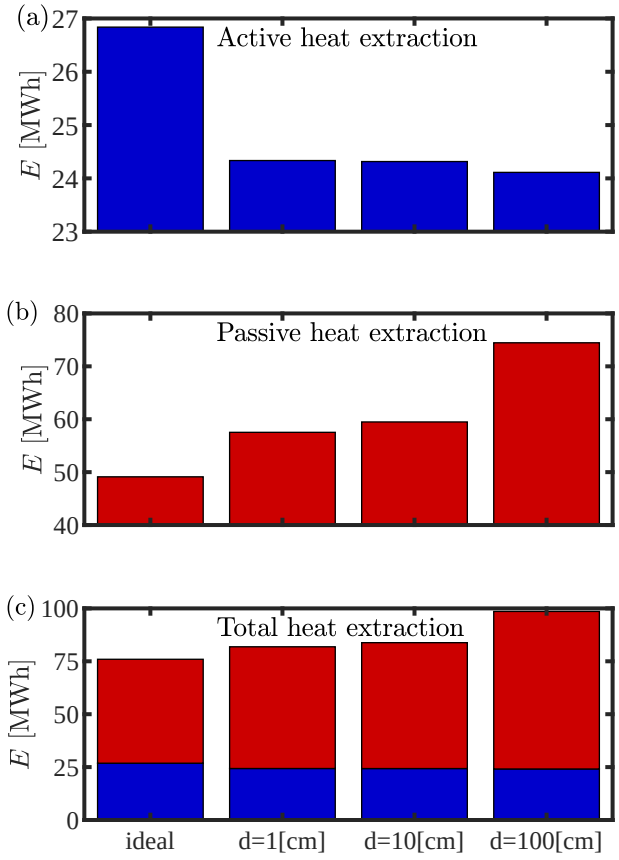

Figure 5-10: Energy extracted by a single freeze pipe in a) the active zone, b) the passive zone, and c) the entire freeze pipe (both active and passive zones) for a period of six months. The red and blue rectangles refer to energy extraction from the ground in the passive and active zones, respectively.

the end of Sec. 5.5.2.

5.6 CONCLUSION

This study examines the influence of freeze-pipe eccentricity on the phase-transition-front expansion and energy consumption of artificial ground freezing (AGF) systems. To this end, a 1+1D semi-conjugate model with a spatial correction in the axial direction is developed. This model solves a series of 1D transient two-phase conduction equation numerically. The transient ground temperature is validated against experimental data from the literature. Then, the coolant temperature and ground phase-transition-front are further verified with a fully-conjugate model from the literature.

The results show that freeze-pipe eccentricity can significantly affect the phase-transition-front profile of the frozen ground expansion, as well as the energy consumption of AGF systems. In the active zone where ground freezing is desired, the freeze-pipe eccentricity profile within the freeze pipe clearly reflects on the profile of the phase-transition-front. Furthermore, freeze pipe eccentricity lengthened the duration of the ground freezing process by 17%. Secondly, in regards to selective artificial ground freezing (S-AGF) applications, the coolant heat gain in the passive zone (where freeze-pipe isolation is desired) is around 20% larger in the case of eccentric freeze-pipe as compared with that of concentric one. However, this percentage can rise to more than 200% if radiation heat transfer is minimized.

In our future work, we aim to conduct a statistical study that examines the uncertainty of eccentric freeze-pipes geometry, such as the uncertainity of the collision distance between the pipes and the pipes orientation. We also aim to investigate the impact of additional operational parameters such as the coolant inlet temperature and flow rate considering eccentric freeze-pipes.

Acknowledgments

The authors would like to thank the FRQNT Development Durable du Secteur Minier-II (2020-MN-284402), Ultra Deep Mining Network (UDMN) (241695 Tri-Council (NCE–UDMN) 2-003). The first author wishes to thank the McGill Engineering Doctoral Award (MEDA) and the FRQNT Doctoral award (2021-B2X-306519), in addition to the graduate excellence awards of the mining department of McGill University.

Bibliography

[1] Alzoubi, M. A., Xu, M., Hassani, F. P., Poncet, S., and Sasmito, A. P., 2020. "Artificial ground freezing: A review of thermal and hydraulic aspects". *Tunnelling and Underground Space Technology,* **104**, p. 103534.

[2] Tang, Y., Xiao, S., and Zhou, J., 2019. "Deformation prediction and deformation characteristics of multilayers of mucky clay under artificial freezing condition". *KSCE Journal of Civil Engineering,* **23**(3), pp. 1064–1076.

[3] Newman, G., Newman, L., Chapman, D., and Harbicht, T., 2011. "Artificial Ground Freezing: An Environmental Best Practice at Cameco's Uranium Mining Operations in Northern Saskatchewan, Canada". In 11th International Mine Water Association Congress Mine Water Managing the Challenges.

[4] Alzoubi, M. A., Madiseh, A., Hassani, F. P., and Sasmito, A. P., 2019. "Heat transfer analysis in artificial ground freezing under high seepage: Validation and heatlines visualization". *International Journal of Thermal Sciences,* **139**, pp. 232–245.

[5] Alzoubi, M. A., Zueter, A., Nie-Rouquette, A., and Sasmito, A. P., 2019. "Freezing on demand: A new concept for mine safety and energy savings in wet underground mines". *International Journal of Mining Science and Technology,* **29**(4), pp. 621–627.

[6] Alzoubi, M. A., Nie-Rouquette, A., Ghoreishi-Madiseh, S. A., Hassani, F. P., and Sasmito, A. P., 2019. "On the concept of the freezing-on-demand (FoD) in artificial

ground freezing for long-term applications". *International Journal of Heat and Mass Transfer,* **143**, p. 118557.

[7] Dong, X., Liu, H., and Chen, Z., 2017. "Mathematical modeling of heat transfer and pressure drops in the single-and dual-pipe horizontal wells". *Journal of Thermal Science and Engineering Applications,* **9**(1).

[8] Dash, S., and Sahoo, S., 2019. "A study on natural convection in a cold square enclosure with two vertical eccentric square heat sources using the ib–lbm scheme". *Journal of Thermal Science and Engineering Applications,* **11**(5).

[9] Haidar, C., Boutarfa, R., Sennoune, M., and Harmand, S., 2020. "Numerical and experimental study of flow and convective heat transfer on a rotor of a discoidal machine with eccentric impinging jet". *Journal of Thermal Science and Engineering Applications,* **12**(2).

[10] Neto, J. V., Martins, A., Neto, A. S., Ataíde, C., and Barrozo, M., 2011. "Cfd applied to turbulent flows in concentric and eccentric annuli with inner shaft rotation". *The Canadian Journal of Chemical Engineering,* **89**(4), pp. 636–646.

[11] Chang, K. D., and Lacy, H. S., 2008. "Artificial Ground Freezing in Geotechnical Engineering ". In International Conference on Case Histories in Geotechnical Engineering.

[12] Haciislamoglu, M., and Langlinais, J., 1991. "Effect of pipe eccentricity on surge pressures".

[13] Ali, M. A., El-Maghlany, W. M., Eldrainy, Y. A., and Attia, A., 2018. "Heat transfer enhancement of double pipe heat exchanger using rotating of variable eccentricity inner pipe". *Alexandria engineering journal,* **57**(4), pp. 3709–3725.

[14] Kadivar, M., Moghimi, M., Sapin, P., and Markides, C., 2019. "Annulus eccentricity optimisation of a phase-change material (pcm) horizontal double-pipe thermal energy store". *Journal of Energy Storage,* **26**, p. 101030.

[15] Dawood, H., Mohammed, H., Sidik, N. A. C., Munisamy, K., and Wahid, M., 2015. "Forced, natural and mixed-convection heat transfer and fluid flow in annulus: A review". *International Communications in Heat and Mass Transfer,* **62**, pp. 45–57.

[16] Hosseini, R., Ramezani, M., and Mazaheri, M., 2009. "Experimental study of turbulent forced convection in vertical eccentric annulus". *Energy Conversion and Management,* **50**(9), pp. 2266–2274.

[17] Trombetta, M. L., 1971. "Laminar forced convection in eccentric annuli". *International Journal of Heat and Mass Transfer,* **14**(8), pp. 1161–1173.

[18] Liu, Y., Li, K.-Q., Li, D.-Q., Tang, X.-S., and Gu, S.-X., 2021. "Coupled thermal–hydraulic modeling of artificial ground freezing with uncertainties in pipe inclination and thermal conductivity". *Acta Geotechnica*, pp. 1–18.

[19] Ratzel, A., Hickox, C., and Gartling, D., 1979. "Techniques for reducing thermal conduction and natural convection heat losses in annular receiver geometries".

[20] Hachicha, A. A., Rodríguez, I., and Ghenai, C., 2018. "Thermo-hydraulic analysis and numerical simulation of a parabolic trough solar collector for direct steam generation". *Applied Energy,* **214**, pp. 152–165.

[21] Vitel, M., Rouabhi, A., Tijani, M., and Guérin, F., 2016. "Thermo-hydraulic modeling of artificial ground freezing: Application to an underground mine in fractured sandstone". *Computers and Geotechnics,* **75**, pp. 80–92.

[22] Tounsi, H., Rouabhi, A., and Jahangir, E., 2020. "Thermo-hydro-mechanical modeling of artificial ground freezing taking into account the salinity of the saturating fluid". *Computers and Geotechnics,* **119**, p. 103382.

[23] Wang, B., Rong, C., Cheng, H., Yao, Z., and Cai, H., 2020. "Research and Application of the Local Differential Freezing Technology in Deep Alluvium". *Advances in Civil Engineering,* **2020**.

[24] Zueter, A., Nie-Rouquette, A., Alzoubi, M. A., and Sasmito, A. P., 2020. "Thermal and hydraulic analysis of selective artificial ground freezing using air insulation: Experiment and modeling". *Computers and Geotechnics,* **120**, p. 103416.

[25] Zueter, A. F., Xu, M., Alzoubi, M. A., and Sasmito, A. P., 2021. "Development of conjugate reduced-order models for selective artificial ground freezing: Thermal and computational analysis". *Applied Thermal Engineering*, p. 116782.

[26] Alzoubi, M. A., Nie-Rouquette, A., and Sasmito, A. P., 2018. "Conjugate heat transfer in artificial ground freezing using enthalpy-porosity method: Experiments and model validation". *International Journal of Heat and Mass Transfer,* **126**, pp. 740–752.

[27] Swaminathan, C. R., and Voller, V. R., 1992. "A general enthalpy method for modeling solidification processes". *Metallurgical transactions B,* **23**(5), pp. 651–664.

[28] Faden, M., König-Haagen, A., and Brüggemann, D., 2019. "An optimum enthalpy approach for melting and solidification with volume change". *Energies,* **12**(5), p. 868.

[29] Kaviany, M., 2012. *Principles of heat transfer in porous media*. Springer Science & Business Media, New York.

[30] Cengel, Y. A., Klein, S., and Beckman, W., 1998. *Heat transfer: a practical approach*, Vol. 141. McGraw-Hill New York, New York.

[31] Sladen, W. E., Morse, P. D., and Wolfe S. A., 2018. Geological Survey of Canada Open File 8274. Tech. rep., Natural Resources Canada.

[32] Government of Canada, n.d. Historical data. from https://climate.weather.gc.ca/.

[33] Bejan, A., 2013. *Convection heat transfer*. John wiley & sons, New Jersey.

[34] Shah, R., and London, A., 1978. "Chapter xii - concentric annular ducts". In *Laminar Flow Forced Convection in Ducts*, R. Shah and A. London, eds. Academic Press, New York, pp. 284 – 321.

[35] Ebadian, M., and Dong, Z., 1998. *Forced convection, internal flow in ducts*, Vol. 5. chapter.

[36] Xu, M., Akhtar, S., Zueter, A. F., Auger, V., Alzoubi, M. A., and Sasmito, A. P., 2020. "Development of analytical solution for a two-phase stefan problem in artificial ground freezing using singular perturbation theory". *Journal of Heat Transfer,* **142**(12).

[37] Xu, M., Akhtar, S., Zueter, A. F., Alzoubi, M. A., Sushama, L., and Sasmito, A. P., 2021. "Asymptotic analysis of a two-phase stefan problem in annulus: Application to outward solidification in phase change materials". *Applied Mathematics and Computation,* **408**, p. 126343.

[38] Zhang, S., Yue, Z., Sun, T., Zhang, J., and Huang, B., 2021. "Analytical determination of the soil temperature distribution and freezing front position for linear arrangement of freezing pipes using the undetermined coefficient method". *Cold Regions Science and Technology*, p. 103253.

[39] Zueter, A. F., Newman, G., and Sasmito, A. P., 2021. "Numerical study on the cooling characteristics of hybrid thermosyphons: Case study of the giant mine, canada". *Cold Regions Science and Technology,* **189**, p. 103313.

[40] Vasilyeva, M., Ammosov, D., and Vasil'ev, V., 2021. "Finite element simulation of thermo-mechanical model with phase change". *Computation,* **9**(1), p. 5.

[41] Pei, W., Zhang, M., Lai, Y., Yan, Z., and Li, S., 2019. "Evaluation of the ground heat control capacity of a novel air-l-shaped tpct-ground (altg) cooling system in cold regions". *Energy,* **179**, pp. 655–668.

Chapter 6

Dynamic CFD modeling coupled with heterogeneous boiling for deep two phase closed thermosyphons in artificial ground freezing

Preface

This is the start of the second half of the thesis addressing thermosyphon-based artificial ground freezing systems. First, in this chapter, we examine the boiling phenomena in deep thermosyphons such as that employed in the Giant Mine Remediation Project.

" **A. Zueter**, Muhammad Saad Khan Tareen, and A. P. Sasmito. Conjugate CFD modeling of deep two phase closed thermosyphons in artificial ground freezing. Draft to be submitted to the International Journal of Heat and Mass Transfer"

Abstract

Super-long thermosyphons exceeding 100 meters are being employed more frequently in artificial ground freezing (AGF) applications. In this study, we develop a fully-conjugate computational-fluid-dynamics (CFD) model to fundamentally analyze the heat extraction capacity and profile of super-long thermosyphons in AGF. The CFD model couples a heterogeneous condensation/evaporation mass transfer model inside the thermosyphon with thermosyphon-pool hydrostatic pressure distribution and heat diffusion from the ground. The heterogeneous model also considers the kinetic energy required for bubble nucleation and has been validated against experimental studies from the literature. Three main parameters have been investigated: 1) the fill ratio, 2) the charge pressure inside the thermosyphon, and 3) the wind temperature. The results reveal a no-boiling-zone below 10-25 meters of pool surface. Further, the charge pressure significantly affect the start-up of the thermosyphon. Lastly, lower wind temperature extracts more heat from the ground in a qualitatively similar manner (similar heat flux profile along thermosyphon wall) to that of higher wind temperature. Overall, the results of this study provide fundamental understanding of the performance of super-long thermosyphons in AGF.

Contents

6.1 Introduction

Two-phase-closed-thermosyphons (TPCT) are heat transfer devices of simple construction with no moving parts. While they have been firstly invented by by Perkin and Buck by the end of the nineteenth century [1], [2], Erwin Long (an Alaska based engineer) obtained the US patent for successfully employing TPCT in artificial ground freezing (AGF) systems in 1965 [3]. The first known field installation of these devices dates back to 1960 for foundations stabilization of communication sites at Aurora (Manitoba, Canada) and Glenallen (Alaska, US) [4]. Since then, TPCT have attracted a worldwide interest especially in cold regions due to their passive ability to utilize the available cold wind to freeze the ground. In the 1970s, 120,000 TPCT were installed to support the 800-miles-long Trans-Alaska pipeline built on continuous and discontinuous permafrost regions [5]. In China, 20,000 TPCT were installed between 2006-2009 to raise the permafrost table underlying the 142-km-long Chaidaer-Muli railway [6]. Further, TPCT are widely used across Qinghai-Tibet Plateau, China, to protect the underlying permafrost of railways [7], roadways [8], and power transmission towers [9], [10]. The vast majority of present TPCT in permafrost protection applications extend to around 5-30 meters below the ground surface. Nevertheless, much deeper TPCT at the Giant Mine Remediation Project are needed to contain arsenic waste stored in underground chambers. Particularly, 706 deep thermosyphon, in addition to 152 shallow ones, will be installed to freeze the ground around the contaminated chambers and, thus, prevent arsenic leakage [11]. The deep TPCT can extend to 100-160 meters below the ground surface. The multiphysics boiling and condensation phenomena of deep thermosyphons is different from that of shallow ones.

A TPCT has two main sections: 1) evaporator – embedded in ground and 2) condenser – exposed to cold air. A refrigerant inside the TPCT absorbs heat from the ground in the evaporator section and evaporates as a result. It then flows upwards towards the condenser section, where it exudes the absorbed heat to the ambient air as shown in Figure 6-1(a). Upon releasing the heat, it condenses and falls down towards the evaporator section, thus, creating

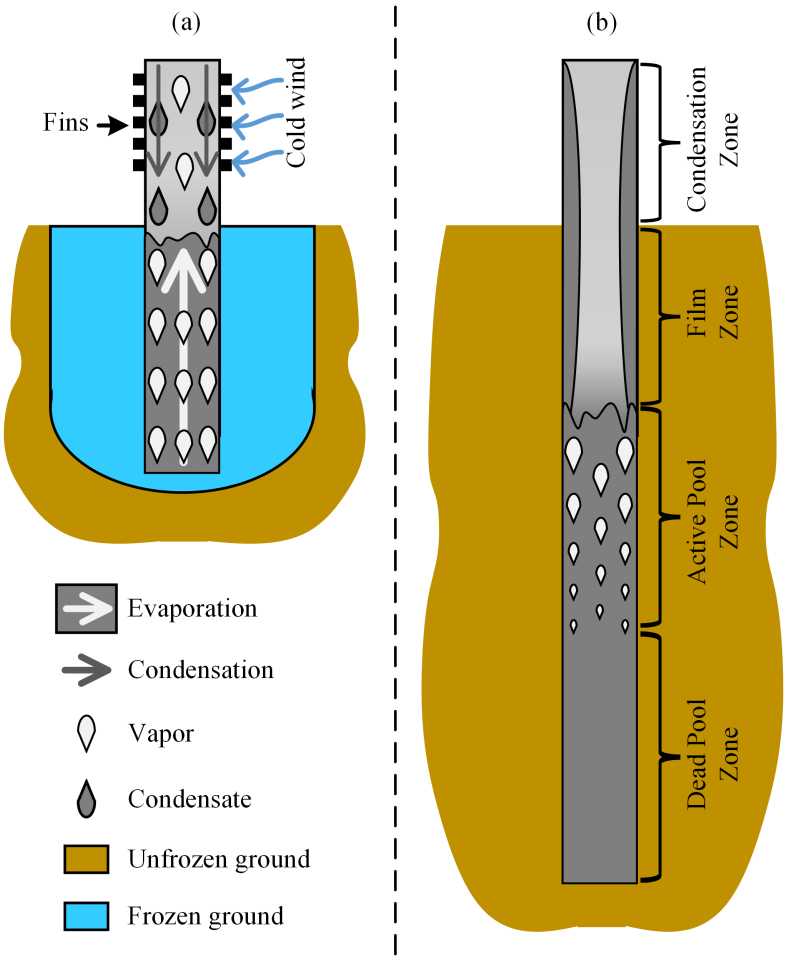

Figure 6-1: Not-to-scale schematic illustrating a) the operating principle of passive artificial ground freezing systems using thermosyphons and b) the various heat extraction/dissipation zones in the case of deep thermosyphons.

a continuous cycle of heat absorption and release. Thermosyphon-based AGF operation is a multi-scale and multi-physics problem with two aspects: 1) TPCT condensation-evaporation cycle and 2) heat diffusion in the rock. In shallow thermosyphons, the boiling temperature across the evaporator is almost uniform due to the relatively uniform pressure distribution across the liquid pool, which is almost equivalent to the overlying vapor pressure. Nonetheless, deeper TPCT contains a much larger liquid pool which linearly increases the hydrostatic pressure along the pool depth. The linear increase in the pressure profile consequently increases the boiling temperature, which creates four unique zones, as shown in Fig. 6-1(b). The first zone from the top is the condensation zone, adjacent to cold wind where the vapor

refrigerant condeses and falls back to the evaporator. The second zone is the film zone, which extracts heat through a liquid film falling towards the pool surface. The third zone is the active pool zone in which the pool boils as heat is extracted from the ground. The hydrostatic pressure increases linearly with pool depth which in turn increases the boiling temperature and slows down the boiling rate. When the boiling temperature exceeds the pool temperature, a dead pool zone is formed, where heat is extracted through conduction and single-phase natural convection.

Previous scientific research has proposed various mathematical models of different complexity to model *shallow* TPCT in AGF systems. A simplified TPCT cycle by Abdalla et al. [12], [13] assumes a super-conductor thermosyphon and directly correlates ambient air flow with the heat flux at the evaporator wall. As indicated by results, size of the thaw settlements in the permafrost regions, below warm pipelines, was significantly reduced. A thermal resistance network model was derived by Zhang et al. [14] that accounted for the thermal resistance of condensation and evaporation cycles. They demonstrated that the frozen grounds below the Qinghai-Tibet railways and roads are ensured to be protected with TPCT embankment. The thermal resistance network model was extended by Pei et al. [15], [16] using L-shaped and inclined TPCT embankments. Yang et al. [17], [18], [19] used the same thermal network model, but considered a different boiling phenomena in the film-boiling zone. Recently, Zueter et al. [20] derived the first thermal network model for *hybrid* TPCT that run year-round by employing the cold wind in winter seasons and refrigeration plants in warmer seasons. Such numerical studies modeled the expansion of frozen grounds successfully. However, little attention has been given to full-scale modeling of the boiling and condensation phenomena in thermosyphons, especially in AGF applications.

Apart from AGF, thermosyphons have been used as a heat transfer device in several applications such as geothermal energy extraction [21], [22], [23] and electronics cooling [24], [25], [26]. Accordingly, CFD studies that examine the boiling and condensation phenomena in thermosyphons have been conducted in the literature for various purposes. Alizadehdakhel

et al. [27] derived a 2D CFD model for thermosyphons based on the conservation principles of mass, momentum, and energy. The volume-of-fluid (VoF) method [28] is employed to model the equivalent thermophysical properties, as well as the velocity and temperature fields, across the thermosyphon. The evaporation and condensation rate, $S_{v\to\ell}$, are modeled using Schepper et al. [29] correlation given as

$$S_{v\to\ell} = \begin{cases} \beta_c \ \chi \ \rho_v \ \alpha_v \ (T_{sat} - T)/T_{sat} & , T < T_{sat} \text{ (condensation)}; \\ \beta_e \ \rho_\ell \ \alpha_\ell \ (T_{sat} - T)/T_{sat} & , T > T_{sat} \text{ (evaporation)}, \end{cases} \tag{6.1}$$

where ρ, β_c, β_e, χ, α_v, α_ℓ and T represent the density, condensation frequency, evaporation frequency, mole fraction of heat-transfer-fluid inside the thermosyphon (water in Alizadehdakhel et al. [27] experiment), volume fraction of vapor phase, volume fraction of liquid phase, and temperature, respectively. The subscripts v, ℓ, and sat refer to vapor phase, liquid phase, and saturation (temperature), respectively. The mole fraction of water is added to the condensation source term due to water's tendency to formulate non-condensable gases. Formation of non-condensable gases can significantly reduce the long-term condenser efficiency as the these gases occupy the top region of the condenser, thus, decreasing the heat exchange area with the condenser heat sink. This was an issue in the operation of ammonia-filled thermoysphons along the Trans-Alaska pipeline. Currently, CO_2 is preferred over ammonia in cold thermosyphon applications due to its chemical stability.

Fadhl et al. [30] used a similar CFD methodology examining water as the working fluid inside the thermosyphon and validated the model against experimental data however without including the mole fraction effect on the condensation. This can be attributed to the short duration of experimental studies as compared to the much longer time needed for condensable gases to form and thus have an evident impact. Fadhl et al. [31] then tested thermosyphon performance with other commercial refrigerants such as R134a and R404a. The bubbles formed in these refrigerants are much smaller than that of water, possibly due to the different

critical nucleation site radius. Xu et al. [32] considered the effect surface wettability for mini-thermosyphons in electriconics cooling applications. Kamburova et al. [33] and Abdullahi et al. [34] numerically investigated the impact of the condenser capacity and thermosyphon inclination angle, respectively. Jouhara et al. [35] extended the geometry to 3D in order to observe the geyser boiling phenomena mathematically. Kafeel and Turan [36] derived a more complex Eulerian mathematical model that treats each phase independently.

The discussed CFD studies thus far consider short thermosyphons (less than 10 meters) and assume that bubble nucleation is initiated once the liquid temperature exceeds the saturation temperature. Wang et al. [37] conducted a pioneering study which considered the excess temperature needed, dT_i, to form a nucleation site and thus adjusted the evaporation model as

$$S_{\ell \to v} = \begin{cases} \beta_e \rho_\ell \alpha_\ell (T_{sat} - T)/T_{sat} & , 1 > \alpha_v > 0 \text{ and } T > T_{sat} (\text{gas expansion}); \\ 0 & , \alpha_v = 0 \text{ and } T < T_{sat} + dT_i (\text{no nucleation}); \\ \beta_e \rho_\ell \alpha_\ell (T_{sat} - T)/T_{sat} & , \alpha_v = 0 \text{ and } T > T_{sat} + dT_i (\text{nucleation}). \end{cases} \tag{6.2}$$

This improved model was employed to observe the geyser boiling phenomena of water [37] and investigate lab-scale thermosyphons in shallow geothermal applications using ammonia [38]. After that, Wang et al. [39] derived a novel pressure-based evaporation model based on the Hertz-Knudsen kinetic theory of gases [40]. The pressure-based model also considers the variation of the saturation pressure according to the liquid's temperature. Wang et al. [41] demonstrated that the variation of the saturation pressure in deep thermosyphons can be quite significant in geothermal applications due to the huge hydrostatic pressure accumulating at the bottom of the thermosyphon.

According to the literature presented above, the following research gaps need to be addressed regarding the operation of thermosyphons in artificial ground freezing applications in particular and other applications in general:

- Full-scale CFD models of thermosyphon-based AGF systems using CO_2 have not been conducted yet. Previous AGF literature model thermosyphons using a simplified thermal resistance network model assuming ideal evaporation and condensation. Nonetheless, thermosyphon operation is limited by several operational parameters especially very deep ones such as those operating at the Giant Mine.

- The heterogeneous nature of the boiling phenomena in thermosyphons has not been considered in previous CFD models where nucleation sites should *only* be formed alongside the thermosyphon shell.

- The impact of the initial charge pressure has not yet been investigated for the case of deep TPCTs (even the shallow ones to the best of authors knowledge).

- Lack of CFD models for thermosyphons exceeding 100 meters in depth, such as those installed at the Giant Mine.

Thus, the primary purpose of this study is to develop a full-scale CFD model for deep-thermosyphon-based AGF systems coupled with heterogeneous boiling phenomena. Specifically, CFD model for TPCT is initially developed and then validated against the experimental results that are available in the literature. The TPCT CFD model is then coupled with the heat flow in the ground model from our previous work [42], [43] that is principally based on enthalpy-porosity method [44]. This model is also extended to field conditions to examine the fundamental and applied impact of three main parameters: 1) thermosyphon fill ratio, 2) thermosyphon charge pressure, and 3) cold wind temperature. This paper is presented with the following sequence of demonstration:

1. Presentation of a mathematical model for TPCT alongside the heat-flow-in-the-ground model.

2. Validation of TPCT model with experimental results from the literature.

3. Examination of the effects of FR, thermosyphon charge pressure (ICP) and wind temperature in AGF.

6.2 Mathematical Modeling

A 2D CFD model is built following the conservation principles of mass, momentum, and energy, alongside the heterogeneous bubble nucleation theory. There are three main computational zones: 1) ground occupied by porous rocks, 2) steel pipes, and 3) TPCT filled by a refrigerant, as shown in Fig. 6-2(a). Mathematical modeling of each zone in addition to their corresponding boundary conditions are provided in the next three subsections.

6.2.1 Mathematical modeling of the ground

The enthalpy-porosity method has been implemented to calculate the temperature profile of the ground. Local thermal equilibrium (LTE) is assumed due to low porosity of the ground and small difference between thermal conductivity of sand particles and water. Zueter et al. [42] provided an elaborate justification for using LTE in AGF applications as employed in multiple AGF studies [43], [45]. Thus, the temperature distribution can be calculated using a one-temperature model given as:

$$\frac{\partial(\overline{\rho_g c_{p,g}} T)}{\partial t} = \nabla \cdot (\overline{k}_g \nabla T) + S, \tag{6.3}$$

where the subscript g refers to the ground and the source term, S, accounts for the latent heat as:

$$S = -\phi \rho_w L_w \frac{\partial \gamma}{\partial t}, \tag{6.4}$$

where $\rho_w L_w$ is the volumetric latent heat of water, ϕ is the ground porosity, and γ is the liquid fraction. In the mushy zone where both liquid water and ice water coexist, γ is calculated by linear interpolation of the temperature with respect to the solidus and liquidus

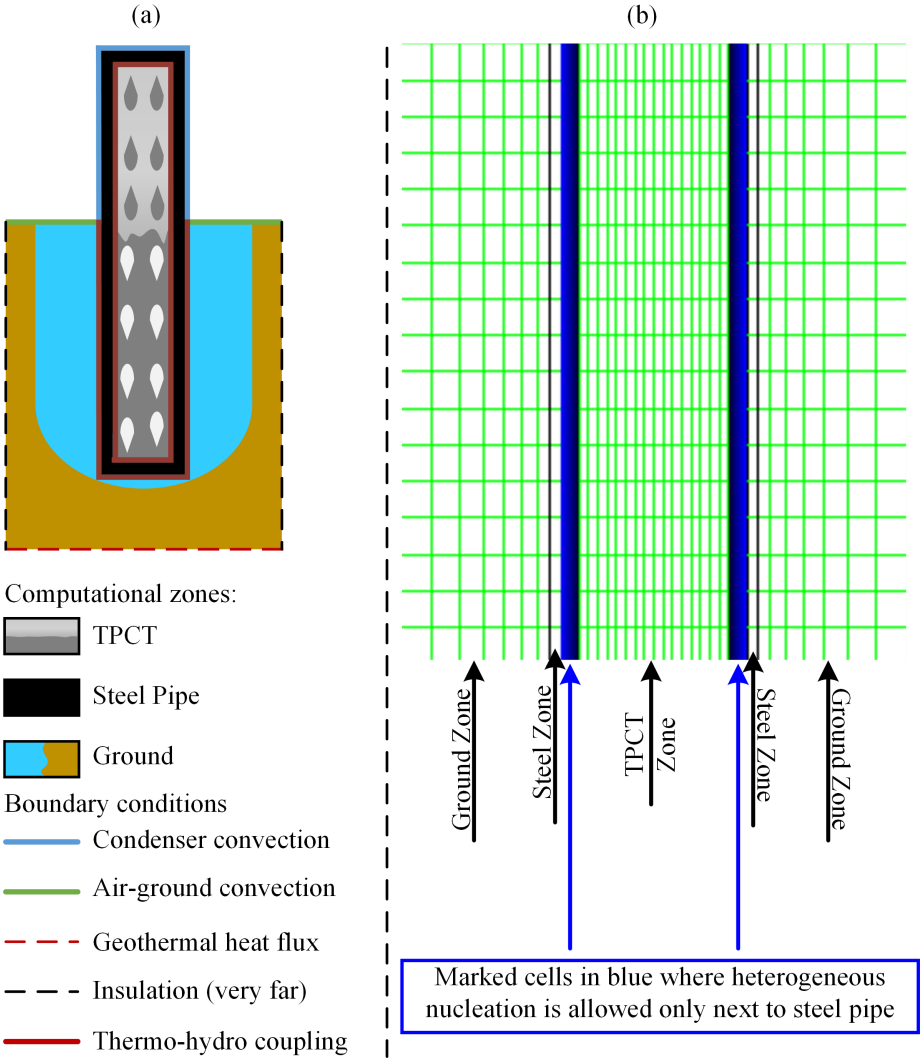

Figure 6-2: Not-to-scale schematic illustrating a) the computational zones and their boundary conditions and b) part of the mesh highlighting the heterogeneous boiling conditions where nucleation is only allowed in the marked cells right next to steel pipe.

Material	ρ [kg/m^3]	c_p [J/(kg·K)]	k [W/(m·K)]	μ[Pa s]
Liquid CO_2 [46]	959	2396	0.117	1.09E-4
Vapor CO_2 [46]	Ideal gas	1643	18.0×10^{-2}	1.42×10^{-5}
Liquid NH_3 [46]	645	4592	89.1×10^{-2}	1.79×10^{-4}
Vapor NH_3 [46]	Ideal Gas	2613	23.0×10^{-2}	8.19×10^{-6}
Frozen rock [47]	2926	814	3.45	-
Unfrozen rock [47]	2927	822	3.44	-

Table 6.1: Thermophysical properties of the materials used in this study. The ground porosity is 1% according to the measurements of the Giant Mine bedrock [47].

temperatures. The thermophysical properties of ground and water can be found in Table 6.1.

The ground zone is enclosed by several boundaries, as shown in Figure 6-2(a). On the top, the ground is subjected to atmospheric heat convection given as

$$-\overline{k}_g \frac{\partial T}{\partial n}\bigg|_{top\ boundary} = h(T|_{top\ boundary} - T_a), \tag{6.5}$$

where T_a is the air temperature, h is the atmospheric heat transfer coefficient, and n is a normal vector to the boundary. One the sides, a boundary independent insulation is modeled 0.5 m away from the thermosyphon, so that the temperature distribution in the vicinity of the thermosyphon is not affected by the side boundaries. This is mathematically expressed as:

$$\frac{\partial T}{\partial n}\bigg|_{side\ boundaries} = 0. \tag{6.6}$$

Geothermal heat flux at the bottom boundary is set as:

$$-\overline{k}\frac{\partial T}{\partial n}\bigg|_{bottom\ boundary} = 0.06[\mathrm{W/m^2}] \tag{6.7}$$

Finally, thermal coupling between the ground zone and the steel zone is given as:

$$\overline{k_g}\frac{\partial T_g}{\partial n}\bigg|_{pipe-ground} = k_s \frac{\partial T_s}{\partial n}\bigg|_{pipe-ground} \tag{6.8}$$

where the subscript s refers to the steel zone.

6.2.2 Mathematical modeling of the steel pipe

Heat flow in the steel is calculated as:

$$\frac{\partial(\rho_s c_{p,s} T_s)}{\partial t} = \nabla \cdot (k_s \nabla T_s) \tag{6.9}$$

The outer wall of the steel pipe in the evaporator section is in contact with the ground. Coupling between the ground and the steel pipe is already shown in equation (6.8). In the condenser section above the ground level, convective heat of the wind is modeled as:

$$h\ (T_{cw} - T_\infty) = k_s \frac{\partial T_s}{\partial n}\bigg|_{cw} \tag{6.10}$$

where h is the heat transfer coefficient of the wind approximated at 150 [W/(m^{2}K)], T_∞ is the wind temperature, and subscript cw refers to the condenser wall. In this study, three cases of wind temperature are considered: 1) -15 [°C], 2) -20 [°C], and 3) -30 [°C]. Along the inner walls of the TPCT, the steel pipe zone is thermally coupled with the TPCT zone as:

$$k_r \frac{\partial T_r}{\partial n}\bigg|_{pipe-TPCT} = k_s \frac{\partial T_s}{\partial n}\bigg|_{pipe-TPCT}, \tag{6.11}$$

where the subscript r refers to the operating refrigerant.

6.2.3 Mathematical modeling of the TPCT

Novelty of this work lies in its capability to fully couple the evaporation and condensation cycles of the TPCT with ground freezing. The volume-of-fluid (VoF) model has been adapted in this study due to its superior computational efficiency over other CFD techniques for modeling evaporation and condensation. In addition, the VoF model has demonstrated sufficient reliability in many TPCT studies for non-AGF systems.

The VoF model expresses the continuity of the refrigerant with two equations for the 1) liquid phase and 2) vapor phase. Continuity equation of the liquid phase is given as:

$$\frac{\partial}{\partial t}(\rho_\ell \alpha_\ell) + \nabla \cdot (\alpha_\ell \rho_\ell \vec{u}) = -m_{tr}, \tag{6.12}$$

where $\vec{u}$ is the velocity field and α_ℓ is the liquid fraction of the refrigerant (not to be confused with γ and ϕ which are correlated to the ground domain) whereas subscripts ℓ and v denote the liquid phase and vapor phase, respectively. The liquid to vapor mass transfer source term (boiling/condensation rate) depends on 1) the nucleation temperature, T_{nuc}, when a new bubble needs to be formed and 2) pressure-dependent saturation temperature $T_{sat} = f(P)$ for condensation or expansion of developed bubble. Heterogeneous bubble nucleation, in which bubbles are formed on the wall surface, prevails over homogeneous bubble nucleation, where bubbles are formed inside the bulk of the liquid [48]. This is attributed to the very high number of embryos (exceeding 10^{12}) that need to be created for homogeneous boiling. Accordingly, in this study, bubble nucleation is allowed only on computational nodes attached to the solid surface, as shown in Fig. 6-2(b).

The mass transfer source is thus calculated according to five different cases as per Eq. (6.13) and Table 6.2.

$$m_{tr} = \begin{cases} \beta_e \rho_\ell \alpha_\ell (T - T_{sat})/T_{sat} & , \alpha_\ell < 1 \text{ and } T > T_{sat} \quad \text{(case 1);} \\ 0 & , \alpha_\ell = 1 \text{ and } T < T_{nuc} \quad \text{(case 2);} \\ 0 & , \alpha_\ell = 1 \text{ and } T > T_{nuc} \text{ and none-wall cell} \quad \text{(case 3);} \\ \beta_e \rho_\ell \alpha_\ell (T - T_{sat})/T_{sat} & , \alpha_\ell = 1 \text{ and } T > T_{nuc} \text{ and wall-cell} \quad \text{(case 4);} \\ \beta_c \rho_v \alpha_v (T - T_{sat})/T_{sat} & T < T_{sat} \quad \text{(case 5);} \end{cases} \tag{6.13}$$

where β_e and β_c are the evaporation and condensation frequency, respectively, and subscript v refer to vapor state.

Case 1:	Expansion (or contraction) of an already developed bubble.
Case 2:	Bubble nucleation is not allowed until reaching the nucleation temperature.
Case 3:	Homogeneous nucleation within the bulk liquid is not allowed.
Case 4:	Heterogeneous nucleation: Bubble nucleation is only allowed on a solid surface.
Case 5:	Condensation

Table 6.2: Summary of boiling and condensation cases of Eq. 6.13.

The saturation temperature is determined by curve-fitting the temperature-pressure saturation curve [46] as:

$$T_{sat}(P) = c_1\ P^4 + c_2\ P^3 + c_3\ P^2 + c_4\ P + c_5, \tag{6.14}$$

where the coefficients c_1 through c_5 can be found in Table (6.3).

Material	c_1 [K/Pa^4]	c_2 [K/Pa^3]	c_3 [K/Pa^2]	c_2 [K/Pa]	c_5 [K]
CO_2	-8.049×10^{-26}	1.285×10^{-18}	-8.645×10^{-12}	3.8×10^{-05}	203
NH_3	-6.656×10^{-24}	4.238×10^{-17}	-1.016×10^{-10}	1.32×10^{-4}	232

Table 6.3: The coefficients of equation (6.14).

Rohsenow [49] determined the nucleation temperature following a semi-analytical derivation as

$$T_{nuc} = T_{sat} + \frac{8\sigma T_{sat}\nu_v q}{h_{fg}k_\ell} Pr_\ell \tag{6.15}$$

As there are only two phases in the thermosyphon, the vapor volume fraction, α_v, in equation (6.13) is the compliment of the liquid fraction, α_ℓ, as:

$$\alpha_v = 1 - \alpha_\ell \tag{6.16}$$

The conservation of momentum is given as:

$$\frac{\partial(\rho\ \vec{u})}{\partial t} + \nabla\cdot(\rho\ \vec{u}\ \vec{u}) = -\nabla P + \nabla\cdot\left[\mu(\nabla\vec{u} + \nabla\vec{u}^T)\right] + \rho\ \vec{g} + S_{st} \tag{6.17}$$

where $\vec{g}$ is the gravitational acceleration and S_{st} is the surface tension source term. The thermosyphical properties of the refrigerant are set according to the phase of the each computational node as listed in Table 6.1. Nonetheless, the density of the vapor phase is assumed to obey the ideal gas law. When both liquid and vapor phases exist together in the same computational node, the thermophysical properties are calculated based on volume averaging.

The energy conservation is expressed as:

$$\frac{\partial(\rho_r c_{p,r} T_r)}{\partial t} + \nabla \cdot (\rho_r c_{p,r} T_r \ \vec{u}_r) = \nabla \cdot \left[k_r (\nabla T_r)\right] + S_{fg}, \tag{6.18}$$

where the source term, S_{fg}, is added to incorporate the latent heat of vaporization and is calculated with respect to the mass transfer source term, m_{tr}, as:

$$S_{fg} = -m_{tr} \ h_{fg}, \tag{6.19}$$

where h_{fg} is the specific latent heat of the refrigerant.

The refrigerant is fully bounded by the steel shell. Thermal coupling between the refrigerant and the steel shell is given in Eq. 6.11. Further, a no-slip condition is imposed as

$$\vec{u}|_{steel \ wall} = 0 \tag{6.20}$$

6.3 Numerical method

A two-dimensional implicit CFD model was developed with the aid of ANSYS FLUENT/18.1 to compute the mathematical model as prescribed by the governing equations and boundary conditions. The computation of the continuity and momentum equations were coupled together while the computation of energy equation was segregated from the rest. Furthermore,

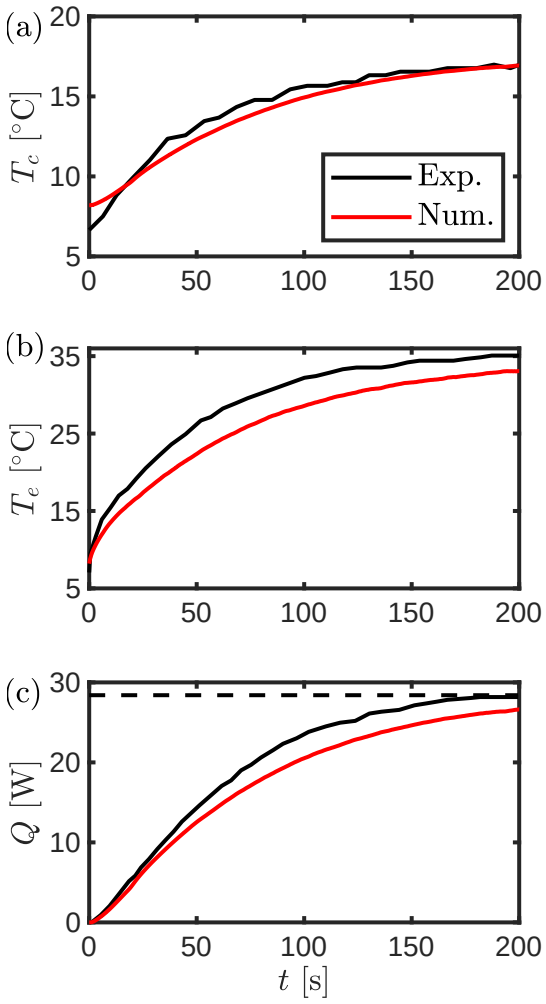

Figure 6-3: Validation of the numerical model against the experimental measurements of Wang et al. [37]: a) condenser wall temperature, b) evaporator wall temperature, and c) heat extraction at the condenser (the dashed line represents the input heat transfer rate at the evaporator section in the experiment and model)

the governing equations were discretized by second-order schemes in space and explicit first-order schemes in time. The convergence criteria of the continuity and momentum equations were set at 1E-4 whereas that of the energy equation was set at 1E-8. A mesh independent study is conducted and ensured in this study.

6.4 Results and discussion

In this section, the mathematical model is firstly validated against experimental measurements. Then, the impact of the following operational parameters on the performance of thermosyphons in field-scale conditions is examined: 1) filling ratio of the working fluid, 2) charge pressure, and 3) air temperature. In all field simulations, apart from validation in Sec. 6.4.1, the thermosyphon is filled with pressurized CO_2. Furthermore, the length of thermosyphon evaporator, adiabatic, and condenser sections is set to: 100 meters, 2 meters, and 6.27 meters, respectively, as per field thermosyphons data [20]. The thermosyphon diameter is 10 centimeters. In field conditions, the ground is initialized at a temperature of 1[°C], whereas the initial thermosyphon temperature is set equal to the saturation temperature of the thermosyphon charge pressure, which is 2.5[MPa] unless otherwise stated. Additionally, the wind temperature is set at -20 [°C], except in the last subsection, where it is varied from -30 [°C] to -15 [°C]. The base fill-ratio is also set at 75% unless otherwise stated.

6.4.1 Model validation

The mathematical model of this study includes two main parts: 1) The ground freezing model using the enthalpy method, and 2) The VOF model of TPCT using the Lee model. The former of these parts have been validated in our previous work [42]. Thus, this subsection is dedicated to validate the VOF model. The experimental and mathematical study of Wang et al. [37] was selected for validation purposes.

The experimental setup is composed of a Ø9×1 [mm] cylindrical thermosyphon filled

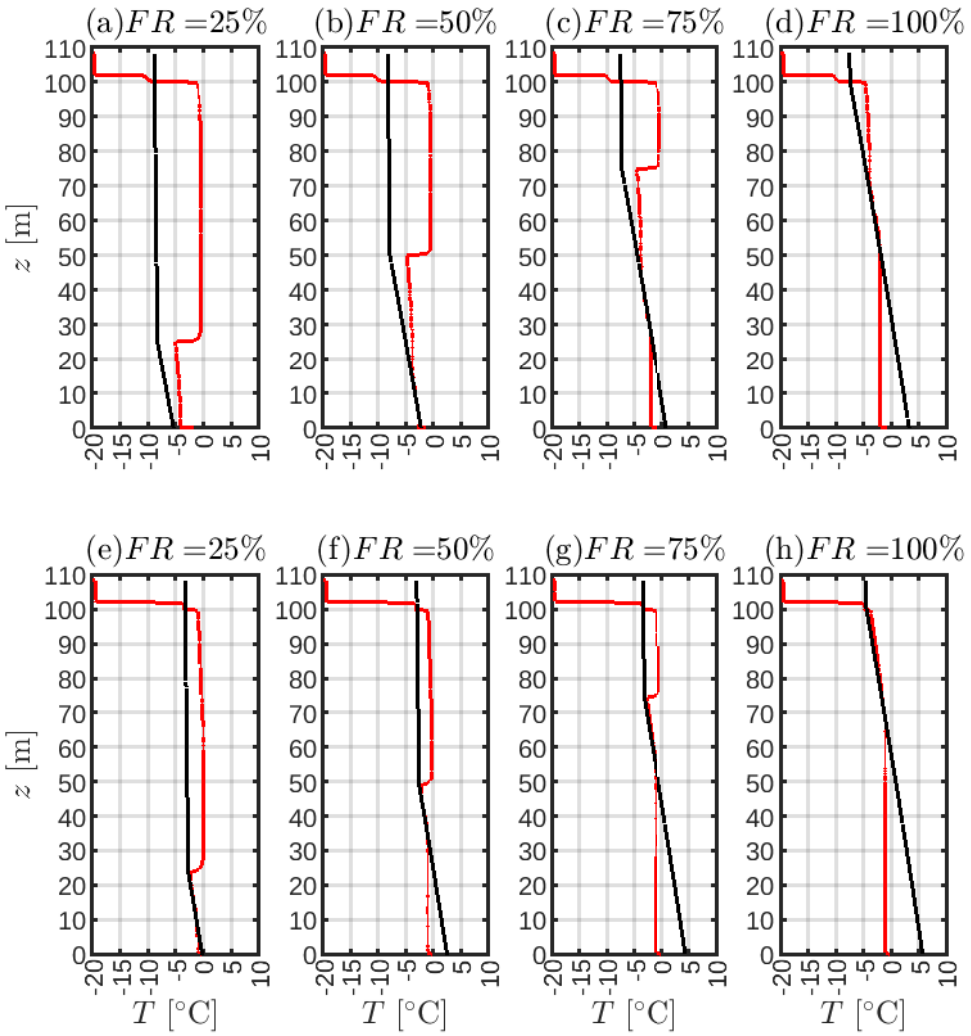

Figure 6-4: Thermosyphon wall temperature (in red) and nucleation temperature (in black) along the thermosyphon wall at different fill ratios. Subplots (a-d) are plotted after one hour of operation, whereas subplots (e-h) are plotted after 10 hours of operation. The bottom of the thermosyphon is considered as a reference point at $z = 0$; thus, the ground level is at $z = 100$ [m].

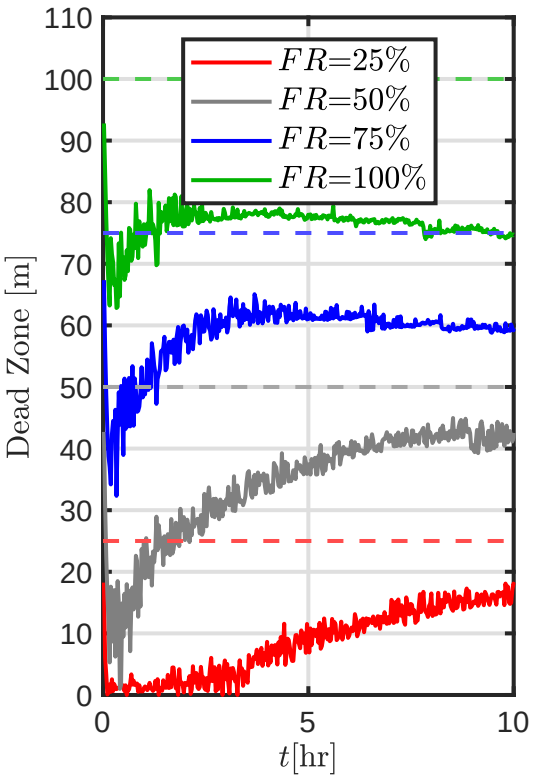

Figure 6-5: Extent of dead zone in the thermosyphon at different fill ratios through the first 10 hours of operation - the dashed lines represent the pool surface given each fill ratio

with ammonia. The lengths of the evaporator, adiabatic, and condenser sections are 20 cm, 10 cm, and 20 cm, respectively. The evaporator is subject to fixed heat flux of 5026.6 [W/m^2] whereas, the condenser is cooled by a flow of water having an overall heat transfer coefficient of 539 [W/(m^{2}K)] and temperature of 8.2 [°C]. As can be seen from Fig. 6-3, the experiment was initialized at a temperature of around 8 [°C] and lasted for 200 [s]. The average temperature of the evaporator and condenser were determined using eight thermocouples installed along the wall. Our numerical model agrees well with the experimental data, as shown in Fig. 6-3.

6.4.2 Impact of thermosyphon fill ratio

In this subsection, the impact of fill ratio of CO_2 inside the thermosyphon is investigated. The fill ratio is the initial volume of liquid CO_2 divided by the volume of the evaporator. Four fill ratios are investigated in the present study: $FR = 100\%$, $FR = 75\%$, $FR = 50\%$, and $FR = 25\%$.

The fill ratio evidently impacts the axial distribtion of the nucleation temperature, T_{nuc}, as can be seen in Fig. 6-4. While T_{nuc} is uniform above the pool level, hydrostatic pressure of the liquid column causes the nucleation temperature to increase linearly at a rate of 0.125 [°]C per meter depth of the pool. Accordingly, increase in the nucleation temperature across the pool is linearly proportional to the fill ratio. For instance, after one hour of operation, the nucleation temperature at $FR = 25\%$ has decreased by around 3 [° C] from the pool surface at $z = 25$[m] to the bottom of the thermosyphon. On the other hand, in the case of $FR = 100\%$, the nucleation temperature has increased by around 12 [°C] from the pool surface at $z = 100$[m] to the bottom of the thermosyphon. It is also observed that the nucleation temperature increases with time. For instance, by comparing Fig. 6-4(a) with Fig. 6-4(e), the nucleation temperature line shifts to the right by around 6 [°C]. As the thermosyphon extracts heat from the ground, the temperature and pressure inside the thermosyphon increases, which in turn also increases the nucleation temperature.

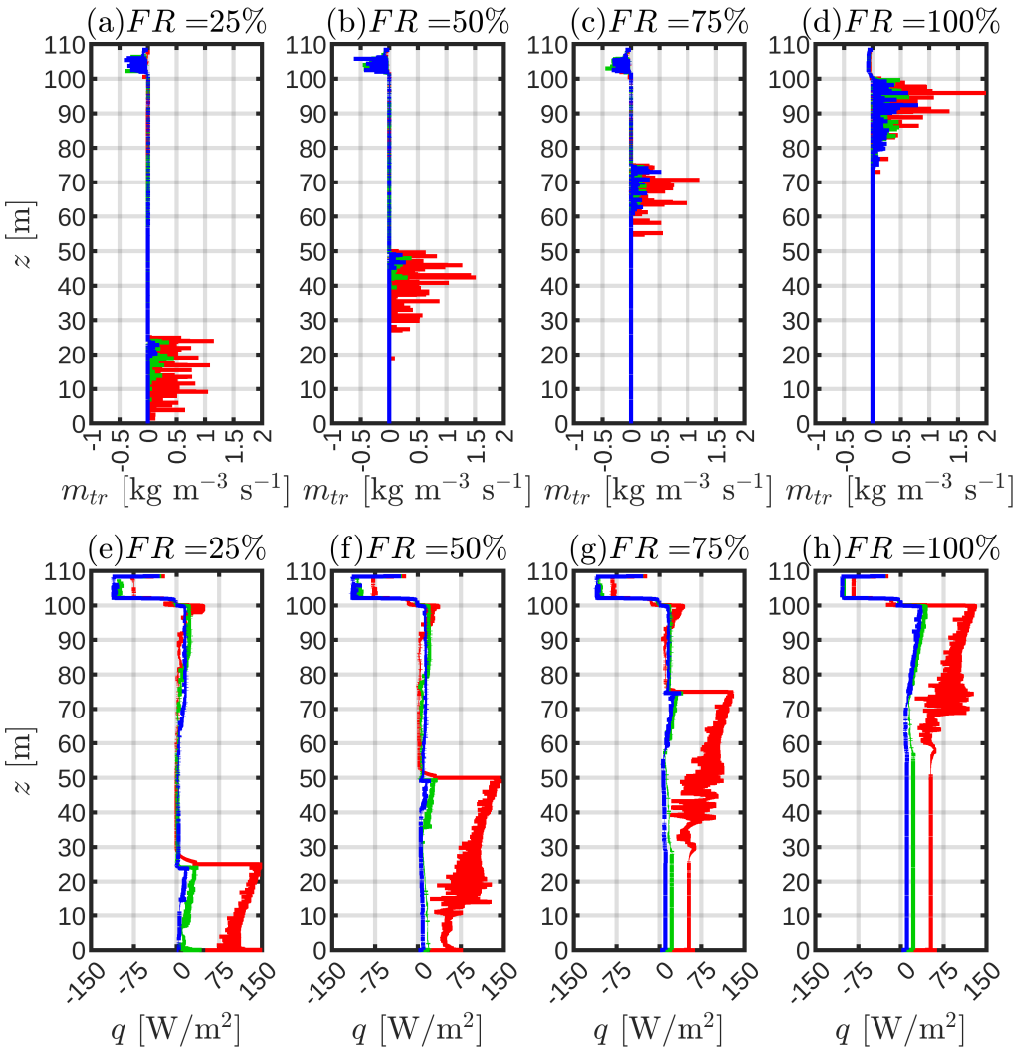

Figure 6-6: Mass transfer rate and heat flux along the thermosyphon wall at different fill ratios (positive mass transfer rate denotes evaporation while negative mass transfer rate represents condensation). The red, green, and blue lines are plotted after one hour, five hours, and 10 hours of operation, respectively

The proportional increase of T_{nuc} along the thermosyphon depth substantially affects the boiling phenomena inside the pool. At a fill ratio of 25% in the first hour, the wall temperature is always higher than the nucleation temperature − indicating that boiling occurs throughout the pool depth, as shown in Fig. 6-4(a). However, as the fill ratio increases, the wall temperature intersects with the nucleation temperature at higher axial positions − creating larger *dead zones* where boiling does not occur, as schematically illustrated in Fig. 6-1(b). The axial position of the pool dead zone increases in the first hours as the thermosyphon reaches a semi-steady state, as can be seen in Fig. 6-5. Thermosyphons with higher fill ratios reach a steady state faster than the lower ones due to the less distance needed for the vapor volume to travel from the pool surface to the condenser. While the dead zone is proportional to the fill ratio, the active pool zone tends to be nonetheless larger at higher fill ratios. The effect of the dead zone on the boiling rate as well as the heat flux along the thermosyphon wall is evident in Fig. 6-6(a-d). At higher fill ratios, no boiling occurs at the bottom of the thermosyphon until the wall temperature is higher than the nucleation temperature. Nonetheless, the boiling rate in the active zone at higher fill ratios after 10 hours of operation, is found to be higher than that of the lower ones due to the feedback from the condenser. As for the film zone, the boiling rate is found to be negligible, compared to that of the pool zone.

The axial heat extraction profile heavily relies on the the relationship between the fill ratio and the boiling rate, as can be seen in Fig. 6-6(e-h). In the dead zone, the heat flux is uniform − implying that heat is mainly extracted by conduction. On the other hand, in the active zone, the heat flux fluctuates due to boiling phenomena but increases near the pool surface due to the lower nucleation temperature in that region. In all cases, the boiling rate and heat extraction capacity decrease with time − as the ground temperature decreases. Nevertheless, the heat flux profile of the film zone becomes larger with time, indicating that the film is developing. At a fill ratio of 75%, heat extraction is observed throughout the film zone, as shown in Fig. 6-6(g). On the other hand, at a fill ratio of 25%, the depth of the heat

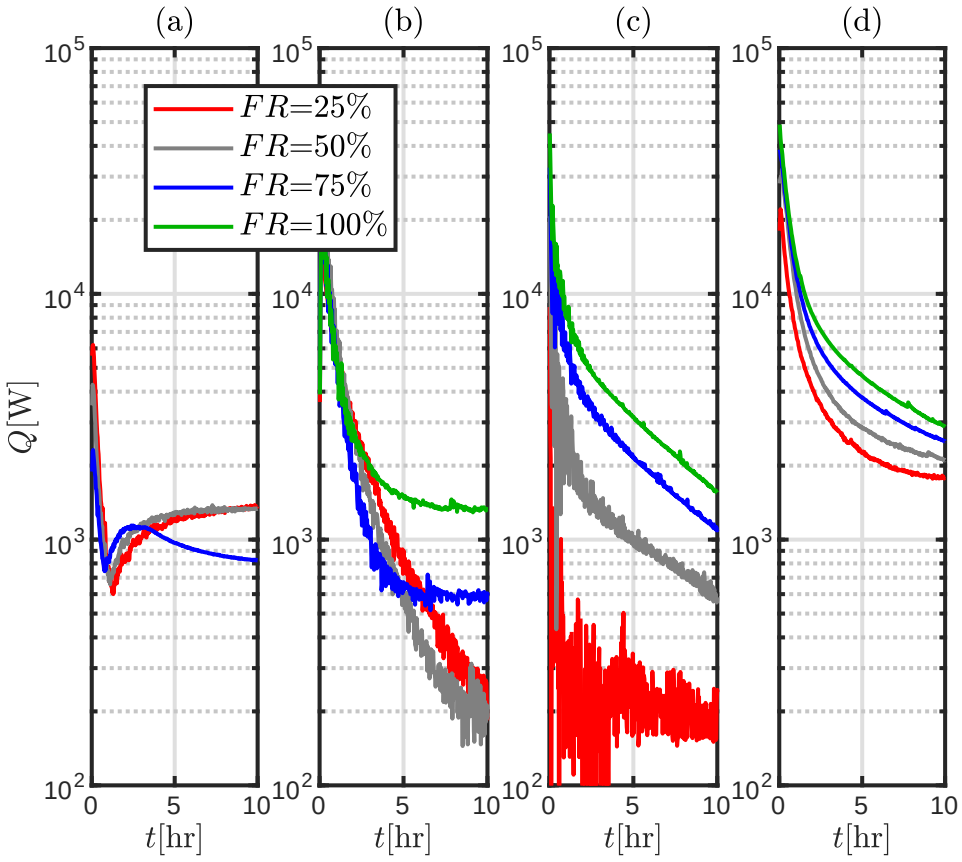

Figure 6-7: Heat transfer rate at different fill ratios in the a) film zone, b) active pool zone, and c) dead pool zone, in addition to the d) total heat transfer rate

extraction profile in the film zone is increased to 40 meters ($z = 60$ [m]) after of 10 hours of operation.

The amount of heat extracted in each zone depends on the fill ratio, as can be seen in Fig. 6-7. Evidently, heat extracted in the film-zone is inversely proportional to the fill ratio down to $FR = 50\%$, indicating that the film cold energy is utilized around a depth of 50 meters, as can be seen in Fig. 6-7(a). On the other hand, the pool active zone is proportional to the fill ratio down to $FR = 50\%$, below which the effect of the fill ratio becomes negligible, as can be seen in Fig. 6-7(b). Also, as for the dead pool zone, the amount of heat extracted is larger at higher fill ratios due to the larger volume of the dead zone, as can be seen in Fig. 6-7(c). Nevertheless, heat extracted at the dead zone decreases exponentially and is expected to have a minimal contribution once the thermosyphon reaches a steady state. Overall, after 10 hours of operation, the amount of heat extracted is proportional to the fill ratio, as shown in Fig. 6-7(d).

Heat extracted in each zone can be in the form of latent heat or sensible heat, as can be seen from Fig. 6-8. In the active pool zone, sensible heat is *initially* higher than latent, as shown in Fig. 6-8(a-d). However, as thermosyphons approach steady state, latent form of heat becomes more dominant than sensible heat. This happens more rapidly at higher fill ratios because of the faster feedback from the condenser which accelerates the steady-state behavior. As for the film zone, it can be seen that sensible heat is much more dominant than latent heat.

6.4.3 Impact of thermosyphon charge pressure

The charge pressure of the thermosyphon can significantly influence the initial saturation temperature along the depth of the thermosyphon, as seen in Fig. 6-9.

For instance, initializing the thermosyphon at a pressure of 1.5 [MPa] results in an initial vapor saturation temperature of -16.6[°C]; however, an initial charge pressure of 3.5 [MPa] results in a vapor saturation temperature of -1[°C], as shown in Fig. 6-9(a,c). After ten

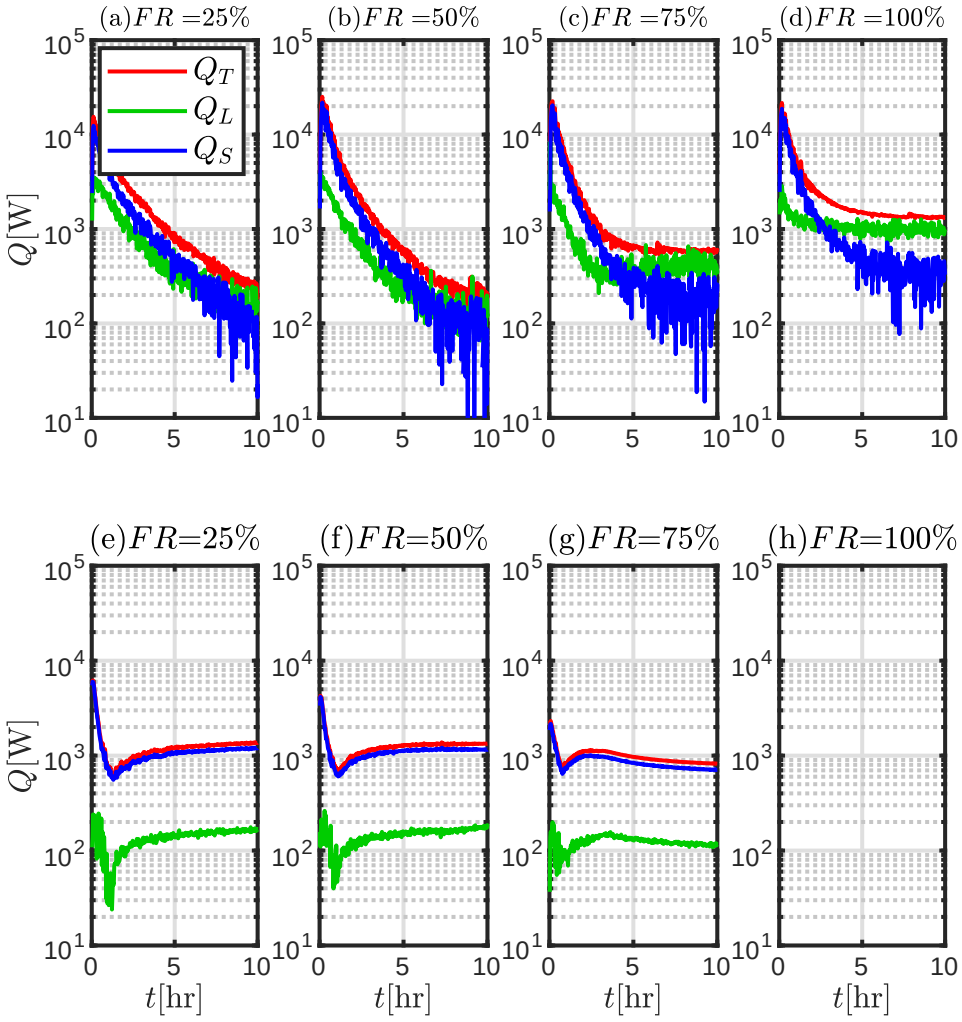

Figure 6-8: Modes of heat transfer at different fill ratios where Q_S, Q_L, and Q_T represent sensible heat transfer, latent heat transfer, and total heat transfer, respectively. Subplots (a-d) are calculated at the active pool zone, whereas subplots (e-g) are calculated at the film zone (there is no film zone at $FR = 100\%$).

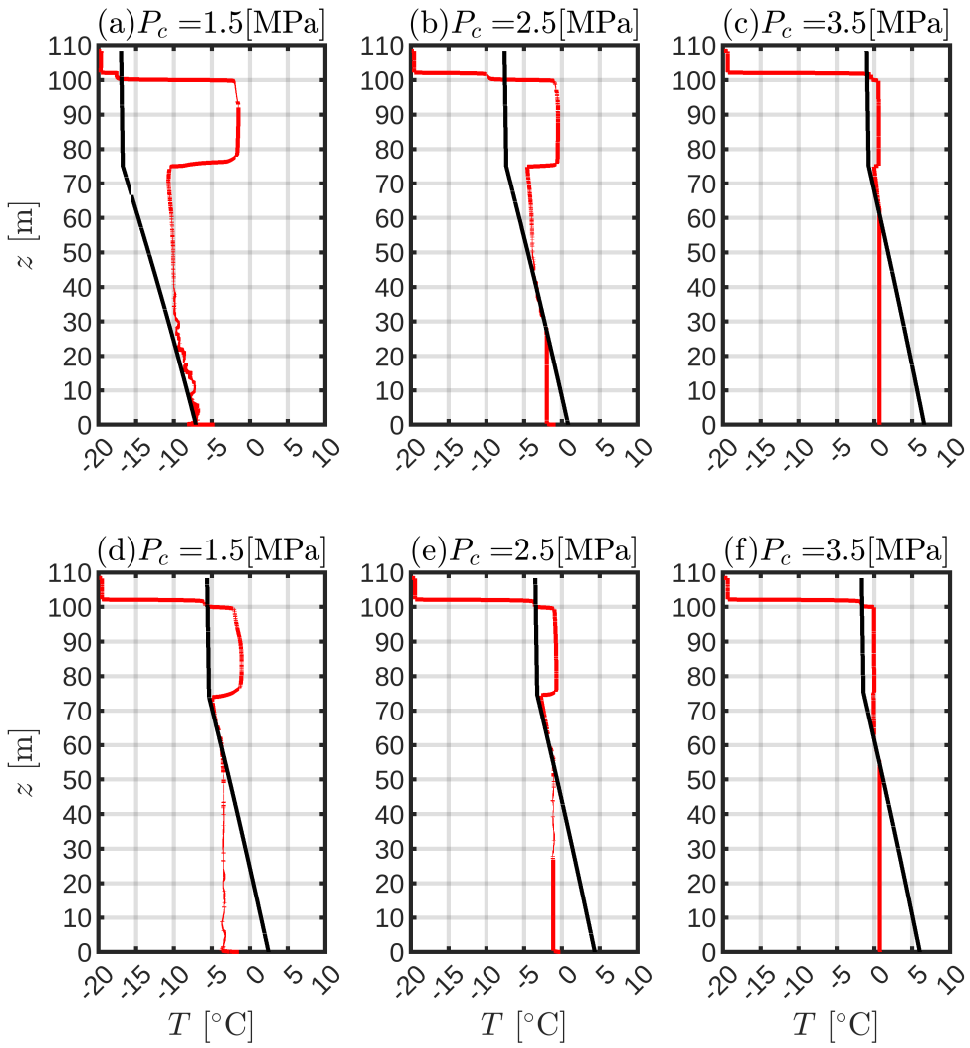

Figure 6-9: Thermosyphon wall temperature (in red) and nucleation temperature (in black) along the thermosyphon wall at different charge pressures. Subplots (a-c) are plotted after one hour of operation, whereas subplots (d-f) are plotted after 10 hours of operation. The bottom of the thermosyphon is considered as a reference point at $z = 0$; thus, the ground level is at $z = 100$ [m].

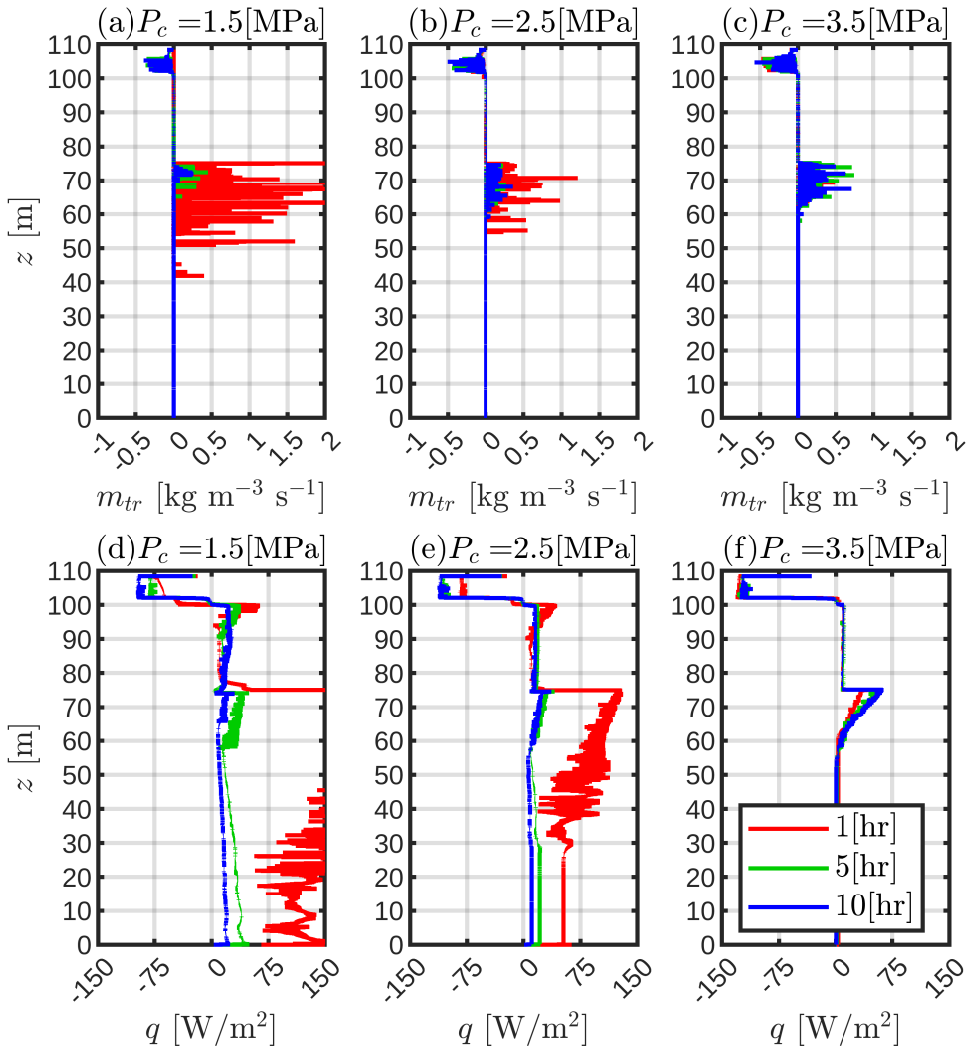

Figure 6-10: Mass transfer rate and heat flux along the thermosyphon wall at different charge pressure. (positive mass transfer rate denotes evaporation while negative mass transfer rate represents condensation). The red, green, and blue lines are plotted after one hour, five hours, and 10 hours of operation, respectively

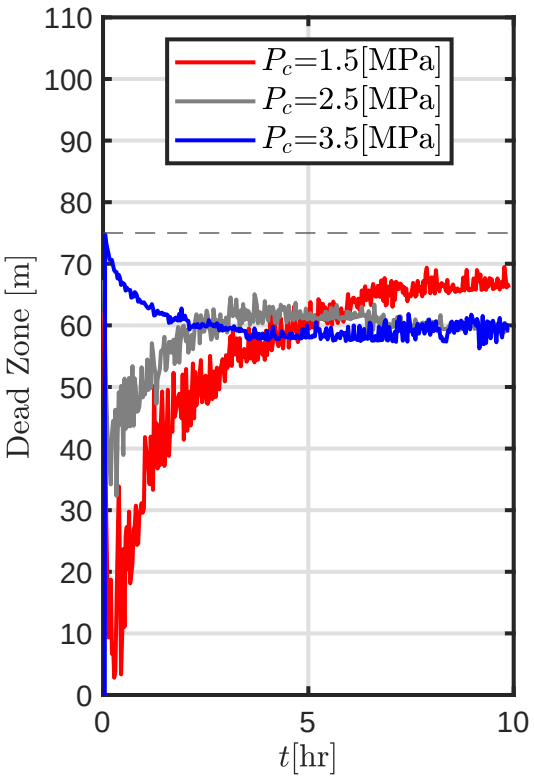

Figure 6-11: Extent of dead zone in the thermosyphon at different charge pressures through the first 10 hours of operation - the dashed lines represent the pool surface for all cases

hours of operation the vapor saturation temperature increases substntially at the cases of low initial charge pressure. Particularly, at an initial charge pressure of 1.5 [MPa], the vapor saturation temperature has increased by 11 [°C] (from -16 [°C] to -5 [°C]), as shown in Fig. 6-9(a,d). At a charge pressure of 2.5 [MPa], the vapor saturation temperature also increased but by 5 [°C] only, as shown in Fig. 6-9(b,e). Interestingly, at even higher initial pressure of 3.5 [MPa] the vapor saturation temperatures slightly *decreases* by 1 [°C]. Apparently, as the three cases approach steady state, the saturation temperature line converge to the same profile. The higher initial temperature difference at lower charge pressure results in a higher initial evaporation rate and heat flux, as can be seen in Fig. 6-10. This leads to a lower wall temperature, as shown in Fig. 6-9(c), which causes the evaporation rate and heat flux to decrease significantly after longer periods. As shown in Fig. 6-11, the dead zone at lower charge pressure is initially lower than that at higher pressures, but becomes larger with time as the wall temperature decreases and the saturation temperature increases. Another important observation from Fig. 6-10 is the more stable start-up of the thermosyphon at higher charge pressure. At lower charge pressures of 1.5[MPa] and 2.5[MPa], the heat extraction rate is very high initially and then decreases with time. On the other hand, at initial charge pressure of 3.5 [MPa], the heat extraction rate increases slowly and progressively, which is preferable on starting-up the thermosyphon. This is possibly the reason that field thermosyphons at the Giant Mine can be charged up to 5 [MPa] [11].

Similar qualitative trends are observed in different heat extraction zones along the thermosyphon at initial charge pressure of 1.5 [MPa] and 2.5 [MPa], as shown in Fig. 6-12. In the film zone, the amount of heat extracted is similar in both scenarios, as shown in Fig. 6-12(a). The initial fluctuation of heat flux at a charge pressure of 1.5[MPa] is attributed to very low feedback from the condenser in the first few hours, as implied in Fig. 6-10(a), due to the low saturation temperature of condensation at lower charge pressure. For an initial charge pressure of 3.5 [MPa], the initial heat extraction rate is almost negligible due to the low thermal gradient between the initial vapor saturation temperature and the ground. As

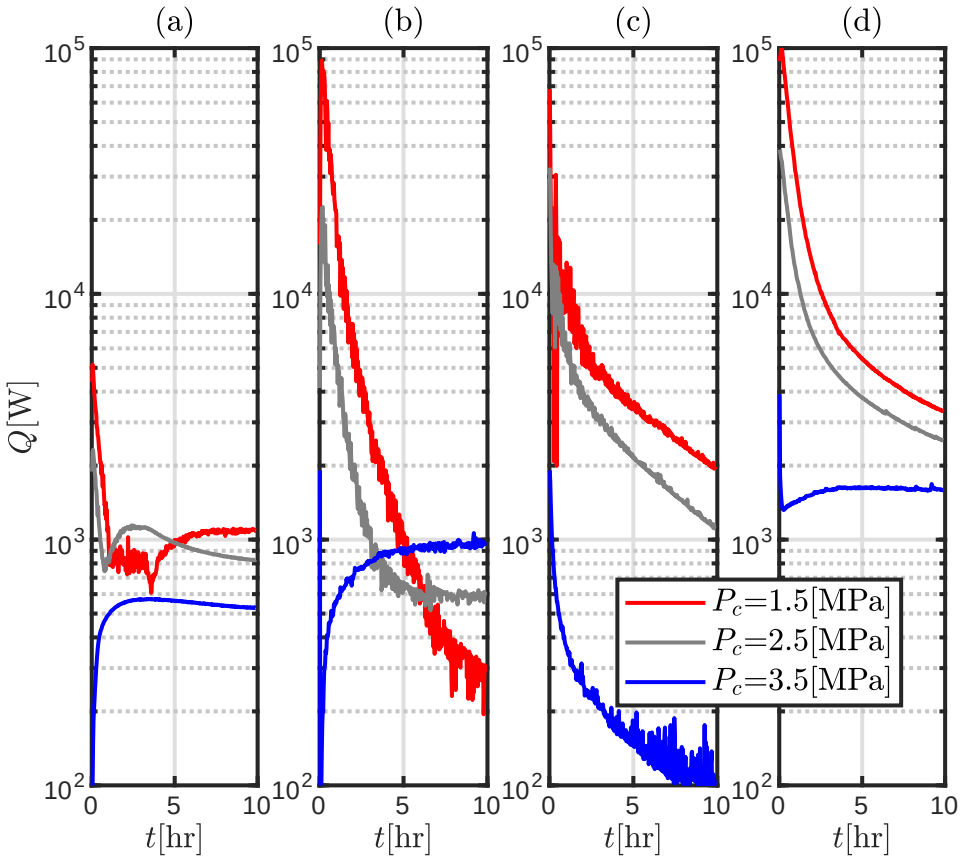

Figure 6-12: Heat transfer rate at different charge pressures in the a) film zone, b) active pool zone, and c) dead pool zone, in addition to the d) total heat transfer rate

film feedback develops from the condenser, the heat extraction rate increases. In the pool active zone, heat extraction changes rapidly in the first few hours of operation, as can be seen in Fig. 6-12(b). However, higher charge pressure extracts more heat after a certain period as steady-state is reached faster at higher charge pressure, as discussed in the previous paragraph. In regards to the dead zone, lower charge pressures extracts more heat due to the lower associated initial temperature − which is set according to the charge pressure − as shown in Fig. 6-12(c). Overall, lower charge pressure extracts more heat, mainly because the dead-zone. Nevertheless, the three scenarios are expected to be equal as the simulations reach steady state, due to the exponential decrease of heat extraction in the dead-zone. In the active pool zone, decreasing the charge pressure delays latent heat extraction in the pool active zone, as can be seen in Fig. 6-13(a-c). As for the film zone, it is observed again that the sensible heat extraction is more dominant compared to the latent heat extraction. At lower charge pressure, it is observed that the latent heat extraction approaches zero in the first few hours − implying an absence of the film, as already discussed in Fig. 6-10(a) and Fig. 6-12(a).

6.4.4 Impact of wind temperature

The last parameter investigated in this study is the wind temperature. Three different wind temperatures are investigated: 1) $T_{air} = -15[°C]$, 2) $T_{air} = -20[°C]$, and 3) $T_{air} = -30[°C]$. Evidently, lower wind temperature increases the condensation rate, which in turn increases the evaporation and heat extraction rate, especially after longer periods, as shown in Fig. 6-14. The dead-zone is also shrunk at lower wind temperature, as observed in Fig. 6-15, after three hours of operation. This is attributed to the cooler feedback from the condenser, which in turn decreases the temperature of CO_2 below the saturation temperature. Overall, the cooler the air temperature, the lower the feedback temperature from the condenser, and higher the heat extraction capacity of thermoysphons in all zones − except for the dead-zone, as shown in Fig. 6-16. The deadzone is too far from the pool surface to be affected

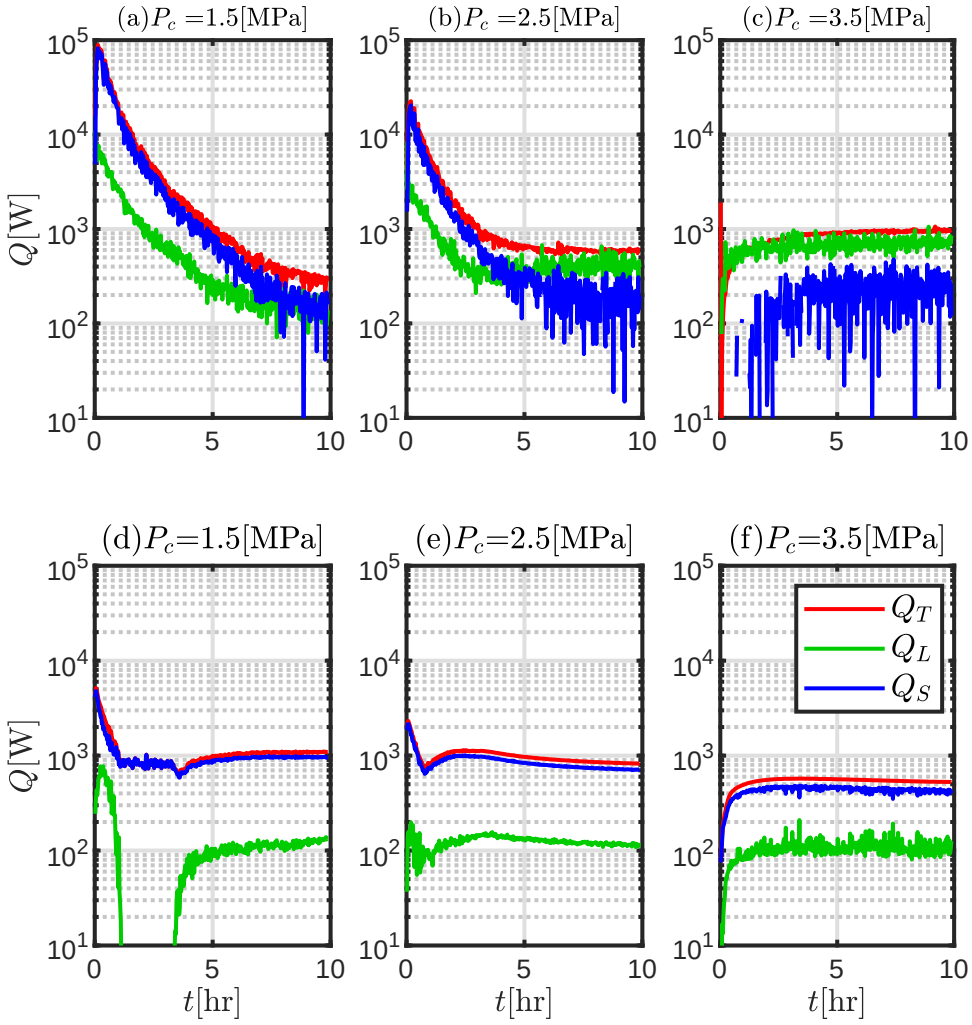

Figure 6-13: Modes of heat transfer at different charge pressures where Q_S, Q_L, and Q_T represent sensible heat transfer, latent heat transfer, and total heat transfer, respectively. subplots (a-c) are calculated at the active pool zone, whereas subplots (d-f) are calculated at the film zone.

by the wind temperature in the first ten hours. Further, the mode of heat extraction is qualitatively similar in all scenarios, as shown in Fig. 6-17, but quantitatively different.

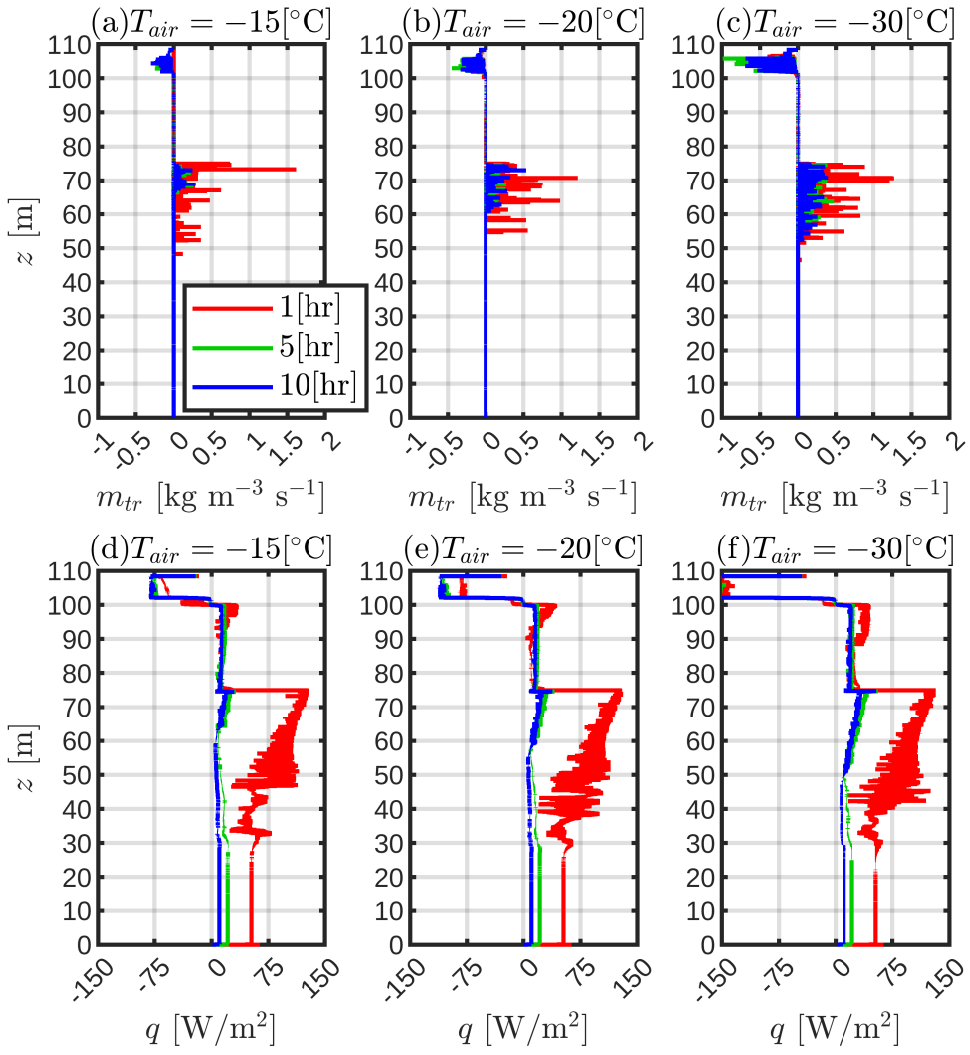

Figure 6-14: Mass transfer rate and heat flux along the thermosyphon wall at different wind temperatures (positive mass transfer rate denotes evaporation while negative mass transfer rate represents condensation). The red, green, and blue lines are plotted after one hour, five hours, and 10 hours of operation, respectively.

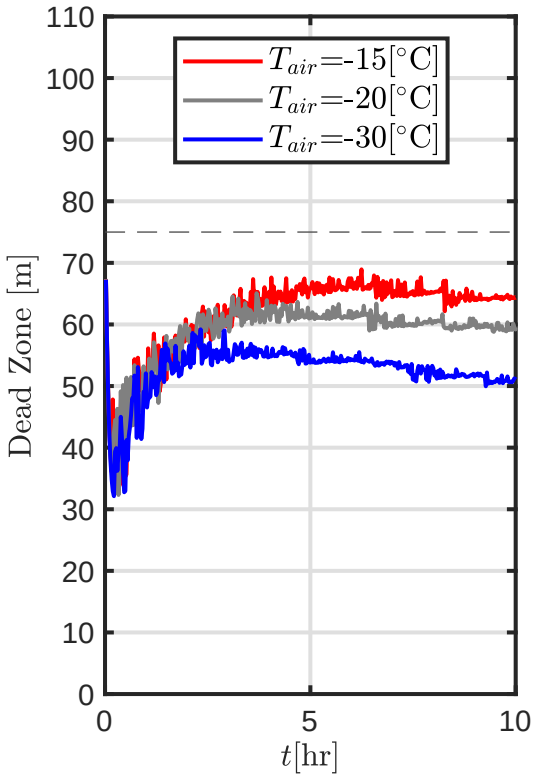

Figure 6-15: Extent of dead zone in the thermosyphon at different wind temperatures through the first 10 hours of operation - the dashed lines represent the pool surface for all cases

6.5 Conclusion

In this study, a CFD model is developed for super-long thermosyphons in artificial ground freezing applications, such as the Giant Mine Remediation Project. The CFD model is based on coupling a ground freezing model and mass transfer model in the thermosyphon, in order to capture the evaporation and condensation phenomena. Particularly, a novel heterogeneous mass transfer model, that takes into account the kinetic energy of bubble nucleation, is derived in this study. Furthermore, the impact of the hydrostatic pressure on the boiling phenomena is addressed in the model. The ground freezing model is validated in a previous work, whereas, the thermosyphon mass transfer model is validated against an experimental study from the literature.

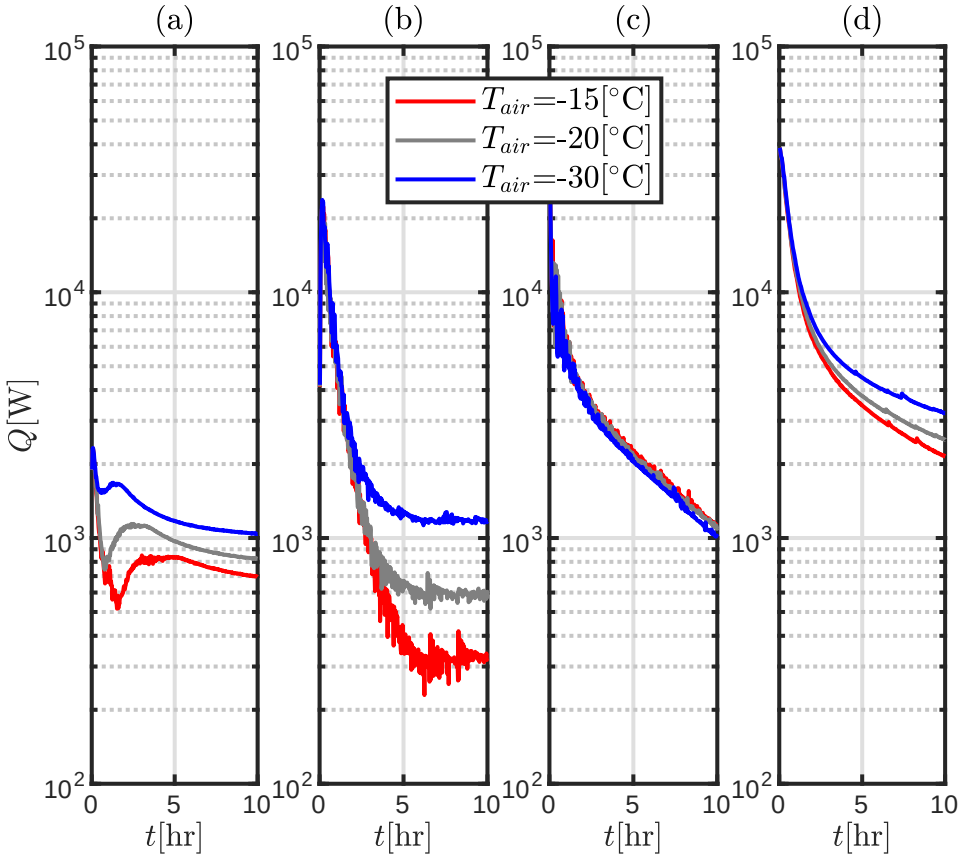

Figure 6-16: Heat transfer rate at different wind temperatures in the a) film zone, b) active pool zone, and c) dead pool zone, in addition to the d) total heat transfer rate

In this study, three different parameters have been considered, to analyze their impact on the heat extraction capacity and profile of thermosyphons: 1) The filling ratio of the thermosyphons, 2) the charge pressure of the thermosyphon, and 3) the wind temperature. The following observations are interpreted from the results:

- After hours of operation, the extent of the active pool zone – where boiling occurs – ranges between 10 to 25 meters from the pool surface. If the thermosyphon is filled by more than that, a dead zone with no boiling is formed.

- Sensible heat extraction dominates the pool active zone in the first few hours, but latent heat extraction becomes more significant as the thermosyphon reaches steady

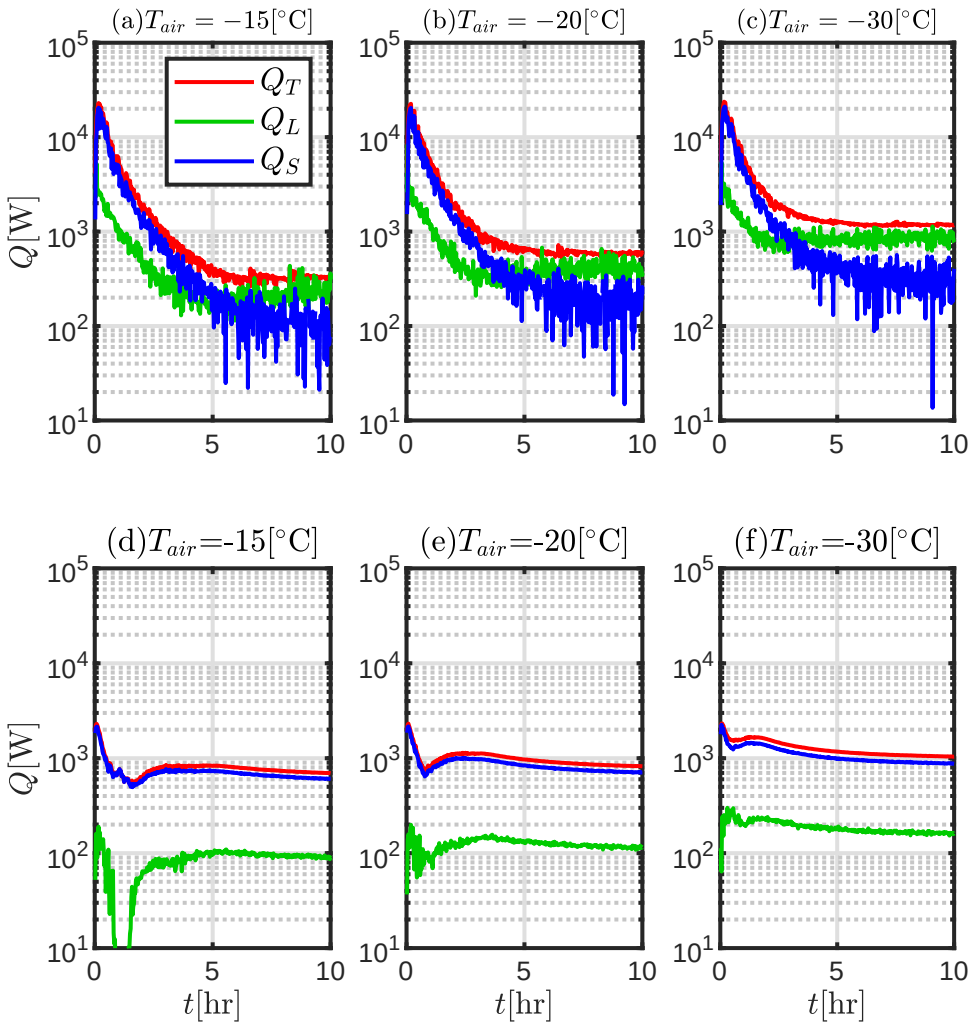

Figure 6-17: Modes of heat transfer at different wind temperatures where Q_S, Q_L, and Q_T represent sensible heat transfer, latent heat transfer, and total heat transfer, respectively. subplots (a) though (c) are calculated at the active pool zone, whereas subplots (d) through (f) are calculated at the film zone.

state.

- In the film zone, sensible heat extraction dominates throughout the operation of the thermosyphon.

- Decreasing the charge pressure decreases the saturation temperature of the thermosyphon initially, but eventually approaches a similar saturation temperature profile.

- Lower wind temperature increases the heat extraction capacity in the film zone and the active pool zone.

In our future work, we will use this dynamic analysis of deep thermosyphons to verify reduced-order models that feature higher computational efficiency. The reduced-order models will be implemented to analyze deep thermosyphon applications over long periods (years) considering the seasonal temperature.

Acknowledgments

The authors would like to thank the FRQNT Development Durable du Secteur Minier – II (2020-MN-284402) and Ultra Deep Mining Network (UDMN) (241695 Tri-Council (NCE – UDMN) 2-003). The first author wishes to thank the McGill Engineering Doctoral Award (MEDA) and the FRQNT Doctoral award (Grant No. 2021-B2X-306519).

Bibliography

[1] J. P. Zarling, F. D. Haynes, Thermosyphon-based designs and applications for foundations built on permafrost, in: Society of Petroleum Engineers - International Arctic Technology Conference, Anchorage, 1991, pp. 449–458. doi:10.2523/22114-ms.

[2] H. Ma, Heat Pipes, John Wiley & Sons, New Jersey, 2006.

[3] E. Long, Means for Maintaining Permafrost Foundations (1965).

[4] E. Long, The Long Thermopile, in: First International Conference on Permafrost, Lafayette, 1963, pp. 487–491.

[5] C. E. Heuer, Application of Heat Pipes on the Trans-Alaska Pipeline., Tech. Rep. 79-26 (1979).

[6] B. Zhang, Y. Sheng, J. Chen, J. Li, In-situ test study on the cooling effect of two-phase closed thermosyphon in marshy permafrost regions along the Chaidaer-Muli Railway, Qinghai Province, China (2011). doi:10.1016/j.coldregions.2010.10.012.

[7] H. Yandong, W. Qingbai, D. Jianhua, L. Jing, Z. Mingli, Y. Zeguo, Numerical simulation of efficient cooling by coupled RR and TCPT on railway embankments in permafrost regions, Applied Thermal Engineering 133 (2018) 351–360.

[8] W. Zhi, S. Yu, M. Wei, Q. Jilin, J. C. Wu, Z. Wen, Y. Sheng, W. Ma, J. L. Qi, J. C. Wu, Analysis on effect of permafrost protection by two-phase closed thermosyphon and

insulation jointly in permafrost regions, Cold Regions Science and Technology 43 (3) (2005) 150–163.

[9] Q. Yu, Z. Zhang, G. Wang, L. Guo, X. Wang, P. Wang, Z. Bao, Analysis of tower foundation stability along the Qinghai–Tibet Power Transmission Line and impact of the route on the permafrost, Cold Regions Science and Technology 121 (2016) 205–213. doi:10.1016/j.coldregions.2015.06.015.

[10] L. Guo, Y. Xie, Q. Yu, Y. You, X. Wang, X. Li, Displacements of tower foundations in permafrost regions along the Qinghai–Tibet Power Transmission Line, Cold Regions Science and Technology 121 (2016) 187–195. doi:10.1016/j.coldregions.2015.07.012.

[11] Crown Indigenous Relations and Northen Affiars Canada, Giant Mine Remediation Project– Arsenic Trioxide Frozen Shell Management and Monitoring Plant, Tech. rep. (2021).

[12] B. Abdalla, C. Fan, C. Mckinnon, V. Gaffard, Numerical study of thermosyphon protection for frost heave, in: ASME 2015 34th International Conference on Ocean, Vol. 5A, Newfoundland, 2015, pp. 1–6.

[13] B. A. Abdalla, H. Mei, C. McKinnon, V. Gaffard, Numerical evaluation of permafrost thawing in arctic pipelines and mitigation strategies, in: Arctic Technology Conference 2016, Newfoundland, 2016.

[14] M. Zhang, Y. Lai, J. Zhang, Z. Sun, Numerical study on cooling characteristics of two-phase closed thermosyphon embankment in permafrost regions, Cold Regions Science and Technology 65 (2) (2011) 203–210.

[15] W. Pei, M. Zhang, Z. Yan, S. Li, Y. Lai, Numerical evaluation of the cooling performance of a composite L-shaped two-phase closed thermosyphon (LTPCT) technique in permafrost regions, Solar Energy 177 (2019) 22–31.

[16] W. Pei, M. Zhang, Y. Lai, Z. Yan, S. Li, Evaluation of the ground heat control capacity of a novel air-L-shaped TPCT-ground (ALTG) cooling system in cold regions, Energy 179 (2019) 655–668.

[17] P. Yang, Numerical Analysis and Application Research of Heat Pipe to Solve Soil Frost Heaving Problem, Journal of East China Jiaotong University 15 (4).

[18] W. Cunzhen, S. Zhijian, P. Yang, Theoritic study on the technology of applying heat pipe to solving frost heaving, Chinese Journal of Geotechnical Engineering 24 (3) (2002) 347–350.

[19] P. Yang, W. Cunzhen, Numerical investigations and engineering applications on freezing expansion of soil restrained two-phase closed thermosyphons, International Journal of Thermal Sciences 41 (4) (2002) 341–347.

[20] A. F. Zueter, G. Newman, A. P. Sasmito, Numerical study on the cooling characteristics of hybrid thermosyphons: Case study of the Giant Mine, Canada, Cold Regions Science and Technology 189 (February) (2021) 103313. doi:10.1016/j.coldregions.2021.103313.

[21] A. D. Atrens, H. Gurgenci, V. Rudolph, CO2 thermosiphon for competitive geothermal power generation, Energy & fuels 23 (1) (2009) 553–557.

[22] A. Franco, M. Vaccaro, On the use of heat pipe principle for the exploitation of medium–low temperature geothermal resources, Applied Thermal Engineering 59 (1-2) (2013) 189–199.

[23] H. Liu, X. Wang, L. Zheng, H. Yao, Y. Zhu, Y. Wang, Temperature response and thermal performance analysis of a super-long flexible thermosyphon for shallow geothermal utilization: Field test and numerical simulation, International Journal of Heat and Mass Transfer 192 (2022) 122915. doi:10.1016/j.ijheatmasstransfer.2022.122915.

[24] N. Lamaison, C. L. Ong, J. B. Marcinichen, J. R. Thome, Two-phase mini-thermosyphon electronics cooling: Dynamic modeling, experimental validation and application to 2U servers, Applied Thermal Engineering 110 (2017) 481–494.

[25] C.-C. Chang, S.-C. Kuo, M.-T. Ke, S.-L. Chen, Two-phase closed-loop thermosyphon for electronic cooling, Experimental Heat Transfer 23 (2) (2010) 144–156.

[26] T.-E. Tsai, H.-H. Wu, C.-C. Chang, S.-L. Chen, Two-phase closed thermosyphon vapor-chamber system for electronic cooling, International Communications in Heat and Mass Transfer 37 (5) (2010) 484–489.

[27] A. Alizadehdakhel, M. Rahimi, A. A. Alsairafi, CFD modeling of flow and heat transfer in a thermosyphon, International Communications in Heat and Mass Transfer 37 (3) (2010) 312–318. doi:10.1016/j.icheatmasstransfer.2009.09.002.

[28] C. W. Hirt, B. D. Nichols, Volume of fluid (VOF) method for the dynamics of free boundaries, Journal of computational physics 39 (1) (1981) 201–225.

[29] S. C. K. De Schepper, G. J. Heynderickx, G. B. Marin, Modeling the evaporation of a hydrocarbon feedstock in the convection section of a steam cracker, Computers & Chemical Engineering 33 (1) (2009) 122–132.

[30] B. Fadhl, L. C. Wrobel, H. Jouhara, Numerical modelling of the temperature distribution in a two-phase closed thermosyphon, Applied Thermal Engineering 60 (1-2) (2013) 122–131. doi:10.1016/j.applthermaleng.2013.06.044.

[31] B. Fadhl, L. C. Wrobel, H. Jouhara, CFD modelling of a two-phase closed thermosyphon charged with R134a and R404a, Applied Thermal Engineering 78 (2015) 482–490. doi:10.1016/j.applthermaleng.2014.12.062.

[32] Z. Xu, Y. Zhang, B. Li, C. C. Wang, Y. Li, The influences of the inclination angle and evaporator wettability on the heat performance of a thermosyphon by simulation

and experiment, International Journal of Heat and Mass Transfer 116 (2018) 675–684. doi:10.1016/j.ijheatmasstransfer.2017.09.028.

[33] V. Kamburova, A. Ahmedov, I. K. Iliev, I. Beloev, I. R. Pavlović, Numerical modelling of the operation of a two-phase thermosyphon, Thermal Science 22 (2018) S1311–S1321. doi:10.2298/TSCI18S5311K.

[34] B. Abdullahi, A. El-Sayed, R. K. Al-Dadah, S. Mahmoud, A. F. Mahrous, N. M. az Muhammad, S. B. Abbakar, Experimental and numerical investigation of thermosyphon heat pipe performance at various inclination angles, Journal of Advanced Research in Fluid Mechanics and Thermal Sciences 44 (1) (2018) 85–98.

[35] H. Jouhara, B. Fadhl, L. C. Wrobel, Three-dimensional CFD simulation of geyser boiling in a two-phase closed thermosyphon, International Journal of Hydrogen Energy 41 (37) (2016) 16463–16476. doi:10.1016/j.ijhydene.2016.02.038.

[36] K. Kafeel, A. Turan, Axi-symmetric simulation of a two phase vertical thermosyphon using Eulerian two-fluid methodology (2013).

[37] X. Wang, Y. Wang, H. Chen, Y. Zhu, A combined CFD/visualization investigation of heat transfer behaviors during geyser boiling in two-phase closed thermosyphon, International Journal of Heat and Mass Transfer 121 (2018) 703–714.

[38] X. Wang, H. Yao, J. Li, Y. Wang, Y. Zhu, Experimental and numerical investigation on heat transfer characteristics of ammonia thermosyhpons at shallow geothermal temperature, International Journal of Heat and Mass Transfer 136 (2019) 1147–1159.

[39] X. Wang, Y. Zhu, Y. Wang, Development of pressure-based phase change model for CFD modelling of heat pipes, International Journal of Heat and Mass Transfer 145 (2019) 118763. doi:10.1016/j.ijheatmasstransfer.2019.118763.

[40] M. Knudsen, The cosine law in the kinetic theory of gases, National Aeronautics and Space Administration, 1967.

[41] X. Wang, H. Liu, Y. Wang, Y. Zhu, CFD simulation of dynamic heat transfer behaviors in super-long thermosyphons for shallow geothermal application, Applied Thermal Engineering 174 (March) (2020) 115295. doi:10.1016/j.applthermaleng.2020.115295.

[42] A. Zueter, A. Nie-Rouquette, M. A. Alzoubi, A. P. Sasmito, Thermal and hydraulic analysis of selective artificial ground freezing using air insulation: Experiment and modeling, Computers and Geotechnics 120 (2020) 103416.

[43] A. F. Zueter, M. Xu, M. A. Alzoubi, A. P. Sasmito, Development of conjugate reduced-order models for selective artificial ground freezing: Thermal and computational analysis, Applied Thermal Engineering 190 (2021) 116782.

[44] M. A. Alzoubi, A. Nie-Rouquette, A. P. Sasmito, Conjugate heat transfer in artificial ground freezing using enthalpy-porosity method: Experiments and model validation, International Journal of Heat and Mass Transfer 126 (2018) 740–752.

[45] A. F. Zueter, A. G. Madiseh, F. P. Hassani, A. P. Sasmito, Effect of Freeze Pipe Eccentricity in Selective Artificial Ground Freezing Applications, ASME Journal of Thermal Science and Engineering Applications 14 (2022) 011015.

[46] National Institute of Standards and Technology, NIST chemistry webbook (2018). URL https://webbook.nist.gov/

[47] SRK Consulting (Canada) Inc., Freeze Optimization Study Update for MVEIRB and Parties Aboriginal Affairs and Northern Development Freeze Optimization Study Update for MVEIRB and Parties, Tech. Rep. August, Ottawa (2012).

[48] V. Guichet, S. Almahmoud, H. Jouhara, Nucleate pool boiling heat transfer in wickless heat pipes (two-phase closed thermosyphons): A critical review of correlations, Thermal Science and Engineering Progress 13 (2019) 100384.

[49] W. M. Rohsenow, J. P. Hartnett, Y. I. Cho, Handbook of heat transfer, Vol. 3, McGraw-Hill New York, 1998.

Chapter 7

Numerical study on the cooling characteristics of hybrid thermosyphons: Case study of the Giant Mine, Canada

Preface

The CFD model presented in the previous chapter is computationally expensive. In order to examine AGF applications in field-scale for long periods of time, Alternative approaches need to be considered. In this chapter, we derive a novel thermal network model for hybrid thermosyphons employed in the Giant Mine Remediation tests.

" **A. F. Zueter**, G. Newman, and A. P. Sasmito. Numerical study on the cooling characteristics of hybrid thermosyphons: Case study of the Giant Mine, Canada. *Cold Regions Science and Technology*, 189:103313, 2021. doi.org/10.1016/j.coldregions.2021.103313"

Abstract

Hybrid thermosyphons have been installed in several permafrost protection applications due to their ability to operate continuously irrespective of seasonal temperature variations. In winter seasons, the thermosyphon operates passively by transferring energy between the ground and cold ambient air; while in warmer/summer seasons, an active refrigeration plant is used as a substitute for colder climate to extract the heat and freeze the ground. This study presents a novel conjugate mathematical model of hybrid thermosyphons based on thermal resistance networks, coupled with transient two-phase artificial ground freezing heat flow based on the enthalpy method. The model is validated against laboratory experimental data from literature and field test data from the Giant Mine in Yellowknife, Canada. Various design and operating parameters are investigated with the aim to maximizing ground heat extraction while minimizing energy consumption. The results indicate that active refrigeration substantially accelerates the formation of the desired frozen ground volume. After a certain time, passive cooling mode can be continuously adopted to reduce the energy consumption of refrigeration plants while maintaining the desired frozen ground thickness. Finally, the model can be used to assist engineers and practitioners to optimize the design of hybrid thermosyphon for permafrost protection or other ground freezing applications.

Contents

7.1 Introduction

The Giant Mine used to be one of the major driving forces of economic growth of the Northwest Territories (Canada) in the second half of the twentieth century [1]. More than 7,000,000 oz of gold were produced from around 20,000,000 tonnes of milled ore [2]. During the production process, the ore was roasted to high temperatures creating more than 237,000 tonnes of highly toxic arsenic trioxide waste [1]. The arsenic waste has been stored in underground chambers and stopes extending from around 20 to 90 meters below ground surface. These chambers and stopes used to be securely surrounded by solid impenetrable permafrost [3]. Nonetheless, due to global warming and underground activities, permafrost thawing has been intensifying, thereby increasing the risk of arsenic leakage. Consequently, industrial teams initiated the Giant Mine Remediation Project to assess different options of long-term management of the arsenic dust. Ultimately, encapsulating the arsenic waste within an artificially frozen shell was selected due to its construction reliability, robustness, and low risk on the workers and communities [4]. Following that, optimization studies were conducted to test different artificial ground freezing (AGF) techniques. A full-scale field test was developed around one of the smaller arsenic chambers which included conventional ground freezing, passive thermosyphon freezing (e.g. climate only), and hybrid thermosyphon freezing. The field test site was fully instrumented so that a complete understanding of the performance, as well as the capital and operating costs, could be established for each technology. Ultimately, passive thermosyphons with an optional conversion to hybrid cooling have been selected and construction will commence in 2021.

In addition to the Giant Mine, several AGF applications have tested and installed hybrid thermosyphon technologies. The first commercial use of this technology dates back to 1984 in Galena, Alaska, where it was used to freeze and stabilize the foundations of a communication site [5], [6]. Perhaps a more notable application of hybrid thermosyphons was the containment of contaminated water at the Oak Ridge National project in 1997 [7], [8]. In this case, fifty hybrid thermosyphons were used to create a frozen wall preventing the

leakage of radionuclides rich water. More recently, hybrid thermosyphons have been widely used in civil and mining applications in Canada. For example, they have been employed to speed up ground freezing for earlier construction of the Inuvik Hospital (Northwest Territories, Canada), to increase the efficiency of partially damaged passive thermosyphons of the Female Young Offender Facility (Northwest Territories, Canada), and to protect frozen ground affected by heat supply lines at the Simon Allaituq School (Nunavut, Canada) [9]. In the mining industry, the Diavik Diamond Mine (Northwest Territories, Canada) installed hybrid thermosyphons to accelerate the ground freezing associated with the construction of the mine dams [10] and the Lac De Gras dikes [9]. Furthermore, it is reported that hybrid thermosyphons are being employed more frequently in Russia [11]. In general, hybrid thermosyphons are attracting a widespread interest in the fields of AGF and permafrost protection because of their high operational adaptability to different ground and weather conditions.

A hybrid thermosyphon is made of a conventional refrigerant filled thermosyphon with the addition of a hybrid mechanical cooling unit as as shown in Fig. 7-1. They feature two types of condensers: an active condenser and passive condensers. Active condensers require a refrigeration system to supply a low temperature coolant during warm seasons, as shown in Fig. 7-1(a). This coolant is pumped through a helical coil to condense the refrigerant and extract its heat. On the other hand, passive condensers are equipped with radiator fins which exploit the cooling capacity of the ambient air during cold seasons to extract heat from the refrigerant, as can be seen from Fig. 7-1(b). In addition to the two condenser sections, hybrid thermosyphons comprise an evaporator section embedded in the ground. Overall, the thermosyphon operation is a multi-scale and multi-physics problem.

Accordingly, many mathematical studies have investigated *passive* cooling of thermosyphons in AGF applications. Yang et al., Lu et al., and Duan et al. [12], [13], [14] built mathematical models based on fields measurements to evaluate heat absorption by thermosyphons. To the best of our knowledge, the first to develop a coupled thermal resistance model of passive

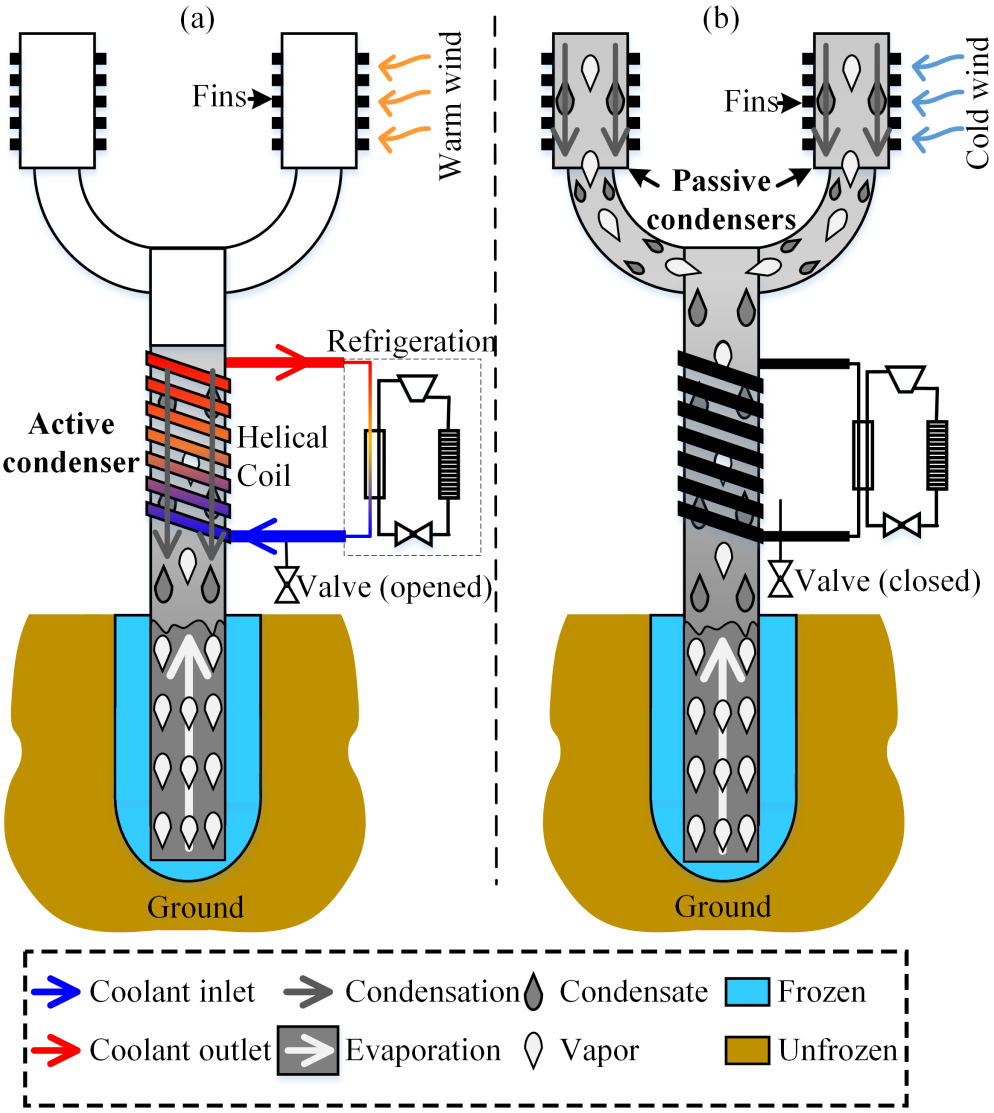

Figure 7-1: The operating principle of hybrid thermosyphons in artificial ground freezing applications: a) Active operation employing a refrigeration plant during warm season and b) passive operation utilizing cold air temperature during cold seasons (not-to-scale).

thermosyphons for AGF applications is Yang et al. [15], [16], [17] in 1998, in attempts to monitoring the freezing expansion of soil in the vicinity of construction foundations. Their model discretized the ground in 2D cylindrical co-ordinates and included the thermal resistance of the wind, condenser wall, liquid film condensation, liquid film boiling, pool boiling, and evaporator wall, as can be depicted from Fig. 7-2(a). Zhi et al. [18], Xu et al. [19], and Abdalla et al. [20], [21] simplified the thermal resistance network by considering a superconductor thermosyphon, linking the ambient air temperature with the outer wall temperature of the evaporator by a single thermal resistance located between the ambient air and the condenser, as shown in Fig. 7-2(b). Nevertheless, they added a switch, S_1, to deactivate the natural convection cycle of the thermosyphon when the evaporator temperature is lower than the condenser temperature; In addition, a 3D numerical model for the ground was considered. Wang et al. and Tian et al. [22], [23] assumed a similar superconductor thermal resistance model, but selected Nusselt correlations that depended on the wind velocity in their calculation of the wind thermal resistance. In 2011, Zhang et al. [24] used a 3D numerical model while extending the thermal resistance model by including the conduction, evaporation, and condensation thermal resistances inside the thermosyphon in addition to the S_1 switch and wind thermal resistance, as shown in Fig. 7-2(c). Film and pool boiling regimes were modeled by a single Nusselt correlation [25] applicable to both regimes. Since then, this 3D thermal resistance model has been used by many researchers to investigate passive cooling of thermosyphons for AGF applications [26], [27], [28], [29], [30]. Recently, Pei et al. [31], [32] firstly considered the inclination angle of the thermosyphon by modifying the evaporation and condensation correlations.

While there is a considerable amount of literature on passive thermosyphons [33], [34], [35], [36], [37] and conventional freeze-pipes [38], [39], [40], [41], [42], few studies have considered hybrid thermosyphons as an AGF technique. Haynes et al. [43] performed a series of experiments on hybrid thermosyphons to study the effects of the coolant inlet temperature and flow rate on the equivalent thermal conductance of hybrid thermosyphons. The

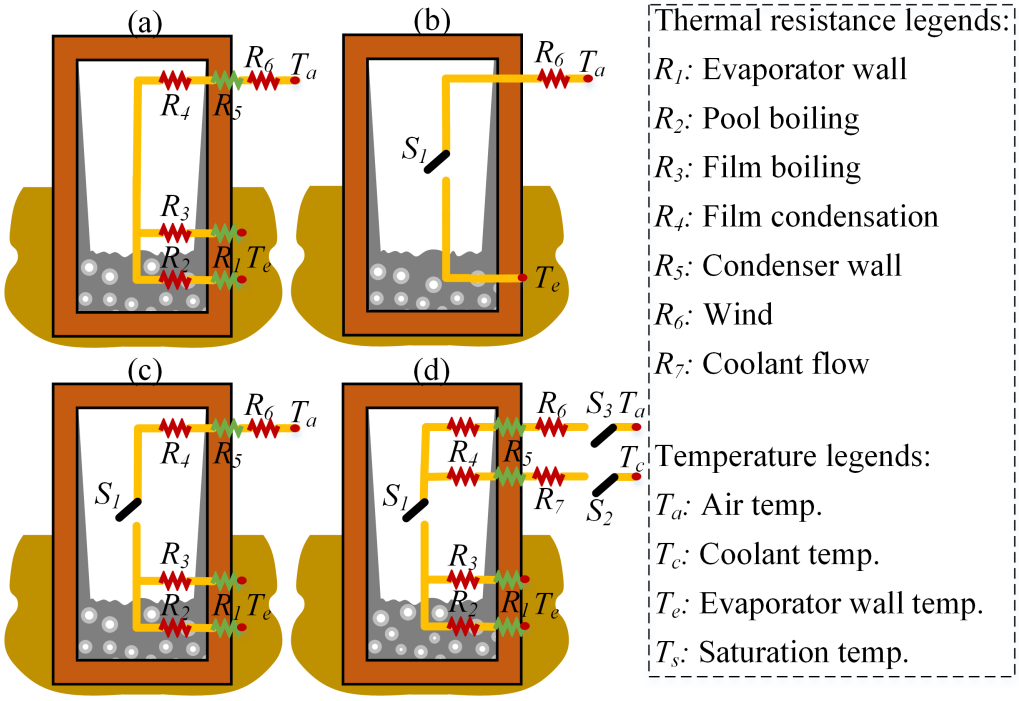

Figure 7-2: Progression of thermal resistance models of thermosyphons: a) The first passive cooling model developed by Yang et al. [15], [16], [17], b) passive cooling model assuming thermosyphon as a super-conductor [18], [19], [20], [21], [22], [23], c) the most widely used passive cooling model [24], [26], [27], [28], [29], [30], [31], [32], and d) hybrid cooling model of the present study (not-to-scale).

maximum inlet temperature and minimum inlet flow rate of the coolant were found to be -16 [°C] and 0.24 [kg s^{-1}], respectively, to obtain an equivalent thermal conductance of 3 [W $m^{-1}K^{-1}$] or greater — which is considered adequate for most foundation stabilization applications in Alaska [43]. Wagner and Yarmak [44], [45] investigated the quickness of frozen barrier formation by conducting several tests in Alaska. The frozen body thickness reached to 1 [m] during the active operation in the summer which lasted for 60 days, and then extended to 3.8 [m] during the passive operation in the winter season.

Previous work on hybrid thermosyphon technologies of AGF applications is limited to the experimental level. Nevertheless, there is a need for mathematical modeling of these technologies to better understand the underlying physics of their operation and thereby improve their performance in the field. As a consequence, the aim of our work is to develop a reliable coupled heat transfer model of hybrid thermosyphons. To this end, a thermal resistance model will be developed and validated against experimental measurements from the literature and field data from the Giant Mine technical reports [3], [46]. The model will be then employed to study the influence of various operational parameters on the performance of hybrid thermosyphons, namely the frozen ground expansion and the cooling load of refrigeration plants.

The paper is organized as follows. First, the mathematical model is presented, including a detailed derivation of the thermal resistance model of hybrid thermosyphons. After that, the model is validated against experimental measurements from the literature and field data from the Giant Mine tests. Finally, a set of parametric studies are conducted to analyze the design of hybrid thermosyphons

7.2 Mathematical model formulation

In this section, the governing equations and boundary conditions of the hybrid thermosyphon model are presented.

7.2.1 Governing equations

The computational domain of the present study is made up of the ground, a porous medium that consists of rock and water. Throughout this study, the saturated porosity of the ground does not exceed 10%, and the thermophysical properties of the rock and water are very close to that of the experimental study of Zueter et al. [39]. For this range of properties, Zueter et al. [39] determined that the local thermal equilibrium (LTE) assumption [47] is valid. Energy conservation in the ground can thus be expressed by balancing the diffusive and transient terms of the temperature field considering a one-temperature model as

$$\frac{\partial(\overline{\rho c_p}T)}{\partial t} = \nabla \cdot (\overline{k}\nabla T) + S, \tag{7.1}$$

where $\overline{\rho c_p}$ and $\overline{k}$ are the equivalent heat capacity and thermal conductivity of the ground (rock and water), while the source term, S, is added to include the latent heat of the water and is expressed as

$$S = -\frac{\partial(\gamma\overline{\rho L})}{\partial t}, \tag{7.2}$$

where $\overline{\rho L}$ is the equivalent volumetric latent heat of the ground and γ is the liquid fraction calculated based on the temperature as

$$\gamma = \begin{cases} 0 & , \ T < T_{sol}; \\ \frac{T - T_{sol}}{T_{liq} - T_{sol}} & , \ T_{sol} \leq T \leq T_{liq}; \\ 1 & , \ T > T_{liq}, \end{cases} \tag{7.3}$$

where T_{sol} and T_{liq} denote the solidus and liquidus temperatures, respectively. The equivalent latent heat content is related to the ground porosity, ϕ, as

$$\overline{\rho L} = \phi \rho_w L_w, \tag{7.4}$$

where ρ_w and L_w are the density and latent heat of water, respectively.

7.2.2 Boundary conditions

The thermosyphon boundary condition is the source of heat extraction from the ground and will therefore be analyzed separately in Section 7.2.2. After that, mathematical modeling of the other boundaries will be presented in Section 7.2.2.

Hybrid thermosyphon boundary condition

The thermosyphon boundary condition is modeled with the aid of a thermal resistance network, as shown in Fig. 7-2(d) and listed below:

1. Evaporator wall (R_1): The conductive thermal resistance of the evaporator wall, R_1, is given as [48]

$$R_1 = \frac{1}{2\pi k_{steel} \ell_e} ln\Big(\frac{D_{o,e}}{D_{i,e}}\Big), \tag{7.5}$$

   where k_{steel}, ℓ_e, $D_{o,e}$, and $D_{i,e}$ are the thermal conductivity of steel, length of the evaporator section, outer diameter of the evaporator wall, and inner diameter of the evaporator wall, respectively.

2. Liquid film and pool boiling ($R_{2,3}$): Immura's correlation [25] for the heat transfer coefficient of combined liquid film and pool boiling is adapted in this study as it has been employed and verified in multiple studies [49], [50]. The overall heat transfer coefficient is expressed as

$$h_{2,3} = 0.32 \left[\frac{\rho_f^{0.65} k_f^{0.3} c_{p,f}^{0.7} g^{0.2} q_e^{0.4}}{\rho_g^{0.25} h_{fg}^{0.4} \mu_f^{0.1}} \right] \Big(\frac{P_s}{P_{atm}}\Big)^{0.3} \tag{7.6}$$

   where g, μ, h_{fg}, and P_{atm} are the gravitational acceleration, viscosity, latent heat of vaporization, and atmospheric pressure, respectively. The subscripts f, g, and s refer to the liquid, gas, and saturated state of the refrigerant inside the thermosyphon. The

overall boiling thermal resistance, $R_{2,3}$, can now be determined as

$$R_{2,3} = \frac{1}{h_{2,3} A_{i,e}}, \tag{7.7}$$

where $A_{i,e}$ is the area of inner wall of the evaporator section.

3. Film condensation (R_4): The heat transfer coefficient correlation derived by Nusselt [51] is selected due to its agreement with the laminar flow regime of this study, as well as its frequent reliability [52]. The film condensation heat transfer coefficient is given as

$$h_4 = 0.925 \left[\frac{k_f^3 \rho_f^2 g h_{fg}}{\mu_f q_n \ell_n} \right]^{1/3}. \tag{7.8}$$

where q_n is the heat flux through the condenser while L_n is the length of the condenser. The condensation thermal resistance can then be calculated as

$$R_4 = \frac{1}{h_4 A_{i,n}}, \tag{7.9}$$

where $A_{i,n}$ is the area of the inner side wall of the condenser.

4. Condenser wall (R_5): The conductive thermal resistance of the condenser wall is given as [48]

$$R_5 = \frac{1}{2\pi k_{steel} \ell_n} ln\Big(\frac{D_{o,n}}{D_{i,n}}\Big), \tag{7.10}$$

where $D_{o,n}$ and $D_{i,n}$ are the height of the condenser section, the outer diameter of the condenser wall, and the inner diameter of the condenser wall, respectively.

5. Air-fin (R_6): The Nusselt number of air flow across the condenser relies on the Reynolds

number of the wind, Re_a, as [48], [53]

$$Nu_a = \frac{h_6 D_{o,c}}{k_a} = \begin{cases} \eta_{fin}\ 0.989 Re_a^{0.330} Pr_a^{1/3} & ,\ Re_a < 4; \\ \eta_{fin}\ 0.911 Re_a^{0.385} Pr_a^{1/3} & ,\ 4 \leq Re_a < 40; \\ \eta_{fin}\ 0.683 Re_a^{0.466} Pr_a^{1/3} & ,\ 40 \leq Re_a < 4000; \\ \eta_{fin}\ 0.193 Re_a^{0.618} Pr_a^{1/3} & ,\ 4000 \leq Re_a < 40000; \\ \eta_{fin}\ 0.027 Re_a^{0.805} Pr_a^{1/3} & ,\ 40000 \leq Re_a, \end{cases} \tag{7.11}$$

where η_{fin} is the fin efficiency, which is a function of the fin geometry and determined to be 65% according to the charts of Gardner [48], [54] for circular fins. The thermal resistance of the air flow across the condenser can now be calculated as

$$R_6 = \frac{1}{h_6 A_{fin}}, \tag{7.12}$$

where A_{fin} is the finned area of the condenser. Heat convection from the unfinned part is neglected due to its small contribution in the heat transfer as compared with the finned part.

6. coil-condenser (R_7): In hybrid thermosyphons, helical coils are compactly wrapped around the active condenser region. Active cooling is achieved by pumping a refrigerated liquid into these coils to condense the refrigerant and force the thermosyphon evaporation/condensation cycle. These coils are well insulated to maximize heat extraction from the condenser and minimize heat gain from the ambient air to the coolant. Heat transfer efficiency between such insulated coils and thermosyphons, η_{hc}, is assumed to be 90% as measured experimentally by Wang et al. [55].

   The Nusselt number correlation proposed by Seban and Mclanghin [56], [57] is adapted as its range of Reynolds number, Prandtl number, and Deans number is within the

limits of our study. This correlation is expressed as

$$Nu = \frac{h_7 D_c}{k_c} = 0.065 f_c^{0.33} Re_c^{0.66} Pr_c^{0.33}, \tag{7.13}$$

where f_c is the friction factor of the coolant flow calculated as [58]

$$f_c = \frac{64}{Re_c}\left\{1 - \left[1 - \left(\frac{11.6}{Dn_c}\right)\right]^{0.45}\right\}^{-1} \tag{7.14}$$

where Dn_c is the Deans number. The thermal resistance of the helical coils can then be calculated as

$$R_7 = \frac{1}{\eta_{hc} h_7 A_c}, \tag{7.15}$$

where A_c is the heat transfer area of the coils.

After calculating each individual thermal resistance, the equivalent thermal resistance is determined. The evaluation of the equivalent thermal resistance depends on the status of the three switches shown in Fig. 7-2. S_2 and S_3 are user-controlled representing active and passive cooling regimes. During passive operations in cold seasons, S_3 is switched on to activate passive cooling while S_2 is switched off indicating that the refrigeration plant is inactive. On the other hand, during warm seasons, S_3 is switched off while S_2 is switched on. The coils are often designed to be large enough to ensure that the refrigerant condenses in the active condenser section before reaching the passive condensers. Unlike S_2 and S_3, S_1 is not user-controlled; it represents the status of the natural convection cycle of the refrigerant inside the thermosyphon. Particularly this switch is opened only when the heat sink temperature (air or coolant temperature) is higher than that of the evaporator wall temperature.

Once the equivalent thermal resistance, R_{eq}, is found, the equivalent heat flux across the

evaporator wall, q_e, can be determined as

$$q_e = \frac{Q_{total}}{A_e} = \frac{T_\infty - T_e}{R_{eq} A_e}, \tag{7.16}$$

where subscript e refers to the outer evaporator wall, and T_∞ represents the heat sink temperature. The thermal boundary condition along the evaporator wall can then be expressed as

$$-\overline{k} \frac{\partial T}{\partial n}\bigg|_e = q_e, \tag{7.17}$$

where n is a normal vector to the boundary.

Ground boundary conditions

In addition to the hybrid thermosyphon boundary, other boundary conditions are mathematically modeled. An axi-symmetric boundary is set in most of the simulations where the variations of the temperature field in the angular direction is negligible as compared with that of the radial and axial directions. This boundary is often considered in simulations that involve a single thermosyphon in an axi-symmetric computational domain. In these simulations, the change of temperature in the radial direction equals to zero along the axis of symmetry as [48]

$$\frac{\partial T}{\partial r}\bigg|_{axis} = 0. \tag{7.18}$$

Along the bottom boundary, geothermal heat flux is set as [48]

$$-\overline{k} \frac{\partial T}{\partial n}\bigg|_{bottom\ boundary} = q_{geo}, \tag{7.19}$$

where $q_{geo} = 0.06$ [W/m^2].

Boundary independence study was conducted at the far boundary from the evaporator to ensure that this boundary has no effect on the temperature field near the thermosyphon. The study shows that a distance of 50 [m] is sufficient to obtain a boundary independent

solution. The far boundary is an insulated wall as

$$\left.\frac{\partial T}{\partial n}\right|_{far\ boundary} = 0. \tag{7.20}$$

The top boundary of field simulations is subject to atmospheric convection as

$$-\overline{k}\left.\frac{\partial T}{\partial n}\right|_{top\ boundary} = h(T|_{top\ boundary} - T_a), \tag{7.21}$$

where T_a is the air temperature and the atmospheric heat transfer coefficient is set at 3 [W/(m^{2}K)].

7.3 Choice of numerical parameters

The spatial and transient terms of the governing equation of the ground (Eq. (7.1)) were discretized by second order upwind schemes. The non-linear equations of the thermal resistance network model were solved inside a set of user-defined-functions (UDF) iteratively, in conjunction with the iterative solution of the governing equations of the ground and other boundary conditions listed in Section 7.2.2. ANSYS Fluent 18.1 was used to compute the equations as prescribed by our model and UDFs.

Prior to validating our model and running the parametric studies, mesh independence study was conducted and ensured. The selected mesh size and type greatly relies on the simulation scenario as we have conducted various 3D and 2D simulations of different length scales. In all cases, the mesh and geometry were generated with the aid of ANSYS Fluent 18.1.

7.4 Validation

The model was validated in three consecutive stages. First, the passive cooling regime was validated against an experimental study from the literature [59]. After that, this passive model was extended to field scale and validated against field data from the Giant Mine test study [3]. Lastly, the active cooling regime was incorporated to the passive cooling model, and the combined model was validated against field data from the Giant Mine freezing optimization study (FOS) [46].

7.4.1 Passive cooling validation against an experimental study

Mathematical modeling of the passive cooling mode was validated against the experimental study of Pei et al. [59]. The experimental setup consisted of a thermosyphon filled by ammonia, a 9.8% porous soil, and fans, as shown in Fig. 7-3. Prior to starting the experiment, the soil temperature was uniformly set at 16 [°C] as recorded by multiple thermocouples. After that, air was blown by a fan for 72 hours at a speed of 2.8 m/s and a sinusoidal temperature of

$$T[^{\circ}C] = -12\ sin\left(\frac{2\pi}{216}\ t[hr]\right). \tag{7.22}$$

The transient temperature data of three thermocouples, shown in Fig. 7-3, were reported. More details about the experiment can be found in [59].

Very good agreement is noted between the results of our mathematical model and the experimental measurements, as shown in Fig. 7-4. The sinusoidal behavior of the temperature profile is caused by the sinusoidal variation of the air temperature, as noted from Eq. 7.22. The thermosyphon extracts heat from the ground when the air temperature is lower than the evaporator temperature, resulting in reduction of ground temperature. Nevertheless, as the thermosyphon is inactive when the air temperature is higher than the evaporator wall temperature (S_1 opens), the temperature of the ground near the thermosyphon increases due to the incoming heat from the surrounding warmer ground. The small time lag between

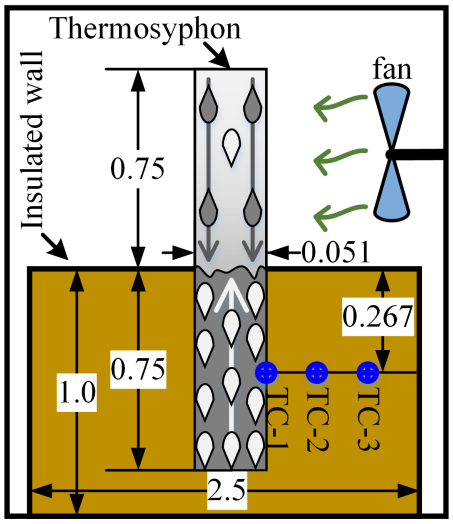

Figure 7-3: Non-to-scale schematic of the experimental setup of Pei et al. [59]. The blue circles indicate the thermocouples (TC) positions (please refer to Fig. 7-1 to find the labels of other symbols). TC-1 is fixed at the outer wall of the evaporator, while TC-2 and TC-3 are displaced 0.2 [m] and 0.5 [m] from the thermosyphon, respectively. The ground volume is 2.5 [m] $\times$ 1.84 [m] $\times$ 1.0 [m].

the numerical results and the experimental data of the ground temperature is attributed to the uncertainty of the thermal diffusivity of the sand and exact phase change temperature of the water content.

7.4.2 Passive cooling validation against the Giant Mine field test study

Although thermosyphons have been used in the AGF industry for many decades prior to the Giant Mine Remediation Project, most of the applications have thermosyphons installed closer to the ground surface. However, the arsenic chambers which need to be frozen at the Giant Mine are 75 meters deep with one extra zone requiring thermosyphons to be 140m deep. For this reason, a preliminary experimental study was initiated at the Giant Mine in 2002 to ensure the capability of thermosyphons to extract heat over longer depths.

The field experiment involved a 102.1[m] deep thermosyphon (refer to Table 7.1 for details on the geometry [60]) embedded in layered ground. Specifically, the top five meters of the

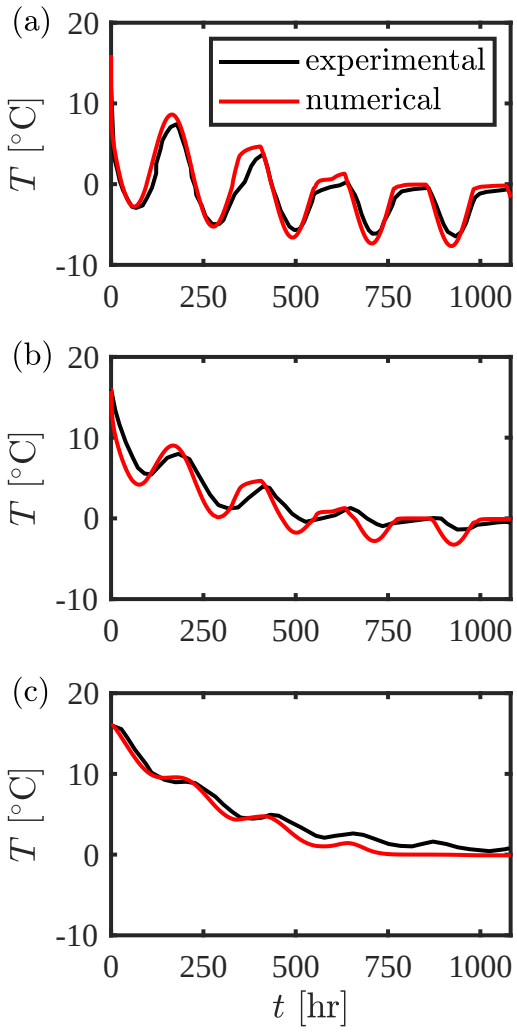

Figure 7-4: Validation of the present model against the experimental study of Pei et al. [59] a) At the evaporator wall (TC-1), b) horizontal distance of 0.2 [m] from the evaporator wall (TC-2), and c) horizontal distance of 0.5 [m] from the evaporator wall (TC-3). The position of the thermocouples is shown in Fig. 7-3.

property	value
Finned area of passive condenser	39 [m^2]
Evaporator outer diameter	73 [mm]
Evaporator thickness	5.3 [mm]
Condenser outer diameter	88.9 [mm]
Condenser thickness	8 [mm]

Table 7.1: Geometry of the test thermosyphon used in the passive model validation. Details on the geometry can be found in [60].

ground was overburden (clay and silt mixture), sitting above bedrock (greenstone). The thermosyphon was charged by pressurized carbon dioxide rather than ammonia since the latter tends to form non-condensable gases that occupy significant portions of the condenser and thereby reduce the condenser efficiency. In addition, ammonia was avoided since it poses significant health and safety risks on the workers. The thermophysical properties of the overburden, bedrock, and carbon dioxide are listed in Table 7.2. Approximately 20 thermocouples were fixed either directly to the outer wall of the evaporator to monitor heat transfer across the ground-pipe contact, or within an adjacent instrumentation hole to monitor cooling in the ground. This hole was originally targeted to be 2 meters away from the thermosyphon, but vertical alignment survey revealed that the distance between the thermosyphon and the thermocouples ranges between 2.1 [m] and 2.8 [m], as shown in Fig. 7-5(a). After completing the installation, the field experiment started on the fifth of March 2002, and the initial results were reported on the third of May 2002. The temperatures of the ground and evaporator wall in these two dates were measured, as shown in Fig. 7-5(b) and Fig. 7-5(c), respectively.

The accuracy of our mathematical model was tested against the field data measurements. The air temperature and speed data were not averaged (curve-fitted) as Fong et al. [63] found that heat transfer calculations are highly influenced by the instantaneous variations of environmental data. Instead, hourly data measured by the Giant Mine weather station [64] were adopted in this study, as shown in Fig. 7-6. The results demonstrated the ability

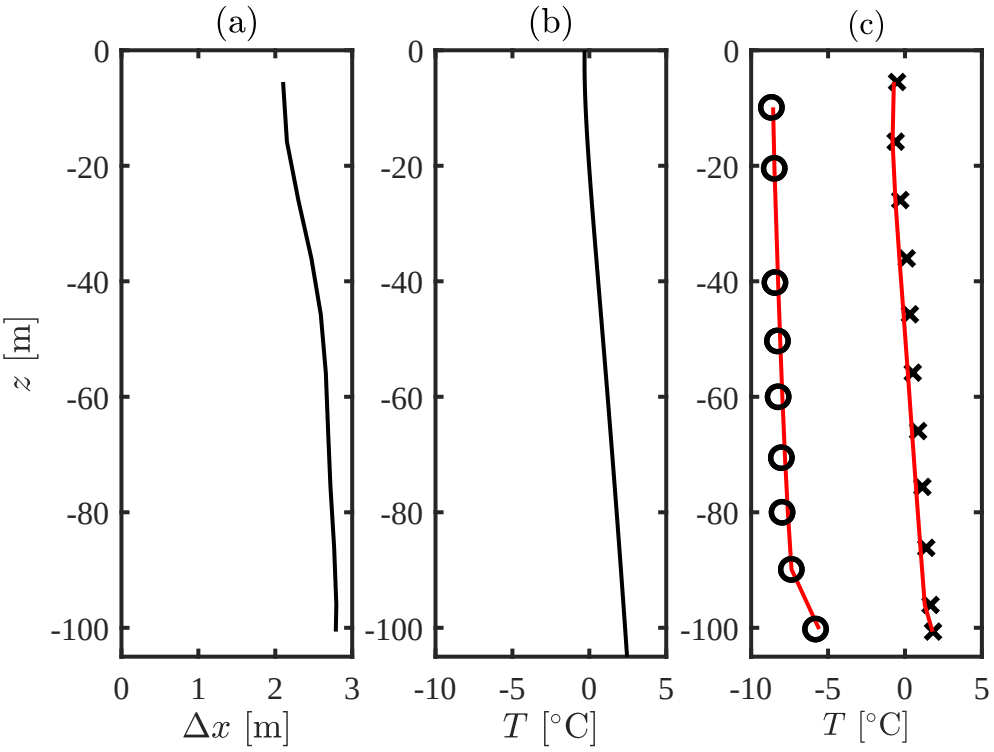

Figure 7-5: Validation of the passive cooling model of the present study against the Giant Mine field test [3]: a) Displacement of the instrumentation hole from the thermosyphon, b) Initial ground temperature as measured by the thermocouples and then curve-fitted, and c) validation of our mathematical model (red line) against the experimental measurements of the temperature on the thermosyphon wall (o) and in the instrumentation hole (×).

Material	ρ [kg/m^3]	c_p [J/(kg·k)]	k [W/(m·k)]	μ [Pa s]
Condensate CO_2 [61]	959	2396	0.117	1.09E-4
Vapor CO_2 [61]	81.9	1643	18.0E-2	1.42E-5
R-507 [62]	1263	1279	89.1E-2	2.61E-4
Frozen overburden [3]	1867	1158	2.09	-
Unfrozen overburden [3]	1900	1564	1.40	-
Frozen rock-1 [3]	2958	784	2.61	-
Unfrozen rock-1 [3]	2959	792	2.59	-
Frozen rock-2 [46]	2926	814	3.45	-
Unfrozen rock-2 [46]	2927	822	3.44	-

Table 7.2: Thermophysical properties of the materials used in the Giant Mine tests. Rock-1 and rock-2 refer to the bedrock of the passive experiment and the bedrock of the hybrid experiment, respectively. The water content of the bedrock is 1% in all field simulations [3], [46].

of the mathematical model to anticipate the evaporator and ground temperatures in field dimensions. The temperature of the ground 5 meters below the surface is noted to be slightly warmer than that of 10 meters below the surface due to the presence of the highly porous overburden at the top. The significance of layered ground modeling is studied in detail by Zhou et al. [65]. Overall, the ground temperature decreased by around 0.5 [°C] throughout the depth of the thermosyphon. Such a small difference in temperature is expected since only a single thermosyphon was operated during relatively warm months (as compared to winter seasons) and for a short period of time. Still, this study successfully achieved its primary objective of operating deep thermosyphons in AGF applications.

7.4.3 Hybrid cooling validation against the Giant Mine field data

Following the success of deep lone thermosyphons test, the freezing performance of multiple AGF techniques were investigated at full field scale around the perimeter of one of the smaller arsenic chambers, as shown in Fig. 7-7. From this study, we have selected group F to validate our hybrid thermosyphon model. This group includes four hybrid thermosyphons and three

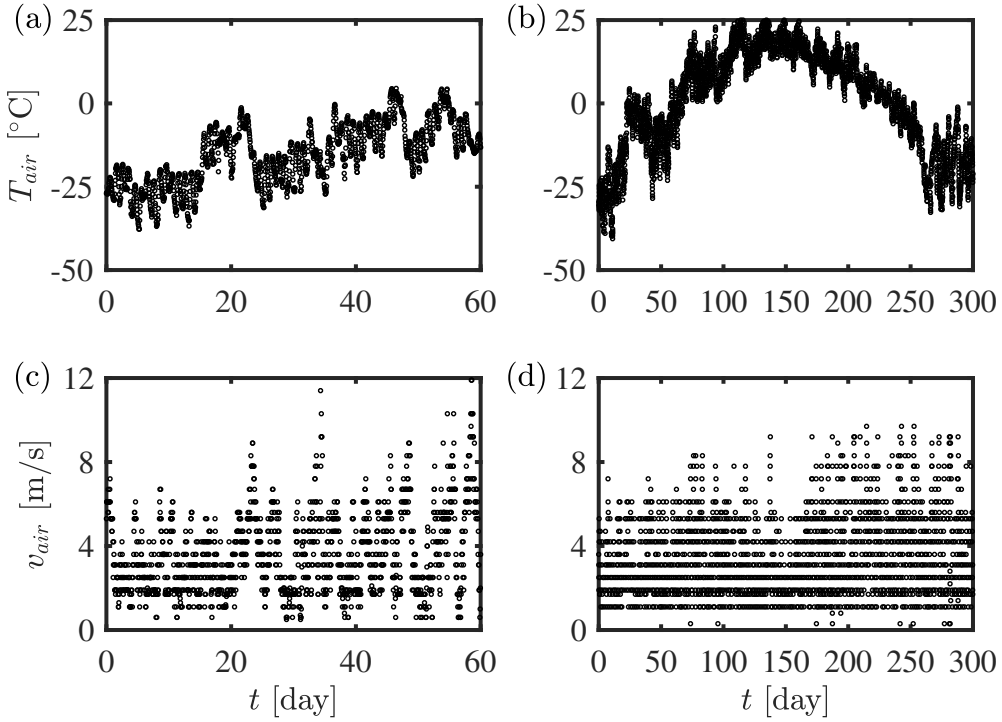

Figure 7-6: Hourly air data measured by the Giant Mine weather station [64]: Air temperature data of the a) passive thermosyphon test and b) hybrid thermosyphon test, and air speed data of the c) passive thermosyphon test and d) hybrid thermosyphon test.

property	value
Finned area of passive condenser	39 [m^2]
Thermosyphon outer diameter	114 [mm]
Thermosyphon thickness	10 [mm]
Helical coil outer diameter	10.3 [mm]
Helical coil thickness	1.7 [mm]
Helical coil height	2.4 [m]

Table 7.3: Geometry of hybrid thermosyphons used in our calculations [46].

instrumentation holes as shown in Fig. 7-7. The thermosyphons were initially set on the passive cooling mode from the 5^{th} of March 2011 till the 25^{th} of May 2011, as noted from Fig. 7-8(a). From this date onward, active cooling mode was adopted for a period of around 7 months. A type of hydrocarbon refrigerants called R-507 was chosen to be the coolant of the active cooling regime because of its environmentally friendly and non-corrosive qualities. The geometry of the hybrid thermosyphons and the thermophysical properties of R-507 [62] can be found in Table 7.3 and Table 7.2, respectively.

The results of our mathematical model are in a good agreement with the field measurements, as can be seen from Fig. 7-8(b). During passive operation, the heat flux fluctuated due to the hourly variation of the wind temperature and speed. By the end of the passive operation, the air temperature became warmer than the evaporator temperature. Consequently the natural convection cycle inside the thermosyphon stopped, cutting the heat transfer circuit (the S_1 switch shown in Fig. 7-2(d) is opened) and resulting in a zero heat flux. This led to an increase in the ground temperature by the end of the passive regime. Once active operation is switched on (S_2 is closed), the heat flux significantly increased, and the ground freezing process resumed. The results also show that the ground temperature dropped faster in the active cooling mode as compared with the passive one. This would be the case of such hybrid thermosyphons using coolants running at low temperatures (around -35 [°C]) and high flow rates (20-100 [kg/hr]). The small deviations of the third instrumentation hole is likely due to the spatial variations of the water content of the bedrock especially near the

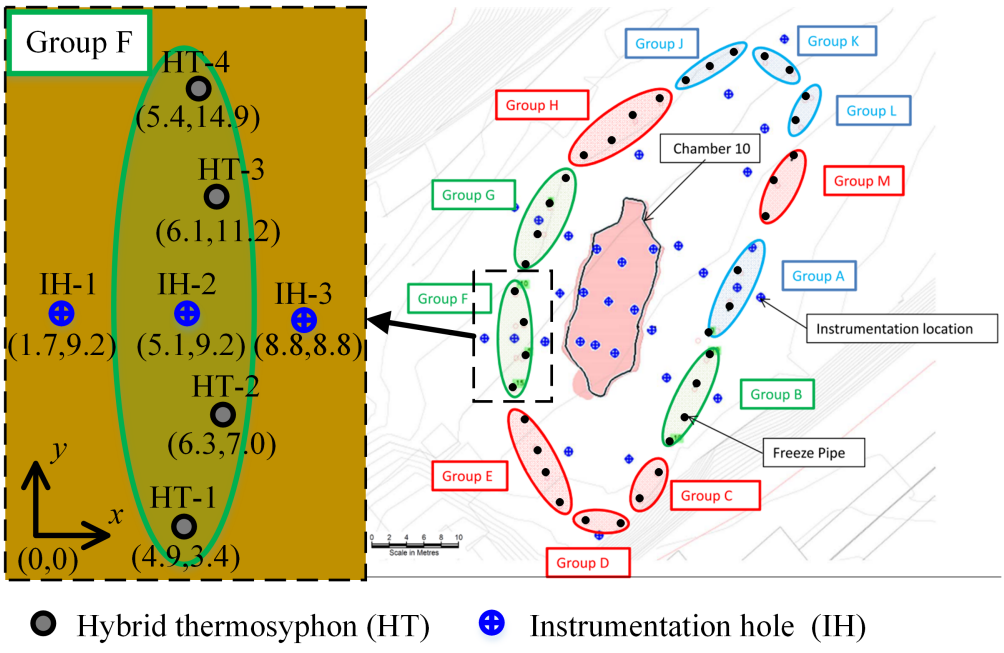

Figure 7-7: Freeze optimization study (FOS) of the Giant Mine surrounding one of the arsenic chambers included 12 different groups to compare between various AGF techniques [46]. In this study, group F is selected which involves four hybrid thermosyphons (HT) and three instrumentation holes (IH). Non-to-scale coordinates of each HT and IH are provided in the zoomed figure with respect to an arbitrary reference point.

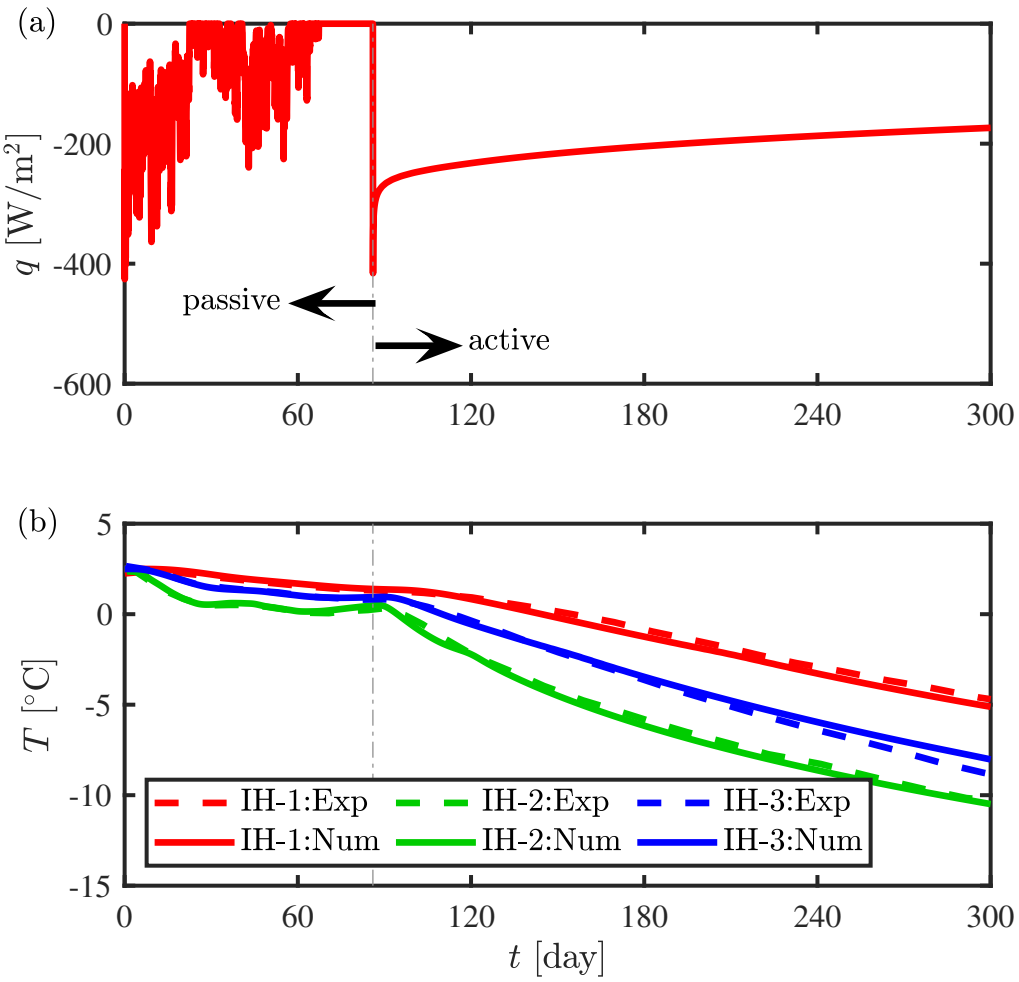

Figure 7-8: Mathematical modeling results of the Giant Mine Field tests [46]: a) Averaged heat flux extracted by the four hybrid themrosyphons during passive and active operations and b) validation of the hybrid model of the present study against the temperature measurements recorded by three different instrumentation holes (IH), shown in Fig. 7-7. The heat flux of each thermosyphon is calculated based on the heat-flux boundary condition coupling the ground with the thermosyphons (Eq. (7.17)). The calculated heat flux of each thermosyphon was found to be almost identical due to their identical operational parameters although there are very small differences because of their different spatial positions.

chamber.

7.5 Results and discussion

In this section, the frozen ground development and cooling load of hybrid thermosyphons are investigated. First, the change of the frozen ground profile is analyzed for a period of two years. After that, the impact of various parameters are investigated to understand and optimize hybrid thermosyphons.

7.5.1 Year-round frozen barrier profile

The extent of the frozen ground profile was tracked on a monthly basis for two years, as shown in Fig. 7-9. Active cooling was switched on during warmer seasons from the 15th April till the 15th of October, thereby operating the thermosyphon actively six months a year.

In the first year, the frozen ground extents increased for two months due to the colder climate in January and February. The positive slope of the phase transition front was caused by the geothermal gradient of the initial condition. In March, the air temperature increased which significantly decreased heat extraction by the thermosyphon; consequently, the frozen ground shrank due to heat gain from the underlying and surrounding ground. By the end of April, the frozen ground expanded again as active cooling was activated on the 15th April. In the following months, though the active layer (few meters deep from ground surface) thawed due to the warm air, the frozen body continued to dilate as long as active cooling was operated until the middle of October.

By the end of October, the frozen ground extent slightly decreased since active cooling was switched off. Despite the cold wind temperature of the winter season, the frozen ground tended to contract throughout the passive operation in the second year. This could be understood by conducting a simple energy balance on the frozen ground based on the first

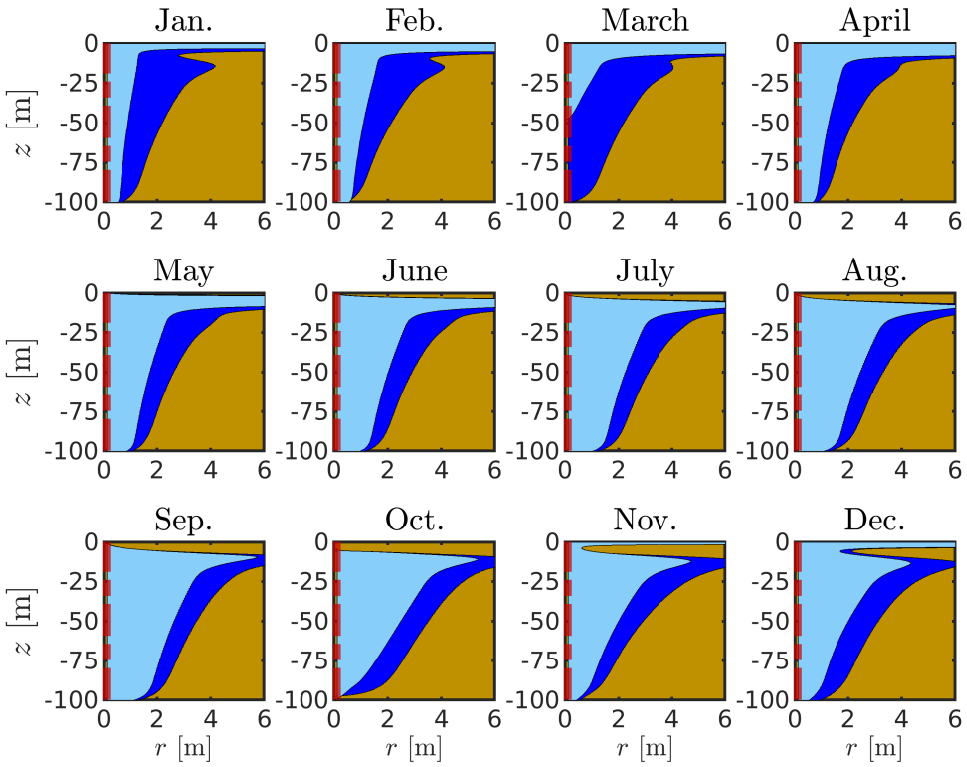

Figure 7-9: Monthly deformation of the frozen ground throughout the operation of a single hybrid thermosyphon for a period of two years. The dashed line represents the axis of symmetry of the thermosyphon and the computational domain. Light blue corresponds to the frozen ground in the first year of each month, while dark blue shows the increased frozen ground volume in the second year of the same month. The operational parameters are: $T_c = -30[^{\circ}\text{C}]$, $\dot{m}_c = 60[\text{kg/hr}]$, and $\tau = 6$ [months], whereas the geometry of helical coil is given in Table 7.3. The results are plotted at the end of each month.

law of thermodynamics:

$$\dot{E}_f = \dot{E}_{in} - \dot{E}_{out} = \dot{E}_r - \dot{E}_t - \dot{E}_s \tag{7.23}$$

where $\dot{E}_f$ is the transient change of energy of the frozen ground, $\dot{E}_r$ is the rate of incoming heat from surrounding unfrozen rocks, $\dot{E}_t$ is the rate of heat extraction of the thermosyphon during passive operation, and $\dot{E}_s$ is heat extraction/addition from the ground surface. The decline of frozen ground size correlates to a positive $\dot{E}_f$ indicating that energy added by the surrounding unfrozen rocks is higher than that extracted by the thermosyphon. This is primarily attributed to the very low temperature of the frozen ground following the active operation due to the low coolant temperature (-30 [°C]). Nonetheless, after switching on active cooling again in the middle of April of the second year, the frozen ground expanded again in a similar manner of that of the first year.

In the second year, the extent of the frozen ground is larger at a depth of 10 meters than on the ground surface even during winters seasons. This indicates that the cold energy absorbed by the ground surface (top few meters) in the first year was lost due to the summer season heating. On the other hand, the deeper portion of the ground stores the cold energy more effectively since it is away from the ground surface. At these deeper levels, the cold energy is lost to the warmer surrounding ground only which is much less significant than seasonal ground thawing observed on the surface.

7.5.2 Parametric analysis

In this section, we will study the impact of different operational parameters of hybrid thermosyphons on the frozen ground expansion and the heat extracted by hybrid thermosyphons in passive and active modes.

Simulation	$E(t = 1[\text{yr}])$ [MWh] active	$E(t = 1[\text{yr}])$ [MWh] passive	$E(t = 2[\text{yr}])$ [MWh] active	$E(t = 2[\text{yr}])$ [MWh] passive
Base-case	30.8	17.1	60.5	33.4
$T_c = -20[^\circ\text{C}]$	20.7	17.4	40.5	34.4
$T_c = -40[^\circ\text{C}]$	40.8	16.8	80.3	32.6
$\dot{m}_c = 20[\text{kg/hr}]$	25.1	17.3	49.3	34
$\dot{m}_c = 100[\text{kg/hr}]$	33.5	17.0	65.7	33.2
$\tau = 4[\text{mo.}]$	21.0	18.2	41.3	35.7
$\tau = 8[\text{mo.}]$	40.5	15.1	79.4	28.7
$R^* = 5$	13.4	17.7	26.6	35.1
$R^* = 15$	38.8	16.9	76.1	32.8
double-coil	42.2	16.8	82.6	32.5

Table 7.4: Active and passive energy extracted by the coolant in different simulation scenarios. The simulation parameters of the base case are $T_c = -30[^\circ\text{C}]$, $\dot{m}_c = 60[\text{kg/hr}]$, $\tau = 6$ [months], $R^* = 10$, and a single helical coil.

Coolant temperature

Reducing the coolant temperature enlarged the frozen ground even during winter seasons when active cooling was switched off, as shown in Fig.7-10. This implies that the benefits of active cooling are still realized throughout the year despite its intermittent operation. Nonetheless, the transient expansion rate of the frozen ground volume lessened as the coolant temperature is reduced, even though decreasing the coolant temperature resulted in a linearly proportional increase in the cooling load of active freezing plants, as noted in Table 7.4. For example, by examining winter-time subplots of the first and second years shown in Fig. 7-10, the radius of the frozen ground at a depth of 50 meters expands by 67%, 60%, and 50% at coolant temperatures of -20 [°C], -30 [°C], and -40 [°C], respectively. This observation indicates that lower coolant temperature consumed more energy to over-cool the frozen ground. Accordingly, it might be desirable to intensively reduce the coolant temperature (e.g., -40 [°C]) in early stages of operation to speed up the freezing process, but then increase the coolant temperature in subsequent years to reduce the cooling load.

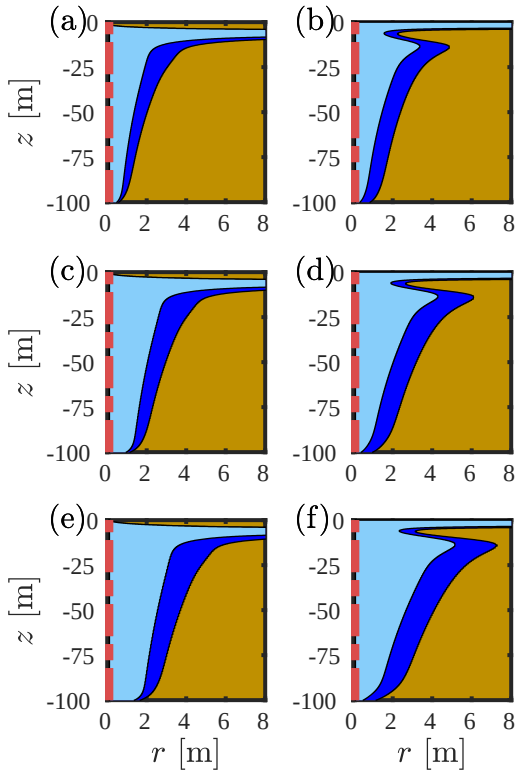

Figure 7-10: The effect of coolant temperature on the frozen ground volume during summer seasons (1st of July) and winter seasons (31st of December): a) $T_c = -20$ [°C] - summer, b) $T_c = -20$ [°C] - winter c) $T_c = -30$ [°C] - summer, d) $T_c = -30$ [°C] - winter, e) $T_c = -40$ [°C] - summer, f) $T_c = -40$ [°C] - winter. Other operational parameters and description of the figure colors can be found in the caption of Fig. 7-9.

Coolant flow rate

At the Giant Mine freeze study, a high coolant flow rate was often considered to exist between 20 [kg/hr] to 100 [kg/hr], in order to ensure that the coolant continued to extract heat throughout the length of the helical coil. Increasing the coolant flow rate resulted in higher Reynolds number and Nusselt number, as can be noted from Eq. (7.13). Since the Nusselt number is inversely proportional to the thermal resistance of the flow (R_7), heat extracted is higher at larger flow rates, leading to a larger frozen ground as shown in Fig. 7-11. Specifically, after two years of operation, the extent of frozen ground at a flow rate of 100 [kg/hr] was larger by 7% and 25% as compared to that of 60 [kg/hr] and 20 [kg/hr], respectively (these percentages are calculated at a depth of 50 meters). Nevertheless, as more heat was extracted at higher flow rates, the resulting cooling load was higher, as mentioned in Table 7.4.

Active cooling operation period

In the Giant mine, the coolant often runs at low temperature of around -35 [°C] and high flow rates of around 60 [kg/hr]. Active cooling is therefore usually larger than passive cooling despite the cold temperature of the ambient air, as demonstrated in Fig. 7-8. A larger frozen ground is therefore expected as the active cooling operation period, τ, increases, as shown in Fig. 7-12. Specifically, the frozen ground radius at a depth of 50 meters increased by 30.9% and 63.9% when τ was increased from 4 months to 6 months and 8 months, respectively. Longer τ however indicates that the refrigeration plants were operated for a longer time. Accordingly, the cooling load almost doubled when τ was increased from 4 months to 8 months, as noted in Table 7.4. Although the passive operational period at $\tau = 4$ [mo.] is twice as long as that of $\tau = 8$ [mo.], the increase in passive energy extraction amounts to 25% only after two years of operation. This is attributed to the warm air temperature in the spring and fall seasons, causing the thermosyphon to be almost idle for around 3 months per year as implied by Fig. 7-13(b).

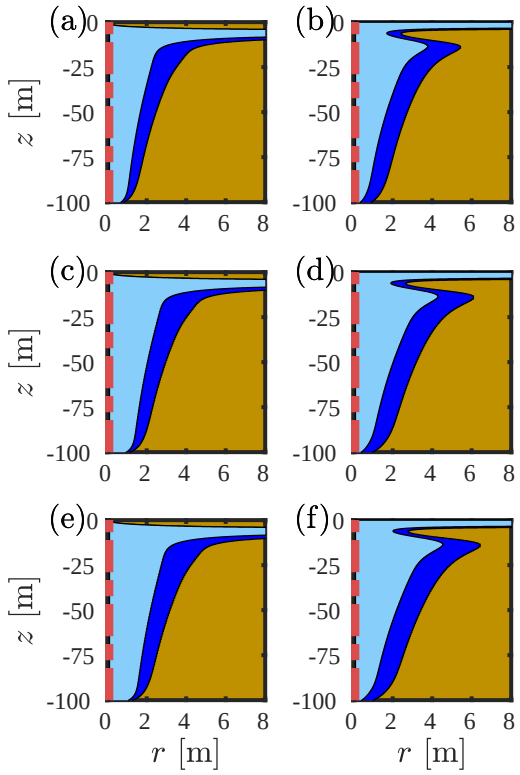

Figure 7-11: The effect of coolant flow rate on the frozen ground volume during summer seasons (1st of July) and winter seasons (31st of December): a) $\dot{m}_c = 20$ [kg/hr] - summer, b) $\dot{m}_c = 20$ [kg/hr] - winter c) $\dot{m}_c = 60$ [kg/hr] - summer, d) $\dot{m}_c = 60$ [kg/hr] - winter, e) $\dot{m}_c = 100$ [kg/hr] - summer, f) $\dot{m}_c = 100$ [kg/hr] - winter. Other operational parameters and description of the figure colors can be found in the caption of Fig. 7-9.

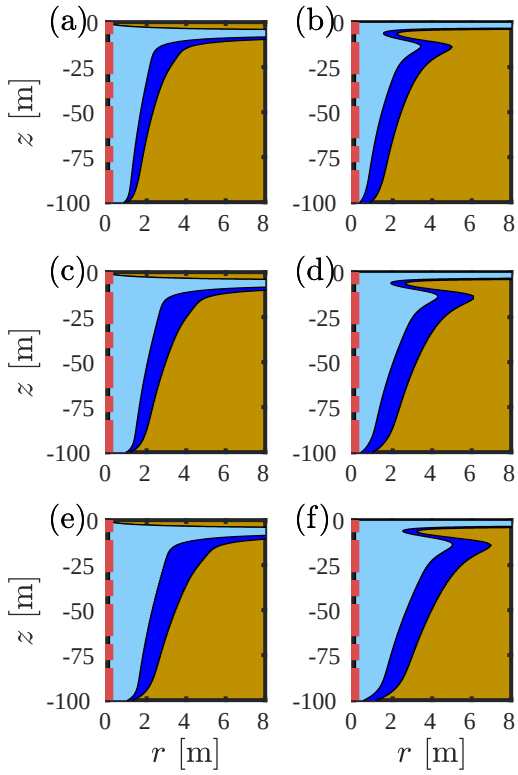

Figure 7-12: the effect of active cooling operational period per year, τ, on the frozen ground volume during summer seasons (1st of July) and winter seasons (31st of December): a) $\tau = 4$ [months] - summer, b) $\tau = 4$ [months] - winter c) $\tau = 6$ [months] - summer, d) $\tau = 6$ [months] - winter, e) $\tau = 8$ [months] - summer, f) $\tau = 8$ [months] - winter. Other operational parameters and description of the figure colors can be found in Fig. 7-9.

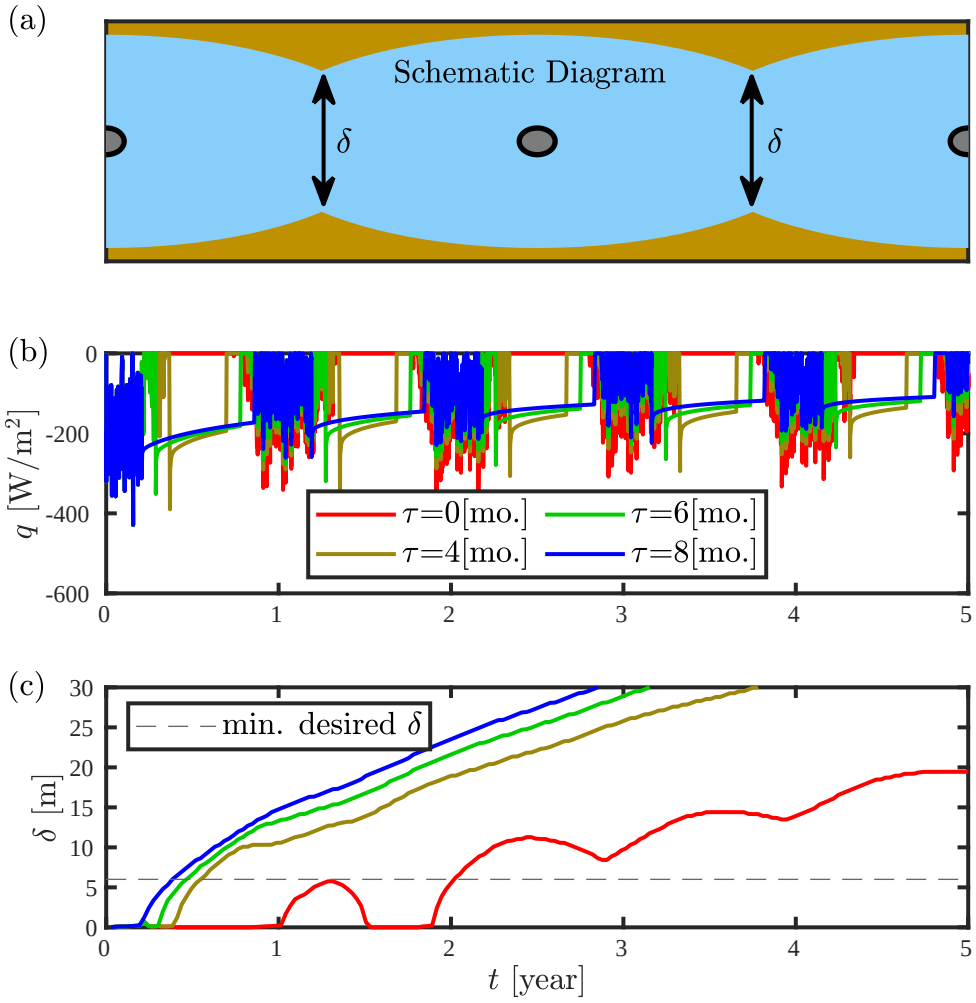

Figure 7-13: Thermal analysis on the influence of active cooling operational period per year, τ, when multiple thermosyphons are adjacent to each other. a) A non-to-scale schematic illustrating the lateral thickness of the frozen ground, δ. The gray circles represent thermosyphons while blue and brown colors indicate frozen and unfrozen ground. b) Transient heat flux extracted by the thermosyphons, and c) transient lateral ground thickness at different τ ($\tau = 0$ indicates a fully passive operation). All the results plotted in this figure and Fig. 7-14 are obtained by simulating multiple thermosyphons in a straight row as shown in sub-figure (a).

In reality, several hybrid thermosyphon applications involve a series of adjacent thermosyphons working together, rather than a single thermosyphon, to create a frozen barrier, as shown in Fig. 7-13(a). The spacing between them is designed according to the desired duration to reach a particular δ, which is the laterally outward frozen ground thickness from the row of the pipes as shown in Fig. 7-13(a). In other words, freezing needs to continue until a minimum desired δ is reached. Assuming the desired δ to be 6[m], running the thermosyphons actively for 8 months ($\tau = 8$ [mo.]) could achieve this objective in 4.5 months, as can be seen from Fig. 7-13(c). Similarly, when $\tau = 4$ [mo.], 6.5 months were needed to obtain $\delta = 6$[m]. On the other hand, if the thermosyphons were operated passively only without the use of mechanical refrigeration, δ would extend to 6 [m] after more than two years. Evidently, adding mechanical refrigeration units to the thermosyphon substantially speed up the freezing process.

Once the desired δ is reached, active cooling units may no longer be needed especially in arctic regions, where the ambient air temperature is low enough to effectively operate the thermosyphon passively. Fig. 7-13(c) shows that passive cooling is sufficient to maintain the desired δ after around two years of operation even if it was not preceded by active cooling. This observation is important as maintaining long active operation period for long lasting AGF systems, such as the arsenic containment of the Giant Mine, can result in additional cooling load of around 20 [MWh] per year per thermosyphon, as can be seen from Fig. 7-14(a). Furthermore, the evaporator wall temperature becomes very low after few years of operation resulting in a significant decrease during passive heat extraction at longer τ, as shown in Fig. 7-14(b). Consequently, in the case of the Giant Mine, active cooling would be needed in the early stages to accelerate the formation of the desired frozen ground in the first year, but the cold ambient temperature could be reliably utilized to passively run the thermosyphon and maintain the desired frozen body thickness without running refrigeration plants in the following years.

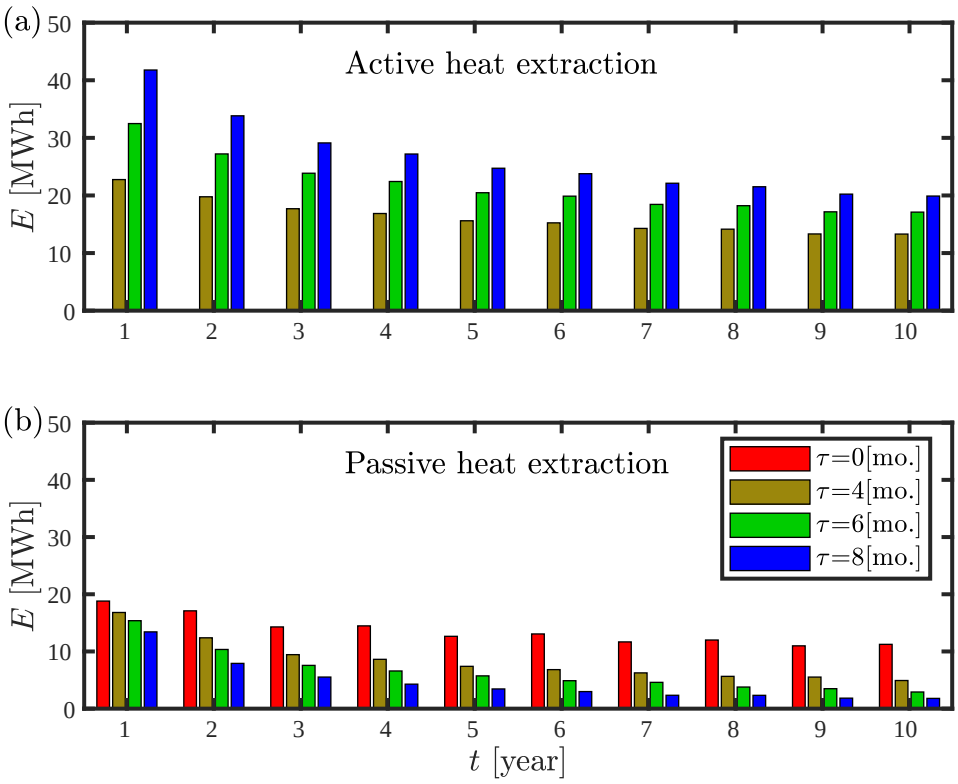

Figure 7-14: Influence of active operation period per year, τ, on the a) active, and b) passive heat extraction from the ground by every thermosyphon when multiple thermosyphons are working together as shown in Fig. 7-13(a) ($\tau = 0$ indicates a fully passive operation).

Helical coil curvature ratio

The curvature ratio, R^*, of the helical coil is defined as the radius of the thermosyphon divided by the radius of the helical coil. In this subsection, the curvature ratio of the coil was changed from 5 to 15 by changing the coil diameter given the same coil height and thermosyphon diameter. Increasing the curvature ratio enhances the active freezing process as can be depicted from Fig. 7-15. This is attributed to the higher Reynolds number and thereby heat transfer coefficient of the coolant flow at larger curvature ratios. Particularly, the heat transfer coefficient rises from 42 [W/m^{2}k] at $R^* = 5$ to 236 [W/m^{2}k] at $R^* = 15$. The higher heat extraction at larger R^* resulted in larger cooling load as can be seen from Table 7.4. Despite the enhanced heat extraction at higher curvature ratios, increasing R^* led to a longer coil which may increase the overall coolant temperature (depending on the mass flow rate) and accordingly reduce heat extraction from the ground. Thus, these results may somewhat overestimate the enhancement of heat extraction at higher curvature ratios, especially at low mass flow rate.

Number of helical coils

Varying the number of helical coils was one of the design concerns of hybrid thermosyphons in the Giant Mine FOS. For this reason, field testing was conducted with single-coil thermosyphons and double-coil thermosyphons. It was observed that a double-coil thermosyphon had a similar thermal effect on the ground as that of a single-coil thermosyphon.

The results of the present study agree with the field observations. As can be seen from Fig. 7-16, the frozen ground of a double-coil thermosyphon was larger by only few centimeters than that of a single-coil thermosyphon. while marginal increase was caused by the larger surface area of a double-coil thermosyphon, a significant enhancement on the freezing rate would not be possible since heat conduction from the ground is slower than heat convection of the coils. However, the influence of doubling the number of coils could be larger if shorter coils are considered or if the length of the evaporator piping is extended.

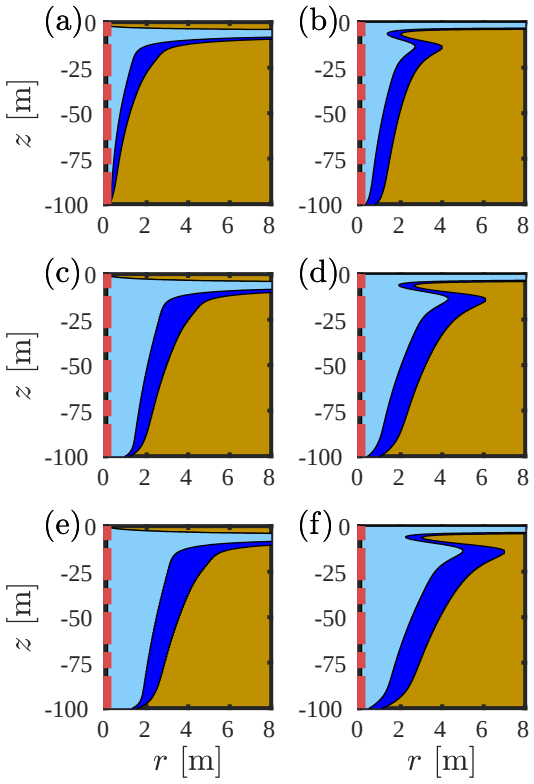

Figure 7-15: The effect of the curvature ratio of the helical coil, R^*, on the frozen ground volume during summer seasons (1st of July) and winter seasons (31st of December): a) R^*=5 - summer, b) R^*=5 - winter c) R^*=10 - summer, d) R^*=10 - winter, e) R^*=15 - summer, f) R^*=15 - winter. Other operational parameters and description of the figure colors can be found in the caption of Fig. 7-9.

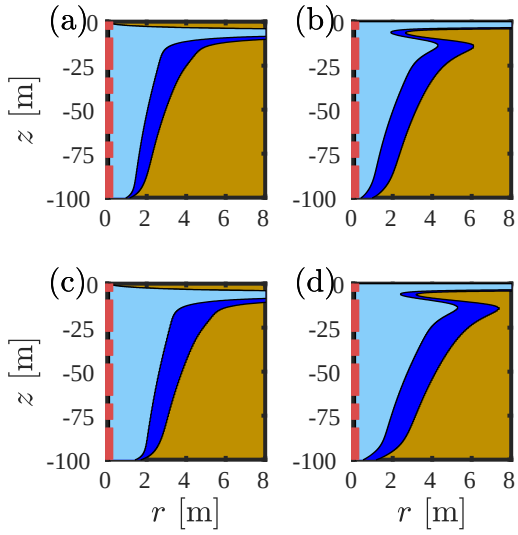

Figure 7-16: The effect of the number of helical coils on the frozen ground volume during summer seasons (1st of July) and winter seasons (31st of December): a) single coil - summer, b) single coil - winter c) double coil - summer, d) double coil - winter. Other operational parameters and description of the figure colors can be found in the caption of Fig. 7-9.

7.6 Conclusion

A hybrid thermosyphon is an artificial ground freezing (AGF) technique that balances climate induced cooling, mechanical cooling and ground heat extraction. During cold seasons, hybrid thermosyphons operate passively by taking advantage of the cold air temperature; nonetheless, during warm seasons, they run actively with the aid of refrigeration plants, which refrigerate a coolant that flows around the thermosyphon through a helical coil. In this study, a new mathematical model of hybrid thermosyphons has been developed for ground freezing applications. Particularly, a conjugate thermal resistance network model was derived to find the net heat flux extracted by a hybrid thermosyphon. The equivalent heat flux in the condenser section of a thermosyphon was then applied to the ground heat extraction, which is itself modeled by a two-phase transient energy conservation equation. This conjugate model was firstly validated against experimental measurements from the literature. After that, the model was extended to field dimensions and then further validated against field data from the Giant Mine preliminary tests and freeze optimization studies.

Following the validation of our thermal resistance model, a set of parametric studies were carried out to analyze and optimize the operational parameters of hybrid AGF systems. First, decreasing the coolant temperature and increasing the coolant flow rate enlarged the frozen ground, but decreasing the coolant temperature to below -30 [°C] resulted in overcooling the frozen ground at the cost of unnecessary energy consumption. Second, increasing active operation period might be desired in the first year of operation; however, shorter operation periods (around 3 months) or fully passive operation can maintain the targeted frozen ground in the following years with a lesser energy consumption. Third, doubling the number of coils does not provide significant freezing advantage for the evaporator pipe lengths considered here, especially if long coils (more than 2 meters high) are selected. Lastly, the cooling rate of thermosyphons is highly influenced by the curvature ratio of the coils (helical coil curvature diameter divided by the coil diameter); particularly, tripling the curvature ratio from 5 to 15 increased the heat transfer coefficient of the coil by one order of magnitude, from 42 [W/(m^{2}K)] to 236 [W/(m^{2}K)].

In our future work, we aim to improve the applied and fundamental aspects of this work. We will propose an innovative cold energy storage technology that minimizes the need for refrigeration plants. Further, we aim to find the optimal combination of operational parameters to obtain the optimum frozen ground thickness based on the energy consumption for the Giant Mine.

Acknowledgments

The authors would like to thank the FRQNT Development Durable du Secteur Minier – II (2020-MN-284402), Ultra Deep Mining Network (UDMN) (241695 Tri-Council (NCE – UDMN) 2-003). The first author wishes to thank the McGill Engineering Doctoral Award (MEDA).

Bibliography

[1] [GovernmentofCanada2018] Government of Canada, History of Giant Mine (2018). URL https://www.aadnc-aandc.gc.ca/

[2] R. Silke, The Operational History of Mines in the Northwest Territories, Canada, Tech. rep., Yellowknife (2009).

[3] Steffen Robertson and Kirsten (Canada) Inc., Giant Mine Ground Freezing, Tech. rep., Vancouver (2002).

[4] Government of Canada, The Remediation Project's Frozen Block Method (2018). URL www.aadnc-aandc.gc.ca

[5] E. Yarmak, E. L. Long, Recent developments in thermosyphon technology, in: Cold Regions Engineering: Cold Regions Impacts on Transportation and Infrastructure, Anchorage, 2002, pp. 656–662.

[6] E. L. Long, E. Yarmak, Engineering and economic variables of long duration frozen barriers, in: International Symposium on Ground Freezing and Frost Action in Soils, Louvain-la-Neuve, 2000, pp. 169–173.

[7] S. W. Lynn, S. Rock, C. Rhodes, Evaluation of a vertical frozen soil barrier at oak ridge national laboratory, Remediation 10 (3) (2000) 15–33.

[8] E. Yarmak, Permafrost foundations thermally stabilized using thermosyphons, in: Offshore Technology Conference, Copenhagen, 2015, pp. 639–650.

[9] I. Holubec, Flat loop thermosyphon foundations in warm permafrost, Tech. rep., I. Holubec Consulting Inc., Northwest Territories (2008).

[10] Indian and Northern Affairs of Canada, Giant Mine Remediation Project: Developer's Assessment Report - Environmental Assessment, Tech. Rep. October, Northwest Territories (2010).

[11] A. Wagner, Review of Thermosyphon Applications, Tech. rep., US Army Corps of Engineers, Hanover (2014).

[12] Y.-P. Yang, S.-H. Zhou, Q.-C. Wei, Numerical Analysis of Proper Thermosyphon Inclination Angle Used in Permafrost Embankment, China Railway Science 27 (3) (2006) 1–7.

[13] G.-F. Lu, Y.-P. Yang, Q.-C. Wei, L.-X. Zhang, Study of using thermosyphon-insulated board to enhance the stability of permafrost embankment, Journal of the China Railway Society 29 (6) (2007) 118–122.

[14] D. Duan, Y. Yang, Q. Wei, L. Zhang, Study on enhancing the stability of permafrost embankments with thermosyphon-insulated boards, Journal of Beijing Jiaotong University 32 (1) (2008) 24–28.

[15] P. Yang, Numerical Analysis and Application Research of Heat Pipe to Solve Soil Frost Heaving Problem, Journal of East China Jiaotong University 15 (4).

[16] W. Cunzhen, S. Zhijian, P. Yang, Theoritic study on the technology of applying heat pipe to solving frost heaving, Chinese Journal of Geotechnical Engineering 24 (3) (2002) 347–350.

[17] P. Yang, W. Cunzhen, Numerical investigations and engineering applications on freezing expansion of soil restrained two-phase closed thermosyphons, International Journal of Thermal Sciences 41 (4) (2002) 341–347.

[18] W. Zhi, S. Yu, M. Wei, Q. Jilin, J. C. Wu, Z. Wen, Y. Sheng, W. Ma, J. L. Qi, J. C. Wu, Analysis on effect of permafrost protection by two-phase closed thermosyphon and insulation jointly in permafrost regions, Cold Regions Science and Technology 43 (3) (2005) 150–163.

[19] J. Xu, A. Eltaher, P. Jukes, Three-dimensional FE model for pipeline in permafrost with thermosyphon protection, in: Arctic Technology Conference, Vol. 1, Houston, 2011, pp. 535–544.

[20] B. Abdalla, C. Fan, C. Mckinnon, V. Gaffard, Numerical study of thermosyphon protection for frost heave, in: ASME 2015 34th International Conference on Ocean, Vol. 5A, Newfoundland, 2015, pp. 1–6.

[21] B. A. Abdalla, H. Mei, C. McKinnon, V. Gaffard, Numerical evaluation of permafrost thawing in arctic pipelines and mitigation strategies, in: Arctic Technology Conference 2016, Newfoundland, 2016.

[22] J.-L. Wang, S.-M. Liao, Numerical heat transfer analysis and optimization for thermosyphons coupled with natural ground in permafrost regions, China Railway Science 27 (6) (2006) 1–6.

[23] Y.-H. Tian, J.-K. Liu, Y.-P. Shen, 3-D finite element analysis of cooling effect of Qinghai-Tibet Railway embankment with thermosyphons in permafrost regions, Chinese Journal of Geotechnical Engineering 35 (2013) 113–119.

[24] M. Zhang, Y. Lai, J. Zhang, Z. Sun, Numerical study on cooling characteristics of two-phase closed thermosyphon embankment in permafrost regions, Cold Regions Science and Technology 65 (2) (2011) 203–210.

[25] H. Imura, H. Kusuda, J.-I. Ogata, T. Miyazaki, N. Sakamoto, Heat transfer in two-phase closed-type thermosyphons, JSME Transactions 45 (1979) 712–722.

[26] Y. Mu, G. Li, Q. Yu, W. Ma, D. Wang, F. Wang, Numerical study of long-term cooling effects of thermosyphons around tower footings in permafrost regions along the Qinghai-Tibet Power Transmission Line, Cold Regions Science and Technology 121 (2016) 237–249.

[27] M. Zhang, W. Pei, Y. Lai, F. Niu, S. Li, Numerical study of the thermal characteristics of a shallow tunnel section with a two-phase closed thermosyphon group in a permafrost region under climate warming, International Journal of Heat and Mass Transfer 104 (2017) 952–963.

[28] W. Pei, M. Zhang, S. Li, Y. Lai, L. Jin, W. Zhai, F. Yu, J. Lu, Geotemperature control performance of two-phase closed thermosyphons in the shady and sunny slopes of an embankment in a permafrost region, Applied Thermal Engineering 112 (2017) 986–998.

[29] L. Chen, W. Yu, Y. Lu, W. Liu, Numerical simulation on the performance of thermosyphon adopted to mitigate thaw settlement of embankment in sandy permafrost zone, Applied Thermal Engineering 128 (2018) 1624–1633.

[30] H. Yandong, W. Qingbai, D. Jianhua, L. Jing, Z. Mingli, Y. Zeguo, Numerical simulation of efficient cooling by coupled RR and TCPT on railway embankments in permafrost regions, Applied Thermal Engineering 133 (2018) 351–360.

[31] W. Pei, M. Zhang, Z. Yan, S. Li, Y. Lai, Numerical evaluation of the cooling performance of a composite L-shaped two-phase closed thermosyphon (LTPCT) technique in permafrost regions, Solar Energy 177 (2019) 22–31.

[32] W. Pei, M. Zhang, Y. Lai, Z. Yan, S. Li, Evaluation of the ground heat control capacity of a novel air-L-shaped TPCT-ground (ALTG) cooling system in cold regions, Energy 179 (2019) 655–668.

[33] Y. Lai, H. Guo, Y. Dong, Laboratory investigation on the cooling effect of the embankment with L-shaped thermosyphon and crushed-rock revetment in permafrost regions, Cold Regions Science and Technology 58 (3) (2009) 143–150.

[34] Y. Song, L. Jin, J. Zhang, In-situ study on cooling characteristics of two-phase closed thermosyphon embankment of Qinghai-Tibet Highway in permafrost regions, Cold Regions Science and Technology 93 (2013) 12–19.

[35] S. Wang, L. Jin, H. Peng, J. Chen, K. Mu, Damage analysis of the characteristics and development process of thermosyphon embankment along the Qinghai-Tibet Highway, Cold Regions Science and Technology 142 (2017) 118–131.

[36] J. Wu, W. Ma, Z. Sun, Z. Wen, In-situ study on cooling effect of the two-phase closed thermosyphon and insulation combinational embankment of the Qinghai-Tibet Railway, Cold Regions Science and Technology 60 (3).

[37] M. Zhang, Y. Lai, Y. Dong, L. Jin, W. Pei, J. Harbor, Laboratory investigation of the heat transfer characteristics of a two-phase closed thermosyphon, Cold Regions Science and Technology 95 (2013) 67–73.

[38] M. A. Alzoubi, M. Xu, F. P. Hassani, S. Poncet, A. P. Sasmito, Artificial ground freezing: A review of thermal and hydraulic aspects, Tunnelling and Underground Space Technology 104 (2020) 103534.

[39] A. Zueter, A. Nie-Rouquette, M. A. Alzoubi, A. P. Sasmito, Thermal and hydraulic analysis of selective artificial ground freezing using air insulation: Experiment and modeling, Computers and Geotechnics 120 (2020) 103416.

[40] M. A. Alzoubi, A. Zueter, A. Nie-Rouquette, A. P. Sasmito, Freezing on demand: A new concept for mine safety and energy savings in wet underground mines, International Journal of Mining Science and Technology 29 (4) (2019) 621–627.

[41] M. Xu, S. Akhtar, A. Zueter, V. Auger, M. Alzoubi, A. P. Sasmito, Development of analytical solution for a two-phase Stefan problem in artificial ground freezing using singular perturbation theory, Journal of Heat Transfer. 142 (12) (2020) 122401.

[42] M. A. Alzoubi, A. P. Sasmito, Thermal performance optimization of a bayonet tube heat exchanger, Applied Thermal Engineering 111 (2017) 232–247.

[43] D. F. Haynes, J. P. Zarling, W. F. Quinn, G. E. Gooch, Laboratory tests with a hybrid thermosyphon, in: Proceedings of the 10th International Conference on Ocean, Offshore and Arctic Engineering, Vol. 4, American Society of Mechanical Engineers, Stavanger, 1991, pp. 93–99.

[44] A. M. Wagner, Creation of an artificial frozen barrier using hybrid thermosyphons, Cold Regions Science and Technology 96 (2013) 108–116.

[45] A. M. Wagner, E. Yarmak, The performance of artificial frozen barriers, in: ISCORD 2013: Planning for Sustainable Cold Regions, 2013, pp. 116–127.

[46] SRK Consulting (Canada) Inc., Freeze Optimization Study Update for MVEIRB and Parties Aboriginal Affairs and Northern Development Freeze Optimization Study Update for MVEIRB and Parties, Tech. Rep. August, Ottawa (2012).

[47] M. Kaviany, Principles of Heat Transfer in Porous Media, Springer Science & Business Media, 2012.

[48] Y. A. Cengel, Heat and Mass Transfer: Fundamentals and Applications, 3rd Edition, McGraw-Hill, Boston, 2007.

[49] J. Gao, Y. Lai, M. Zhang, D. Chang, The thermal effect of heating two-phase closed thermosyphons on the high-speed railway embankment in seasonally frozen regions, Applied Thermal Engineering 141 (2018) 948–957.

[50] V. Guichet, S. Almahmoud, H. Jouhara, Nucleate pool boiling heat transfer in wickless heat pipes (two-phase closed thermosyphons): A critical review of correlations, Thermal Science and Engineering Progress 13 (2019) 100384.

[51] W. Nusselt, The condensation of steam on cooled surfaces, Z. Ver. Dtsch. Ing 60 (1916) 541–546.

[52] V. Guichet, H. Jouhara, Condensation, evaporation and boiling of falling films in wickless heat pipes (two-phase closed thermosyphons): A critical review of correlations, International Journal of Thermofluids 1 (2020) 100001.

[53] A. Zukauskas, Heat Transfer from Tubes in Crossflow, in: Advances in heat transfer, Vol. 8, Elsevier, 1972, pp. 93–160.

[54] K. A. Gardner, Efficiency of extended surface, Transactions of ASME 67 (1945) 621–631.

[55] X. Wang, H. Yao, J. Li, Y. Wang, Y. Zhu, Experimental and numerical investigation on heat transfer characteristics of ammonia thermosyhpons at shallow geothermal temperature, International Journal of Heat and Mass Transfer 136 (2019) 1147–1159.

[56] B. K. Hardik, P. K. Baburajan, S. V. Prabhu, Local heat transfer coefficient in helical coils with single phase flow, International Journal of Heat and Mass Transfer 89 (2015) 522–538.

[57] R. A. Seban, E. F. McLaughlin, Heat transfer in tube coils with laminar and turbulent flow, International journal of heat and mass transfer 6 (5) (1963) 387–395.

[58] C. M. White, Streamline flow through curved pipes, Proceedings of the Royal Society of London. Series A, Containing Papers of a Mathematical and Physical Character 123 (792) (1929) 645–663.

[59] W. Pei, M. Zhang, S. Li, Y. Lai, Y. Dong, L. Jin, Laboratory investigation of the efficiency optimization of an inclined two-phase closed thermosyphon in ambient cool energy utilization, Renewable Energy 133 (2019) 1178–1187.

[60] M. Noel, D. Hockley, Thermal analysis of an experimental thermosyphon installed at the Giant Mine in Yellowknife, NT, Canada, in: 57th Canadian Geotechnical Conference and 5th joint CGS-IAH Conference, Quebec, 2004.

[61] M. Fong, M. A. Alzoubi, J. C. Kurnia, A. P. Sasmito, On the performance of ground coupled seasonal thermal energy storage for heating and cooling: A Canadian context, Applied Energy 250 (2019) 593–604.

[62] Government of Canada, Historical Data (2019).
URL https://climate.weather.gc.ca/

[63] J. Zhou, W. Zhao, Y. Tang, Practical prediction method on frost heave of soft clay in artificial ground freezing with field experiment, Tunnelling and Underground Space Technology 107 (2021) 103647.

[64] N/A, 2009 ASHRAE handbook : fundamentals, inch-pound Edition, American Society of Heating, Refrigerating and Air-Conditioning Engineers, Inc. (ASHRAE), Atlanta, GA., 2009.

[65] National Institute of Standards and Technology, NIST chemistry webbook (2018).
URL https://webbook.nist.gov/

Chapter 8

Cold energy storage as a solution for year-round renewable artificial ground freezing: Case study of the Giant Mine Remediation Project

Preface

While hybrid thermosyphons investigated in the previous chapter can run on sustainable resources during cold seasons, they require substantial energy expenditures in warm seasons. A set of 100 hybrid thermosyphons is estimated to consume around 3.5 GWh [1] and correspondingly produce 575 ton of CO_2, 35 kg of CH_4, and 70 kg of N_2O. Accordingly, in this study, we propose a novel cold energy storage concept for the case of the Giant Mine Remediation Project in particular, but can be generalized to other artificial ground freezing applications.

" **A. F. Zueter** and A. P. Sasmito. Cold energy storage as a solution for year-round

renewable artificial ground freezing: Case study of the Giant Mine Remediation Project. *Submitted to Applied Energy* "

Abstract

In cold regions, passive thermosyphons are often employed in permafrost protection and artificial ground freezing (AGF) applications. While passive thermosyphons utilize available cold wind during cold seasons, energy-intensive refrigeration plants are sometimes needed to run thermosyphons in warmer seasons. In this study, we propose a novel cold energy storage (CES) concept that operates thermosyphons year-round using renewable energy resources. Our proposed system is based on additional energy storage ground coupled thermosyphons (ST) and heat extraction pipes (HEP). In cold seasons, the STs store wind cold energy, which is then transferred in warmer seasons using HEPs to the site of interest. The system is mathematically demonstrated using well-validated numerical models derived in our previous work against field data from the Giant Mine Remediation Project (GMRP). The results reveal that our proposed system enhances the heat extraction capacity of primary thermosyphons by more than 15%, and the freezing process is achieved one year faster. Overall, this study presents the foundation of a innovative concept that can help run thermosyphons using renewable resources in cold regions, especially at the GMRP.

Contents

8.1 Introduction

The Giant Mine was a major economic force of the Northwest Territories (NT), producing 7 million ozt of gold over the second half of the twentieth century [2], [3]. Despite these economic benefits, gold mining created a massive environmental burden amounting for 237,000 tons of a lethal byproduct called arsenic, which has been stored in underground chambers [2]. Arsenic leakage poses several environmental and social catastrophes. The mine waste is situated along the shoreline of Yellowknife Bay on Great Slave Lake, one of the largest freshwater bodies in Canada. Arsenic concentration in Yellowknife Bay is five times higher than that of drinkable water [4], influencing the fish habitat. The Dettah First Nation people, who are closest to the mine, are severely affected by this catastrophe as they cannot safely practice hunting and fishing in the vicinity – not to mention the demise and health issues in the 1950s due to arsenic consumption [5]. To mitigate the impact of arsenic leakage, the Canadian Government initiated the Giant Mine Remediation Project (GMRP) in collaboration with the Yellowknives Dene First Nation. Among various containment methods, a reliable one called the frozen block was selected, where the environmental waste is encapsulated in a frozen shell. To this end, artificial ground freezing (AGF) systems will be indefinitely employed. Nonetheless, active AGF approaches can result in huge economic and environmental costs; a set of 150 hybrid thermosyphons, that may employ refrigeration plants in summer seasons, annually consume around 3.5 GWh [1] and correspondingly produce 575 ton of CO_2, 35 kg of CH_4, and 70 kg of N_2O [6]. The energy expenditures and greenhouse emissions thus amount for 1% of the provincial ones [6]. Accordingly, a novel AGF method based on renewable energy is needed to securely contain environmental waste of the GMRP while substantially reducing the environmental and economic costs.

In cold regions as the NT, thermosyphon technologies are common in the AGF industry due to their ability to passively transfer cold energy from the winter wind to the ground. While passive cooling of thermosyphons is sufficient in some applications, active refrigeration techniques are sometimes combined with passive thermosyphons to maintain heat extraction

from the ground in summer seasons. For instance, hybrid thermosyphons, which combine passive and active cooling methods, have been used in the construction of the Diavik Mine dams and dikes [7], as well as the containment of hazardous waste at the Oak Ridge National Project [8]. In other applications featuring hybrid cooling methods, active freeze-pipes are initially installed in ground boreholes to accelerate the formation of the frozen ground by passing a refrigerated coolant through the pipes. Once the desired frozen ground is formed, active pipes are removed, and a passive/hybrid thermosyphon is installed to reduce the cooling load especially during cold seasons. Such active followed by passive refrigeration system has been installed to support the foundations of the Kuparuk River Module Crossing in Russia [9] and is also proposed for the GMRP. Overall, active refrigeration plants can increase the system reliability and heat extraction capacity; however, they require intensive energy resources.

Consequently, several studies have been conducted to passively enhance the heat extraction capacity of thermosyphons either by 1) integrating other static components to the ground or 2) improving the design of thermosyphons. Guo et al. [10] observed that vegetation cover effectively insulates the ground in warm seasons thus reducing cold energy dissipation. Xu et al., [11] and Varmalov et al. [12] demonstrated that integrating artificial insulation boards can further preserve the cold energy in the ground. In attempts to enhance the insulation, Zhou et al. [13] proposed a tri-layered asphalt pavement that feature a decreasing thermal conductivity from top to bottom. On the other hand, Zhong et al. [14] developed new asphalt mixture that decreases its thermal conductivity while maintaining its strength. Despite the benifits of insulation boards, several studies reported that crushed rock revetments have to be integrated as well to better preserve the ground's cold energy [15], [16], [17], [18].

Other studies focused on improving the thermosyphon geometry as well as thermosyphons layout to enhance their heat extraction capacity. Lyazgin et al. [19] increased the daily operational hours of thermosyphons by manufacturing the thermosyphon vessel from aluminum

alloys (instead of traditional steel vessels) due to its high thermal conductivity. Bayasan et al. [20] increased the heat extraction capacity of the condensers by adding secondary fins on primary fins. Zhang et al. [21] proposed employing a nanofluid of favorable thermal conductivity as the working fluid inside the thermosyphon to decrease its thermal resistance. In another attempt to decrease the thermal resistance inside the thermosyphon, Solomon et al. [22] proposed using a grooved heat pipe to accelerate the evaporation/condensation cycle. In regards to the evaporator section, Tian et al. [23] observed that inclined evaporators are preferred due to their ability to maintain a uniform temperature (frozen front) below highway embankments. Kukkapalli et al. [24], [25] designed T-shape and Y-shape, in addition to tree-like T-shape and Y-shape, evaporators; the numerical analysis revealed that the thermal performance of these designs is preferable over the traditional type of L-shaped thermosyphons. Pei et al. [26] suggested using adjustable evaporator section to tune the ground temperature profile. Further, Pei et al. [27], [28], Chang et al. [29], and Chen et al. [30] proposed alternating thermosyphons layout accross Qinghai-Tibet Roadway to enhance the frozen front profile.

While hybrid thermosyphons utilizng active refrigeration plants have been studied extensively in the literature [1], [31], [32], limited number of studies considered running thermosyphons in warm seasons using sustainable energy resources. Wagner et al. [33] recently proposed using solar panels to run mechanical refrigeration for hybrid thermosyphons, especially in remote areas not connected to the national grid. Alzoubi et al. [34], [35] conducted mathematical analysis confirming the high potential of the cold energy storage concept to run the ground freezing process indefinitely. However, the mathematical model did not consider the cold energy storage medium.

In this study, we propose an innovative cold energy storage (CES) concept to run thermosyphons during warm seasons as well as cold ones. In our proposed system, several thermosyphons are used to store cold energy in the ground during cold seasons. In warm seasons, the cold energy is extracted and directed towards application of interest. Conjugate

numerical model, which has been developed and validated in our previous work [1] against GMRP fields data and a well-controlled experimental study conducted by Pei et al. [36], is employed and adapted to simulate our CES concept. The capacity of our proposed model is then examined by testing it for the case of the GMRP. The impact of operational parameters on the CES system as well as heat extraction at the Giant Mine system is addressed.

8.2 Methodology

In this study, we are proposing a CES concept to assist passive thermosyphons to run year-round. The conceptual methodology will be thus be firstly described followed by the mathematical one.

8.2.1 Conceptual methodology

At the GMRP, several 100 meters deep thermosyphons operate next to each other to encapsulate the arsenic chambers extending from 25 meters to 75 meters below the ground surface, as shown in Fig. 8-1 and Fig. 8-2(a-2). The present form of thermosyphons can operate passively during winter seasons only due to the natural availability of cold wind. In this study, we are proposing a novel cold energy storage concept to allow thermosyphons to run passively year-round for the case of the GMRP in particular and other permafrost protection applications in general.

In our proposed system, There are two sets of thermosyphons working simultaneously: 1) Primary thermosyphons (PT), operating in the site of interest, which is the GMRP in this study, as shown in Fig. 8-2(a-2) and 2) storage thermosyphons (ST), as shown in Fig. 8-2(a-1). In winter seasons, PTs extract heat from the ground to freeze zones of interest, as shown in Fig. 8-2(b-2). Concurrently, STs store cold energy, as shown in Fig. 8-2(b-1), in a nearby location. In warm seasons, the finned sections of the PTs and STs become idle due to the absence of cold wind. To keep PTs active, the cold energy stored by the STs is then

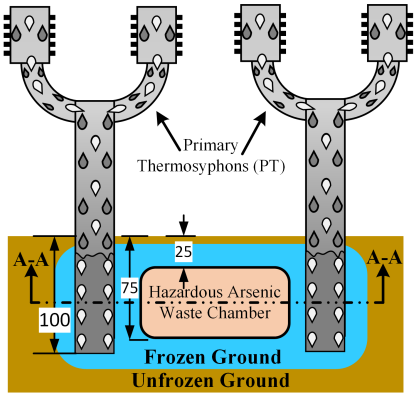

Figure 8-1: Arsenic containment at the Giant Mine Remediation Project using thermosyphons

transferred to the PTs, as shown in Fig. 8-2(c-1,c-2). Particularly, a HTF passes through a heat extraction pipe (HEP), extracts the stored cold energy, and then transfers the cold energy to the PT through a helical coil acting as a secondary condenser.

In practical field scenarios, a single thermosyphon is not sufficient to freeze the ground of large scale applications such as the GMRP. Instead, several PTs operate next to each other, as can be seen from Fig. 8-2(b-2). Consequently, there is a need for several STs to provide enough cold energy. Thus, an important parameter of interest for performance optimization is the spacing between the PTs as well as the STs. This study will focus more on the CES concept; accordingly, the effect STs spacing will be examined. Throughout this study, the number of PTs is set to be equal to the number of STs; thus, each ST provides cold energy for one PT.

8.2.2 Mathematical Methodology

In this subsection, the mathematical model used to demonstrate our idea is presented.

Governing equations

A porous ground occupying the GMRP area is considered as the computational domain of the present study. The local thermal equilibrium (LTE) assumption [37] is valid as shown

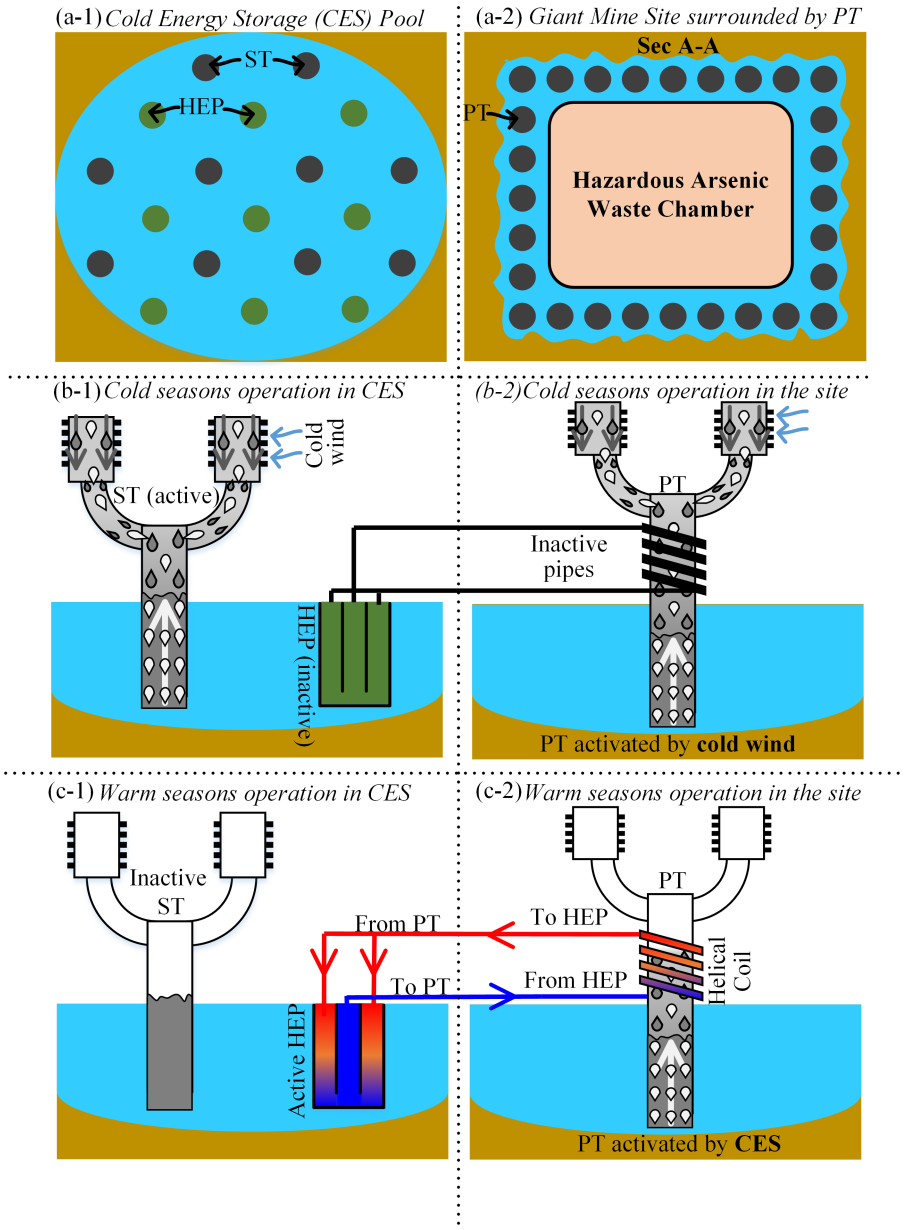

Figure 8-2: Illustration of the conceptual methodology of the present study: a-1) Top view of the cold energy storage (CES) pool showing the storage thermosyphons (ST) and heat extraction pipes (HEP) arranged in a diamond configuration, (a-2) horizontal cross-sectional view of primary thermosyphons (PT) encapsulating the arsenic chambers (refer to Fig. 8-1 to see the position of A-A section), b-1) charging operational mode of CES during cold seasons, b-2) the operation of PT in cold seasons utilizing cold wind, c-1) discharging operation mode of CES, and c-2) the operation of PT in our proposed CES system in warm seasons using stored cold energy.

by Zueter et al. [38]. Energy balance in the ground can thus be expressed as

$$\frac{\partial(\overline{\rho c_p}T)}{\partial t} = \nabla \cdot (\overline{k}\nabla T) + S, \tag{8.1}$$

where $\overline{\rho c_p}$ and $\overline{k}$ are the equivalent heat capacity and thermal conductivity of the ground (rock and water), while the source term, S, represents the latent of the water content as

$$S = -\frac{\partial(\gamma\overline{\rho L})}{\partial t}, \tag{8.2}$$

where $\overline{\rho L}$ is the ground volumetric latent heat related to the ground porosity as

$$\overline{\rho L} = \phi\rho_w L_w, \tag{8.3}$$

where ρ_w and L_w are the density and latent heat of water, respectively. γ is the liquid fraction as

$$\gamma = \begin{cases} 0 & , \ T < T_{sol}; \\ \frac{T-T_{sol}}{T_{liq}-T_{sol}} & , \ T_{sol} \leq T \leq T_{liq}; \\ 1 & , \ T > T_{liq}, \end{cases} \tag{8.4}$$

Boundary conditions

Along the bottom boundary, geothermal heat flux is set as [39]

$$-\overline{k}\frac{\partial T}{\partial n}\bigg|_{bottom\ boundary} = q_{geo}, \tag{8.5}$$

where $q_{geo} = 0.06$ [W/m^2]. At the side boundary which represents the middle distance between two thermosyphon, thermal symmetry is considered as

$$\frac{\partial T}{\partial n}\bigg|_{side\ boundary} = 0. \tag{8.6}$$

The top boundary of field simulations is subject to atmospheric convection as

$$-\overline{k}\frac{\partial T}{\partial n}\bigg|_{top\ boundary} = h_{atm}(T|_{top\ boundary} - T_a), \tag{8.7}$$

where T_a is the air temperature and the atmospheric heat transfer coefficient, h_{atm} is set at 3 [W/(m^{2}K)].

The thermosyphon boundary is coupled to the ambient air temperature or helical coil temperature using a thermal resistance network model as

$$q_e = \frac{Q_{total}}{A_e} = \frac{T_\infty - T_e}{R_{eq}A_e} = -\overline{k}\frac{\partial T}{\partial n}\bigg|_e, \tag{8.8}$$

where subscript e denotes the evaporator section. The equivalent thermal resistance, R_{eq} is determined follwing a thermal network model is explained in Fig. 8-3. Various Nusselt correlations were employed to determine each thermal resistance as

$$R = \frac{1}{hA} \tag{8.9}$$

where h is the heat transfer coefficient and A is the heat transfer area. Starting at the evaporator, Imura's correlation [40] is employed to determine the heat transfer coefficient of boiling as

$$h_{2,3} = 0.32\left[\frac{\rho_f^{0.65}k_f^{0.3}c_{p,f}^{0.7}g^{0.2}q_e^{0.4}}{\rho_g^{0.25}h_{fg}^{0.4}\mu_f^{0.1}}\right]\left(\frac{P_s}{P_{atm}}\right)^{0.3} \tag{8.10}$$

where the thermophysical properties of CO_2 can be found in Table 8.1. The condensation heat transfer coefficient is modeled using the Nusselt theory as [41]

$$h_4 = 0.925\left[\frac{k_f^3\rho_f^2 g h_{fg}}{\mu_f q_n \ell_n}\right]^{1/3}. \tag{8.11}$$

where q_n is the heat flux through the condenser while L_n is the length of the condenser. The

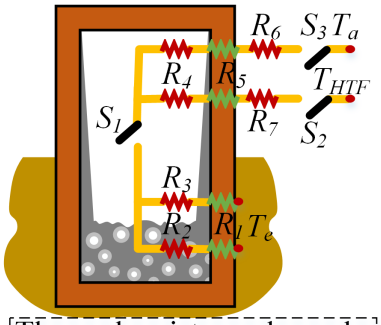

Thermal resistance legends:

R_1: Evaporator wall

R_2: Pool boiling

R_3: Film boiling

R_4: Film condensation

R_5: Condenser wall

R_6: Wind

R_7: Coolant flow

Temperature legends:

T_a: Air temp.

T_{HTF}: HTF temp (equal to outlet of the CES).

T_e: Evaporator wall temp.

Figure 8-3: thermal resistance network model of thermosyphons

Material	ρ [kg/m^3]	c_p [J/(kg·k)]	k [W/(m·k)]	μ [Pa s]
Condensate CO_2 [42]	959	2396	0.117	1.09E-4
Vapor CO_2 [42]	81.9	1643	18.0E-2	1.42E-5
Frozen rock [43]	2926	814	3.45	-
Unfrozen rock [43]	2927	822	3.44	-

Table 8.1: Thermophysical properties of the CO_2, the working fluid inside thermosyphons, and bedrock of the Giant Mine site. The water content is 1% of all field simulations.

ground heat is eventually extracted by cold wind or chilled coolant from CES. The Nusselt number is modeled based on the Reynolds number, Re_a, as [39], [44]

$$Nu_a = \frac{h_6 D_{o,c}}{k_a} = \begin{cases} \eta_{fin}\ 0.989 Re_a^{0.330} Pr_a^{1/3} & ,\ Re_a < 4; \\ \eta_{fin}\ 0.911 Re_a^{0.385} Pr_a^{1/3} & ,\ 4 \leq Re_a < 40; \\ \eta_{fin}\ 0.683 Re_a^{0.466} Pr_a^{1/3} & ,\ 40 \leq Re_a < 4000; \\ \eta_{fin}\ 0.193 Re_a^{0.618} Pr_a^{1/3} & ,\ 4000 \leq Re_a < 40000; \\ \eta_{fin}\ 0.027 Re_a^{0.805} Pr_a^{1/3} & ,\ 40000 \leq Re_a, \end{cases} \tag{8.12}$$

where fin efficiency, η_{fin}, is set at 65% based on the fin geometry as per charts of Gardner [39], [45] for circular fins. Finally, the Nusselt number of the HTF flow across the helical coil is calculated based on Seban and Mclanghin correlation [46], [47] as

$$Nu = \frac{h_7 D_c}{k_c} = 0.065 f_c^{0.33} Re_c^{0.66} Pr_c^{0.33}, \tag{8.13}$$

where f_c is the friction factor of the coolant flow calculated as [48]

$$f_c = \frac{64}{Re_c} \left\{ 1 - \left[1 - \left(\frac{11.6}{Dn_c} \right) \right]^{0.45} \right\}^{-1} \tag{8.14}$$

where Dn_c is the Deans number. The switches S_2 and S_3 are actively controlled by the specified operational duration for CES and passive cooling. On the other hand, the S_1 switch inside the thermosyphon is added to deactivate the thermosyphon when the natural convection cycle stops due to lower evaporator temperature than condenser temperature. More detailed description and evaluation of the thermal resistance network can be found in our previous work [1].

In order to quantify the amount of heat extracted by HEPs, the axial HTF temperature,

$T_{htf}(z)$, is correlated to the ground through a convective boundary condition as

$$q_g(z) = -k_g \frac{\partial T_g(z_c)}{\partial n}\bigg|_{o,w} = h(z)\Big[\, T_g(z)|_{o,w} - T_{htf}(z)\Big], \tag{8.15}$$

where the HTF temperature evolution is monitored using a space marching algorithm based on the first law of thermodynamics as

$$\Delta T_{htf}(z) = \frac{q_g(z)}{\dot{m}_{htf} c_{p,htf}}, \tag{8.16}$$

where $T_{htf}(z = 0)$ and $T_{htf}(z = L)$ correspond to the HTF inlet and outlet temperatures, respectively. All details on the evaluation of the heat transfer coefficient and space marching algorithm can be obtained from our previous work [49], [50]. The total amount of heat extracted by HEP can be determined based on the inlet and outlet temperatures of the HTF as

$$\dot{Q}_{HEP} = \dot{m}_{htf} c_{p,htf}\Big(T_{htf}(z = L) - (T_{htf}(z = 0)\Big) \tag{8.17}$$

Throughout this study, the initial temperature of the ground is set according to geothermal temperature gradient recorded in the field approximated by the following correlation:

$$T_{initial}[K] = 278.8e^{-c_1} + 4.065E13e^{-c_2} \tag{8.18}$$

where $c_1 = \left(\frac{z[m]-351.1}{2292}\right)^2$, $c_2 = \left(\frac{z[m]+754.7}{133.4}\right)^2$, and z is the depth from ground surface.

8.3 Choice of numerical parameters

Second-order upwind schemes were selected to discretize the spatial and transient terms of the governing equation of the ground (Eq. (8.1)). ANSYS Fluent 18.1 was used to compute the equations as prescribed by our model and user-defined functions. Mesh independence and time-step independence studies was conducted and ensured. The selected mesh size and

type greatly relies on the simulation scenario as we have conducted various 3D simulations of different length scales. In all cases, the mesh and geometry were generated with the aid of ANSYS Fluent 18.1. The mathematical methodology has been validated against field data in our previous work [1].

8.4 Results and Discussion

This section is divided into three main subsections. First, we will examine the capacity of a single thermosyphon to store cold energy in the ground. Second, a pool of STs will be modeled independently to examine how the storage capacity is affected when multiple STs are installed. Finally, a coupled model that links heat extraction of PTs with STs is simulated. Throughout this section, hourly weather data as measured by the Giant Mine Weather Station is used as per Fig 8-4.

8.4.1 Maximum storage capacity of a single thermosyphon

In this section, we evaluate the maximum energy that can be stored by a single thermosyphon installed near the GMRP site to serve as a workbench for the upcoming discussion on the results. Accordingly, a single thermosyphon was modeled over ten years of similar geometry to those installed at the GMRP as per Table 8.2. In order to evaluate the maximum energy stored by a single thermosyphon, the outer boundaries of the computational domain, r_o, are gradually increased until the model becomes independent from the distance between the thermosyphon and the outer boundaries.

By increasing the distance between the thermosyphon and outer boundaries gradually, a boundary independent solution is obtained at a distance of around 15 meters, as shown in Fig. 8-5. Evidently, as the distance increases, the stored energy becomes larger due to the higher thermal capacity of the ground at larger volumes. Nevertheless, at a distance of around 15 meters, the stored energy is purely dominated by the capacity of thermosyphon to extract

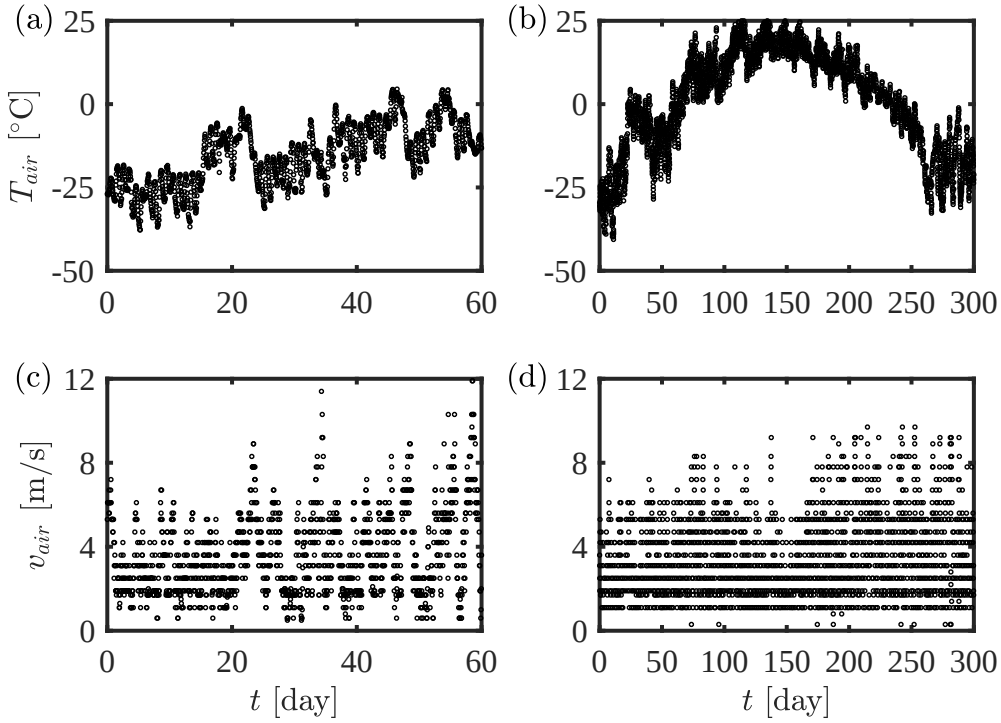

Figure 8-4: Hourly air data measured by the Giant Mine weather station [51]: Air temperature data of the a) passive thermosyphon test and b) hybrid thermosyphon test, and air speed data of the c) passive thermosyphon test and d) hybrid thermosyphon test.

property	value
Finned area of passive condenser	39 [m^2]
Thermosyphon outer diameter	0.114 [m]
Thermosyphon thickness	6 [mm]
Helical coil outer diameter	10.3 [mm]
Helical coil thickness	1.7 [mm]
Helical coil height	2.4 [m]

Table 8.2: Geometry of thermosyphons used in this study. The coil geometry is applicable to PTs only (there is no coil STs).

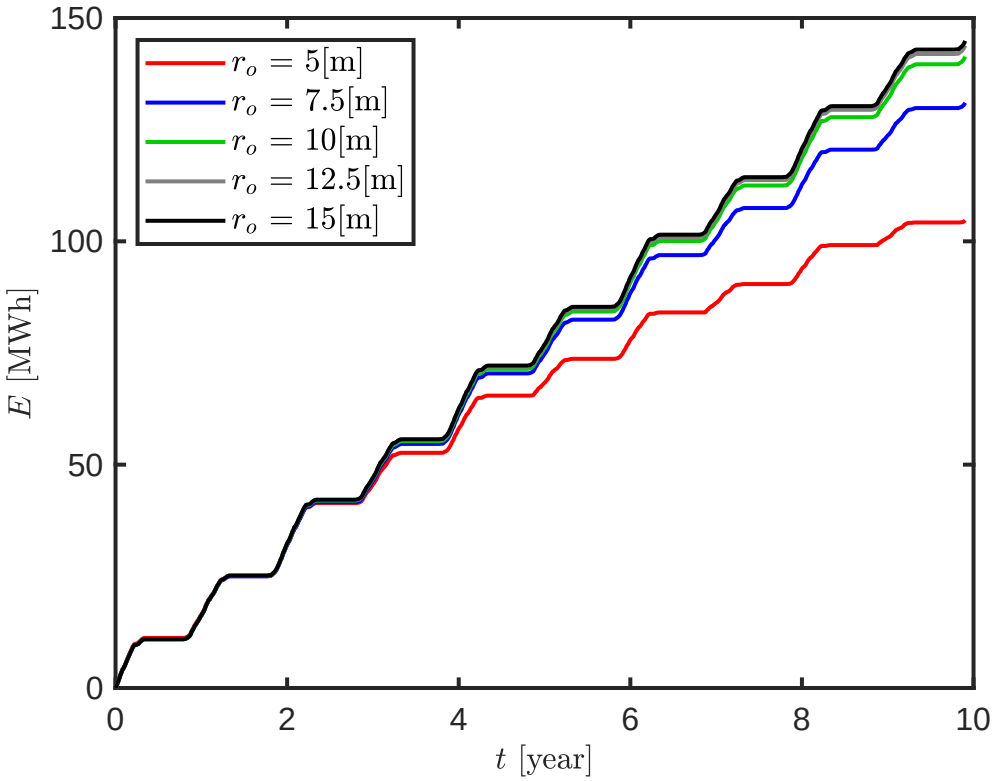

Figure 8-5: Maximum energy stored by a single thermosyphon operating independently is estimated at 150 [MWh] over 10 years.

wind cold energy rather than ground volume. The intermittent increase of stored energy is attributed to the seasonal weather conditions. In winter seasons, the air temperature is low enough to run the thermosyphon thus increasing the amount of cold energy stored. On the other hand, the thermosyphon becomes idle during warm seasons leading to a dormant period interrupting the heat extraction process.

8.4.2 Energy Strored by Several Adjacent Thermosyphons

In practical field scenarios, a single ST cannot store sufficient energy especially for grand applications such as the GMRP. Consequently, instead of installing a single ST, several thermosyphons should be installed next to each other to increase the amount of cold energy stored.

The cold energy of thermosyphons is extracted by a heat extraction pipe (HEP), as shown in Fig. 8-2(c-1). In this study, we considered using a 30% calcium chloride solution due its thermal stability as well as industrial reliability in the field (e.g., AGF of the Cigar Lake Uranium Mine [49], [50]). Also, the ST and HEP are arranged in a diamond configuration shaped as a bilateral right-angle triangle as shown in Fig. 8-2(a-1). The length of each of the bilateral sides is denoted d.

While there are several geometrical parameters that can be extensively studied and optimized, this study aims at demonstrating the concept of cold energy storage. Three main operational parameters are highlighted in this subsection: 1) The distance between the ST and HEP (d), 2) the volume flow rate of the heat transfer fluid (VF), and 3) the inlet temperature of the HTF (T_{in}).

Effect of distance between ST and HEP

As noted in Section 8.4.1, the larger the ground in vicinity of a thermosyphon, the higher the thermal storage capacity. Nevertheless, to effectively extract cold energy through HEP, sufficient amount of cold energy should travel the distance between the HEP and ST. Accordingly, the distance has been varied from 1 to 3 meters to better estimate the optimum spacing resulting in highest heat extraction for the case of the GMRP.

The parametric analysis shows that the amount of cold energy stored is proportional to d, as shown in Fig. 8-6(a). The added benefit of increasing d however becomes less as d increases. For instance, increasing d from 1[m] to 2[m] results in an increase in stored energy by around 30 [MWh] after 10 years (for each single ST and HEP); on the other hand increasing d, from 2[m] to 3[m] increases the energy stored by only 7[MWh] after the same time.

While larger ground volume has the capacity of storing more energy, the amount of energy extracted highly depends on how close the HEP to the ST as well, as can be seen from Fig. 8-6(b,c). In the short term, a closer distance is desired since less time is needed

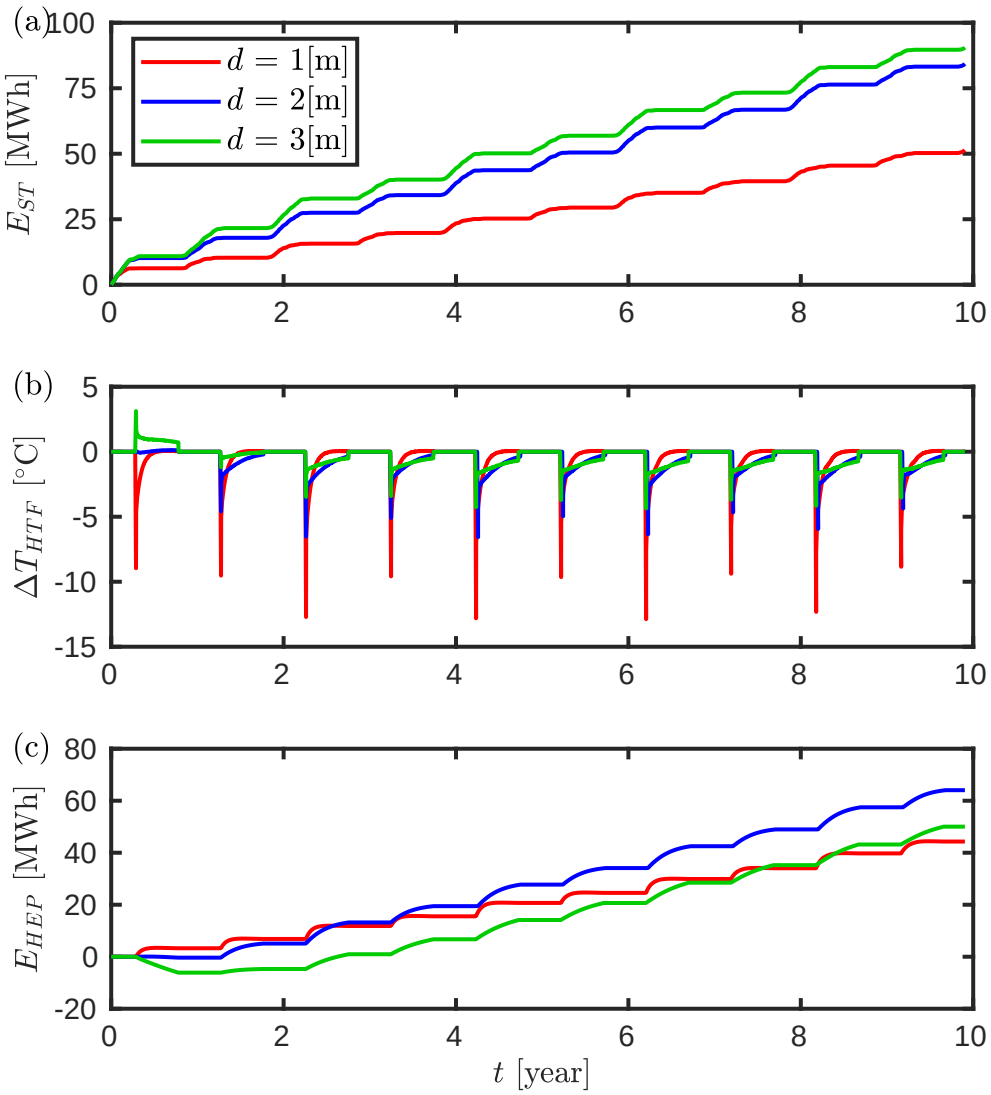

Figure 8-6: Effect of spacing between ST and HEP on the a) amount of energy stored by each ST, b) temperature difference across the HTF outlet and inlet to the CES, $\Delta T_{HTF} = T_{HTF,outlet} - T_{HTF,inlet}$, and c) amount of energy extracted by each HEP ($T_{in} = -5°$[C] and $VF = 1$ [m^3/hr]).

for cold energy to march from the ST to HEP. After the first winter, cold energy is only extracted when $d = 1$[m]. At higher d, positive temperature difference is observed between the inlet and outlet of HTF, implying that the HTF extracted *hot* energy (as in goethermal energy extraction applications using HEP [52], [53]), which is undesirable in cold energy storage for AGF applications. It takes 1 winter and 2 winters for cold energy energy to be extracted at $d = 2$[m] and $d = 3$[m], respectively. Despite that, the cold energy extracted in the case of $d = 2[m]$ becomes higher than that of $d = 1[m]$ after around 3 winters, due to the higher amount of cold energy stored in the former.

To better understand the difference in performance at different d, the concepts of local efficiency, η_l, and global efficiency, η_g, are introduced. The local efficiency is defined as the amount of energy extracted by HEP, E_{HEP}, divided by the amount of energy stored by ST, E_{ST}, ($\eta_l = E_{HEP}/E_{ST}$) in the *same* system. On the other hand, η_g compares E_{HEP} by the maximum energy that can be stored by a single thermosyphon shown in Fig. 8-5 ($\eta_g = E_e/E_{max}$). The results reveal that η_l is inversely proportional to d, as can be deduced from Fig. 8-7(a). This implies that most energy stored is extracted at lower d; in the case of $d = 1$[m], 85% of the energy stored is extracted after 10 years, as compared to 75% and 55% at $d = 2$[m] and $d = 3$[m], respectively.

Since higher local efficiency does not necessarily imply higher heat extraction, the concept of global efficiency is introduced where the maximum energy that can be stored by a thermosyphon is used as a reference. In a similar trend of Fig. 8-6(c), $d = 1$[m] provides best performance in the short term, but $d = 2$[m] is preferred between the second and tenth years of operation. The global efficiency at $d = 1$[m] quickly reaches a semi-steady state at 28% indicating that the system already extracts maximum amount possible of cold energy stored in every winter. In other words, the maximum global efficiency at $d = 1$[m] is 28%. The case of $d = 2$[m] is approaching the same behavior after 10 years at $\eta_g \sim 50\%$. When $d = 3$[m], the global efficiency is progressively increasing and will be higher than other cases after longer periods.

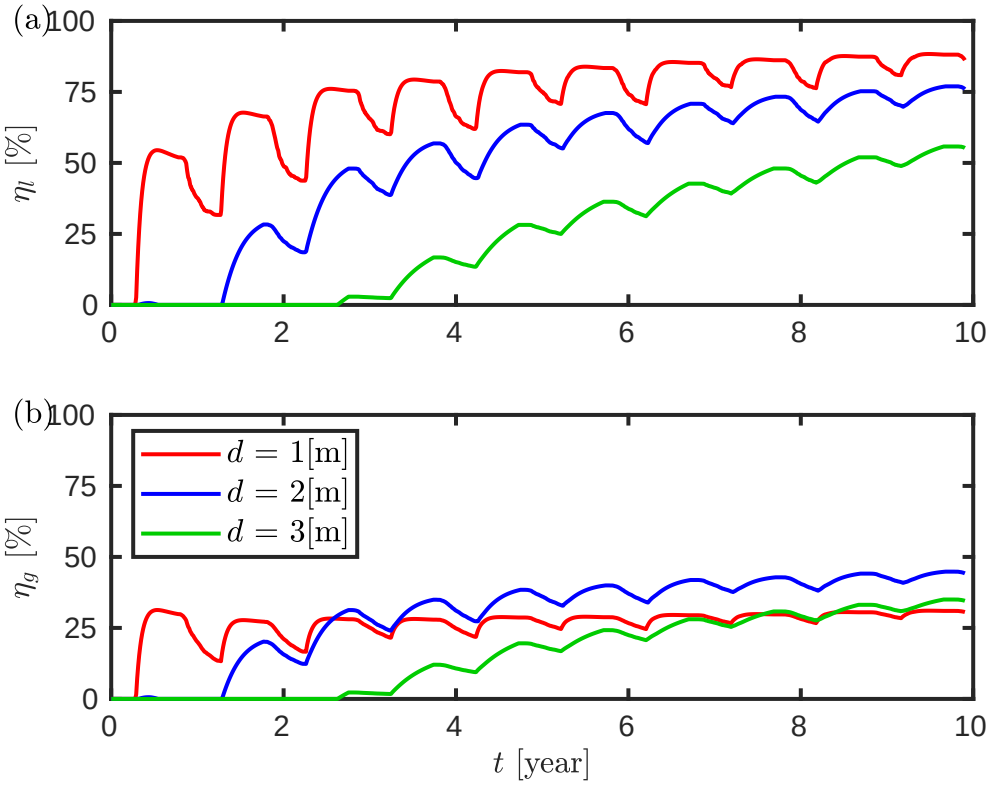

Figure 8-7: Effect of spacing between ST and HEP on the a) local efficiency (η_l) and b) global efficiency (η_g)

Overall, the spacing should be determined based on the desired payback period; shorter spacing can result in faster payback but less cold energy in the long run, and vice-versa. Thus, when implementing the concept of cold energy storage, it might be desired to alternate d to compromise between the speed of the payback as well the long-term cold energy stored.

Effect of HTF volume flow rate

The volume flow rate, VF, of the HTF is an essential operational design parameter in energy systems. Thus, the VF was changed in this subsection from 0.5[m^3/hr] to 1.5[m^3/hr]. The results show that the amount of energy stored by ST is similar regardless of the volume flow rate. This is attributed to the same spacing between HEPs and STs (equal d) as well as same atmospheric conditions, as noted in Fig. 8-8(a). Nonetheless, the temperature difference between the inlet and outlet of the HTF, ΔT_{HTF}, is highly affected by the volume flow rate; particularly, lower flow rate results in higher temperature difference, as can be seen in Fig, 8-8(b). The volume flow rate of the HTF can thus be controled to ensure the chemical and thermal stability of the HTF as well as freeze-pipe walls. Despite the differences in ΔT_{HTF}, the amount of energy extracted, E_{HEP}, is the same as observed in Fig. 8-8(c). It should be noted here that the flow is laminar in all scenarios; consequently, increasing the flow rate does not result in higher flow Nusselt number [54]. Thus, the amount of energy extracted is similar. Once the flow exceeds turbulence threshold the Nusselt number will be affected by the flow rate which will increase the heat extraction capacity. Nonetheless, in laminar conditions considered in this study, η_l and η_g are similar at different laminar flow rates due to the similar energy extracted and stored in all scenarios.

Effect of HTF inlet temperature

In field scenarios, the inlet temperature of the HTF is controlled by the amount of heat gained by the HTF at the PT. In this subsection, we aim at understanding how the HTF inlet temperature affects the efficiency of the CES system. As can be observed from Fig. 8-

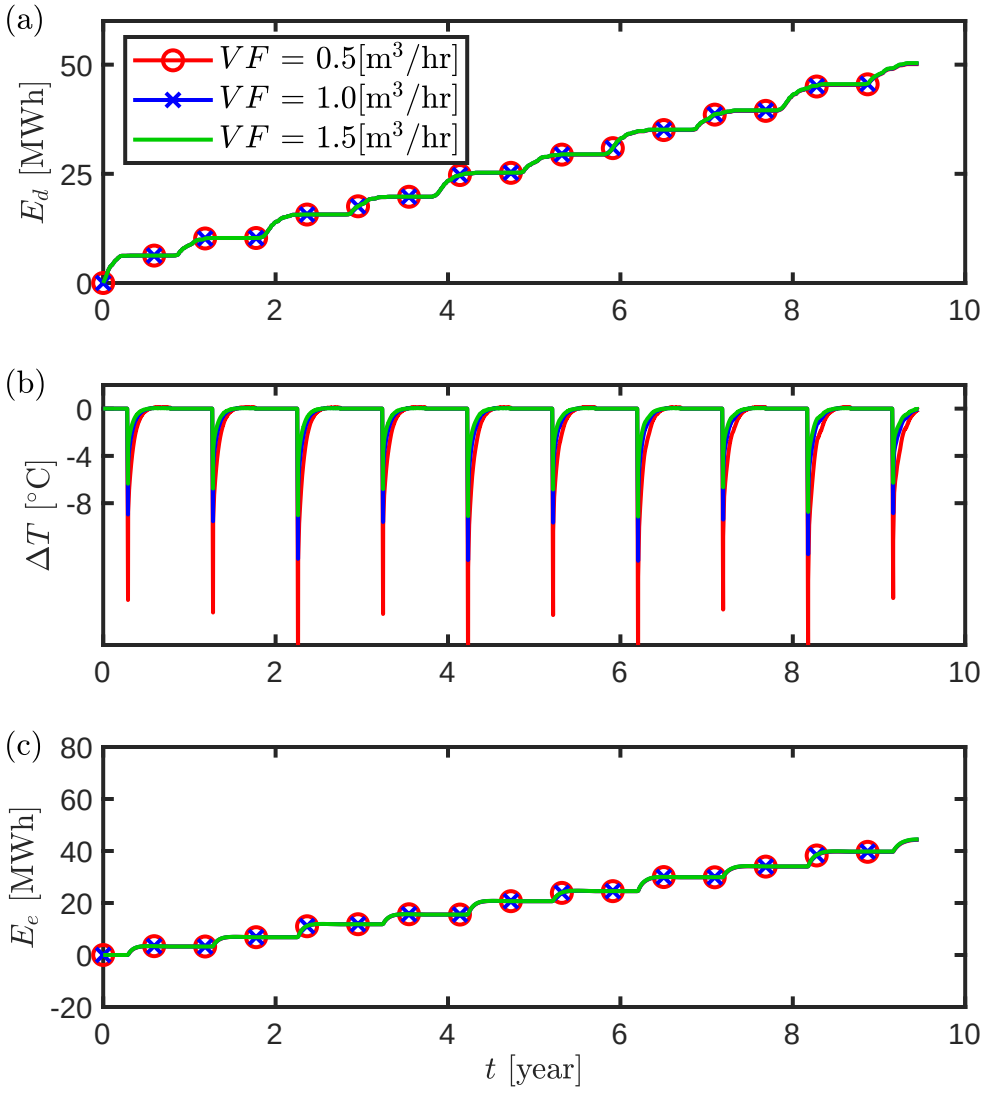

Figure 8-8: Effect of the volume flow rate of the HTF on the a) amount of energy stored by each ST, b) temperature difference between the HTF inlet and outlet, and c) amount of energy extracted by each HEP ($d = 1[\mathrm{m}]$ and $T_{in} = -5[^\circ\mathrm{C}]$)

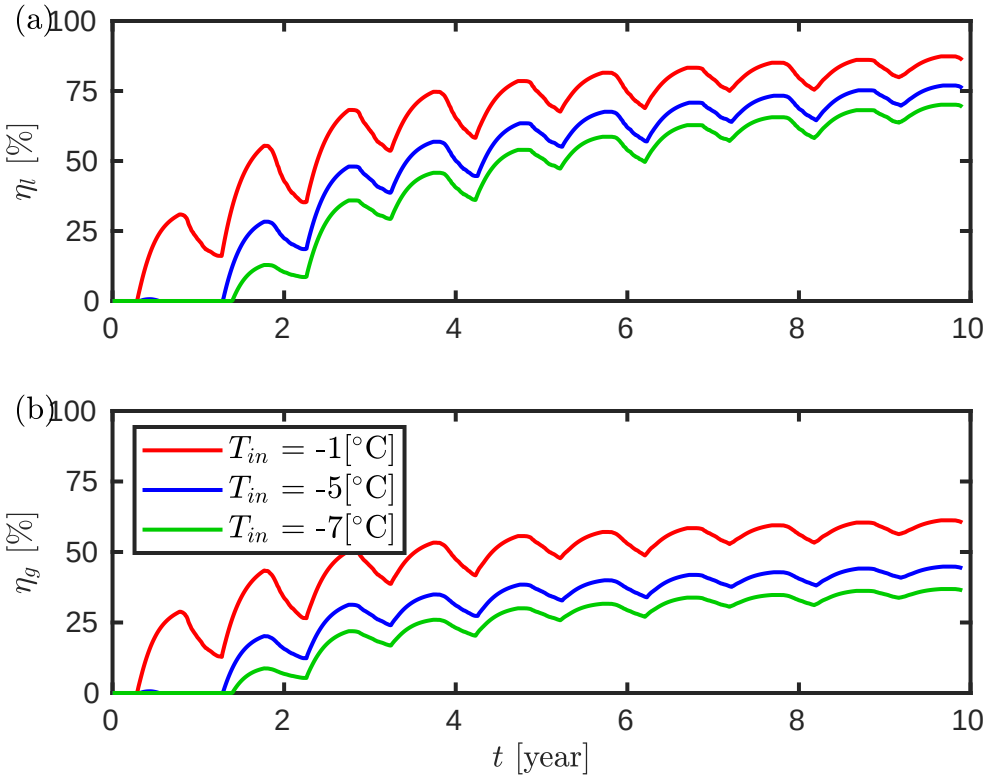

Figure 8-9: Effect of HTF inlet temperature on the a) local efficiency (η_l) and b) global efficiency (η_g) - $d = 2$[m] and $VF = 1$ [m^3/hr]

9, increasing the inlet HTF temperature linearly increases the system efficiency. At higher inlet temperatures, more energy can be extracted as deduced from Eq. 8.17. Further, higher inlet temperature can initiate energy extraction earlier than lower ones. For instance, when the inlet temperature is set at -1[°C], cold energy extraction starts from the first summer. Nevertheless, at inlet temperatures of -3[°C] and -5[°C], two winters were needed to charge the ground with sufficient cold energy so ground temperature of the wall is lower than the HTF inlet temperature.

8.4.3 Giant Mine coupling with CES

In this section, we couple the CES pool with the ground freezing process at the GMRP. First, we examine the effect of spacing in the CES system as well as discharging period on

the heat extraction capacity of PTs. Particularly, $d = 1$[m] and $d = 2$[m] are considered due to the lower CES effeciency at higher d as observed in the previous subsection. Lastly, the potential advantage of utilizing a CES system is discussed by comparing it with a traditional system without CES. In this subsection, the volume flow rate of the HTF is set at 1 [m^3/hr]. Also, T_{in} and T_{out} are now coupled with PT, such that the inlet temperature of the HTF to the HEP equals to the outlet temperature of the HTF from the PT calculated using energy balance (heat extracted by the PT in Eq. (8.8)). Similarly, the inlet temperature of the HTF to the PT equals to the outlet temperature of the HTF from the HEP as determined in Eq. (8.17).

Analysis on the CES discharging period & spacing

In this subsection, we examine the capability of the CES system to provide cold energy to PTs by operating discharging period for four and six months. The impact of the spacing between STs and HEPs is also considered in the analysis.

First, a cold energy discharging period is set at four months to test the capability of the CES system to provide cold energy for short periods. When $d = 1$[m], ΔT_{HTF} (with respect to the CES system) is higher than that of $d = 2$[m] at the start of each discharging period, as can be seen from Fig. 8-10(a). This is attributed to the lower local temperature near the HEP at lower d. However, as the local cold energy is consumed, higher ΔT_{HTF} is noted when $d = 2$[m] because of the larger amount of cold energy stored. The only exception is the first year due to the longer period needed for the cold energy to travel from the STs to the HEPs, as discussed in Section 8.4.2. The differences of the HTF temperature profile is reflected on the heat-rate transferd during warm seasons by HEPs, as shown in Fig. 8-10(b). As for the PTs, the heat-rate fluctuates significantly when heat is extracted during cold seasons due to the hourly variation of wind temperature and speed as per Fig. 8-4. However, It can be noted that the discharging period has the capacity to be extended for more than four months as the PTs are idle for around two months after each discharging period.

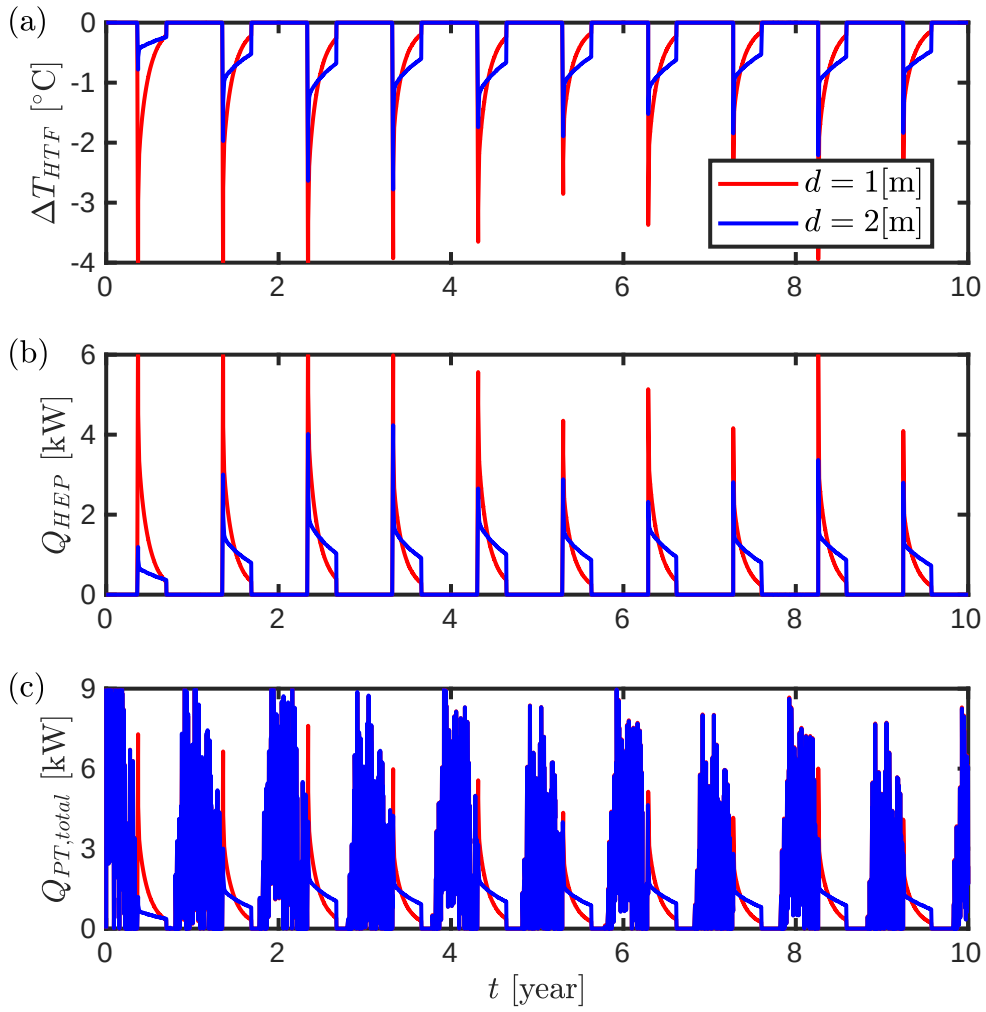

Figure 8-10: Effect of d when the discharging period is four months: a) HTF temperature difference between the CES inlet and outlet , b) Heat-rate extracted by each HEP, and c) Heat extraction rate by each PT.

When increasing the discharging period to six months, a similar trend is observed in regards to ΔT_{HTF} and Q_{HEP} with few exceptions. Since the discharging period is now longer, the case of $d = 2$[m] can provide higher power for longer periods especially after the third year due to the higher amount of energy stored, as shown in Fig. 8-11 and Fig. 8-12(a). Specifically, the amount of cold energy transferred is initially higher at $d = 1$[m] for the first two years. After that, energy transferred at $d = 2$[m] catches up and becomes slightly higher in a 10 year period, as can be seen in Fig. 8-12(b). This however does not results in a substantial increase in E_{PT} over a 10 year period, as observed in Fig. 8-12(d) due to the relatively high wind heat extraction of PTs during cold seasons, as can be seen from Fig. 8-12(c). In the longer run after ten years, it is expected that a CES spacing of two meters to have a larger impact.

Comparison with a traditional system

We end this study by highlighting the potential advantage of using a CES system. In Section 8.4.3, a longer discharging period only enhanced the performance of the overall system. Accordingly, in this section, HEPs are operated whenever the air temperature is too warm to run PTs, thus preventing PTs from becoming idle. In other words, energy stored in the CES pool is utilized whenever the air temperature is higher than the monitored evaporator temperature of the PT.

As can be seen from Fig. 8-13(a), the total energy extracted by a CES integrated PT is around 15% higher than a traditional thermosyphon without a storage system. Thus, the potential of a CES system to increase the efficiency of AGF applications is demonstrated, which is the main scope of this study proposing the concept of CES in AGF. The main evident difference between the two systems is the long idle period of a traditional thermosyphon with CES during warms seasons, as can noted in Fig. 8-13(b). Traditional thermosyphons remain idle for around 6 months a year, whereas our proposed system with integrated CES pool allow the thermosyphon to run year-round. In the first two years, it is observed that a CES

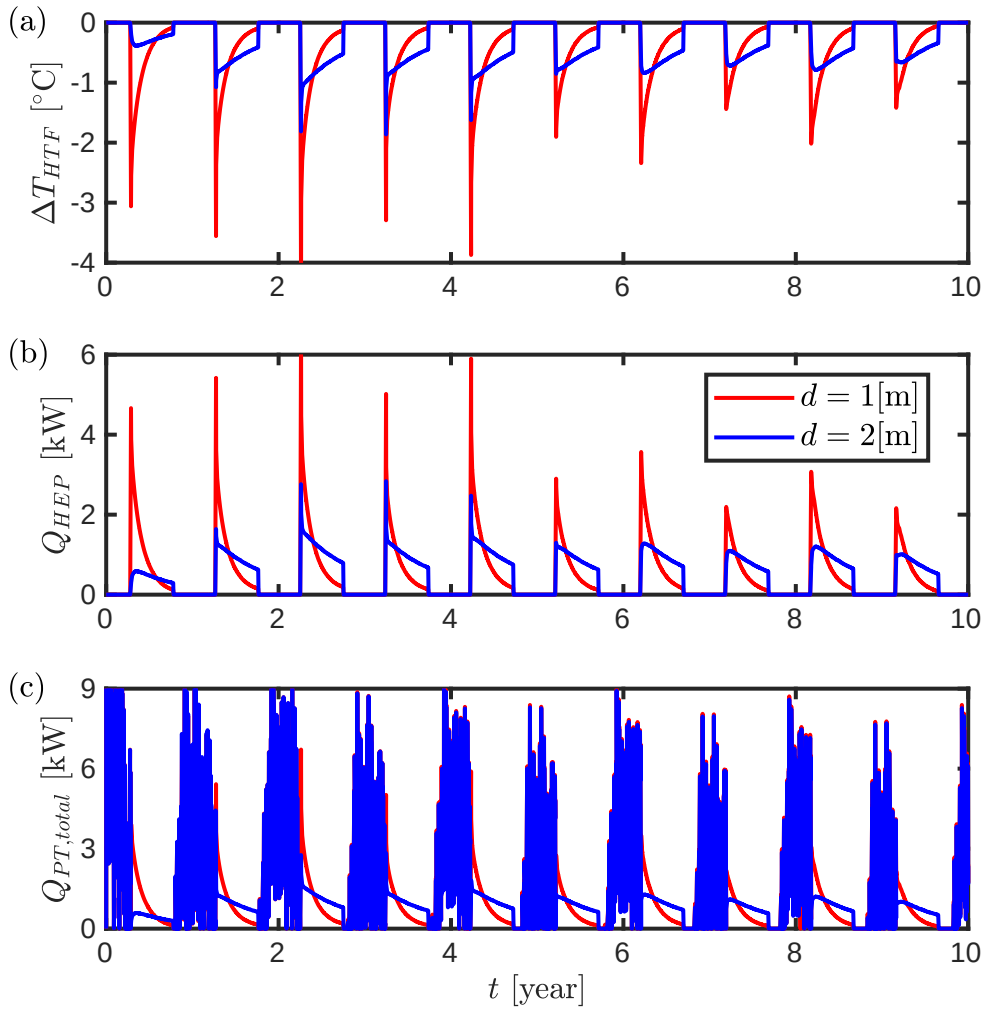

Figure 8-11: Effect of d when the discharging period is six months: a) HTF temperature difference between the CES inlet and outlet , b) Heat-rate extracted by each HEP, and c) Heat extraction rate by each PT.

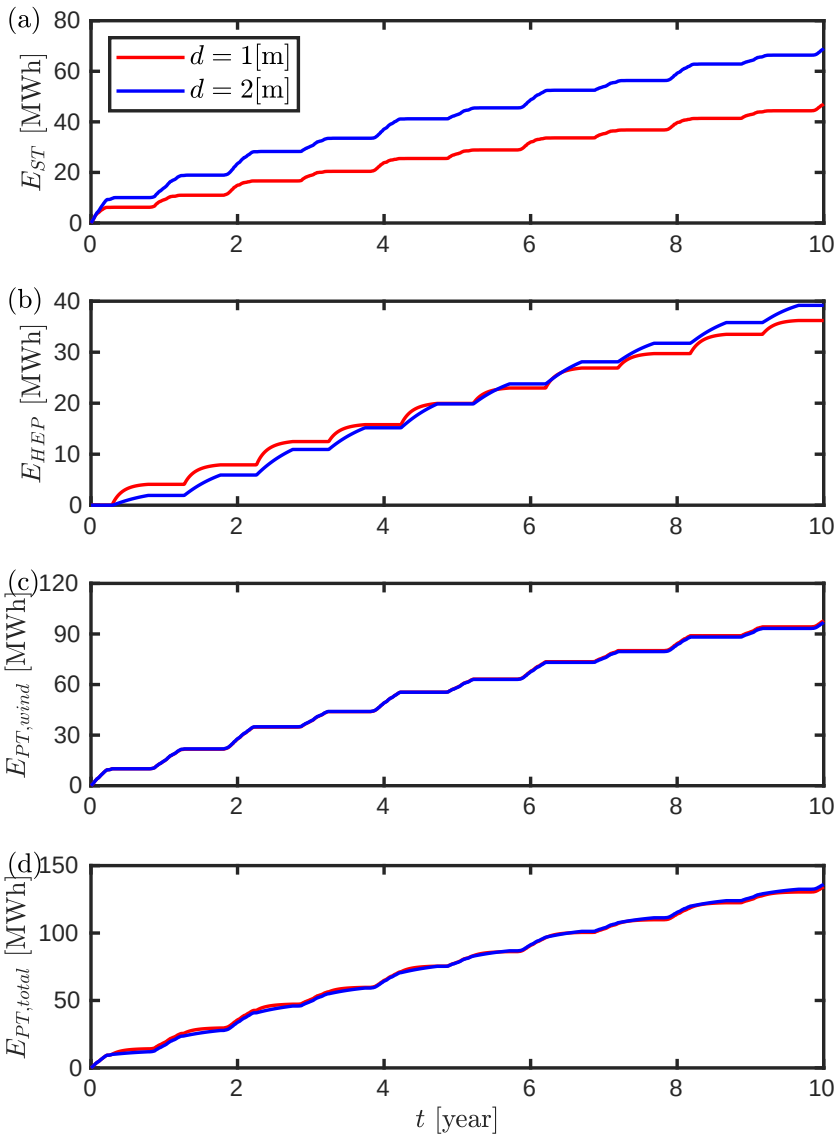

Figure 8-12: Effect of d when the discharging period is six months: a) Amount of cold-energy deposited by each ST in the CES pool, b) amount of cold energy extracted by each HEP, and c) Amount of enery extracted by each PT passively from available cold wind, and d) amount of energy extracted by each PT from CES pool.

system with $d = 1$[m] performs better than that of a CES system with $d = 2$[m]. Afterwards, the amount of energy extracted by PTs becomes larger when $d = 2$[m], as discussed in the previous sections.

The increased energy extracted by adding a CES system also increases the extent of the frozen ground throughout the depth of the PTs, as shown in Fig. 8-14. Typically, a lateral frozen ground thickness of six meters is often desired to ensure the availability of an impenetrable frozen body. At the top of the chambers, the six-meters limit is reached within 1.2 years in all scenarios, at different d or without a CES system, as can be seen in Fig. 8-14(a). However, as traditional thermosyphons without CES become dormant during warm seasons, the ground thaws below the six-meters threshold after 1.8 years. At deeper levels of the thermosyphon, the freezing time becomes larger due to the geothermal temperature gradient (see Eq. (8.18)). At the middle of the chambers (depth of 50 meters), the six-meters limit is permanently maintained after 1.3 years when a CES system is employed. Nevertheless, the frozen ground formed by a traditional system thaws in the summer of the second year; a continuous six-meters δ is only formed after 2 years of operation. At the bottom of the chambers, the freezing time needed with a CES pool is around 1.9 years, as compared to 2.9 years without a CES system. Overall, the effect of integrating a CES pool is evident on decreasing the freezing time. Once the ground freezing process is completed, the CES pool can then be employed in various applications, such as heating of buildings or geothermal power generation.

8.5 Conclusion

In this study, a novel ground coupled cold energy storage (CES) concept is proposed for application of artificial ground freezing (AGF) and permafrost protection applications in cold regions. The proposed system is based on traditional passive thermosyphons supported by a CES pool that runs passive thermosyphons during warm seasons. The CES pool is

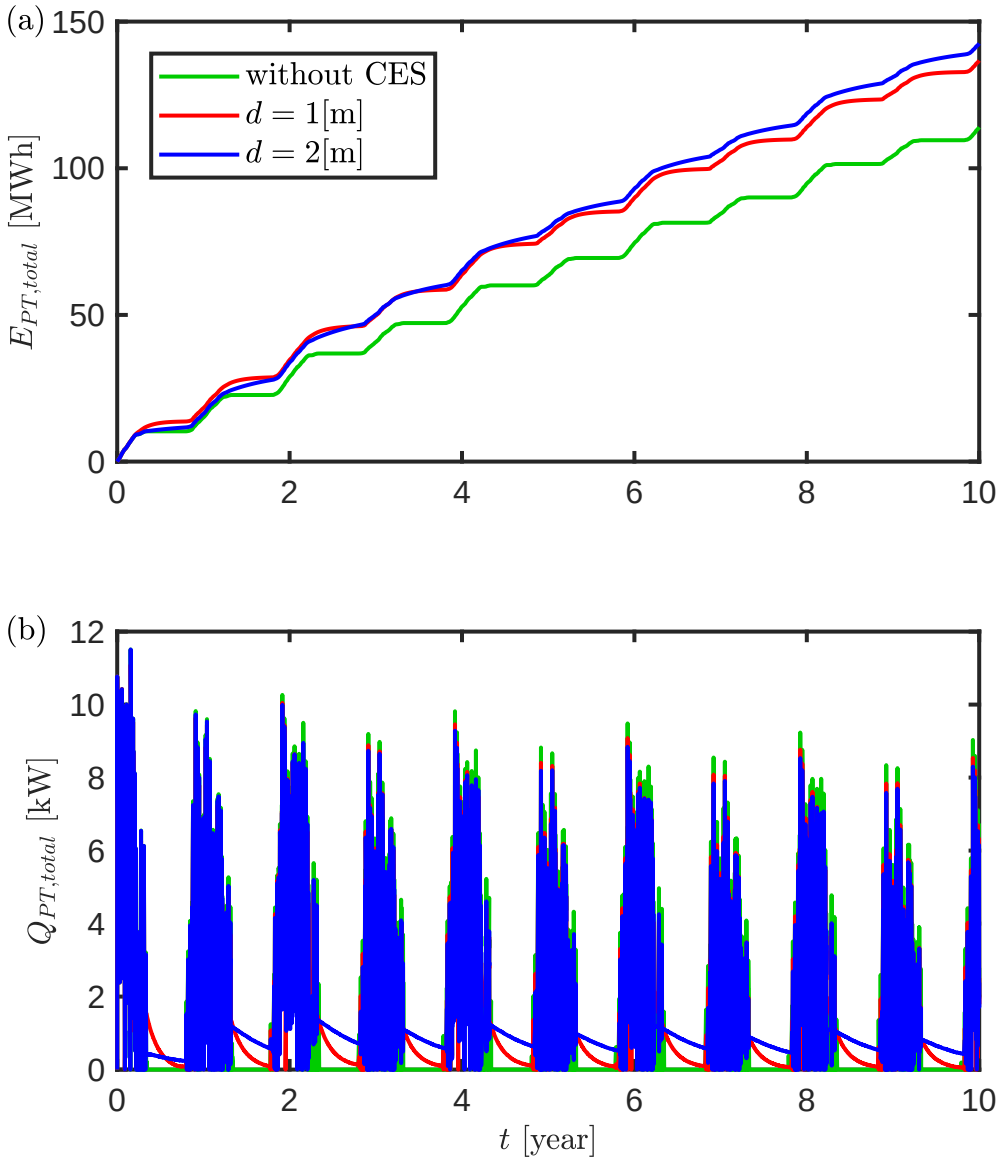

Figure 8-13: Effect of integrating a CES system: a) total Energy extracted by each PT, and b) Heat rate extracted by each PT

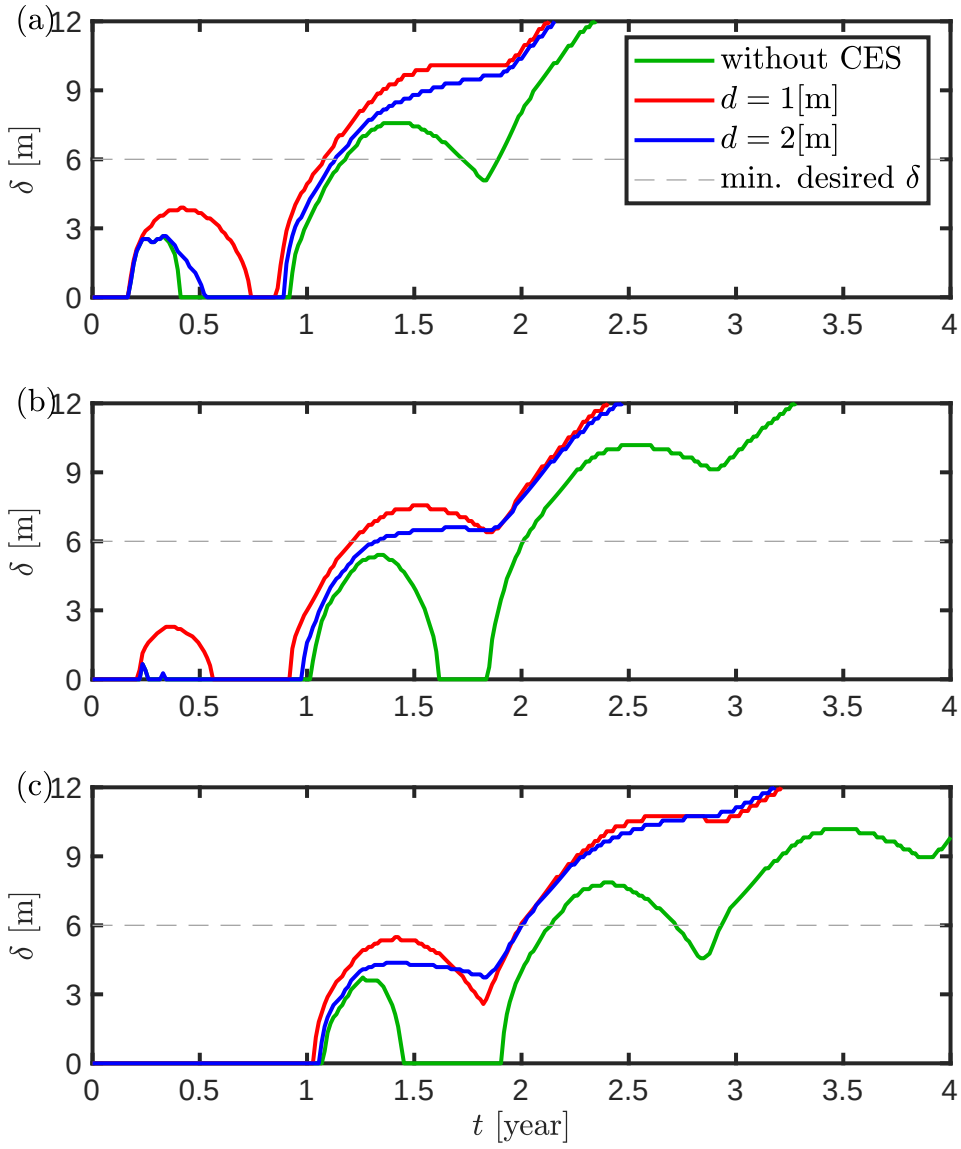

Figure 8-14: Effect of integrating a CES system on the lateral frozen ground thickness at a depth of a) 20 meters (5 meters above the contaminated chambers), b) 50 meters (middle of the contaminated chambers), and c) 80 meters (5 meters below the contaminated chambers)

made up of cold-energy storage thermosyphons (ST) and heat extraction pipes installed in the ground nearby the primary thermosyphons (PTs) operating in the site of interest. In cold seasons, while the PTs extract energy using naturally available cold wind, STs also utilize the cold wind to store cold energy. In warm seasons, HEPs transfer this cold energy to the primary thermosyphons (PT) operating on the site of interest, which is the Giant Mine in the present study. The proposed concept has been demonstrated by a well-validated numerical model.

In the results section, the effect of three parameters on the capacity and efficiency of the CES system is firstly investigated: 1) Spacing between STs and HEPs in the CES pool (d), 2) volume flow rate of the heat transfer fluid (HTF) in the HEP, and 3) inlet temperature of the HTF. The results reveal that there is an optimum spacing that yield in maximum cold energy extracted at each year of operation; shorter d is preferable in the short term and vice versa. Further, the volume flow rate of the HTF has negligible effect when the flow is laminar. Additionally, The inlet HTF temperature is linearly proportional to the CES efficiency.

Lastly, the CES system is coupled to the PTs for the case of the Giant Mine Remediation Project (GMRP). Our proposed system demonstrated an increase in the heat extraction of PTs by more than 15% as compared with a traditional system (without a CES). Accordingly the freezing process is completed one year faster with a CES system. As compared with hybrid thermosyphons that employ active mechanical refrigeration plants, our innovative concept save 2.3 [GWh] and 990 tons of CO_2 for every 100 thermosyphons.

In our future work, we will conduct optimization analysis to investigate the impact of several operational parameters, such as the discharging duration of cold energy, the CES layout & number of units.

Acknowledgments

The authors would like to thank the FRQNT Development Durable du Secteur Minier – II (2020-MN-284402) and Ultra Deep Mining Network (UDMN) (241695 Tri-Council (NCE – UDMN) 2-003). The first author wishes to thank the McGill Engineering Doctoral Award (MEDA) and the FRQNT Doctoral award (Grant No. 2021-B2X-306519),

Bibliography

[1] Government of Canada, History of Giant Mine (2018).
URL https://www.aadnc-aandc.gc.ca/

[2] R. Silke, The Operational History of Mines in the Northwest Territories, Canada, Tech. rep., Yellowknife (2009).

[3] Canada North Environmental Services, Giant Mine Human Health and, Tech. rep. (2018).

[4] H. Paulson, New study shows low risk to public health 70 years after Giant Mine's toxic legacy (2021).
URL https://www.cbc.ca/

[5] A. F. Zueter, G. Newman, A. P. Sasmito, Numerical study on the cooling characteristics of hybrid thermosyphons: Case study of the Giant Mine, Canada, Cold Regions Science and Technology 189 (February) (2021) 103313. doi:10.1016/j.coldregions.2021.103313.

[6] Environment and Climate Change Canada, Canada emission factors for grid electricity, Tech. rep. (2019).
URL https://bullfrogpower.com

[7] I. Holubec, Flat loop thermosyphon foundations in warm permafrost, Tech. rep., I. Holubec Consulting Inc., Northwest Territories (2008).

[8] E. Yarmak, E. L. Long, Recent developments in thermosyphon technology, in: Cold Regions Engineering: Cold Regions Impacts on Transportation and Infrastructure, Anchorage, 2002, pp. 656–662.

[9] J. W. Rooney, C. H. Riddle, R. L. Scher, Foundation rehabilitation at ADOT/PF Jim River maintenance camp, in: Society of Petroleum Engineers - Arctic Technology Conference 2011e, Anchorage, 1991, pp. 829–840. doi:10.2523/22226-ms.

[10] L. Guo, Z. Zhang, X. Wang, Q. Yu, Y. You, C. Yuan, Y. Xie, T. Gou, Stability analysis of transmission tower foundations in permafrost equipped with thermosiphons and vegetation cover on the Qinghai-Tibet Plateau, International Journal of Heat and Mass Transfer 121 (2018) 367–376. doi:10.1016/j.ijheatmasstransfer.2018.01.009.

[11] L. Xu, Y. Shen, L. Zhang, Study on Stability of Low Embankment of the High Temperature Permafrost in Qinghai-Tibet Railway, in: International Conference on Railway Engineering, 2004.

[12] S. P. Varlamov, Thermal monitoring of railway subgrade in a region of ice-rich permafrost, Yakutia, Russia, Cold Regions Science and Technology 155 (2018) 184–192.

[13] Q. Y. Zhu, W. Wang, S. Y. Wang, X. F. Zhou, G. Y. Liao, S. J. Wang, J. B. Chen, Unilateral heat-transfer asphalt pavement for permafrost protection, Cold Regions Science and Technology 71 (2012) 129–138.

[14] Y. Zhong, T. Ma, X. Huang, Asphalt mixture design and thermology experiments on heat-resistant surfaces in permafrost regions, Journal of Testing and Evaluation 43 (4) (2015) 833–840.

[15] W. Pei, M. Zhang, Z. Yan, S. Li, Y. Lai, Numerical evaluation of the cooling performance of a composite L-shaped two-phase closed thermosyphon (LTPCT) technique in permafrost regions, Solar Energy 177 (November 2018) (2019) 22–31.

[16] M. Zhang, Y. Lai, Q. Wu, Q. Yu, T. Zhao, W. Pei, J. Zhang, A full-scale field experiment to evaluate the cooling performance of a novel composite embankment in permafrost regions, International Journal of Heat and Mass Transfer 95 (2016) 1047–1056. doi:10.1016/j.ijheatmasstransfer.2015.12.067.

[17] W. Ma, Z. Wen, Y. Sheng, Q. Wu, D. Wang, W. Feng, Remedying embankment thaw settlement in a warm permafrost region with thermosyphons and crushed rock revetment, Canadian Geotechnical Journal 49 (9) (2012) 1005–1014. doi:10.1139/T2012-058.

[18] Q. Ma, X. Luo, J. Gao, W. Sun, Y. Li, T. Lan, Numerical evaluation for cooling performance of a composite measure on expressway embankment with shady and sunny slopes in permafrost regions, Energy (2022) 123194.

[19] A. L. Lyazgin, R. M. Bayasan, S. A. Chisnik, V. G. Cheverev, G. P. Pustovoit, Stabilization of pile foundations subjected to frost heave and in thawing permafrost, in: Eighth International Conference on Permafrostth International Conference on Permafrost, Zurich, 2003, pp. 21–25.

[20] R. M. Bayasan, A. G. Korotchenko, N. G. Volkov, G. P. Pustovoit, A. D. Lobanov, Use of two-phase heat pipes with the enlarged heat-exchange surface for thermal stabilization of permafrost soils at the bases of structures, Applied Thermal Engineering 28 (4) (2008) 274–277. doi:10.1016/j.applthermaleng.2006.02.022.

[21] Y. Zhang, K. Han, B. Xu, Z. Chang, Experimental study on the temperature evenness of heat pipe using magnetic nano-fluids as the working medium in permafrost regions, Advanced Materials Research 614-615 (2013) 327–330. doi:10.4028/www.scientific.net/AMR.614-615.327.

[22] A. B. Solomon, A. M. R. Kumar, K. Ramachandran, B. C. Pillai, C. S. Kumar, M. Sharifpur, J. P. Meyer, Characterisation of a grooved heat pipe with an an-

odised surface, HEAT AND MASS TRANSFER 53 (3) (2017) 753–763. doi:10.1007/s00231-016-1856-8.

[23] Y. Tian, Z. Yang, Y. Liu, X. Cai, Y. Shen, Long-term thermal stability and settlement of heat pipe-protected highway embankment in warm permafrost regions, Engineering Geology 292 (2021) 106269.

[24] V. K. Kukkapalli, J. H. Kim, S. Kim, Optimum design of thermosyphon evaporators for roadway embankment stabilization in the arctic regions, Journal of Mechanical Science and Technology 35 (10) (2021) 4757–4764. doi:10.1007/s12206-021-0941-1.

[25] V. Kukkapalli, S. Kim, Roadway embankment stabilization on permafrost using thermosyphons with Y-shaped evaporators, IOP Conference Series: Materials Science and Engineering 507 (1). doi:10.1088/1757-899X/507/1/012017.

[26] W. Pei, M. Zhang, Y. Lai, X. Zhang, T. Luo, A self-adaption horizontal thermosyphon technology in uneven thermal control of roadway embankments in sub-arctic permafrost regions, Transportation Geotechnics (2022) 100714.

[27] W. Pei, M. Zhang, S. Li, Y. Lai, L. Jin, W. Zhai, F. Yu, J. Lu, Geotemperature control performance of two-phase closed thermosyphons in the shady and sunny slopes of an embankment in a permafrost region, Applied Thermal Engineering 112 (2017) 986–998.

[28] W. Pei, M. Zhang, Y. Lai, Z. Yan, S. Li, Evaluation of the ground heat control capacity of a novel air-L-shaped TPCT-ground (ALTG)cooling system in cold regions, Energy (2019) 655–668.

[29] Y. Chang, Y. Qihao, Y. Yanhui, G. Lei, Formation mechanism of longitudinal cracks in expressway embankments with inclined thermosyphons in warm and ice-rich permafrost regions, Applied Thermal Engineering 133 (2018) 21–32.

[30] J. Chen, B. Zhang, R. Song, X. Dong, L. Zhang, C. Ji, Z. Bo, S. Ruifang, D. Xianfu, Z. Luxin, Observation Study on the Stability of Frozen Soil Roadbed Equipped with Thermosyphon in Chaidaer-muli Railway, in: J. Zhao (Ed.), Advanced Materials Research, Vol. 255-260 of Advanced Materials Research, Kunming Univ Sci & Technol; Int Assoc Sci & High Technol, 2011, pp. 4003–4007.

[31] A. M. Wagner, Creation of an artificial frozen barrier using hybrid thermosyphons, Cold Regions Science and Technology 96 (2013) 108–116.

[32] D. F. Haynes, J. P. Zarling, W. F. Quinn, G. E. Gooch, Laboratory tests with a hybrid thermosyphon, in: Proceedings of the 10th International Conference on Ocean, Offshore and Arctic Engineering, Vol. 4, American Society of Mechanical Engineers, Stavanger, 1991, pp. 93–99.

[33] A. M. Wagner, J. B. Maakestad, E. Yarmak, T. A. Douglas, Artificial ground freezing using solar-powered thermosyphons.

[34] M. Alzoubi, S. Ali Ghoreishi-Madiseh, A. P. Sasmito, N. Kunz, A. Guimaraes, Renewable energy-based artificial ground freezing as an adaptation solution for sustainability of permafrost in post-climate change conditions, IOP Conference Series: Earth and Environmental Science 268 (1).

[35] M. A. Alzoubi, S. Poncet, A. P. Sasmito, Hybrid artificial ground freezing as a sustainable solution for containing hazardous-waste in critical environmental projects, Cold Regions Science and Technology 192.

[36] W. Pei, M. Zhang, S. Li, Y. Lai, Y. Dong, L. Jin, Laboratory investigation of the efficiency optimization of an inclined two-phase closed thermosyphon in ambient cool energy utilization, Renewable Energy 133 (2019) 1178–1187.

[37] M. Kaviany, Principles of Heat Transfer in Porous Media, Springer Science & Business Media, 2012.

[38] A. Zueter, A. Nie-Rouquette, M. A. Alzoubi, A. P. Sasmito, Thermal and hydraulic analysis of selective artificial ground freezing using air insulation: Experiment and modeling, Computers and Geotechnics 120 (2020) 103416.

[39] Y. A. Cengel, Heat and Mass Transfer: Fundamentals and Applications, 3rd Edition, McGraw-Hill, Boston, 2007.

[40] H. Imura, H. Kusuda, J.-I. Ogata, T. Miyazaki, N. Sakamoto, Heat transfer in two-phase closed-type thermosyphons, JSME Transactions 45 (1979) 712–722.

[41] W. Nusselt, The condensation of steam on cooled surfaces, Z. Ver. Dtsch. Ing 60 (1916) 541–546.

[42] A. Zukauskas, Heat Transfer from Tubes in Crossflow, in: Advances in heat transfer, Vol. 8, Elsevier, 1972, pp. 93–160.

[43] K. A. Gardner, Efficiency of extended surface, Transactions of ASME 67 (1945) 621–631.

[44] B. K. Hardik, P. K. Baburajan, S. V. Prabhu, Local heat transfer coefficient in helical coils with single phase flow, International Journal of Heat and Mass Transfer 89 (2015) 522–538.

[45] R. A. Seban, E. F. McLaughlin, Heat transfer in tube coils with laminar and turbulent flow, International journal of heat and mass transfer 6 (5) (1963) 387–395.

[46] C. M. White, Streamline flow through curved pipes, Proceedings of the Royal Society of London. Series A, Containing Papers of a Mathematical and Physical Character 123 (792) (1929) 645–663.

[47] A. F. Zueter, M. Xu, M. A. Alzoubi, A. P. Sasmito, Development of conjugate reduced-order models for selective artificial ground freezing: Thermal and computational analysis, Applied Thermal Engineering 190 (2021) 116782.

[48] A. F. Zueter, A. G. Madiseh, F. P. Hassani, A. P. Sasmito, Effect of Freeze Pipe Eccentricity in Selective Artificial Ground Freezing Applications, ASME Journal of Thermal Science and Engineering Applications 14 (2022) 011015.

[49] P. H. Agson-Gani, A. F. Zueter, M. Xu, S. A. Ghoreishi-Madiseh, J. C. Kurnia, A. P. Sasmito, Thermal and hydraulic analysis of a novel double-pipe geothermal heat exchanger with a controlled fractured zone at the well bottom, Applied Energy 310 (January) (2022) 118407. doi:10.1016/j.apenergy.2021.118407.
URL https://doi.org/10.1016/j.apenergy.2021.118407

[50] S. Pokhrel, L. Amiri, A. Zueter, S. Poncet, F. P. Hassani, A. P. Sasmito, S. A. Ghoreishi-Madiseh, Thermal performance evaluation of integrated solar-geothermal system; a semi-conjugate reduced order numerical model, Applied Energy 303 (2021) 1–16.

[51] R. Shah, A. London, Concentric Annular Ducts, in: Laminar Flow Forced Convection in Ducts, Academic Press, New York, 1978, Ch. XII, pp. 284–321.

[52] National Institute of Standards and Technology, NIST chemistry webbook (2018).
URL https://webbook.nist.gov/

[53] SRK Consulting (Canada) Inc., Freeze Optimization Study Update for MVEIRB and Parties Aboriginal Affairs and Northern Development Freeze Optimization Study Update for MVEIRB and Parties, Tech. Rep. August, Ottawa (2012).

[54] Government of Canada, Historical Data (2019).
URL https://climate.weather.gc.ca/

Chapter 9

Scholarly Discussion of Findings

Preface

In this chapter, we present a comprehensive discussion of the thesis findings. We start with highlighting the high impact of our research questions, followed by research gaps. After that, we elaborate on our methodology and outcomes

Contents

9.1 Overview of research problem

Artificial ground freezing (AGF) is a common geotechnical engineering methods employed in some civil and mining applications. AGF systems have demonstrated high reliability as well

as compatibility with a wide range of geological and environmental conditions. Nevertheless, the main disadvantage of AGF methods is their tremendous operational costs when coupled with refrigeration systems, or slow freezing rate when used passively with heat transfer devices in their current form in the industry.

Particularly, the mining industries often operate AGF systems in large scale and for long periods of time. For instance, the Cigar Lake Mine in Northern Saskatchewan, Canada, requires and AGF system that freezes the ground surrounding an ore-body at a depth of 400 meters to 460 meters below the ground the surface. This has led the mining industries to innovate an unusual type of freeze-pipes that include an air insulation layer to minimize the refrigeration load. Specifically, the air insulates the freeze-pipe from the ground surface to the ore-body, covering a distance of 400 meters. Accordingly, a selective artificial ground freezing (S-AGF) system is used in the Cigar Lake Mine.

While literature review of S-AGF analyzed the development of the frozen ground, a comprehensive model to examine the fundamentals of the S-AGF freeze-pipes need to be conducted. The capacity of the air cavity to insulate the ground has not been addressed in the literature of S-AGF. Other aspects regarding the air insulation include the air cavity eccentric geomtrical profile in field applications. Eccentric air cavities can significantly undermine their insulation capacity. Further, a significant research gap in the literature of S-AGF is the availability of accurate fully-coupled models that feature high computational efficiency.

The second part of this thesis address the issue of the Giant Mine contamination (Northerst Territories, Canada). The Giant Gold Mine used to be a major economic force throughout the second half of the twentieth century. Nevertheless, during the mining operations, more than 200,000 tons of toxic arsenic were stored in underground chambers and stopes. After decades of analysis of several arsenic containment methods, AGF was found to be most reliable. Accordingly AGF methods are to be utilized for containing the arsenic over the first stage of project duration lasting for 100 years.

As the Giant Mine is located in a very cold region, the use of thermosyphons as heat

extraction devices can save significant operational costs. This is attributed to the ability of thermosyphons to utilize the ambient air cold temperature to freeze the ground in a cold manner. Although thermosyphons have been used in AGF applications for many several decades, the ground freezing process of the Giant Mine poses several issues that requires more fundamental and applied knowledge. At the fundamental level, thermosyphons used at the Giant Mine are almost 100-meters deep. This creates linear pressure profile along the depth of the thermosyphon due to the high hydrostatic pressure resulting from the large depth of the thermosyphon. At the applied level, the current form of thermosyphons can operate passively in winter seasons only. In warm seasons, the thermosyphons become idle, which significantly slow down the ground freezing process.

In the next section, we will discuss our finding of the AGF methods related to 1) the Cigar Lake Mine and 2) the Giant Mine.

9.2 Discussion of findings

In this thesis, two artificial ground freezing (AGF) systems are modeled: 1) selective artificial ground freezing (S-AGF) and 2) thermosyphon-based artificial ground freezing.

S-AGF systems are currently employed in the Cigar Mine to prevent water infiltration at the mining site at a depth of 400-460 meters below ground surface. Mechanical refrigeration units are energy intensive and result in substantial greenhouse gas emissions, standing against Ottawa's 2050 target of net zero emissions. Accordingly, the first half of our thesis focused on developing fundamental and applied understanding to minimize the cooling load of S-AGF systems and estimate the impact of some operational parameters. Mathematical models of various degrees of complexity are therefore developed in this thesis and validated against experimental measurements.

First of all, a fully-conjugate model coupling the coolant flow, natural convection of air, and ground freezing process is derived and validated against our own experimental

measurements as well as other studies from the literature. Particularly, a computational fluid dynamics (CFD) model of the air and the coolant is developed based on the conservation principles of mass, momentum, and energy. The enthalpy-porosity method is considered for the ground freezing model. This novel S-AGF model demonstrates the importance of adding an air insulation layer along the passive zone to minimize the cooling load of S-AGF systems. In addition, results of scale analysis supported by the fully-conjugate model revealed that the air optimum thickness, L_{opt}, scales as $L_{opt} \sim 2HRa_H^{-1/4}$ where H is the height of the air and Ra_H is the Rayleigh number. This optimum scale minimizes conduction heat transfer across the air cavity without triggering significant natural convection currents.

While this CFD model demonstrates high accuracy and ability to mimic S-AGF systems in lab-scale, it cannot be effectively applied in field-scale due to the typically large domain of S-AGF (hundreds of meters) and long operational time (several moths to years). Thus, a novel reduced-order model for S-AGF systems is derived based on a space marching algorithm to substantially enhance the computational efficiency. The space marching algorithm takes into account the development of the thermal boundary layer of the coolant flow and its effect on the heat extraction capacity along the freeze pipe. The reduced-order model presented the same level of accuracy as that of the fully-conjugate model, but reduced the computational time by more than 99%. After that, more than 30 simulations are conducted utilizng the fast reduced-order models to investigate the impact of the coolant inlet temperature and flow rate. Overall, it is found that reducing the coolant inlet temperature, $T_{in,c}$, is a better approach to speed up the ground freezing process; however, refrigerating the coolant to below -40 [°C] results in over-cooling the frozen ground without significant increase in the speed of the ground freezing process.

Following that, the reduced-order model is adjusted to incorporate the impact of freeze-pipe eccentricity on the cooling load and frozen ground volume. The eccentric behaviour of the freeze-pipe is of quite importance in the field as the inner pipes are observed to zigzag and collide with the casing every 10 meters throughout the 460 meter deep pipes. The novel

model of eccentric S-AGF freeze-pipes shows that, as compared with ideal concentric pipes, freeze-pipe eccentricity causes the cooling load to increase by 20% to 200%, where the lower margin corresponds to high pipes emissivity and vice-versa. Further, freeze-pipe eccentricity slows down the ground freezing process by 17%. Overall, the reduced-order model shows great potential for practical field investigations due to its high accuracy and computational speed.

The second part of the thesis focuses on AGF applications using thermosyphons, which can employ naturally available cold wind during winter seasons to freeze the ground instead of energy intensive refrigeration units. First of all, the operation of deep thermosyphons is found to be challenging in the field due to the significant hydrostatic pressure building up at the bottom sections of the thermosyphons. To obtain a fundamental understanding of thermosyphons operation in AGF, a fully-conjugate CFD model is derived based on the conservation principles of mass, momentum, and energy. Further, a novel pressure-dependent heterogeneous nucleation model is considered in this study to accurately capture the boiling phenomena in deep thermosyphons. The model is validated against an experimental study from the literature and then extended to field-scale similar to that of the Giant Mine. The results indicate that the active boiling zone of thermosyphons can extend from the pool surface to a depth of 10-25 meters under the surface. Underneath the active boiling zone, a dead-zone in which no boiling occurs is observed. Further, in the liquid film zone located above the pool surface, the CFD results show that heat extraction takes the form of sensible heat rather than latent heat (i.e., the liquid film increases in temperature with negligible evaporation). In addition, while the charge pressure of the thermosyphon is found to have a significant initial effect upon starting up the thermosyphon, the effect of the charge pressure becomes negligible towards steady state. Lastly, cooler wind temperature results in higher heat extraction capacity by thermosyphons and deeper active boiling zone.

After that, hybrid thermosyphons are examined due to their capability to freeze the ground in cold seasons, using the cold wind, and warm seasons, through mechanical refriger-

ation units. A novel mathematical model for hybrid thermosyphons is derived and validated against field data from the Giant Mine Remediation Project. The study reveals that incorporating active refrigeration units during warmer seasons can expedite the ground freezing process, but will require significant cooling load and thus greenhouse gas emission equivelant to around 1% of the provincial emissions for every 100 hybrid thermosyphons.

To avoid the tremendous energy expenditures and greenhouse gas emissions, a novel AGF system that runs year-round solely using sustainable energy resources is proposed based on a ground-coupled cold energy storage system. There are two sets of thermosyphons operating in our proposed system: 1) primary thermosyphons located at the Giant Mine site and 2) storage thermosyphons located in the vicinity. In cold seasons, as primary thermosyphons utilize the cold wind to freeze the ground, storage thermosyphons store cold energy inside a nearby ground. In warm season, the stored cold energy is transferred via heat extraction pipes from the cold energy storage pool to the primary thermosyphons. This concept has been demonstrated mathematically using well-validated models against field data and other controlled experimental studies from the literature. The ground freezing process of our proposed system indeed runs year-round purely using sustainable energy resources. The speed of the ground freezing process is one year faster than that of a fully passive system without a mechanical refrigeration unit.

9.3 Contribution to knowledge

This thesis contributes to the fundamental and applied knowledge of the two types of AGF systems presented in the previous section. Starting with S-AGF systems, the following contributions to knowledge are made:

- **Fundamental:** A novel fully-coupled CFD model is developed for S-AGF systems based on the conservation principles of mass, momentum and energy. The model accuracy is validated against experimental measurements conducted at our own laboratories

as well as other experimental studies from the literature.

- **Applied:** Our studies demonstrate that for large AGF applications where the desired ground to be frozen is located at deep levels (tens to hundreds of meters below the ground surface), the use of a S-AGF system can significantly reduce the cooling load due to the air insulation layer in the passive zone where ground freezing is not needed.

- **Fundamental:** A novel scale analysis is conducted supporting the CFD model to understand the heat transfer regimes in the air cavity at different air thickness.

- **Applied:** The scale analysis can be used to approximate the thickness of the cavity resulting in highest insulation and thus lowest heat dissipation in the passive zone thereby minimizing the cooling load in the field.

- **Fundamental:** A novel reduced-order model based on a space marching algorithm is created for S-AGF applications. This model reduced the computational time by more than 99% as compared with the CFD model, while retaining the same level of accuracy.

- **Fundamental:** Our space-marching algorithm is the first to consider the effect of the thermal boundary layer development of the coolant flow on the freeze-pipe heat extraction capacity and profile.

- **Applied:** The reduced-order model is quite useful in practical field applications for the industry to study the impact of various operational parameters, such as the coolant temperature and flow rate.

- **Fundamental:** A novel reduced-order model is derived considering the impact of freeze-pipe eccentricity.

- **Applied:** Freeze-pipe eccentricity slows down the ground freezing process while also increasing heat dissipation in the passive zone by 20%-200% depending on the pipes emissivity.

As for AGF applications using thermosyphons, the following contributions are made:

- **Fundamental:** A novel CFD model is developed for thermosyphons in AGF application based on the conservation principles of mass, momentum, and energy.
- **Fundamental:** A novel pressure-dependent bubble nucleation model is also derived and coupled with the CFD model to capture the phenomena accurately in deep thermosyphons.
- **Applied:** The active boiling zone extends for 10-25 meters from the pool surface.
- **Fundamental:** Heat extraction in the film zone takes the form of sensible heat rather than latent heat.
- **Applied:** The initial charge pressure may have initial effect on starting up the thermosyphon. However, at steady state, the effect of the charge pressure gradually diminishes.
- **Fundamental:** A fully-conjugate mathematical model for hybrid thermosyphons is developed and validated against field data as well as other controlled experimental measurements.
- **Applied:** Active operation of hybrid thermosyphon is energy intensive. It is recommended to employ active refrigeration for the first coupled of years only until building the desired frozen ground. After that, passive operation during winter seasons only can resume the ground freezing process.
- **Applied:** A novel ground-coupled cold energy storage system is proposed to run thermosyphons year-round without employing mechanical refrigeration units. The system is demonstrated mathematically using well-validated models.

9.4 Future directions

The following recommendations are proposed for future on the AGF systems discussed in this study. For S-AGF systems:

- Integrating a mechanical model to the thermo-hydraulic model derived in chapter 2 of this thesis. Ground stresses associated with S-AGF systems cause frequent unplanned interruptions of the mining operations in the Cigar Lake Mine and therefore needs to be addressed.

- Developing a 2D+1D reduced-order model to study S-AGF systems in three dimensions. This will allow researchers and industries to easily examine the impact of freeze-pipes layout on the ground freezing process and cooling load of refrigeration systems. In other words, different freeze pipe configurations can be assessed such as square configuration, diamond configuration, or other innovative configurations.

- Conducting uncertainty analysis to investigate the impact of uncertain geological parameters such as ground porosity and thermal diffusivity.

- Exploring new methods to run S-AGF systems using sustainable energy resources. This can possibly be achieved by integrating an air cavity to thermosyphons.

- Developing a 1+1D model coupled with thermal superposition to optimize S-AGF system in full-scale.

As for thermosyphon-based AGF systems, the following future work can be conducted:

- Optimizing our proposed ground-coupled cold energy storage system by conducting artificial intelligence (AI) analysis that finds the most optimum operational parameters given the time-frame of the project.

- Exploring the possibility of employing the storage thermosyphons in other applications, such as heating of building or geothermal power generation, after completing the ground

freezing process.

- Examining how various CFD algorithms and techniques can affect the boiling phenomena of thermosyphons.

- Our current CFD model requires significant computational resources and very long computational time. Thus, it is desired to developed a reduced-order model that captures the boiling phenomena using a heterogeneous nucleation model while substantially reducing the computational time. Then, the reduced-order models are to be implemented to run thermosyphons for longer periods.

Chapter 10

Conclusion

In this thesis, two artificial ground freezing (AGF) systems are modeled: 1) selective artificial ground freezing (S-AGF) and 2) thermosyphon-based artificial ground freezing. Fundamental and applied objective regarding these systems are considered as follows:

1. Fundamental understanding of natural convection in air enclosures of S-AGF systems.
2. Fundamental understanding of the boiling and condensation phenomena in deep thermosyphons.
3. Coupling mathematical models of heat transfer devices alongside with the ground freezing process.

At the applied level:

1. Development of computationally efficient reduced-order models for field-scale S-AGF applications.
2. Uncovering best practices that can be implemented for S-AGF and H-AGF systems.
3. Proposing novel AGF systems that rely mostly on renewable energy resources.

The objectives are met throughout this thesis as follows:

1. Conjugate CFD models of natural convection of annular air enclosure are derived and validated against experimental data. Further, scale analysis is conducted to further optimize the design of air cavities. The impact of eccentric cavity profile on the insulation capacity of air layers is analyzed.

2. Conjugate CFD models of deep two phase closed thermosyphons are derived based on the Volume of Fluid (VoF) method. Heterogeneous bubble nucleation model is coupled to the VoF methods where boiling only occurs on the walls, and an excess temperature is needed for bubble nucleation to occur.

3. Mathematical models of S-AGF freeze-pipes and thermosyphon-based artificial ground freezing systems are all coupled to the ground freezing process modeled via the enthalpy-porosity method.

At the applied level:

1. 1+1D Reduced-order models of S-AGF systems are derived reducing the computational cost by more that 99% as compared with CFD models, while retaining the same model accuracy.

2. In S-AGF, optimum aspect ratio of air insulation layers are scaled as $L_{opt} \sim 2HRa_H^{-1/4}$. Further, it is recommended to install concentric air cavities and avoid eccentric behavior. As for H-AGF systems, operating the refrigeration units for four months per year can be sufficient, but will still require immense refrigeration load.

3. We proposed a novel system that run thermosyphons passively year-round based on a ground-coupled cold energy storage system. The proposed system does not use refrigeration systems.

More detailed discussion on the outcomes of the study can be found in the previous chapter.

Bibliography

[1] The Mining Association of Canada, The State of Canada's Mining Industry: Facts and Figures 2021 (2021).
URL https://mining.ca/

[2] Government of Canada, Nuclear facility - Cigar Lake Mine (2021).
URL https://nuclearsafety.gc.ca/

[3] CAMECO, Cigar Lake Operation, Tech. rep. (2015).

[4] Your Indigenous Protected And Conserved Areas (2020).

[5] G. P. Newman, D. Maishman, Artificial ground freezing of the McArthur river uranium ore deposit, in: Proceedings: International Conference on Ground Freezing and Frost Action in Soils. Belgium. September, 2000.

[6] Government of Canada, Environment and Climate Change Canada (2019).

[7] R. Silke, The Operational History of Mines in the Northwest Territories, Canada, Tech. rep., Yellowknife (2009).

[8] Steffen Robertson and Kirsten (Canada) Inc., Giant Mine Ground Freezing, Tech. rep., Vancouver (2002).

[9] Canada North Environmental Services, Giant Mine Human Health and Ecological Risk Assessment, Tech. rep. (2018).

[10] CBC News, New study shows 'low risk' to public health 70 years after Giant Mine's toxic legacy (2021).
URL www.cbc.ca

[11] Capital Current, Decades of arsenic poisoning produced by Giant Mine has caused irreversible damage to Dene First Nation land (2021).

[12] P. Evans, D. King, R. Freeman, A. Degray, Summary of Research on the Establishment, Administration and Oversight of the Giant Mine and its Impacts on the Yellowknives Dene First Nation", Tech. rep. (2020).

[13] SRK Consulting (Canada) Inc., Freeze Optimization Study Update for MVEIRB and Parties Aboriginal Affairs and Northern Development Freeze Optimization Study Update for MVEIRB and Parties, Tech. Rep. August (2012).

[14] A. F. Zueter, M. Xu, M. A. Alzoubi, A. P. Sasmito, Development of conjugate reduced-order models for selective artificial ground freezing: Thermal and computational analysis, Applied Thermal Engineering 190 (2021) 116782.

[15] M. A. Alzoubi, M. Xu, F. P. Hassani, S. Poncet, A. P. Sasmito, Artificial ground freezing: A review of thermal and hydraulic aspects, Tunnelling and Underground Space Technology 104 (2020) 103534.